DEVELOPMENT OF A NUMERICAL FRAMEWORK FOR THE MONITORING OF MOIST-CURED AND CORRODED CONCRETE

by

ANDRE MUTUNDA

submitted in accordance with the requirements for

the degree of

DOCTOR OF PHILOSOPHY

in Science, Engineering and Technology

at the

UNIVERSITY OF SOUTH AFRICA

Supervisor: Prof FRANCOIS MULENGA

17 November 2025

Abstract

The durability and long-term performance of concrete are strongly influenced by the complex evolution of cement hydration and corrosion. However, conventional approaches provide limited quantitative means of characterising these processes at the cement-grain scale. This study therefore develops a mathematical and algorithmic framework for analysing the evolution of cement grain colouration (CGC) during hydration and corrosion using colorimetric image analysis and artificial neural networks (ANNs).

Concrete mixtures designed for 30 MPa and 40 MPa compressive strengths were investigated during curing, while the corrosion analysis focused on the 30 MPa mixture exposed to sulphuric acid. Colorimetric images obtained from scanned concrete surfaces were processed to identify characteristic colour types and their temporal evolution. Similarity-frequency matrices were developed to quantify these colour patterns and were subsequently integrated into algorithmic formulations and ANN models. The proposed approach enabled the identification of distinct hydration and corrosion regimes and provided a quantitative description of their evolution over time.

The results showed that C_3S and C_2S contributed differently to hydration development according to the concrete mix and curing period. The developed models also provided predictive insights into compressive strength and temperature evolution. Comparison of white-pixel detection and colour-type similarity approaches demonstrated their complementary applicability: the former supports localised spatial analysis, while the latter provides greater temporal and microstructural resolution.

Overall, the study establishes a quantitative mathematical and algorithmic framework for characterising hydration and corrosion at the cement-grain scale. The proposed approach provides a basis for improved understanding of concrete microstructural evolution and further development of predictive models for concrete performance.

Keywords: Cement hydration; Cement corrosion; Cement grain colouration (CGC); Colorimetric image analysis; Similarity-frequency matrices; Artificial neural networks; Mathematical modelling; Concrete microstructure; C_3S and C_2S; Concrete durability.

DECLARATION

Name: **ANDRE MUTUNDA**

Student number: **62028227**

Degree: Doctor of Philosophy Science, Engineering and Technology **(90040)**

Development of a numerical framework for the monitoring of moist-cured and corroded concrete

I declare that the thesis is my own work and that all the sources that I have indicated and acknowledged by means of means of complete references, and that any use of Artificial Intelligence (AI) has been fully disclosed.

I further declare that I submitted the thesis to the appropriate originality detection system which is endorsed by Unisa and that it falls within the accepted requirements for originality.

I further declare that I have not previously submitted this work, or part of it, for examination at Unisa for another qualification or at any other higher education institution.

I further declare that where Artificial Intelligence (AI) tools have been used in the preparation of this thesis, their use has limited to ethical permissible support, has been disclosed, and does not replace my own original research, my independent critical thinking and analysis, or authorship responsibilities.

I understand that failure to disclose AI use, plagiarism and/or lack of academic integrity may constitute academic misconduct under Unisa's policies.



17 November 2025

SIGNATURE DATE

Acknowledgements

First and foremost, I give thanks to the Lord, the everlasting Jehovah-Jireh, for granting me the strength, patience, and perseverance to complete this thesis.

I am deeply and sincerely grateful to my supervisor, Professor François Mulenga. His exceptional guidance, thoughtful advice, and unwavering support have been the cornerstone of this work. Throughout the journey of this research, his wisdom, encouragement, and dedication have inspired me, shaped my thinking, and greatly enriched both my academic and personal growth. I could not have completed this thesis without his mentorship.

I also wish to express my heartfelt gratitude to my wife, Irene Kamin, whose constant prayers, encouragement, and belief in me have been a source of strength.

To my beloved children Nancy, Hervé, Ruth, Jonathan, Elysée, Gloria, Irene, and Dylan, thank you for your love, patience, and endless inspiration.

Finally, I would like to acknowledge the support and assistance of the staff at Tenke Fungurume Mining, particularly Olivier Tshifungat, Serge Mwamba, Charles Lumpungu, Thadée Katambayi, and Jonathan Kibanza, for their encouragement and help throughout this journey.

Table of contents

Abstract i
Declaration iii
Acknowledgements iv
Table of contents v
List of figures ix
List of tables xix
List of abbreviations and acronyms xxii
CHAPTER 1: INTRODUCTION 1
1.1 Background 1
1.2 State of knowledge and research gaps 2
1.3 Problem statement 3
1.4 Research objectives 4
1.5 Scope and limitations of the study 5
1.5.1 Scope of the study 5
1.5.2 Limitations of the study 5
1.6 Outline of the thesis 6
CHAPTER 2: LITERATURE REVIEW 8
2.1 Introduction 8
2.2 Cement grain hydration in concrete materials 9
2.2.1 Characterization of cement grain microstructure 10
2.2.2 Hydration of cement grain during the early phase 14
2.2.3 Hydration of cement grain during the late phase 20
2.3 Characterization of concrete corrosion due to sulfuric acid attack and subsequent concrete degradation 27
2.3.1 Effects of sulphuric acid on concrete corrosion 27
2.3.2 Characterization of sulphuric acid-induced concrete corrosion and discoloration 34
2.4 Collection of experimental imaging data at macroscopic and microscopic scale 39

2.4.1 Macroscopic acquisition technique of imaging data relating to concrete materials 39
2.4.2 Data extraction using the scanned point method 42
2.4.3 Monitoring disease progression through tissue Colour Changes 44
2.5 Mathematical formulations for concrete material 46
2.5.1 Framework of mathematical formulations for function fitting 47
2.5.2 Framework of mathematical formulations using ANNs 50
2.6 Summary 54
CHAPTER 3: EXPERIMENTAL PROGRAM AND EQUIPMENT 56
3.1 Introduction 56
3.2 Preparation of concrete samples 56
3.2.1 Components of concrete used 57
3.2.2 Preparation of concrete mixtures 58
3.2.3 Curing of concrete samples 62
3.2.4 Compressive strength testing 63
3.3 Protocols used to monitor the colouration of cement grains 65
3.3.1 Preparation of concrete samples used for experimentation 65
3.3.2 Equipment used and experimental tests considered 67
3.3.3 Measurement of cement grain colouration under curing conditions 69
3.3.4 Monitoring of concrete surface colour changes under corrosion conditions 75
3.4 Challenges encountered during the experimental work 77
CHAPTER 4: ANALYSIS OF SCANNED IMAGE DATA 78
4.1 Introduction 78
4.2 Scanned images under curing and corrosion conditions 78
4.2.1 Scanned images under curing conditions 79
4.2.2 Scanned images under corrosion conditions 81
4.3 Methodology for converting coloured images into grey pixel images 83
4.3.1 Images processing under curing and corrosion conditions 84
4.3.2 Black and white pixel values within image processing 92
4.4 Concluding remarks 95
CHAPTER 5: MODELS OF SCANNED POINTS AT CEMENT GRAIN SCALE 96

5.1 Introduction 96
5.2 Computation of scanned points using matrix functions 96
5.3 Artificial neural network architecture for black and white pixel rates .. 98
5.3.1 Implementation of artificial neural network architecture 99
5.3.2 Neural network layer computation and functional fit analysis 104
5.3.3 Training processes of inputs parameters for evaluating output targets 106
5.4 Models of scanned points using artificial neural networks 114
5.4.1 Assessment of black and white pixel rates under curing conditions 114
5.4.2 Assessment of black and white pixel rates under corrosion conditions 121
5.5 Significance of the research findings 125
CHAPTER 6: INVESTIGATION OF HYDRATION AND CORROSION REGIMES WITHIN CONCRETE MIXTURES 127
6.1 Introduction 127
6.2 Hydration and corrosion mechanisms of cement grains 127
6.2.1 Theoretical and methodological foundations of mathematical models for slow-phase hydration and corrosion of cement grains 128
6.2.2 Assessment of theoretical models of cement hydration mechanisms under curing time 130
6.2.3 Assessment of theoretical models of cement hydration mechanisms under exposure time 135
6.3 Advanced analysis of cement grain hydration and corrosion behaviour using colouration features 138
6.3.1 Analytical approach to cement grain hydration and corrosion using colour indicators 138
6.3.2 Framework of mathematical expression for computing the similarity frequencies of cement grain colouration 142
6.3.3 Quantitative modelling of cement hydration and corrosion using colour similarity matrices 151
6.4 Concluding remarks 160

CHAPTER 7: EVALUATION OF CEMENT MICROSTRUCTURES DURING THE SLOW HYDRATION PHASE 162
7.1 Introduction 162
7.2 Development of cement grain hydration mechanisms governed by C_3S and C_2S microstructures during the slow hydration phase 163
7.3 Modelling cement grain hydration governed by C_3S and C_2S microstructures during the slow hydration stage 163
7.4 Modelling C_3S and C_2S effects on mechanical and thermal behaviour of concrete mixtures 167
7.5 Concluding remarks 176
CHAPTER 8: CONCLUSION AND RECOMMENDATIONS 179
8.1 Summary of the findings 179
8.2 Recommendations for future work 182
References 184
Appendices 194

List of figures

Figure 2.1: SEM/EDX micrographs of cement paste showing the early stages of hydration: (a) hydrated cement specimen (HCS), showing C_3S, C_2S and portlandite; and (b) rehydrated cement specimen (RCS), showing C_3S, C_2S and ettringite. 13

Figure 2.2: A comparative study showing the evaluation rates of exothermic heat released by C_3S and C_2S during the early hydration phase (Qi *et al*., 2022)..... 16

Figure 2.3: Comparison of long-term hydration for C_3S and C_2S measured under similar conditions (after Qi *et al*., 2022) 17

Figure 2.4: Composition and thermal treatment specifications for eight cement pastes (Semugaza *et al*., 2023) 18

Figure 2.5: Specific surface area reported for selected types of cement pastes at their respective heat release peak (Semugaza *et al*., 2023)..... 19

Figure 2.6: Exothermic heat released during the early hydration phase for selected types of cement pastes (Semugaza *et al*., 2023) 19

Figure 2.7: Change in compressive strength as a function curing temperature during the late hydration phase: (a) Cement type CEM I 42.5R and (b) cement type CEM II/A-V 42.5R were used (Elkhadiri *et al*., 2023)..... 22

Figure 2.8: Micrographic images of hydrated cement type CEM I 42.5R, influenced by curing temperature and moist-cured age of the specimens. The images are as follows: (a) 4°C at 2 days; (b) 4°C at 28 days; (c) 22°C at 2 days; (d) 22°C at 28 days; (e) 40°C at 2 days (f) 40°C at 28 days (g) 85°C at 2 days (h) 85°C at 28 days (Elkhadiri *et al*., 2023) 23

Figure 2.9: Micrographic images of hydrated cement type (CEM II/A-V 42.5R), influenced by curing temperature and moist-cured age of the specimens. The images are as follows: (a) 4°C at 2 days; (b) 4°C at 28 days; (c) 22°C at 2 days; (d) 22°C at 28 days; (e) 40°C at 2 days (f) 40°C at 28 days (g) 85°C at 2 days (h) 85°C at 28 days (Elkhadiri *et al*., 2023)..... 24

Figure 2.10: Cement grain hydration evaluated over a period of 0 to 30 days with a water-to-cement ratio of 0.40 (Left) and with 0.30 (Right) after Bentz (1997). 26

Figure 2.11: Cement grain hydration evaluated over a period from 0 to 10 days: (left) Degree of hydration as a function of the water-to-cement ratio ranging and (right) Degree of hydration as a function of hydration time (Huang *et al*., 2025) 26

Figure 2.12: Micrographs of hydrated cement paste showing visible damage to the microstructure caused by sulphate attack: (left) intact sample and (right) acid-attacked sample (Devi *et al*., 2022) 29

Figure 2.13: Influence of sulphuric acid concentration of 30 g/ℓ on concrete corrosion, thickness expansion, and aggregate durability (Mutunda, 2019) 30

Figure 2.14: Influence of sulphuric acid concentration of 200 g/ℓ on concrete corrosion, thickness expansion, and aggregate durability (Mutunda, 2019) 30

Figure 2.15: Expansion of aggregate MS (left) and ML (right) at 20 days of immersion in highly concentrated sulphuric solutions of 200 g/ℓ (Mutunda, 2019) 31

Figure 2.16: Evaluation of variations of sulphur concentration using electrical concrete conductivity for concrete mixtures (ML) tested in sulphuric acid solutions of 200 g/ℓ (Mutunda, 2019) 32

Figure 2.17: Colour changes indicating the evolution of concrete corrosion (Shengyuan *et al*., 2012) 37

Figure 2.18: Change in colouration impacted by both sulphur and calcium ions (Taheri *et al.*, 2020) 38

Figure 2.19: Laboratory-scale implementation of the photogrammetric system. On the left, the system is suspended from a steel frame, while on the right, it is mounted on tripods (Habib *et al*., 2014) 40

Figure 2.20: Example of remote sensing monitoring using a photometric system applied to a concrete beam, illustrating deflection-related crack progression with a size of 0.008 m (Left) and 0.001 m (Right) after Jonawski *et al*. (2016) 41

Figure 2.21: Illustration of circular points used for scanning and analysis (Jonawski *et al*., 2016) 43

Figure 2.22: Scanned microscopic images using colour variations contrasting a healthy brain on the left and a Parkinson's diseased brain on the right (Zanaib *et al*., 2020)..... 45

Figure 2.23: Scanned microscopic image using black-and-white-backgrounds showing a brain with cancer (left) and advanced stage of cancer (right) (Zanaib *et al*., 2020)..... 45

Figure 2.24:Mathematical models illustrating the variation in rebar stress as a function of load and displacement (adapted from Samoshkin and Tikhomirov, 2021) 49

Figure 2.25: Representative form of a developed mathematical model for the stress–strain relationship (after Sultan and Hamza, 2023) 50

Figure 2.26: Similitude between neuronal architectures with a human neuron on the left and a model of an artificial neuron on the right (Larsen, 1999) 51

Figure 2.27: Two ANN architectures using each one multiple-input of factors to predict concrete corrosion due to H2SO4 (Hewayde *et al*., 2007): (a) The output layer is the weight loss; (b) The output layer is the compressive strength 53

Figure 3.1: The concrete mixer used for casting 59

Figure 3.2: (Left) Content of the concrete mixer and (Right) recording of the temperature inside the mixer during production..... 60

Figure 3.3: (Left) Concrete sample in the wheelbarrow and (Right) recording of temperature..... 61

Figure 3.4: (Left) Casting of a 150 x 150 x 150 mm concrete cube and (Right) measurement of the surface temperature of the cast concrete 61

Figure 3.5: (a) Curing tank with partial view of concrete cubes and (b) monitoring of water temperature using a thermometer 62

Figure 3.6: (Left) Testing of concrete cube under a cube-press equipment and (Right) Display of the rate of compression 64

Figure 3.7: A concrete cube marked with experimental points for the CGC test with 3 faces presented: (a) Face 1 and (b) both Face 2 and Face 3 66

Figure 3.8: (Left) Lateral and (right) front view of the microscopic scanner 67

Figure 3.9: (Left) Overall view of focus and (Right) support accessory 67

Figure 3.10: (Left) Front view of the thermometer showing the display screen; (Centre) Rear view and (Right) Lateral view of the thermometer 68

Figure 3.11: Flowchart for collecting images of marked points with the microscopic scanner set at 1000x magnification 69

Figure 3.12: (a) Collection of concrete temperature with an infra-red thermometer and (b) overall view showing the device screen 70

Figure 3.13: Image of concrete aimed at with an infra-red thermometer (left) and recording of the temperature (right) 71

Figure 3.14: Sweeping of marked points with a microscopic scanner 73

Figure 3.15: Illustration of both scanning of marked point and indication on screen of the CGC image..... 73

Figure 3.16: Overall view of the computer screen showing the CGC image 74

Figure 3.17: (a) Concrete cube in a container filled with sulphuric acid solution and (b) water-washed concrete cube after 3 days of acid immersion 76

Figure 4.1: Image processing of cement grain colouration for the scanned point 1 for concrete M1 under curing conditions at 3 days (left) and converted black-and-white pixel image (right) 85

Figure 4.2: Image processing of cement grain colouration for the scanned point 1 for concrete M1 under curing conditions at 7 days (left) and converted black-and-white pixel image (right) 85

Figure 4.3: Image processing of cement grain colouration for the scanned point 1 for concrete M1 under curing conditions at 14 days (left) and converted black-and-white pixel image (right) 86

Figure 4.4: Image processing of cement grain colouration for the scanned point 1 for concrete M1 under curing conditions at 21 days (left) and converted black-and-white pixel image (right) 86

Figure 4.5: Image processing of cement grain colouration for the scanned point 1 of concrete M1 under curing conditions at 28 days (left) and converted black-and-white pixel image (right) 87

Figure 4.6: Image processing of cement grain colouration at scanned point 1 of concrete M1 under corrosion conditions at 3 days (left), alongside the corresponding black-and-white pixel image (right) 88

Figure 4.7: Image processing of cement grain colouration at scanned point 1 of concrete M1 under corrosion conditions at 6 days (left), alongside the corresponding black-and-white pixel image (right) 88

Figure 4.8: Image processing of cement grain colouration at scanned point 1 of concrete M1 under corrosion conditions at 9 days (left), alongside the corresponding black-and-white pixel image (right) 89

Figure 4.9: Image processing of cement grain colouration at scanned point 1 of concrete M1 under corrosion conditions at 12 days (left), alongside the corresponding black-and-white pixel image (right) 89

Figure 4.10: Image processing of cement grain colouration at scanned point 1 of concrete M1 under corrosion conditions at 18 days (left), alongside the corresponding black-and-white pixel image (right) 90

Figure 4.11: Image processing of cement grain colouration at scanned point 1 of concrete M1 under corrosion conditions at 24 days (left), alongside the corresponding black-and-white pixel image (right) 90

Figure 4.12: Image processing of cement grain colouration at scanned point 1 of concrete M1 under corrosion conditions at 27 days (left), alongside the corresponding black-and-white pixel image (right) 91

Figure 5.1: ANN architecture for scanned points P_1, P_2, and P_3, illustrating the connections and signal transfer across layers 99

Figure 5.2: ANN architecture for scanned points P_4, P_5, and P_6, illustrating the connections and signal transfer across layers 100

Figure 5.3: ANN architecture for scanned points P_7, P_8, and P_9, illustrating the connections and signal transfer across layers 100

Figure 5.4: Network topology of input, hidden, and output neurons for scanned points P_1, P_2, and P_3, highlighting the interconnections and the associated weight distribution 101

Figure 5.5: Network topology of input, hidden, and output neurons for scanned points P_4, P_5, and P_6, highlighting the interconnections and the associated weight distribution 102

Figure 5.6: Network topology of input, hidden, and output neurons for scanned points P_7, P_8, and P_9, highlighting the interconnections and the associated weight distribution 103

Figure 5.7: Model A/OBWP1 with M1 / 30 MPa and IBWP1 for evaluating the black and white pixel rates into scanned point 1 under curing conditions 115

Figure 5.8: Model F/OBWP6 with M1 / 30 MPa and IBWP6 for evaluating the black and white pixel rates into scanned point 6 under curing conditions 115

Figure 5.9: Model H/OBWP8 with M1 / 30 MPa and IBWP8 for evaluating the black and white pixel rates into scanned point 8 under curing conditions 116

Figure 5.10: Model I/OBWP9 with M1 / 30 MPa and IBWP9 for evaluating the black and white pixel rates into scanned point 9 under curing conditions 116

Figure 5.11: Schematic representation of Model I/scanned point 9 with M1 / 30 MPa in recording at 14 days both the highest and lowest pixel rate under curing conditions..... 117

Figure 5.12: Model A/OBWP1 with M2 / 40 MPa and IBWP1 for evaluating the black and white pixel rates into scanned point 1 under curing conditions..... 118

Figure 5.13: Model F/OBWP6 with M2 / 40 MPa and IBWP6 for evaluating the black and white pixel rates into scanned point 6 under curing conditions..... 118

Figure 5.14: Model H/OBWP8 with M2 / 40 MPa and IBWP8 for evaluating the black and white pixel rates into scanned point 8 under curing conditions..... 119

Figure 5.15: Model I/OBWP9 with M2 / 40 MPa and IBWP9 for evaluating the black and white pixel rates into scanned point 9 under curing conditions 119

Figure 5.16: Schematic representation of Model I/scanned point 9 with M2 / 40MPa in recording at 14 days both the highest and lowest pixel rate under curing conditions..... 120

Figure 5.17: Model A/OBWP1 with M1 / 30 MPa and IBWP1, tested to sulphuric acid of 30 g/ℓ, for evaluating the black and white pixel rates into scanned point 1 under corrosion conditions..... 121

Figure 5.18: Model F/OBWP6 with Mix 1 / 30 MPa and IBWP6, tested to sulphuric acid of 30 g/ℓ, for evaluating the black and white pixel rates into scanned point 6 under corrosion conditions..... 122

Figure 5.19: Model H/OBWP8 with M1 / 30 MPa and IBWP8, tested to sulphuric acid of 30 g/ℓ, for evaluating the black and white pixel rates into scanned point 8 under corrosion conditions..... 122

Figure 5.20: Model I/OBWP9 with M1 / 30 MPa and IBWP9, tested to sulphuric acid of 30 g/ℓ, for evaluating the black and white pixel rates into scanned point 9 under corrosion conditions 123

Figure 5.21: Schematic representation of Model F (scanned point 6) 124

Figure 6.1: Sensitivity of the OWP1 model at scanned point P1 within M1 (30 MPa) in capturing the variation of the theoretical CGH model 131

Figure 6.2: Sensitivity of the OWP3 model at scanned point P3 within M1 (30 MPa) in capturing the variation of the theoretical CGH model 131

Figure 6.3: Sensitivity of the OWP6 model at scanned point P6 within M1 (30 MPa) in capturing the variation of the theoretical CGH model 132

Figure 6.4: Sensitivity of the OWP9 model at scanned point P9 within M1 (30 MPa) in capturing the variation of the theoretical CGH model 132

Figure 6.5: Sensitivity of the OWP1 model at scanned point P1 within M2 (40 MPa) in capturing the variation of the theoretical CGH model 132

Figure 6.6: Sensitivity of the OWP3 model at scanned point P3 within M2 (40 MPa) in capturing the variation of the theoretical CGH model 133

Figure 6.7: Sensitivity of the OWP7 model at scanned point P7 within M2 (40 MPa) in capturing the variation of the theoretical CGH model. 133

Figure 6.8: Sensitivity of the OWP8 model at scanned point P8 within M2 (40 MPa) in capturing the variation of the theoretical CGH model 133

Figure 6.9: Sensitivity of the OWP1 model at scanned point P1 within M1 (30 MPa) in capturing the variation of the theoretical CC model tested to sulphuric acid concentration of 30 g/ℓ..... 136

Figure 6.10: Sensitivity of the OWP2 model at scanned point P2 within M1 (30 MPa) in capturing the variation of the theoretical CC model tested to sulphuric acid concentration of 30 g/ℓ 136

Figure 6.11: Sensitivity of the OWP6 model at scanned point P6 within M1 (30 MPa) in capturing the variation of the theoretical CC model tested to sulphuric acid concentration of 30 g/ℓ 137

Figure 6.12: Modelling of α1-type colour frequency patterns in hydrated cement grains (M1 / 30 MPa) 151

Figure 6.13: Modelling of α2-type colour frequency patterns in hydrated cement grains (M1 / 30 MPa) 152

Figure 6.14: Modelling of α3-type colour frequency patterns in hydrated cement grains (M1 / 30 MPa) 152

Figure 6.15: Modelling of β_1-type colour frequency patterns in hydrated cement grains (M1 / 30 MPa) 152

Figure 6.16: Modelling of α1-type colour frequency patterns in hydrated cement grains (M2 / 40 MPa) 154

Figure 6.17: Modelling of α2-type colour frequency patterns in hydrated cement grains (M2 / 40 MPa) 154

Figure 6.18: Modelling of α3-type colour frequency patterns in hydrated cement grains (M2 / 40 MPa) 155

Figure 6.19: Modelling of β1-type colour frequency patterns in hydrated cement grains (M2 / 40 MPa) 155

Figure 6.20: Modelling of ɣ1-type colour frequency patterns in corroded cement grains (M1 / 30 MPa) with a sulphuric acid concentration of 30 g/ℓ 157

Figure 6.21: Modelling of ɣ2-type colour frequency patterns in corroded cement grains (M1 / 30 MPa) with a sulphuric acid concentration of 30 g/ℓ 157

Figure 6.22: Modelling of ɣ3-type colour frequency patterns in corroded cement grains (M1 / 30 MPa) with a sulphuric acid concentration of 30 g/ℓ 158

Figure 7.1: Modelling of CGH in predicting C_3S and C_2S microstructures within M1 / 30MPa as per Equations (7.1) – (7.4) 165

Figure 7.2: Modelling of CGH in predicting C_3S and C_2S microstructures within M2 / 40MPa as per Equations (7.1) – (7.4) 165

Figure 7.3: Hydration models of C_3S for predicting the CS of the M1 / 30 MPa concrete mix..... 171

Figure 7.4: Hydration models of C_3S for predicting the CT within the M1 / 30 MPa concrete mix..... 171

Figure 7.5: Hydration models of C_2S for predicting the CS of the M1 / 30 MPa concrete mix..... 172

Figure 7.6: Hydration models of C_2S for predicting the CT within the M1 / 30 MPa concrete mix..... 172

Figure 7.7: Hydration models of C_3S for predicting the CS of the M2 / 40 MPa concrete mix..... 174

Figure 7.8: Hydration models of C_3S for predicting the CT within the M2 / 40 MPa concrete mix..... 174

Figure 7.9: Hydration models of C_2S for predicting the CS of the M2 / 40 MPa concrete mix..... 174

Figure 7.10: Hydration models of C_2S for predicting the CT within the M2 / 40 MPa concrete mix..... 175

List of tables

Table 2.1: Overview of photogrammetric systems and macroscopic imaging techniques used for crack propagation analysis under variable load conditions (Jonawski *et al.*, 2016)..... 41

Table 3.1: Mix compositions for M1 (30 MPa) and M2 (40 MPa) concrete cubes60

Table 3.2: Compressive strengths measured during the curing of concrete cubes prepared following M1 and M2 designs..... 65

Table 3.3: Temperatures recorded for concrete cubes of mix design M1 for different curing ages..... 71

Table 3.4: Temperatures recorded for concrete cubes of mix design M2 for different curing ages..... 72

Table 3.5: Experimental procedure of immersion tests under curing conditions 74

Table 3.6: Adopted experimental procedure for immersion tests under corrosion conditions..... 76

Table 4.1: Scanned images under curing conditions for concrete mixture (M1/30MPa)..... 79

Table 4.2: Scanned images under corrosion conditions for concrete mixture (M1/30MPa)..... 81

Table 4.3: Analysis of the distribution of black and white pixel rates for nine scanned points on Face 1 of the M1 concrete cube (30 MPa) under curing conditions after 3 days..... 92

Table 4.4: Analysis of the distribution of black and white pixel rates for nine scanned points on Face 1 of the M1 concrete cube (30 MPa) under curing conditions after 28 days..... 93

Table 4.5: Analysis of the distribution of black and white pixel rates for nine scanned points on Face 1 of the M1 concrete cube (30 MPa) under corrosion conditions after 3 days..... 93

Table 4.6: Analysis of the distribution of black and white pixel rates for nine scanned points on Face 1 of the M1 concrete cube (30 MPa) under corrosion conditions after 27 days 94

Table 5.1: Activation of neural network layers for the rate of black-and-white pixel image under curing conditions at 3 days using M1 / 30 MPa 107

Table 5.2: Activation of neural network layers for the rate of black-and-white pixel image under curing conditions at 7 days using M1 / 30 MPa 108

Table 5.3: Activation of neural network layers for the rate of black-and-white pixel image under curing conditions at 21 days using M1 / 30 MPa 108

Table 5.4: Activation of neural network layers for the rate of black-and-white pixel image under curing conditions at 28 days using M1 / 30 MPa 109

Table 5.5: Activation of neural network layers for the rate of black-and-white pixel image under corrosion conditions at 3 days using M1 / 30 MPa, tested to sulphuric acid of 30 g/ℓ 110

Table 5.6: Activation of neural network layers for the rate of black-and-white pixel image under corrosion conditions at 6 days using M1 / 30 MPa, tested to sulphuric acid of 30 g/ℓ 111

Table 5.7: Activation of neural network layers for the rate of black-and-white pixel image under corrosion conditions at 24 days using M1 / 30 MPa, tested to sulphuric acid of 30 g/ℓ 112

Table 5.8: Activation of neural network layers for the rate of black-and-white pixel image under corrosion conditions at 27 days using M1 / 30 MPa, tested to sulphuric acid of 30 g/ℓ 112

Table 6.1: Distribution of subnetworks according to curing time 128

Table 6.2: Distribution of subnetworks according to corrosion time 129

Table 6.3: Input and output data for assessing the hydration regime 129

Table 6.4: Input and output data for assessing the corrosion regime 130

Table 6.5: Description of colours observed in CGC images during curing of concrete samples: M1 (30 MPa) and M2 (40 MPa) at 28 days 139

Table 6.6: Description of colours observed in CGC images during corrosion of concrete M1 (30 MPa @ 28 days) in 30 g/ℓ sulfuric acid 140

Table 6.7: Colour frequency similarity values associated with CGH on Faces 1 – 8 after 3 days of curing (M1 / 30 MPa) 148

Table 6.8: Colour frequency similarity values associated with CGH on Faces 1 – 8 after 14 days of curing (M1 / 30 MPa) 148

Table 6.9: Colour frequency similarity values associated with CGH on Faces 1 – 8 after 28 days of curing (M1 / 30 MPa) 148

Table 6.10: Colour frequency similarity values associated with CC on Faces 1 – 4 after 3 days of exposure 149

Table 6.11: Colour frequency similarity values associated with CC on Faces 1 – 4 after 12 days of exposure 149

Table 6.12: Colour frequency similarity values associated with CC on Faces 1 – 4 after 27 days of exposure 149

Table 7.1 Material ratios and mix design parameters (M1 / 30 MPa) 168

Table 7.2 Material ratios and mix design parameters (M2 / 40 MPa) 169

List of abbreviations and acronyms

ANN	Artificial neural network
BAP	Black area-proportion
CC	Cement corrosion
CFD	Colour frequency distributions
CGC	Cement grain colouration
CGH	Cement grain hydration
CS	Compressive strength
CT	Concrete temperature
IBWP	Identification indices of black and white image pixels
M1	Concrete mixture with composition of 30 MPa
M2	Concrete mixture with composition of 40 MPa
MBA	Matrix-based algorithms
OBP	Output of black pixel rate
OBWP	Output of black and white pixel rate
OWP	Output of white pixel rate
SCFe	Similarity of colour features
SCFe_CGC	Similarity of colour features in CGC image
SCFr_CGC	Similarity for colour frequencies in CGC image descriptions
WAP	White area-proportion

CHAPTER 1: INTRODUCTION

1.1 Background

Over the past decade, the integration of digital frameworks grounded in complex mathematical formulations has become pivotal to addressing problems of materials science (Ukrainczyk and Ukrainczyk, 2008; Fedosov *et al.*, 2017; Samoshkin and Tikhomirov 2021; Sultan and Hamza, 2023). These mathematical structures have emerged as fundamental tools for modelling the chemical, physical, and mechanical behaviours of construction materials. Unlike earlier methodologies that relied primarily on empirical data and curve fitting techniques, mathematical models now offer a rigorous and systematic framework for representing material phenomena. By enabling the integration of multidimensional datasets within the constraints of physical and mathematical laws, these models offer enhanced predictive accuracy (Fedosov *et al*., 2017; Samoshkin and Tikhomirov 2021; Sultan and Hamza, 2023).

Matrix-based formulations coupled with algorithmic expressions are also increasingly utilized for input/output analysis within artificial neural network (ANN) architectures (Larsen, 1999; Sultan and Hamza, 2023). However, despite their growing use, the application of such matrix-driven approaches remains relatively underexplored in the context of concrete corrosion modelling (Attiogbe and Rizzkala, 1988; Mutunda, 2019; Shengyuan *et al*., 2012). In this thesis, the integration of matrix formulations with algorithmic expressions is crucial for addressing the complex evolution of hydration and corrosion regimes in concrete during the slow phase. This approach enables the identification of correlations between cement microstructures, hydration–corrosion dynamics, and the kinetics of compressive strength and temperature. Moreover, the matrix–algorithm coupling enhances the computational efficiency and predictive accuracy of the artificial neural network (ANN) models developed in this research.

1.2 State of knowledge and research gaps

Despite growing advancements in mathematical modelling, existing theories continue to exhibit significant limitations in the description of the complex mechanisms underlying the behaviour of hydrated and corroded concretes, particularly under moist-curing and slow-corrosion conditions (Bye, 1999; Liu and Deng, 2015; Qi *et al.*, 2021; Semugaza *et al*., 2023; Huang *et al.*, 2025).

Three major gaps are still open for research in the current body of knowledge. First, there is a lack of a comprehensive mathematical framework capable of accurately capturing the evolution of hydrated and corroded concrete. While various empirical approaches exist, none provides a structured formulation that integrates the dynamic interactions between hydration and degradation phenomena (Elkhadiri *et al*., 2009; Liu and Deng, 2015; Zhang *et al*. ,2019; Devi *et al.*,2022; Semugaza *et al*., 2023). Second, current theoretical models fall short in representing the interactions between the microstructures of cement and the resulting physical and mechanical properties of concrete mixtures. Note here that tricalcium silicate (C_3S) and dicalcium silicate (C_2S) are the two key components that dictate the microstructure of cement and govern slow hydration mechanisms in concrete. Furthermore, compressive strength and heat release are the most quoted properties of concrete amongst others (Elkhadiri *et al.,* 2009; Bye, 2011; Jansen *et al.*, 2012). Third, underlying mechanisms that drive the process of concrete corrosion particularly under low concentrations of sulphuric acid (i.e., below 30 g/ℓ) are yet to be elucidated. Indeed, current theoretical models do not describe well the interplay between corrosion and structural deterioration of concrete. The consensus amongst researchers is that this may be attributed to the complex nature of the concrete corrosion phenomenon (Allahverdi *et al*., 2020; Attiogbe and Rizkalla, 1988; Azarza and Gupta, 2017; Hewayde *et al.,* 2007; Liu and Deng, 2015; Mutunda, 2019; Shengyuan *et al*., 2012; Ukrainczyk and Ukrainczyk, 2008).

The research gaps presented above underscore the need for robust mathematical formulations capable of capturing both hydration and corrosion mechanisms.

Particular attention is required for moist-cured and acid-exposed concrete systems so as to better predict and analyse the durability and performance of concrete materials.

1.3 Problem statement

Understanding the coupled processes of hydration and corrosion in concrete remains a major challenge in the field of construction materials. Although extensive research has been carried out on cement hydration, very few existing models examine the role of individual cement grains, such as C_3S and C_2S, while fully accounting for their dynamic interactions and energetic activity (Qi *et al*., 2021; Semugaza *et al.*, 2023; Elkhadiri *et al*., 2023). These microstructural variations significantly influence the evolution of compressive strength and temperature, particularly during the slow hydration phase (Bye, 1999; Elkhadiri *et al*., 2009; Qi *et al*., 2021; Semugaza *et al*., 2023; Vasconcellos *et al*., 2023). Moreover, most macroscopic approaches fail to link these microscopic mechanisms with the global performance of concrete under corrosive environments. The lack of detailed understanding of how microstructural changes govern the transition between hydration and corrosion regimes limits the accuracy of existing predictive models. This gap becomes even more critical when considering the exposure of concrete to low-acid environments, where corrosion progresses slowly and complexly (Devi *et al.*, 2022). In such conditions, the mechanisms controlling the initiation and propagation of degradation are still poorly characterized (Devi *et al*., 2022; Taheri *et al*. ,2020). Consequently, there is a strong need for a mathematical framework capable of describing the hydration and corrosion of concrete as a function of the activity of cement grains. Such a framework would provide new insights into how the intrinsic properties of C_3S and C_2S phases influence the thermal and mechanical evolution of concrete. Addressing this research problem is essential to improve the accuracy of durability predictions and optimize concrete mix designs for longer service life. Furthermore, developing a unified approach that integrates both hydration kinetics and

corrosion dynamics would enhance the understanding of material degradation processes. Ultimately, solving this problem contributes to advancing concrete science by bridging the gap between microstructural behaviour and macroscopic performance. It also supports the development of more sustainable, durable, and resilient concrete materials for modern infrastructure.

1.4 Research objectives

The main objective of this study is to develop a mathematical framework descriptive of the hydration and corrosion of concrete as a function of the activity of grains present in the cement. The secondary research objective is to assess the influence of the key cement microstructures (i.e., C_3S and C_2S) on compressive strength and temperature evolution.

Three research questions were therefore formulated in line with the above objectives:

- What are the prevalent types of hydration and corrosion regimes during the slow phases?
- How do the key cement microstructures (i.e., C_3S and C_2S) influence the evolution of compressive strength and temperature in concrete during slow hydration period, i.e., 3 to 28 days?
- To what extent does the concrete mix design affect the progression of microstructural changes and the dominant hydration regimes under the slow phase?

Addressing these three research questions required a structured experimental program where several concrete mixtures were monitored in terms of compressive strength and temperature as they cure/hydrate or corrode. Relevant data were used to effectively build the mathematical models at cement grain scale as set out for this research study.

1.5 Scope and limitations of the study

1.5.1 Scope of the study

This research investigates hydration and slow corrosion at the cement-grain scale using two concrete mixtures: M1 (30 MPa) and M2 (40 MPa). The hydration study covers the period from 3 to 28 days, whereas corrosion is investigated for M1 over 3 to 27 days.

The study examines the behaviour of C_3S and C_2S and their influence on compressive strength, concrete temperature and microstructural development during the slow hydration phase. The two concrete mixtures were deliberately selected to provide variation in mix design and strength while maintaining a focused experimental programme suitable for developing and evaluating the proposed data-driven numerical framework.

The corrosion investigation uses a 30 g/l sulphuric acid concentration to facilitate gradual corrosion development and provide an appropriate temporal window for monitoring changes in cement grain colouration and pixel characteristics. The study combines scanned surface imaging, colorimetric and pixel-based analysis, mathematical formulations and artificial neural networks (ANNs) to characterise and model the temporal evolution of hydration and corrosion.

1.5.2 Limitations of the study

The study is limited to two concrete mixtures, with corrosion analysis restricted to M1 (30 MPa), and to the defined hydration and corrosion periods. The selected 30 g/l sulphuric acid concentration represents a specific controlled exposure condition and is not intended to represent all possible acid concentrations or environmental conditions.

The proposed mathematical and ANN models are based on the experimentally obtained colorimetric and pixel-based data. Their applicability is therefore dependent on the characteristics, range and distribution of the available dataset, as well as on the assumption that the identified colorimetric features provide

representative indicators of hydration and corrosion evolution at the cement-grain scale.

The experimental programme was conducted under controlled laboratory conditions and does not comprehensively account for the variability of field environments. In addition, detailed chemical and mineralogical analyses and comprehensive statistical validation, including RMSE and AAE analyses, are outside the scope of the present study.

These delimitations define the conditions under which the proposed framework has been developed and evaluated. Further investigation involving additional concrete mixtures, acid concentrations, exposure conditions, larger datasets and complementary chemical or mineralogical analyses would provide opportunities to assess and refine its general applicability and robustness.

1.6 Outline of the thesis

This thesis is structured into eight chapters. Chapter One sets out the general context and scope of the study, emphasising the need for a rigorous mathematical framework to describe hydration and corrosion mechanisms and the role of cement microstructures throughout the service life of concrete.

Chapter 2 reviews the relevant literature on the microstructural characterisation of cement grains and the chemical processes underpinning matrix hardening. Key hydration mechanisms are discussed in terms of heat release and early-age strength development. The chapter also addresses the effects of sulphuric acid corrosion — namely, volumetric expansion, surface degradation and layer discolouration — as well as neural-network-based modelling approaches used to assess corrosion-related deterioration.

Chapter 3 details the experimental programme, including the data collection procedures, the equipment employed, and the laboratory tests carried out to meet the research objectives.

Chapter 4 presents the scanned image datasets obtained under curing and corrosion conditions. A preliminary assessment of colour changes associated with hydration and corrosion at the grain scale is provided, followed by the conversion of coloured images into greyscale pixel data for subsequent analysis.

Chapter 5 develops mathematical models describing slow-phase hydration and corrosion of cement grains. These models draw upon several neural network architectures and incorporate the microstructural characteristics of cement under both curing and corrosive environments.

Chapter 6 investigates hydration and corrosion mechanisms using mathematical and algorithmic tools. It examines the hydration regimes associated with C_3S and C_2S during curing and under mild sulphuric acid exposure.

Chapter 7 focuses on the modelling of C_3S and C_2S microstructures during slow hydration. The models, derived from colorimetric image analysis, are used to relate the behaviour of these phases to strength development and temperature evolution in concrete.

Chapter 8 is the concluding chapter. It summarises the main findings and provides recommendations for future research.

CHAPTER 2: LITERATURE REVIEW

2.1 Introduction

In recent years, the hydration of cement grains has attracted substantial scientific interest, particularly regarding the interaction between hydration kinetics and environmental factors such as curing conditions and service exposure (Bye, 2011; Aïtcin and Flatt, 2016; Semugaza *et al*., 2023; Boughanmi and Megriche, 2023). A comprehensive understanding of these interactions is essential for improving the performance, durability and service life of concrete under realistic exposure conditions.

The interplay between hydration kinetics, notably between the C_2S and C_3S phases, plays a decisive role in determining both the thermal and mechanical evolution of concrete. Yet, the underlying microstructural transformations that govern these coupled processes remain insufficiently elucidated in the current literature (Devi *et al*., 2022; Taheri *et al*., 2020). A deeper exploration of their reaction mechanisms is therefore imperative to link hydration dynamics with the long-term integrity of the cement matrix. Accordingly, the present chapter aims to address these gaps by discussing the methodological limitations of existing analytical approaches and by highlighting the need for more robust indicators capable of capturing these complex behaviours.

This chapter is divided into four main parts. The first section examines the microstructure of cement grains and the chemical reactions responsible for matrix hardening. It also discusses hydration mechanisms, focusing on factors such as heat evolution, compressive strength, curing temperature, and water-to-cement ratio. The second section reviews sulfuric acid-induced corrosion, highlighting mechanisms of volumetric expansion and surface erosion. The third section outlines imaging techniques used in concrete diagnostics and notes their limitations for this study. The final section introduces mathematical models based on ANNs to simulate corrosion-induced degradation in cementitious systems.

2.2 Cement grain hydration in concrete materials

In recent years, cement hydration has attracted substantial scientific interest because of its fundamental influence on the development of concrete microstructure and its subsequent mechanical and durability performance. Particular attention has been given to the interaction between hydration kinetics and environmental factors, including curing conditions and service exposure (Bye, 2011; Aïtcin and Flatt, 2016; Semugaza *et al*., 2023; Boughanmi and Megriche, 2023). Understanding these interactions is essential for improving the performance, durability and service life of concrete under realistic exposure conditions.

As a fundamental chemical component of concrete, cement plays an essential role in improving the physical, chemical, and mechanical properties of the concrete matrix (Roy, 1993; Fernandes and Broekmas, 2013). Over the past decade, significant research on concrete technology have been devoted to the hydration mechanisms of cement grains. And particular attention has been paid to the influence of hydration on both compressive strength and temperature development during the curing process (Bye, 1999; Elkhadiri *et al*., 2009; Qi *et al*., 2021; Semugaza *et al*., 2023; Vasconcellos *et al*., 2023). These studies highlight the critical role of cement microstructure in governing hydration behaviour and performance outcomes. To gain a deeper understanding, it is therefore necessary to examine the chemical interactions within cement grains and their evolution throughout both early and late hydration phases. In this section, the characterization of cement grain microstructure is examined through the chemical interactions that occur between cement components and water during hydration. Both the early and late hydration phases, primarily governed by C_3S and C_2S reactions influencing heat evolution and strength development, are reviewed. Furthermore, experimental investigations addressing these hydration stages from a micrographic perspective are also discussed.

2.2.1 Characterization of cement grain microstructure

Cement particles are generally composed of various chemical elements that play a fundamental role in enhancing the durability of concrete (Boughanmi and Megriche, 2023; Mehta and Monteiro, 2006). During the hydration process, cement grains interact with water not only to initiate chemical reactions but also to bind the inert components of concrete, such as fine and coarse aggregates. The hydration of cement grain is therefore an essential process responsible for the chemical transformation of the microstructure of cement (Bye, 1999; Mehta and Monteiro, 2006; Semugaza *et al*., 2023). During hydration, each cement phase undergoes distinct chemical reactions that contribute differently to the evolution of the matrix. Understanding the specific roles of tricalcium aluminate (C_3A), tetracalcium aluminoferrite (C_4AF), C_3S and C_2S is crucial for linking microstructural changes to mechanical performance. C_3A, C_4AF, C_3S and C_2S are key elements that contribute to the hardening of Portland cement and of concrete mixtures (Bye, 1999). Concrete resistance depends primarily on these four essential components.

Concordant studies show that the hydration process of cement is governed by a series of chemical reactions between the cement components and water (Richardson, 2008; Scrivener and Nonat, 2011; Qi *et al*., 2021; Semugaza *et al*., 2023; Huang *et al*., 2025; Huang *et al*., 2025). Each reaction contributes differently to the development of concrete strength within the hydration time. Therefore, cement components react under the hydration process as follows: First, C_3S reacts rapidly with water to produce calcium silicate hydrate (C-S-H) and calcium hydroxide (CH). This then contributes to the development of the early mechanical strength of concrete, particularly within the first seven days of curing (Bye, 1999; Huang *et al*., 2025). Second, the reaction of C_2S follows and generates additional C-S-H and CH over a longer period. Note here that C_2S reacts more slowly compared to C_3S. The delayed reaction improves the long-term mechanical strength and durability of the concrete (Bye, 2011). Third, C_3A undergoes a rapid and highly exothermic reaction with water, especially in the presence of gypsum.

This reaction, prevalent during the initial phase of hydration, leads to the formation of a salt later converted to monosulfate. The noted reactivity of C_3A influences the setting time and early-age strength development of concrete (Li *et al*., 2020; Huang *et al*., 2025). Fourth, C_4AF reacts moderately with water and contributes to the formation of various hydrates. And although its impact on strength development is less pronounced, its primary role lies in influencing the colour and thermal behaviour of the cement paste.

The hydration reactions described above result in the progressive formation of a solid microstructure that defines the mechanical performance and durability of the hardened concrete (Bye, 2011; Devi *et al*., 2022; Huang *et al*., 2025). Chemical reactions leading to the hydration of cement components are presented as follows (Qi *et al*., 2021):

$$C_3S + 3.1H \rightarrow C_{1.7}\acute{S}H_{1.8} + 1.3CH \quad (2.1)$$

$$C_2S + 2.1H \rightarrow C_{1.7}\acute{S}H_{1.8} + 0.3CH \quad (2.2)$$

$$C_3A + 6H \rightarrow C_3AH_6 \quad (2.3)$$

$$C_4AF + 10H \rightarrow C_3AH_6 + CH + FH_3 \quad (2.4)$$

Note in Equations (2.1) – (2.4) that the symbols C, H, S, A, F and Ś represent CaO, H_2O, SiO_2, Al_2O_3, F_2O_3, and SO_3 respectively.

Three important steps accompany the hydration of cement microstructures expressed in Equations (2.1) – (2.4): the activation, crystallisation, and hardening of cement paste (Mehta and Monteiro, 2006; Sharpley, 2015; Qi *et al*., 2021; Devi *et al*., 2022). Activation takes place when cement microstructures come into contact with water thereby initiating the hydration process. This is followed by the crystallisation of the cement paste. Crystallisation is essentially governed by the plasticity of the cement paste amongst other physical properties (Roy, 1993; Sharpley, 2015). Hardening is the last step during which the cement paste starts to solidify by losing gradually its plasticity (Bye, 1996 & 2011; Roy, 1993).

The rate at which the concrete matrix hardens is dictated by the chemical activation process in Equation (2.1) to (2.4). Here, three distinct phases are involved in hardening concrete: the crystallisation of the cement paste, the hardening of the calcium silicate hydrate as well as the formation of unstable crystals. These three hardening phases govern the microstructure-solidification process of the cement matrix. They play a crucial role in ensuring strength and durability of concrete mixtures while equally inducing salt formation (Bye, 2011; Semugaza *et al*., 2023). Indeed, cement grains solidify through the hydration process that occurs very quickly during the crystallization stage of the cement paste. This kind of microstructure-solidification is more often caused by calcium monosulfoaluminate hydrates (AFm), the proportion of which within the volume of hydrated paste is 15 – 20% (Sharpley, 2015; Souza *et al*., 2020; Devi *et al*., 2022; Huang *et al*., 2025). In addition to this, C_3S and C_4AF are the main component of C-S-H responsible for the low level of solidification observed very early. Both components encourage the high hydration activity occurring within the first 9 to 10 hours of hydration. This is followed by solidification which leads to the hardening of C-S-H present in the cement matrix. The C-S-H component occupies approximately a volume of 50 – 60% in the hydrated paste (Bye 1999; Devi *et al*., 2022). The last phase of microstructure-solidification is related to the formation of unstable crystals of calcium hydroxide $Ca(OH)_2$. These unstable crystals induce the formation of ettringite and portlandite salts. It was argued that ettringite and portlandite salts are responsible for the low microstructure-solidification observed on the superficial faces of concrete matrix (Allahverdi and Škvára, 2000; Mehta and Monteiro, 2006; Liu and Deng, 2015; Guimarãies *et al*., 2016; Devi *et al*., 2022).

Micrography is widely used as an experimental technique for the characterisation and analysis of the physical properties of cement microstructures (Taylor, 1997; Mehta and Monteiro, 2006; Scrivener and Nonat, 2011; Mindess *et al*., 2003; Elkhadiri *et al*., 2009; Han *et al*., 2014; Devi *et al*., 2022). The technique relies on the acquisition of experimental data by means of advanced imaging and analytical

tools such as Scanning Electron Microscopy (SEM), X-ray Diffraction (XRD), and Energy Dispersive X-ray Spectroscopy (EDX). Operating principles and procedures for these instruments are extensively documented in the literature (Taylor, 1997; Mehta and Monteiro, 2006; Scrivener and Nonat, 2011).

In terms of the microstructure analysis of cement, Richardson (2008) employed SEM and EDX to visualize the formation and spatial distribution of hydration products with specific focus on the C-S-H phases. And subsequent studies done by Elkhadiri *et al*. (2009), Liu and Deng (2015), Zhang *et al*. (2019), Devi *et al*. (2022), and Semugaza *et al*. (2023) confirmed the reported observations by Richardson (2008). Figures 2.1 exemplifies the micrographs illustrating the key phases of cement microstructures; namely, C_3S, C_2S, ettringite, and Portlandite under curing conditions.

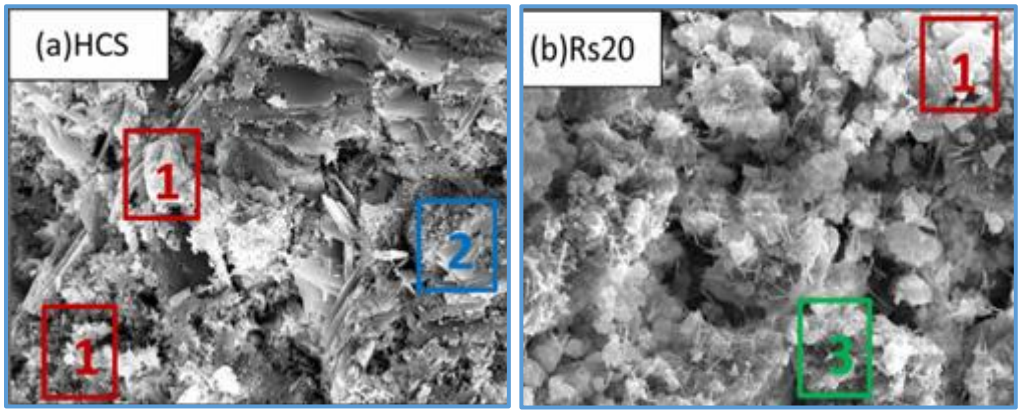

Figure 2.1: SEM/EDX micrographs of cement paste showing the early stages of hydration: (a) hydrated cement specimen (HCS), showing C_3S, C_2S and portlandite; and (b) rehydrated cement specimen (RCS), showing C_3S, C_2S and ettringite.

Figure 2.1 (a) presents a high-resolution scanning electron micrograph of a cement paste at an early stage of hydration, i.e., within the first 60 h (Semugaza *et al*., 2023). EDX analysis was employed to identify plate-like structures, which confirmed the formation of Portlandite. These features are highlighted by a blue rectangle numbered (2) in the image while the C_2S and C_3S phases are indicated by red rectangles labelled (1). In contrast, Figure 2.1 (b) shows distinct needle-like ettringite crystals, which are enclosed in the green rectangle numbered (3). These

ettringite crystals are arranged in radiating clusters, alongside partially hydrated phases of both dicalcium and tricalcium silicate.

During hydration, each cement phase initiates distinct chemical reactions that progressively shape the matrix. The mechanical behaviour of concrete is therefore influenced by the functional contribution of C_3A, C_4AF, C_3S and C_2S. Its hardening follows three main stages — paste crystallisation, C-S-H development, and the appearance of unstable crystals — which together control matrix solidification. These processes underpin the strength and durability of concrete while contributing to salt formation. Nevertheless, for the purpose of this study, which seeks to quantify the evolution of cement microstructures, conventional micrographic analysis remains limited, as it provides only qualitative information on the scanned C_3 and C_2 phases.

2.2.2 Hydration of cement grain during the early phase

This section discusses the early state of the hydration of cement grains with a focus on the compressive strength and heat release of cement microstructures. It also provides an overview of the principal physical factors that govern hydration processes. These factors include curing temperature, moist-curing period, hydration time, and the specific type of cement employed. The influence of these physical parameters on the hydration of cement microstructures is recognized as a key driver in the progressive development of both compressive strength and heat release of concrete mixtures during the moist-curing period (Elkhadiri *et al*., 2009; Jansen *et al*., 2012; Semugaza *et al*., 2023; Vasconcellos *et al*., 2023; Huang *et al*., 2025).

Cement grain hydration is widely accepted to occur in two distinct phases: an early stage marked by rapid chemical reactions and a subsequent late phase characterized by slower long-term microstructural transformations (Huang *et al*., 2025). A detailed account of the long-term microstructural evolution, including the

correlation between physical and mechanical properties in light of these changes, is covered later in Section 2.2.3.

Coming back to the discussion done in Section 2.2.1, the initial hydration of cement grains begins rapidly following the casting of concrete. This early stage is characterized by a significant generation of heat and a notable gain in compressive strength, both of which are predominantly governed by the hydration kinetics of C_3A and C_3S (Bye, 1999; Jansen *et al*., 2012). Conversely, the subsequent phase of hydration unfolds much slowly and is primarily influenced by the chemical reactions of both C_3S and C_2S. The reactions involving C_3S and C_2S occur at reduced rates compared to those associated with C_3A and the early-reacting C_3S compounds (Bye, 1999 & 2011). In addition to this, the relatively delayed hydration of C_3S and C_2S during the early phase plays a beneficial role. It enhances the mechanical performance of concrete mixtures in the long run as cement grain hydration proceeds. Indeed, this delayed reaction contributes significantly to the continued development of compressive strength between 3 days and 28 days of curing (Bentz *et al*., 1997; Bye, 1999; Elkhadiri *et al*., 2023; Huang, 2025). This window period is commonly associated with the maturation and densification of the cementitious matrix as is discussed later in Section 2.2.3.

According to Jansen *et al*. (2012), Bye (2011), and Semugaza *et al*. (2023), the high heat release is largely attributed to the high alkalinity of the chemical components of Portland cement. Allahverdi *et al*. (2020) also highlighted that the presence of internally available high-alkali sulphate ions can significantly alter the chemical behaviour of the cement matrix. These ions have been reported to contribute to the dissolution of C_2S when the concentration of C_3A ranges between 8% and 10% (Bye, 1999). Furthermore, the release of sodium and potassium ions into the pore solution of concrete occurs at a relatively slow rate. Over time, this is accompanied by a reduction in calcium ion concentration within the pore solution and by a rise in pH levels from approximately 12.5 to values exceeding 13. The heat is then released as a result of the above reactions. Several studies have focused on assessing the early hydration rates and the action of C_3S and C_2S cement

microstructures (see for example, Jansen *et al*., 2012; Xu *et al*., 2019; Hu *et al*., 2017; Qi *et al*., 2021; Xie *et al*., 2022; Brevet *et al*., 2023; Semugaza *et al*., 2023). These have led to identifying the different thresholds of interaction between heat peaks and hydration time corresponding to early reactions. Indeed, the early stage of cement grain hydration is marked by a rapid reaction of C_3S with water, which is primarily responsible for the generation of significant exothermic heat. On the other hand, C_2S hydrates at a considerably low rate under identical conditions thereby contributing less to early heat. This can be seen in Figure 2.2 where the heat release associated with the hydration of C_3S and C_2S respectively were experimentally measured over a period of 70 h. The results highlight the dominant role of C_3S and the low thermal contribution of C_2S.

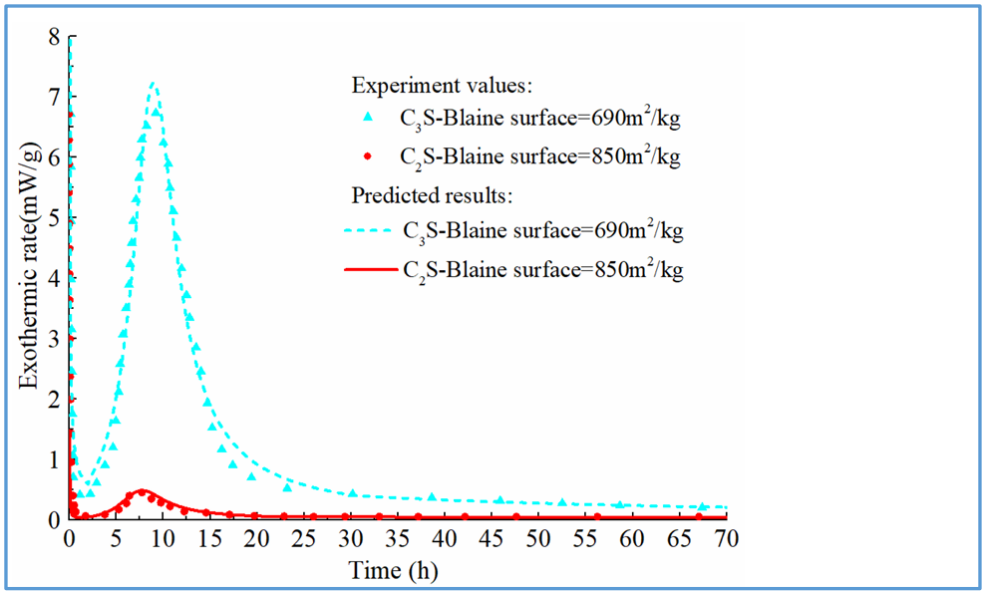

Figure 2.2: A comparative study showing the evaluation rates of exothermic heat released by C_3S and C_2S during the early hydration phase (Qi *et al*., 2022)

Note in Figure 2.2 that maximum heat release (also known as heat release peak) occur after approximately 7.5 h after mixing for both cement components. However, the magnitude of the exothermic peaks for C_3S is at 7 mW/g while that of C_2S is around 0.5 mW/g. In addition to this, the two exothermic heat curves decline at different rates with the heat release associated with C_3S dying out after about 25 h. In contrast, the C_2S curve stabilises around 0.2 mW/g after

approximately 65 h of hydration. Beyond this point, both curves flatten and reach a steady-state of hydration in the range 0 – 0.5 mW/g.

In the same study, Qi *et al*. (2022) assessed the relationship between the degree of hydration and the corresponding hydration time for C_3S and C_2S under identical experimental conditions. Figure 2.3 provides a graphical summary of the findings. One can see the differentiated kinetic behaviours between the two silicate phases and their respective contribution to early and long-term hydration.

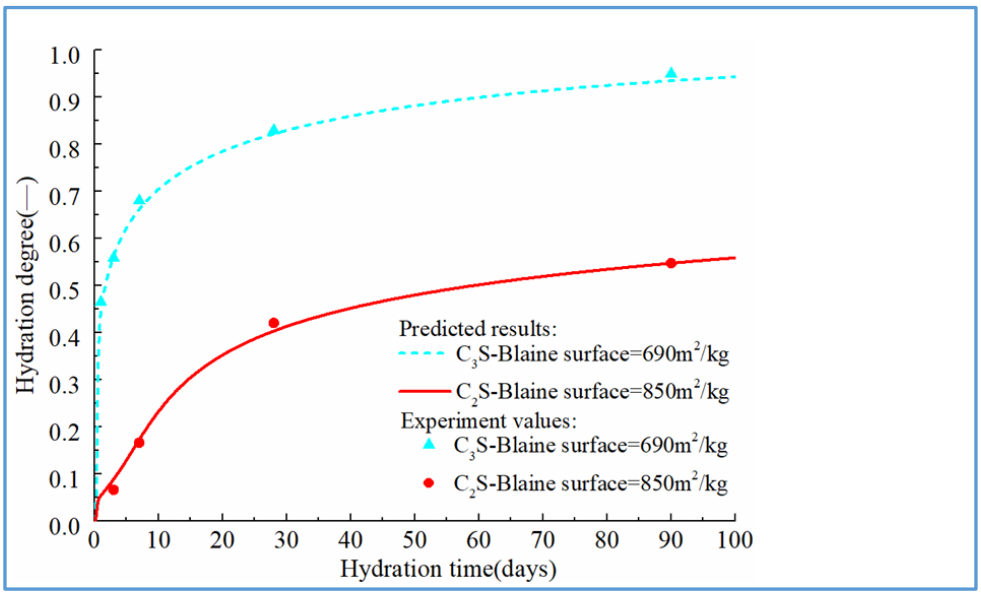

Figure 2.3: Comparison of long-term hydration for C_3S and C_2S measured under similar conditions (after Qi *et al*., 2022)

In a similar type of work, Semugaza *et al*. (2023) examined the influence of varying curing temperatures on the early hydration behaviour of cement pastes with distinct compositions. The study defined the early hydration window as the period spanning from 0 to 60 h. Through a detailed experimental protocol, the temperature evolution of Ordinary Portland Cement (OPC) was compared to that of specially formulated cement pastes. The protocols followed in the preparation of the different cementitious materials tested are summarised in Figure 2.4.

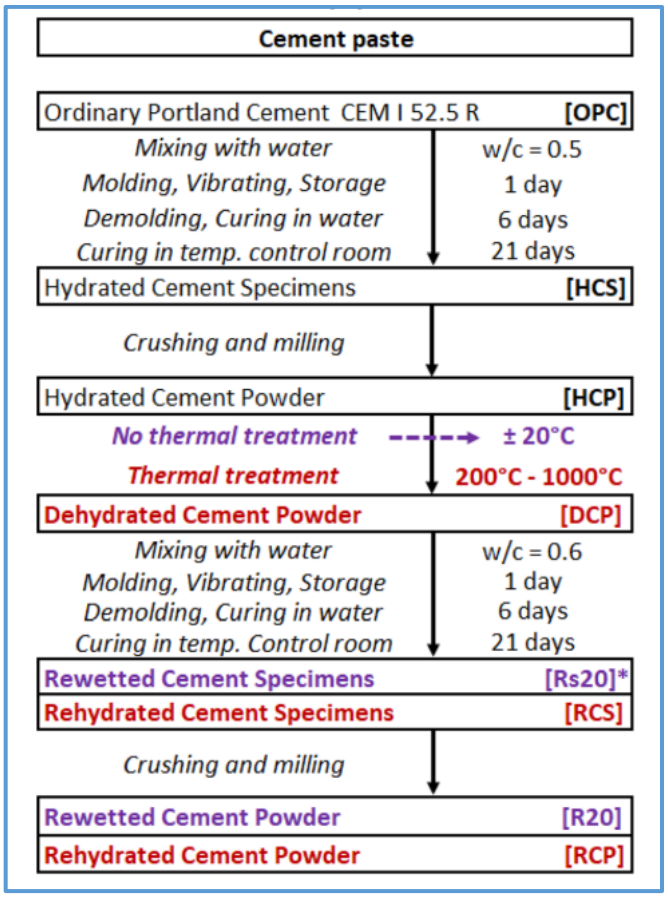

Figure 2.4: Composition and thermal treatment specifications for eight cement pastes (Semugaza *et al*., 2023)

From Figure 2.4, eight cement pastes were prepared as follows: OPC, Hydrated Cement Specimens (HCS), Hydrated Cement Powder (HCP), Dehydrated Cement Powder (DCP), Rewetted Cement Specimens (Rs20), Rehydrated Cement Specimens (RCS), Rewetted Cement Powder (R20), and Rehydrated Cement Powder (RCP). The HCP group was further subdivided into five thermally treated samples labelled Sample 1/D200, Sample 2/D400, Sample 3/D600, Sample 4/D800, and Sample 5/D1000. These five sub-groups corresponded to treatment temperatures of 200°C, 400°C, 600°C, 800°C, and 1000°C respectively. The thermal response and specific surface area of these eight cement pastes are illustrated in Figures 2.5 and 2.6.

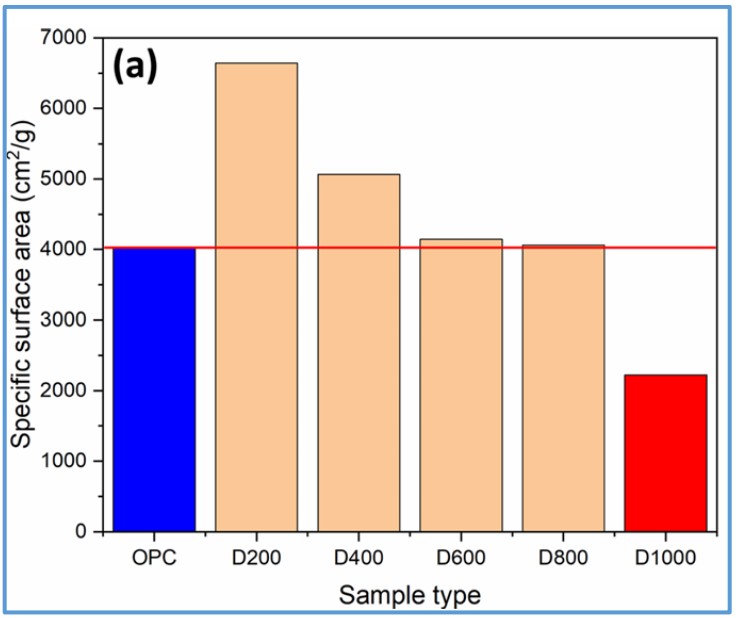

Figure 2.5: Specific surface area reported for selected types of cement pastes at their respective heat release peak (Semugaza *et al*., 2023)

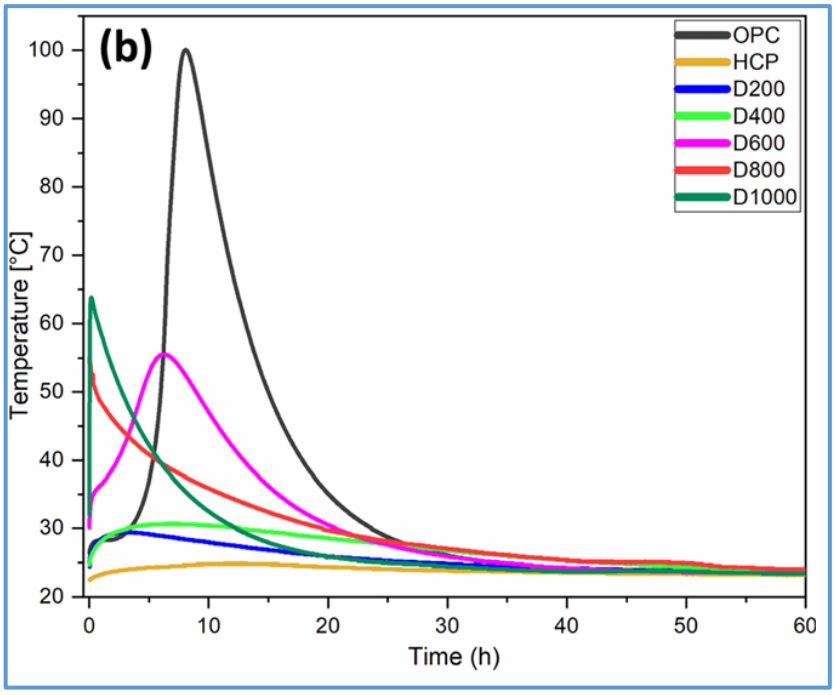

Figure 2.6: Exothermic heat released during the early hydration phase for selected types of cement pastes (Semugaza *et al*., 2023)

As illustrated in Figure 2.5, OPC recorded the highest exothermic peak at close to 100°C after approximately 10 h of hydration. This thermal activity yielded a specific surface area of 4000 cm²/g as shown in Figure 2.6. Conversely, HCP-based cement

pastes showed attenuated thermal responses and variable surface areas, reflecting the impact of prior thermal treatment on their hydration potential. For instance, Sample 5/D1000 reached a peak temperature of 64°C and exhibited a surface area of approximately 2200 cm^2/g. Sample 3/D600 and Sample 4/D800 presented similar thermal profiles peaking at 55°C and surface areas slightly above 4000 cm^2/g (see Figure 2.6). The two types of cement pastes differed in the time it took for the hydration reaction to reach their respective thermal peaks. Sample 1/D200 and Sample 2/D400 also recorded similar thermal peaks at around 30°C, but different specific surface areas (~5000 cm^2/g and 6600 cm^2/g respectively). Figure 2.5 demonstrates that, during the initial hydration period, the OPC sample released more heat than the other tested mixtures. This finding reinforces the assertion that the elevated alkalinity of Portland cement plays a key role in accelerating early-stage exothermic reactions (Bye, 1999; Allahverdi *et al*., 2020).

In summary, reviewing the influence of external physical variables on the microstructure of hydrating cement grains reveals key distinctions between C_3S and C_2S phases. First, C_3S drives a rapid heat release during early hydration, while C_2S has a slower, less pronounced effect (Bye, 1999; Jansen *et al*., 2012; Semugaza *et al.*, 2023; Huang *et al*., 2025). Second, C_3S drives high hydration levels, whereas C_2S remains associated with lower degrees of hydration over time. Last, the sharp heat release peak in early hydration is consistently attributed to the kinetics associated with C_3S. This process is enhanced by the inherent alkalinity of Portland cement (Bye, 1999; Allahverdi *et al*., 2020).

2.2.3 Hydration of cement grain during the late phase

This section is devoted to the physical parameters governing the late hydration phase of cementitious materials. Late hydration refers here to time periods spanning between 3 and 28 days after casting. Physical parameters considered in the review include curing temperature, prolonged hydration time, water-to-cement ratio (w/c), and type of cement. These parameters are discussed because

of their influence on both the evolution of the microstructure and the development of mechanical performance, particularly compressive strength (Molina, 1992; Persson,1996; Bentz *et al*., 1997; Shi *et al*., 2002; Bentz, 2005; Elkhadiri *et al*., 2023; Huang *et al*., 2025).

The effect of curing temperature on the development of compressive strength during the late hydration phase remains relatively underexplored. This is the case particularly in terms of the evolution of hydration mechanisms and the resulting microstructural transformations (Bentz *et al*., 1997; Bye, 2011; Shi *et al*., 2002; Qi *et al*., 2021; Elkhadiri *et al*., 2023; Huang *et al*., 2025). In this light, a critical review of relevant existing studies is necessary to better understand the status of knowledge around this thematic area.

There exist in the literature several studies on the phenomena associated with late-stage hydration. However, most contribute to comparing Portland cement types in terms of the effects of curing temperature, hydration time, moist-curing duration and the water-to-cement ratio (w/c) on the mechanical behaviour of cement microstructures (see for example Bye, 1999; Bentz *et al.*, 1997; Elkhadiri *et al*., 2023; Huang *et al*., 2025). A recent case is the work by Elkhadiri *et al*. (2023) where the development of compressive strength was measured during late-stage hydration. Two cements were considered in this study: CEM I 42.5R and CEM II/A-V 42.5R. Both types were employed in the preparation of cement pastes. The microstructural and mechanical properties of which were evaluated under various curing conditions. Figure 2.7 illustrates the results for various curing conditions of temperature and time.

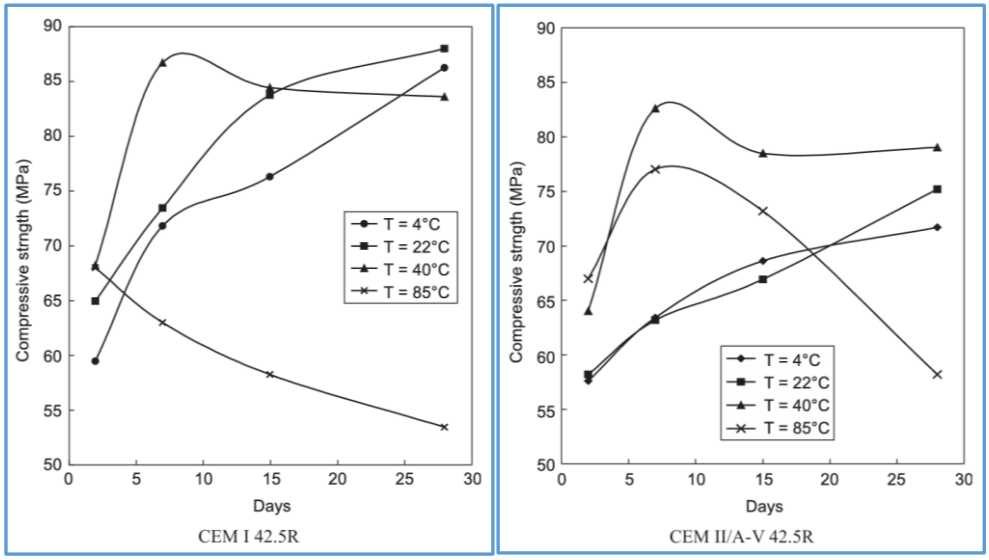

(a) (b)

Figure 2.7: Change in compressive strength as a function curing temperature during the late hydration phase: (a) Cement type CEM I 42.5R and (b) cement type CEM II/A-V 42.5R were used (Elkhadiri *et al*., 2023)

According to the EN 197-1 specifications (European Standard for Common Cements, 2011), CEM I 42.5R is a pure Portland cement containing at least 95% clinker and formulated for high early strength. In comparison, CEM II/A-V 42.5R is a blended cement containing 80 – 94% clinker and 6 – 20% siliceous fly ash. This type of cement enhances durability through partial substitution of clinker with pozzolanic material. It is therefore clear that CEM I 42.5R develops compressive strength faster while also yielding higher strength than CEM II/A-V 42.5R as shown in Figure 2.8. The only exception is that at 85°C of curing, both cements exhibit sharp drops in compressive strength.

Elkhadiri *et al*. (2023) also conducted microstructural analyses of the various samples using micrograph imaging. The tests revealed morphological changes in the cement paste matrix with curing temperature. Figures 2.8 and 2.9 provide visual evidence of the impact of thermal conditions on the formation, growth, and densification of hydration products. They therefore insights into the interplay between microstructure and mechanical properties during the later stages of cement hydration.

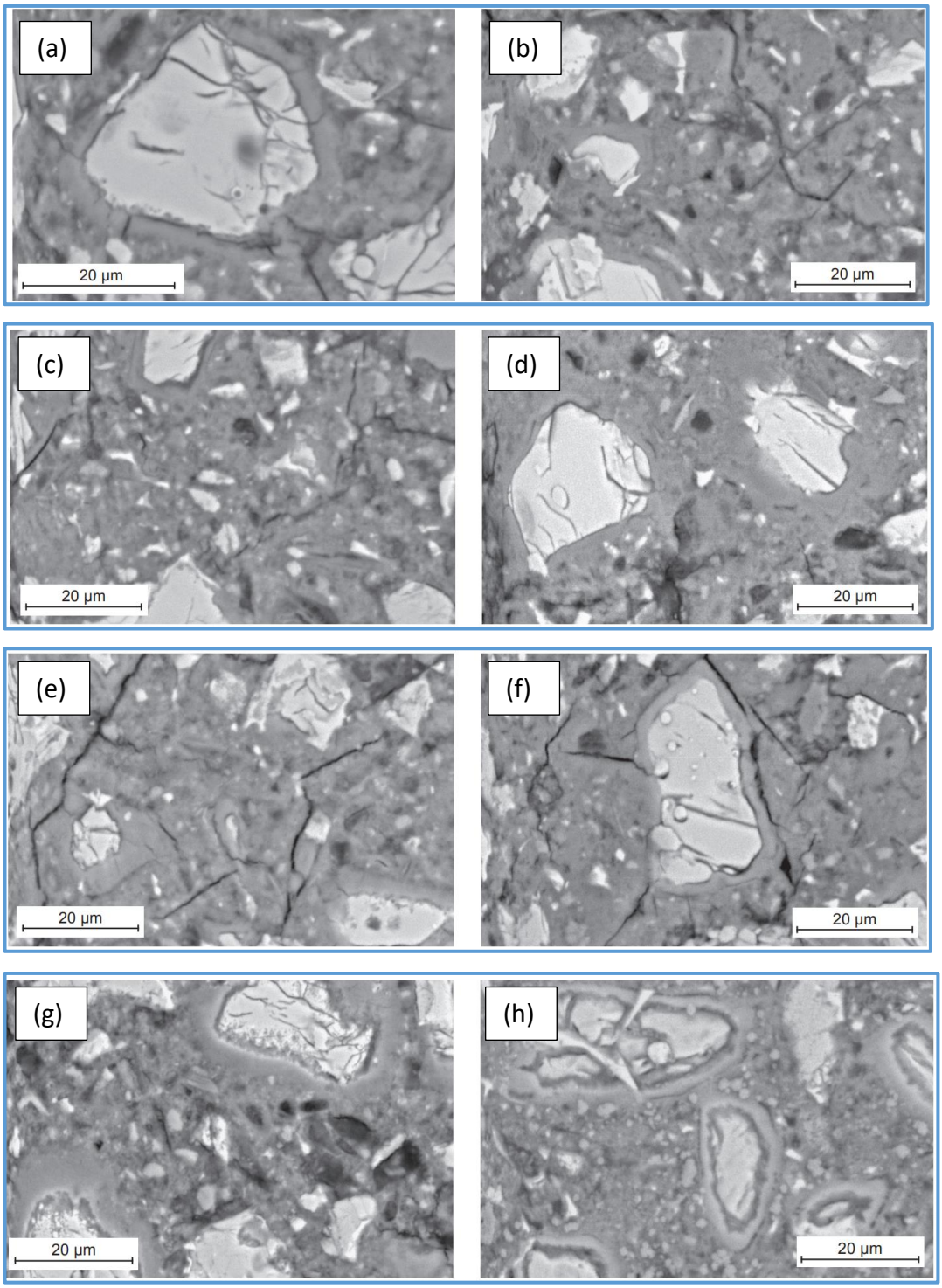

Figure 2.8: Micrographic images of hydrated cement type CEM I 42.5R, influenced by curing temperature and moist-cured age of the specimens. The images are as follows: (a) 4°C at 2 days; (b) 4°C at 28 days; (c) 22°C at 2 days; (d) 22°C at 28 days; (e) 40°C at 2 days (f) 40°C at 28 days (g) 85°C at 2 days (h) 85°C at 28 days (Elkhadiri *et al*., 2023)

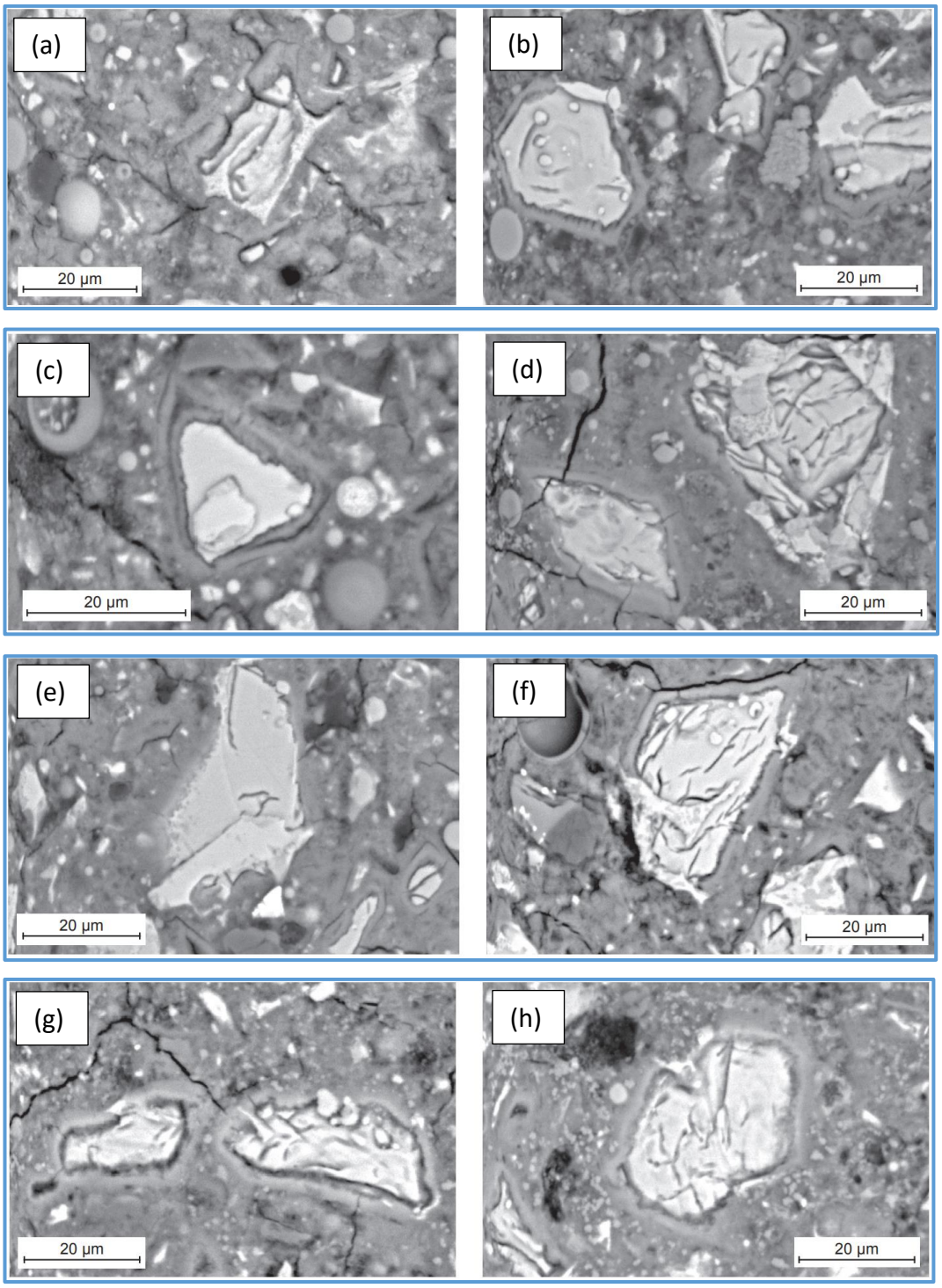

Figure 2.9: Micrographic images of hydrated cement type (CEM II/A-V 42.5R), influenced by curing temperature and moist-cured age of the specimens. The images are as follows: (a) 4°C at 2 days; (b) 4°C at 28 days; (c) 22°C at 2 days; (d) 22°C at 28 days; (e) 40°C at 2 days (f) 40°C at 28 days (g) 85°C at 2 days (h) 85°C at 28 days (Elkhadiri *et al.*, 2023)

Figures 2.8 and 2.9 show the micrographic images of the morphological characteristics of hydrated cement pastes prepared using CEM I 42.5R and CEM II/A-V 42.5R. These pastes were exposed to different curing temperatures and examined at two curing ages, i.e., 2 days and 28 days. Microscopic observations revealed that, after 2 days of curing, only a limited number of cement grains had undergone hydration in both cement types. Figures 2.8a and 2.8c as well as Figures 2.9a and 2.9c exemplify this respectively for each cement paste exposed to 4°C and 22°C curing temperatures. Under these curing conditions, compressive strengths ranged between 55 and 65 MPa for CEM I 42.5R as well as between 60 and 65 MPa for CEM II/A-V 42.5R. At 28 days of curing, the compressive strength showed distinct variations across curing temperatures and cement types. For CEM I 42.5R, values ranged between 85 and 90 MPa for samples cured at 4°C and 22°C before decreasing to 80 MPa at 40°C, and further down to 50 MPa at 85°C (see Figure 2.7a). In the case of CEM II/A-V 42.5R, compressive strength values were approximately 70 – 75 MPa at 4°C and 22°C, increased slightly to 75 – 80 MPa at 40°C, and dropped to 55 – 60 MPa at 85°C (see Figure 2.7b).

In summary, the late-stage hydration study by Elkhadiri *et al*. (2023) showed that cement type, curing temperature, and curing duration affect the hydration process, the microstructural characteristics, and the mechanical strength of cementitious materials. The calcareous cement (i.e., CEM I 42.5R) was found to generally outperform the blended CEM II/A-V 42.5R cement in terms of mechanical strength. This further supported previous work by Bye (1999) and Allahverdi *et al*. (2020). Under the same testing conditions, micrographic observations showed limited hydration of cement grains, with compressive strengths ranging from 55 to 65 MPa. Elevated curing temperatures (40°C and 85°C) enhanced early hydration and microstructural densification. Finally, curing at 85°C resulted in heterogeneous microstructures, negatively affecting long-term mechanical performance.

Another relevant study on cement grain hydration, particularly involving experimental data on the water-to-cement ratio at later stages of hydration, was

initially published by Bentz (1997) and later confirmed by Huang *et al*. (2025). Here, both papers reported that the degree of hydration of cement grains increases proportionally with the rise in the water-to-cement ratio. This is shown in Figures 2.10 and 2.11 where hydration was evaluated during the slow hydration phase experienced within 30 days.

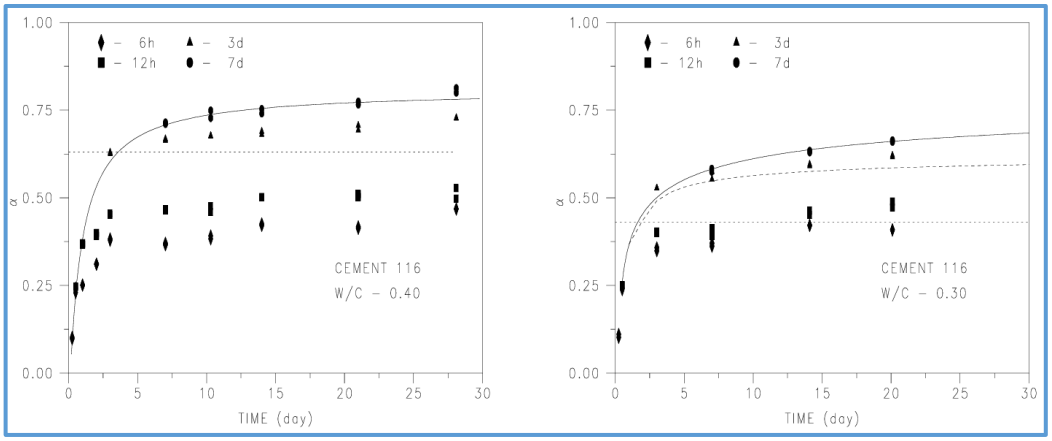

Figure 2.10: Cement grain hydration evaluated over a period of 0 to 30 days with a water-to-cement ratio of 0.40 (Left) and with 0.30 (Right) after Bentz (1997)

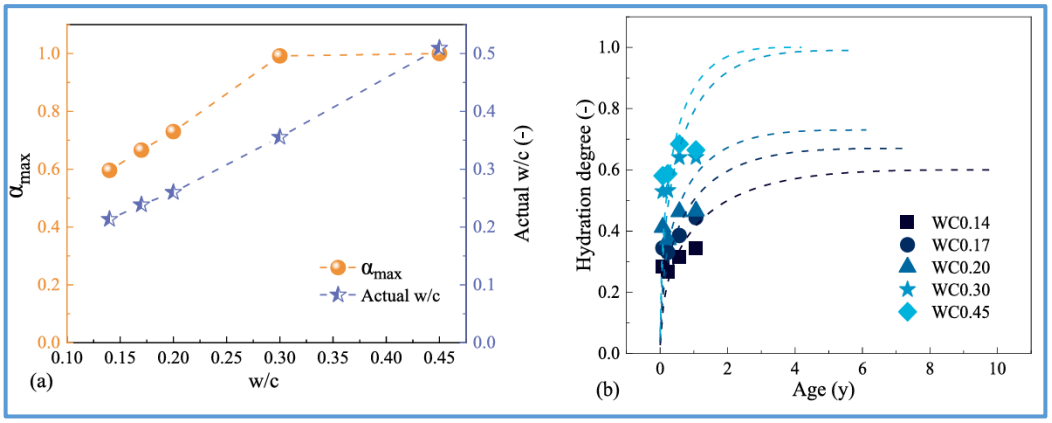

Figure 2.11: Cement grain hydration evaluated over a period from 0 to 10 days: (left) Degree of hydration as a function of the water-to-cement ratio ranging and (right) Degree of hydration as a function of hydration time (Huang *et al*., 2025)

Despite the abundance of studies on the evolution of microstructure and the development of mechanical properties influenced by physical parameters during the early hydration phase, few have focused on the long-term hydration of cement grains in the later stages (Bentz, 2006; Jansen *et al*., 2012; Qi e*t al*., 2022; Elkhadiri

et al., 2023; Semugaza *et al*., 2023; Huang *et al*., 2025). The present research study aims to investigate this less-explored aspect.

2.3 Characterization of concrete corrosion due to sulfuric acid attack and subsequent concrete degradation

In this section, a critical review of selected studies on concrete corrosion induced by sulfuric acid attack is presented. Particular attention is paid to two underlying mechanisms associated with volumetric changes: matrix expansion and surface erosion (Attiogbe and Rizzkala,1988; Shengyuan *et al*., 2012; Liu and Deng, 2015). In addition to this, factors affecting both mechanisms are covered. These factors include acid concentration, mobility of sulphur ions, cement and aggregate type, surface discoloration, and exposure duration.

2.3.1 Effects of sulphuric acid on concrete corrosion

Building on these factors, particularly the influence of acid concentration, the corrosion process is driven by a series of chemical reactions in which sulphuric acid interacts with the calcium hydroxide present around the capillary pores (Raupach, 1991; Pandey and Banerjee, 1998; Allahverdi and Škvára, 2000; Souza *et al*., 2020). This interaction initiates a carbonation-like mechanism that progresses within these pore zones, ultimately resulting in the formation and subsequent transformation of calcium hydroxide.

When sulphuric acid is introduced, three types of chemical reactions follow (Allahverdi and Škvára, 2000):

$$Ca(OH)_2 + H_2SO_4 \rightarrow CaSO_4.2H_2O \quad (2.5)$$

$$3CaO.2SiO_2.3\,H_2O + H_2SO_4 \rightleftarrows CaSO_4.2H_2O + Si(OH)_4 \quad (2.6)$$

$$3CaSO_4 + 3CaO.Al_2O_3.6H_2O + 26H_2O \rightarrow 3CaO.Al_2O_3.3CaSO_4.32H_2O \quad (2.7)$$

Equation (2.5) results in the formation of gypsum ($CaSO_4 \cdot 2H_2O$), while Equation (2.6) leads to the production of gypsum accompanied by a silicate hydroxide

precipitate. Equation (2.7), on the other hand, captures the formation of ettringite, an insoluble compound that typically appears in the final stage of concrete corrosion.

To better understand the impact of sulphuric acid on concrete degradation, it is essential to examine the mechanisms behind the expansion of the concrete matrix and the erosion of its layers. The increase in volume, often observed in concrete exposed to sulphuric acid, arises from the formation of secondary products such as gypsum ($CaSO_4 \cdot 2H_2O$) and ettringite as per Equations (2.5) – (2.7). These products occupy much space than the original constituents (Allahverdi and Škvára, 2000). The resulting volume expansion induces internal stress, leads to cracking and spalling of the concrete surface, and ultimately affects the structural integrity of the concrete (Attiogbe and Rizzkala, 1988; Santhanam *et al*., 2002; Shengyuan *et al*., 2012; Liu and Deng, 2015; Allahverdi *et al*., 2020). Note that the thickness of concrete may initially offer some protection against acid attack. But over time, the matrix becomes more susceptible to cracking and increased volume expansion (Attiogbe and Rizzkala 1988; Allahverdi *et al*., 2020). In this case then, acid concentration accelerates concrete corrosion with sulphur ions becoming more mobile. This subsequently leads to the formation of salts such as ettringite and to the gradual deterioration of the cementitious matrix at microstructural level (Attiogbe and Rizzkala 1988; Shengyuan *et al*., 2012; Taheri *et al*., 2020; Allahverdi *et al*., 2020; Devi *et al*., 2022). Figure 2.12 highlights a case of the deleterious impact of sulphate attack specifically from sulphuric acid on the microstructure of cement. The micrographic images contrast two samples of hydrated cement paste: one in a sound, unaltered condition, and the other subjected to sulfuric acid exposure. The micrograph on the right of Figure 2.12 shows signs of advanced deterioration of the cement microstructure, attributable to the sulphate-induced degradation. Numerous microstructural elements, particularly those visible in grey at the centre of the image, appear to be heavily damaged or entirely destroyed. This is in stark contrast to the left-hand image of Figure 2.12, where several intact microstructures distinguished by their white coloration are still clearly visible.

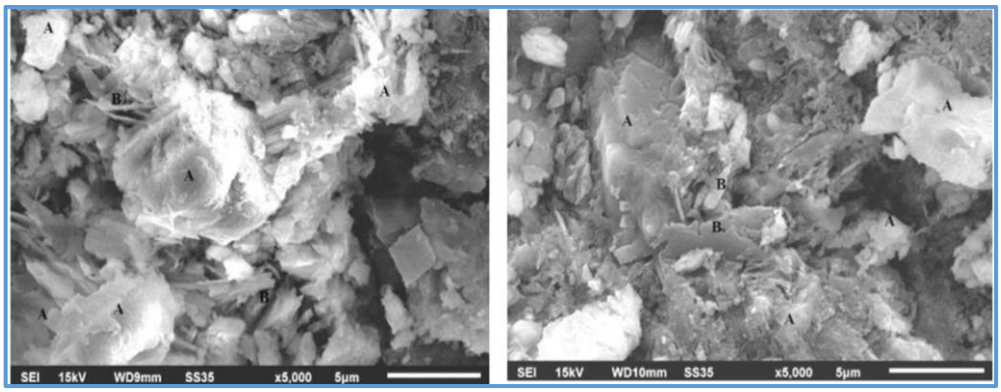

Figure 2.12: Micrographs of hydrated cement paste showing visible damage to the microstructure caused by sulphate attack: (left) intact sample and (right) acid-attacked sample (Devi *et al*., 2022)

In another study, Mutunda (2019) demonstrated that concrete corrosion, characterized in terms of thickness expansion and aggregate durability, is differently influenced by exposure to low (30 g/ℓ) and high (200 g/ℓ) concentrations of sulphuric acid solutions (Figures 2.13 and 2.14). Furthermore, the acceleration of thickness expansion in concrete mixtures was noted to depend predominantly on several parameters. These include the nature of the aggregate composition, the type of cement used, and the mobility of sulphur ions. The experimental program involved concrete mixtures prepared with three types of aggregates: a calcareous aggregate (ML), a siliceous aggregate (MS), and a blend of calcareous and siliceous aggregates (MLS). The cement employed was a Portland cement classified as Type I according to ASTM C150-07. This specific standard recommends the use of Portland Cement-Type I in the mix design of concrete to withstand sulphuric acid.

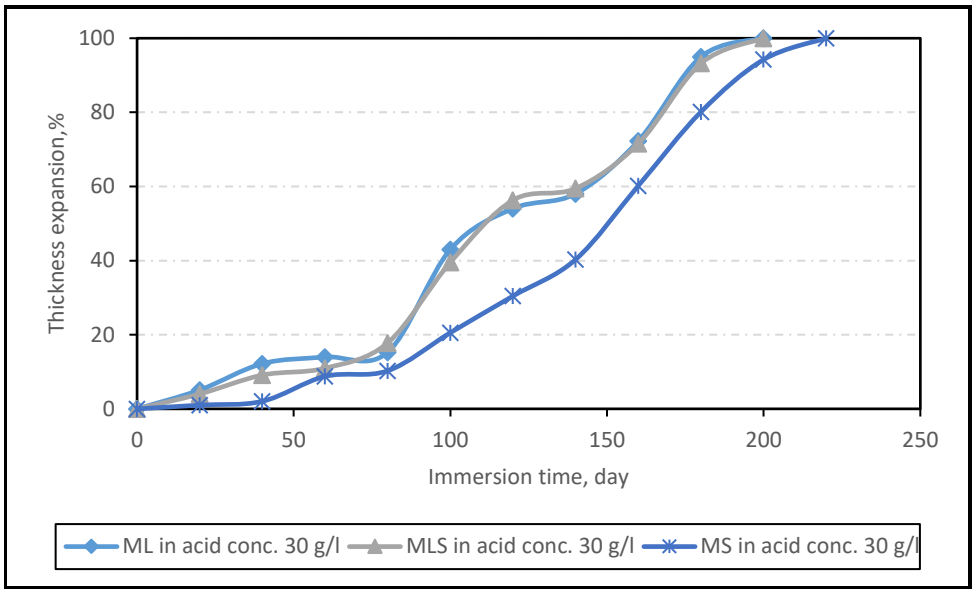

Figure 2.13: Influence of sulphuric acid concentration of 30 g/ℓ on concrete corrosion, thickness expansion, and aggregate durability (Mutunda, 2019)

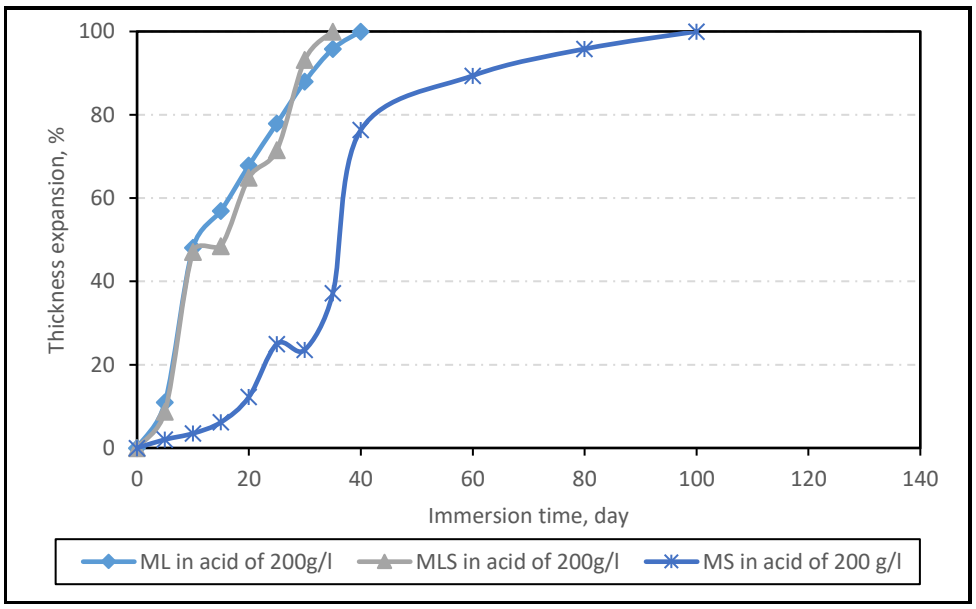

Figure 2.14: Influence of sulphuric acid concentration of 200 g/ℓ on concrete corrosion, thickness expansion, and aggregate durability (Mutunda, 2019)

In Figure 2.13, the concrete mixtures ML, MLS, and MS were immersed in a sulphuric acid solution with a concentration of 30 g/ℓ, whereas in Figure 2.14, the same mixtures were exposed to a more aggressive environment of acid concentration 200 g/ℓ. Thickness expansion was assessed as a function of immersion time under both acid concentrations. As can be seen in Figure 2.13,

immersion in 30 g/ℓ sulphuric acid led to thickness expansion for all three types of concrete. The expanded thickness remained durable for roughly 200 days in mixtures containing calcareous and blended aggregates. In contrast, mixtures containing siliceous aggregates maintained this condition for about 230 days. And looking at Figure 2.14, one notes that the specimens made with MS exhibited greater resistance and longer immersion times compared to those made with calcareous (ML) and blended (MLS) aggregates. Indeed, the durability of the MS specimens was around 100 days, whereas the ML and MLS specimens only lasted 40 and 35 days respectively. These findings demonstrate the superior durability of concrete mixtures incorporating siliceous aggregates under concentrated sulphuric acid solutions. And as shown in Figure 2.15, the left-hand image displays the unaltered structure of the MS aggregate (top), evidencing its resilience against a sulphuric acid solution of concentration 200 g/ℓ after 20 days of exposure. Conversely, the right-hand image shows severe thickness expansion in the concrete made with calcareous aggregates under similar conditions. The formation of the white-coloured ettringite and multiple deep corrosion marks is also noted on the concrete surface.



Figure 2.15: Expansion of aggregate MS (left) and ML (right) at 20 days of immersion in highly concentrated sulphuric solutions of 200 g/ℓ (Mutunda, 2019)

Mutunda (2019) argued that two principal factors contributed to the accelerated corrosion of concrete, its thickness expansion, and a reduced durability of mixtures incorporating calcareous aggregates. The first factor relates to the

enhanced mobility of sulphur ions through the corroded concrete matrix, while the second is linked to the expansive reactions resulting from the intrinsic properties of Portland cement and calcareous aggregates. Figure 2.16 illustrates the evolution of sulphur ion mobility across the corroded concrete thickness when exposed to a highly concentrated sulphuric acid solution (200 g/ℓ), as well as its impact on the durability of mixtures incorporating calcareous and siliceous aggregates respectively.

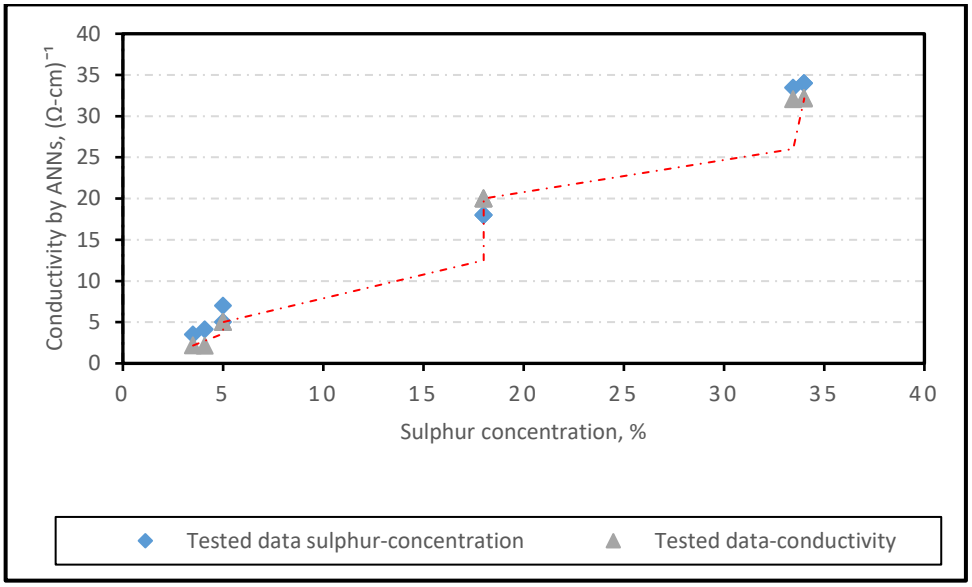

Figure 2.16: Evaluation of variations of sulphur concentration using electrical concrete conductivity for concrete mixtures (ML) tested in sulphuric acid solutions of 200 g/ℓ (Mutunda, 2019)

For concrete mixtures containing ML, the sulphur ion behaviour was monitored under a 200 g/ℓ sulphuric acid solution. The sulphur concentration was noted to vary between 4% and 35%, while electrical conductivity ranged from 2.5 to 35 $(\Omega\text{-cm})^{-1}$. Similarly, for mixtures containing siliceous aggregates (MS), sulphur concentrations and conductivity values fell within comparable ranges. The improved performance of the MS mixtures can be explained by several factors. First, siliceous aggregates possess a higher intrinsic resistance to sulphuric acid than ML, which are more vulnerable to acid-induced deterioration (see Figure 2.15). Second, the aggregate crushing value (ACV) of the MS aggregates, measured at 28.35%, was slightly higher than that of the ML aggregates (26.74%), indicating

a marginally greater mechanical robustness. Finally, as shown in Figure 2.15, concrete incorporating MS exhibited markedly lower expansion, whereas ML-based concrete displayed significant matrix swelling and a more porous surface texture.

In addition, the reduced performance of the ML mixtures when exposed to sulphuric acid can be attributed to two fundamental properties of calcareous aggregates: their inherently alkaline composition and their tendency to undergo alkali–carbonate reactions in acidic environments (Hooton, 1993; Azarsa and Gupta, 2017; Fournier and Bérubé, 2000; Thomas *et al*., 2013). These characteristics intensify the degradation mechanisms, thereby exacerbating the susceptibility of ML mixtures to acid attack compared with MS.

All in all, the observed rise in electrical conductivity associated with the increasing sulphur concentration in both cases is likely a consequence of the elevated ionic content within the concrete matrix (McCarter *et al*., 2000; Lataste *et al*., 2003; Hasan and Taha ,2012, Madhavi and Annamali, 2016; Azarsa and Gupta, 2017).

Equally significant is the effect of cement content on thickness expansion. Variations in cement dosage from 50 kg to 200 kg in ML-based mixtures (under both 30 g/ℓ and 200 g/ℓ acid concentrations) resulted in thickness expansions ranging from 0% to 100% (Mutunda, 2019). This increase in volume is likely associated with the action of alkali sulphates and sulphur ions within the cement microstructure (Attiogbe and Rizzkala, 1988; Türkel *et al.,* 2007; Hasan and Taha, 2012).

In summary, sulphuric acid attack drives a rapid expansion of the concrete matrix and accelerates the erosion of its outer layers. This degradation is intensified by both the acid concentration and the high mobility of sulphur ions. Concretes made with calcareous aggregates show markedly greater vulnerability than those containing siliceous aggregates. Their expansion, along with that of Portland cement, stems from the intrinsic alkalinity of these materials. Together, these

factors sharply amplify the destructive mechanisms triggered by sulphuric acid exposure.

2.3.2 Characterization of sulphuric acid-induced concrete corrosion and discoloration

This section reviews the characterisation of concrete deterioration and discoloration induced by sulphuric acid. The first part discusses the role of sulphate-related reactions in concrete deterioration and examines the resistance of different cement and aggregate combinations to such effects. The subsequent discussion considers key experimental studies linking corrosion mechanisms to observable changes in concrete appearance and surface characteristics.

2.3.2.1 Influence of alkali-sulphate ions on cement

This section highlights the important role of alkali–sulphate ions in the deterioration of concrete mixtures and examines how different cements and aggregates resist in the presence of these ions. Understanding these interactions is crucial for selecting durable materials. The following discussion presents the key chemical mechanisms and experimental evidence that support these choices.

Concrete degradation is strongly affected by alkali–sulphate ions present in the pore solution of cementitious materials (Fernandes and Broekmas, 2013; De Souza *et al*., 2020). These ions initiate chemical reactions that weaken both the chemical and mechanical properties of the cement matrix and reduce aggregate hardness. Such deterioration may arise from either internal or external alkali sulphates (Ekolu and Ngwenya, 2014; De Souza *et al*., 2020).

External alkali–sulphate sources typically originate from acidic environments, whether natural or industrial. Internal concentrations, however, depend primarily on water content and the chemical composition of cement and aggregates. Internal alkali sulphates ($K_2SO_4.2CaSO_4$) in Portland cement form during clinker cooling (Bye, 1999). During hydration, these ions react within the cementitious

phase, enhancing the performance of C_3A, C_4AF, C_3S, and C_2S. The hardening and expansion behaviour of Portland cement paste further depend on the capacity of these phases to withstand sulphate attack (El Chabib, 2004).

Lataste *et al.* (2003) observed that variations in ionic concentration are mainly governed by the mobility of chloride (Cl^-), hydroxide (OH^-), and sulphate (SO_4^{2-}) ions, which directly influence corrosion severity. Bye (1999) indicated that internal alkali sulphate ions can trigger the dissolution of C_2S when the C_3A content lies between 8% and 10%. This process progressively releases sodium and potassium ions while reducing calcium concentrations, consequently raising the pH from around 12.5 to levels exceeding 13.

Binici *et al*. (2009) demonstrated that additives such as calcium aluminate (CA) and ground granulated blast-furnace slag (GGBFS) produce denser hydration structures and improve sulphate resistance. In contrast, control specimens without additives displayed higher porosity and more microcracking. Incorporating 10% CA and GGBFS was shown to significantly enhance cement durability.

In their research, Türkel *et al*. (2007) confirmed that both the physical and chemical properties of cement strongly influence acid resistance, comparing pozzolanic and Portland cements over 120 days. The authors suggested that the superior resistance of Portland cement to sulphuric acid may be linked to the reduction of C_3A content during cement hydration. Khitab *et al*. (2013) further noted that although certain aggregate properties can improve resistance, alkali–sulphate attack may still compromise them. Calcareous aggregates are particularly vulnerable, whereas siliceous aggregates generally perform better due to their higher compactness and lower moisture content (Quiroga and Fowler, 2004).

In general, the findings of Türkel *et al.* (2007) are consistent with results from other researchers, including Zivica and Bajza (2001) and Pavlik (1994), who likewise demonstrated that Portland cement exhibits greater resistance to sulphuric acid solutions than pozzolanic cement. In view of this collective evidence, Portland

cement was selected as the binder for the laboratory concrete mixtures in this study, enabling a controlled and systematic assessment of its performance under aggressive conditions (see Section 3.2.1).

2.3.2.2 Colorimetric changes associated with sulphuric acid-induced concrete corrosion

To further understand how sulphuric acid progressively alters the visual and physical characteristics of concrete, this subsection reviews experimental studies linking corrosion mechanisms to measurable colour changes. In practice, colour variation represents an observable indicator of the progression of sulphuric acid-induced deterioration and provides a basis for monitoring changes at the concrete surface.

Shengyuan *et al*. (2012) were among the first to systematically examine concrete corrosion by combining quantitative measurements with visual assessment of colour changes in eroded layers. In their programme, concrete specimens were immersed in sulphuric acid solutions with varying pH levels for 150 days, using water-to-cement (w/c) ratios ranging from 0.40 to 0.70. Their observations confirmed that corrosion is not only governed by pH level, w/c ratio, and exposure duration, but also that the resulting colour change in the degraded material provides a qualitative indication of the severity and progression of corrosion. As illustrated in Figure 2.17, corrosion can be characterised through visual colourimetry, with three distinct hues typically observed: grey (top-left), yellow (top-right), and white (bottom-right). Grey denotes mild corrosion; yellow indicates a more advanced stage of degradation; and white corresponds to the presence of calcium sulphate precipitates (see Equations 2.5–2.7), which are characteristic of the final phase of concrete disintegration. At this stage, the pH of the acidic solution approaches 2.5, indicating a highly acidic environment associated with the advanced degradation of the concrete matrix. It should be clarified that this pH value refers to the acidic solution during the corrosion process, rather than to the pH of the concrete itself or its pore solution.

Acid concentration, immersion time, and the nature of the concrete constituents are widely recognised as the primary factors influencing corrosion under acidic exposure. In addition to these, the mobility of sulphur ions within the corroded surface layer has been shown to play a critical role in accelerating the rate of deterioration (Attiogbe and Rizzkala, 1988; Mutunda, 2019).



Figure 2.17: Colour changes indicating the evolution of concrete corrosion (Shengyuan *et al*., 2012)

In a related field of investigation, Lee *et al*. (2009) studied colour evolution and material property changes in concrete exposed to elevated temperatures. Their aim was to consider colour alteration as a key parameter, examined alongside weight loss and residual compressive strength, in order to establish the relationship between thermal-induced colour changes and corresponding material degradation. Concrete samples with different water-to-cement ratios were heated to target temperatures ranging from 100°C to 800°C in an electric oven, after which their colour, mass loss, and compressive strength were recorded. The results revealed a consistent relationship between the development of a reddish hue at high temperatures and both increased weight loss and reduced residual strength.

In another study, Taheri *et al*. (2020) assessed concrete corrosion by correlating the depth of the corroded layer with observable changes in the colour of the concrete matrix. Samples were exposed to acid solutions with pH levels of 0.25

and 1 for durations of 2 weeks, 1 month, and 3 months. The varying degrees of deterioration were examined using Scanning Electron Microscopy (SEM).

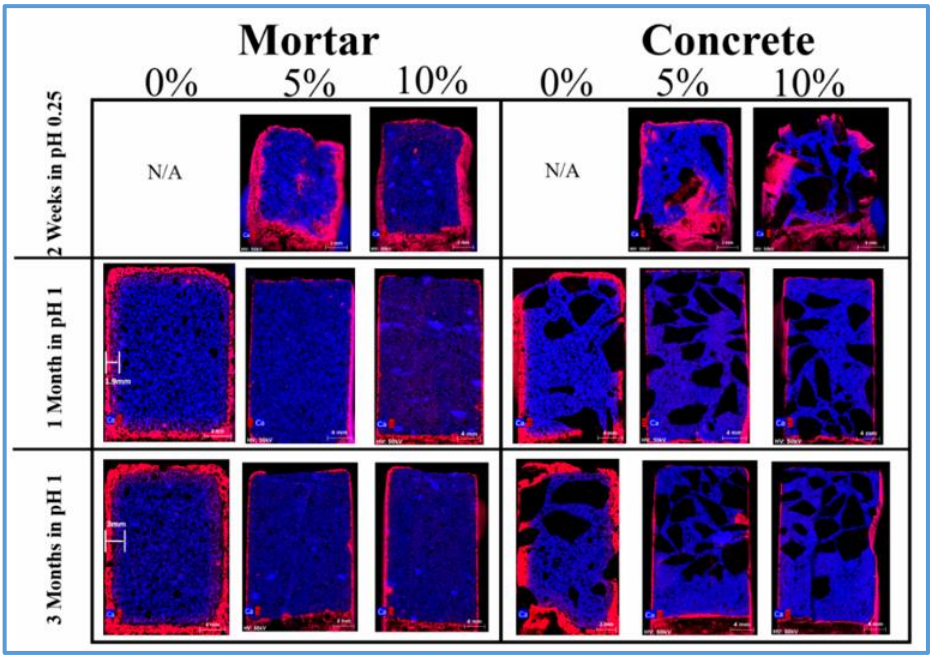

Figure 2.18: Change in colouration impacted by both sulphur and calcium ions (Taheri *et al.*, 2020)

Figure 2.18 presents elemental colour mapping of calcium (blue) and sulphur (red) in mortar and concrete specimens containing 0%, 5%, and 10% mullite, immersed in pH 1 solutions for 1 and 3 months, and in pH 0.25 for 2 weeks. The red regions, corresponding to sulphur ion presence, surround the expanded corroded layer, while the blue zones within the inner perimeter indicate areas rich in calcium ions.

The existing literature offers only qualitative descriptions of colour changes associated with concrete expansion, leaving a gap in quantitative approaches to microstructural characterisation. This thesis aims to address this limitation by establishing a controlled dataset of scanned concrete surfaces and constructing a quantitative image-based framework to assess microstructural evolution under hydration and sulphuric-acid corrosion.

The central premise is that colour patterns in scanned images carry measurable signatures of microstructural transformation. Leveraging these variations offers a

non-invasive means of monitoring cement behaviour and enhancing understanding of degradation mechanisms.

Studies also show that sulphate ions significantly influence hydration chemistry and microstructural stability. Internal alkali sulphates may induce C_2S dissolution and affect the reactivity of major phases, while their mobility contributes to internal corrosion. Additives such as CA and GGBFS, however, can improve durability by enhancing sulphate resistance. Corrosion-induced colour shifts—typically progressing from grey to yellow and finally white—serve as reliable indicators of degradation severity and the formation of calcium sulphate products in the later stages of disintegration.

2.4 Collection of experimental imaging data at macroscopic and microscopic scale

The present section outlines the methodological framework established for the acquisition of experimental imaging data at both macroscopic and microscopic scales under controlled laboratory conditions. Relevant imaging techniques are compared in terms of their respective strengths and limitations.

2.4.1 Macroscopic acquisition technique of imaging data relating to concrete materials

In contemporary concrete science, remote sensing represents a sustainable and widely adopted approach for data collection, both under controlled laboratory conditions and in situ (Kwak *et al*., 2013; Godycka *et al*., 2014; Koken *et al*., 2014; Habib *et al*., 2014; Janowski *et al*. 2016; Yu *et al*., 2017). Remote sensing techniques leverage photometric systems to acquire two-dimensional (2D) high-resolution image data. The original 2D data is then transformed into three-dimensional (3D) representations (Habib *et al*.,2014; Janowski *et al*. 2016; Comminal *et al*.,2020). Note that the image acquisition process associated with remote sensing is generally complemented by a scanning system equipped with a

synchronized camera. This addition enables precise data processing and 3D rendering based on macroscopic observations. Figure 2.19 provides an example of the implementation of a laboratory-scale photogrammetric system. Here, multiple digital cameras are used for data collection following the protocol that can be found in the work by Habib *et al*. (2014).



Figure 2.19: Laboratory-scale implementation of the photogrammetric system. On the left, the system is suspended from a steel frame, while on the right, it is mounted on tripods (Habib *et al*., 2014)

In their study on concrete structures, Janowski *et al*. (2016) demonstrated that the progression and widths of cracks could be monitored effectively using Remote Sensing Techniques (RST). The photogrammetric system used was also found to enable the easy assessment of loads and deflections of concrete structures through scanned imagery. For instance, Figure 2.20 shows that a load ranging from 0 kN to 140.70 kN was found to correspond to a deflection of 0 mm to 1 mm. An overview of photogrammetric systems and macroscopic imaging methods employed for the evaluation of crack propagation under varying loading conditions is provided in Table 2.1. These techniques enable the monitoring of structural behaviour by capturing surface deformations and tracking the development of visible cracks over time.

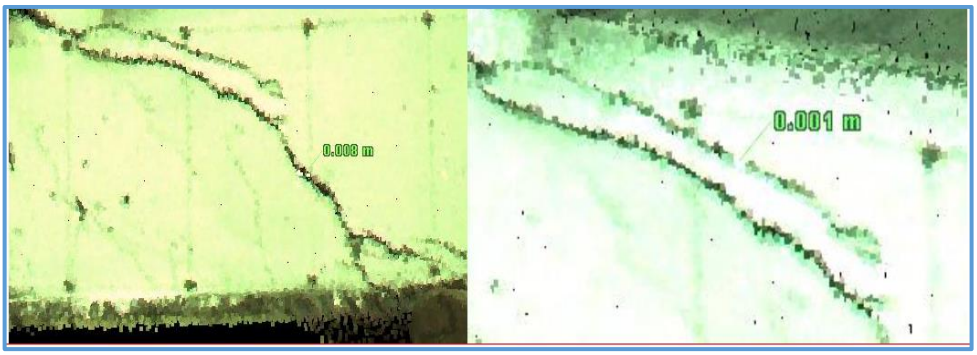

Figure 2.20: Example of remote sensing monitoring using a photometric system applied to a concrete beam, illustrating deflection-related crack progression with a size of 0.008 m (Left) and 0.001 m (Right) after Jonawski *et al*. (2016)

Table 2.1: Overview of photogrammetric systems and macroscopic imaging techniques used for crack propagation analysis under variable load conditions (Jonawski *et al*., 2016)

No.	COMPARATIVE ANALYSIS			
	Load [kN]	*Cracks in real element*	*Cracks in virtual model*	*View on the scan*
1	0	-	-	
1	10	-	-	
2	30	-	-	
3	50	√ [a]	-	
4	70	√ [b]	-	
5	90	√ [b]	√ [b]	
6	140.7	√ [c]	√ [c]	

Table 2.1 is effectively a scale matching seven incrementally applied loads ranging from 0 kN to 140.7 kN with corresponding scanned samples receiving the same

load. Notably, a pronounced flexural (bending) crack is observed under the maximum applied load of 140.

In summary, the image acquisition process in remote sensing is typically combined with a scanning system and a synchronized camera. This approach allows for accurate data processing and three-dimensional rendering based on macroscopic observations. A laboratory-scale photogrammetric system can also be implemented using this method. In the field of construction materials, it enables the scanning of concrete surfaces for detailed macroscopic imaging. The technique further facilitates the analysis of crack development in concrete beams and the prediction of their potential failure.

2.4.2 Data extraction using the scanned point method

This section outlines a laboratory-based technique used to mark the perimeter of the area from which data are collected when monitoring scanned points on a concrete beam with remote sensing technology. The method offers the advantage of precisely defining the scanning zones by applying circular markers, thereby ensuring targeted and accurate data acquisition on the concrete surface (Remondino and Hakim, 2006; Rőnnholm, 2009; Jonawski *et al*., 2016; Habib *et al*., 2014).

In their laboratory study, Habib *et al*. (2014) employed this perimeter-marking technique to support the extraction of scanned image data using remote sensing. The use of marker points enabled the authors to obtain a greater volume of reliable data, which in turn facilitated detailed analyses of beam deflection and crack characterisation.

A further example of applying circular marker points as a scanning data collection technique on concrete surfaces is provided by Jonawski *et al*. (2016). In their work, circular point markings were applied to a concrete beam to monitor crack propagation under variable loading conditions, as illustrated in Figure 2.21.

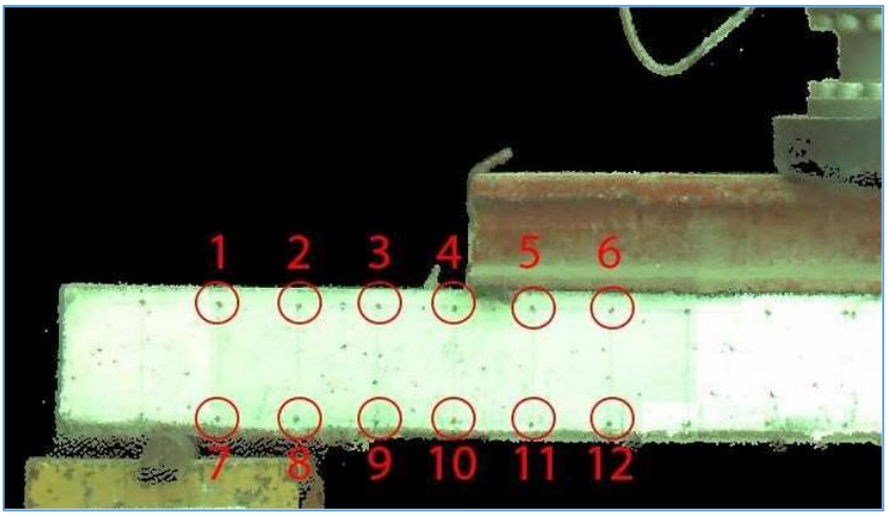

Figure 2.21: Illustration of circular points used for scanning and analysis (Jonawski *et al*., 2016)

The scanned point method offers several advantages, including non-destructive data acquisition and the ability to capture complex geometries with high spatial resolution. Scanned point for macroscopic photogrammetry also offers a non-invasive, low-cost way to monitor crack growth and deformations in concrete structures under load, with adequate resolution for both laboratory and in situ utilization (Remondino and Hakim, 2006; Habib *et al*.,2014; Jonawski *et al*., 2016).

Despite their practical advantages, these approaches present several limitations, such as susceptibility to lighting conditions, surface texture variability, and reduced accuracy at the microscale level (Gorthi and Rastogi, 2010; Habib *et al*.,2014; Jonawski *et al*., 2016). These drawbacks are critical when scanning fine-scale cement microstructures throughout the surface of concrete mixture. It is in this light that the present study explored the use of the same laser-based microscopic scanning technique used in medical diagnostics. It is believed that such an approach may enable high-resolution and sub-millimetre detection of concrete surface. The scanning equipment and procedures are presented later in Section 3.3.4 of Chapter 3. It is anticipated that the evolution of hydration and corrosion phenomena can be accurately monitored for selected cementitious materials. But before all this, an overview of the principles and technological advances underpinning microscopic imaging systems used in the medical field is

provided in the following section. This is to lay the conceptual foundation upon which is based the experimental adopted for this doctoral research.

2.4.3 Monitoring disease progression through tissue Colour Changes

In order to contextualize the innovative imaging methodology employed in the present thesis, it is pertinent to examine the evolution and cross-disciplinary application of scanned microscopic images. The medical field has played a pioneering role in the development and implementation of high-precision laser-based imaging systems. These systems are used for diagnostic purposes and allow a detailed analysis of tissue architecture and pathological changes at microscale (Daanen and Hong, 2008; Ares *et al*., 2014; Haleem and Javaid, 2019; Al-Sharify *et al*., 2020). This section presents a succinct review of scanned microscopic images commonly utilized in medical diagnostics. The review specifically focuses on approaches that monitor the progression of diseases based on the temporal variation in tissue colouration.

Scanning technologies have extensively developed in the field of medical science. They are used to collect imaging data from various microscopic points located on the structure being scanned (Haleem and Javaid, 2019; Daanen and Hong, 2008; Ares *et al*., 2014; Al-Sharify *et al*., 2020).

In their paper, Al-Sharify *et al*. (2020) compared cases of scanned microscopic images of healthy human brains with diseased ones. The group of researchers was then able to identify colour variations and black-and-white backgrounds in support of the diagnosis of certain suspected illnesses. Figures 2.22 and 2.23 illustrate two examples of scanned microscopic images associated with brain cancer and Parkinson's disease.

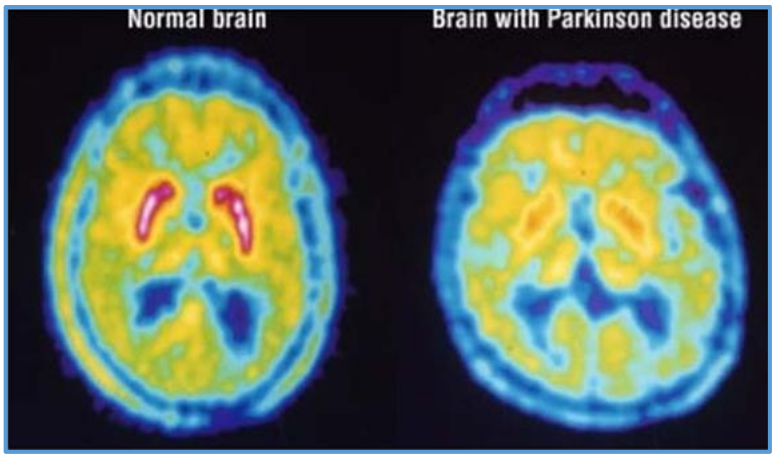

Figure 2.22: Scanned microscopic images using colour variations contrasting a healthy brain on the left and a Parkinson's diseased brain on the right (Zanaib *et al*., 2020)

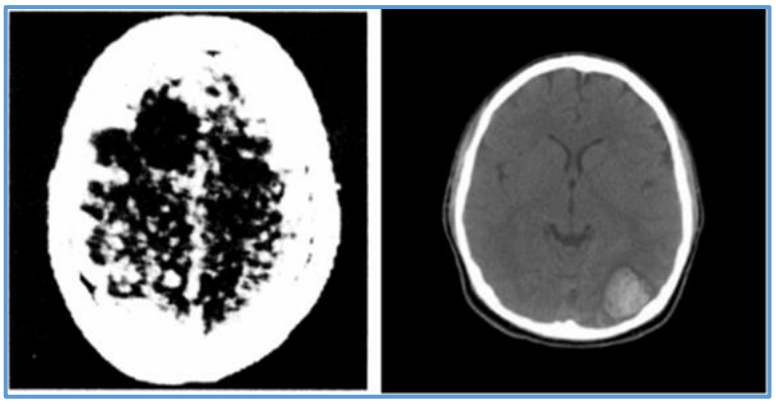

Figure 2.23: Scanned microscopic image using black-and-white-backgrounds showing a brain with cancer (left) and advanced stage of cancer (right) (Zanaib *et al*., 2020)

The left side of Figure 2.22 shows the colour-scanned image of a healthy brain alongside a brain affected by Parkinson's disease on the right (i.e., Figure 2.22 right). A comparison of the two images in terms of colour variance reveals that two caterpillar-shaped cells in bright red and white tones. These features in Figure 2.22 (left) are indicative of a healthy brain. In contrast, the same cells appear completely deteriorated in the image of the brain affected by Parkinson's disease. A faded pink coloration is also apparent suggesting cellular corrosion. Similarly, Figure 2.23 illustrates examples of black-and-white scanned images of a brain at different stages of cancer. An initial scan of the brain of a patient with cancer is displayed on the left while the right-hand side scan shows the progression of the disease. In the left-hand image, the cancerous region is represented in black

against a white background whereas the progression of the same region appears in a greyish tone on the right indicating an advanced stage of the disease.

The conversion of colour images into black-and-white representations is a well-established technique in greyscale medical image processing (Brady, 1982; Landini *et al*., 2008; Altinay and Kose, 2017). Over the past two decades, this field has advanced notably through the integration of specialised algorithms and mathematical frameworks, enabling the precise characterisation of image features at the pixel scale (Landini *et al*., 2008; Altinay and Kose, 2017).

Building on these developments, the present thesis extends the use of colour-based and greyscale imaging concepts to the domain of concrete analysis. It is hypothesised that both the original colour information and its transformed black-and-white pixel patterns can be exploited as part of a methodological framework for modelling scanned points on the surfaces of concrete cubes. This dual-image approach provides a basis for capturing the physical progression of hydration and corrosion across cement microstructures.

Furthermore, the evolution of hydration and corrosion in cement grains and concrete materials is assessed through colorimetric analysis, which serves as a quantitative and qualitative means of tracing microstructural changes when coupled with the proposed mathematical formulations.

To support this methodological framework, the following section reviews the key mathematical formulations that underpin the implementation of this approach.

2.5 Mathematical formulations for concrete material

This section is dedicated to review some articles which applied the mathematical formulations in their respective research in term of resolving complex issue related to science of materials.

2.5.1 Framework of mathematical formulations for function fitting

Over the past decade, mathematical formulations have become central to describing the complex chemical, physical, and mechanical behaviours of construction materials (Fedosov *et al*., 2017; Samoshkin and Tikhomirov, 2021; Sultan and Hamza, 2023). Unlike earlier empirical approaches, these models provide a structured way to integrate multidimensional data while respecting fundamental laws, improving both predictive accuracy and interpretation of material behaviour. In this thesis, such formulations are employed to capture the slow-phase mechanisms of hydration and corrosion, enabling a robust analysis of cement microstructural responses through ANN frameworks.

A clear example of this approach is provided by Fedosov *et al*. (2017), who applied mathematical models to describe three types of processes in cement concrete: dissolution and leaching under low-hardness water, reactions with chemically active liquids producing soluble compounds, and corrosion in aggressive environments where salt crystallisation in pores generates internal stresses. Selected mathematical formulations from their study are presented below (Fedosov *et al*., 2017).

$$k\frac{\partial C(\delta,\tau)}{\partial x} = \beta\left[C_{\text{subjected}}(\tau) - C(\delta,\tau)\right] \tag{2.8}$$

$$-S.\rho_{\text{concrete}}.k\frac{\partial C(\delta,\tau)}{\partial x} = \nu_{\text{liquid}}.\rho_{\text{liquid}}.\frac{\partial \acute{C}(\delta,\tau)}{\partial \tau} \tag{2.9}$$

Equations (2.8) and (2.9) describe the complex physical and chemical processes in cement concrete in which k is the coefficient of mass conductivity (diffusion); $C_{\text{subjected}}(\tau)$ represents the equilibrium concentration for the transferred component from the surface of the solid body; β is the mass transfer coefficient in the liquid and $C(\delta,\tau)$ refers to the concentration of calcium hydroxide in the liquid as a function of both coordinate δ and time τ. Moreover, S is the inner surface of the tank, whereas ρ and v are respectively the density and volume of materials.

Further applications of mathematical formulations are found in the works of Samoshkin and Tikhomirov (2021) and Sultan and Hamza (2023). These studies demonstrate how mathematical models can be constructed and validated using both theoretical and experimental data.

In the first case, Samoshkin and Tikhomirov (2021) developed a mathematical model to describe the nonlinear bond behaviour of reinforced concrete. Their model was used to solve the static pull-out problem and confirmed the validity of the theoretical assumptions and algorithms used to represent reinforced concrete deformation. A representative equation from their work is given below:

$$f = \frac{1}{\alpha}\, exp\left[\left(\frac{\sigma_s^2}{m}\,\frac{\alpha}{B}\right)^{1/2} - 1\right] \quad m = \frac{p\, A_c\, E_S\, E_c}{A_S\,(E_c\, A_c + E_S\, A_S)} \tag{2.10}$$

Where f represents the resistance of concrete to the displacement of reinforcement; (A_c, E_c) and (A_s, E_s) denote the cross-sectional areas and elastic moduli of concrete and steel reinforcement; p is the reinforcement perimeter; α, m and B are bond parameters related to the tested reinforcement-concrete pair. In addition, σ_s represents the normal stresses in the reinforcing bar.

Equation (2.10) was applied to compute the variation of rebar stress as a function of load and displacement. Figure 2.24 illustrates the response of the model with rebar stresses shown to increase from 0 to approximately 550 MPa as the loaded-end displacement rises from 0 to 0.8 mm.

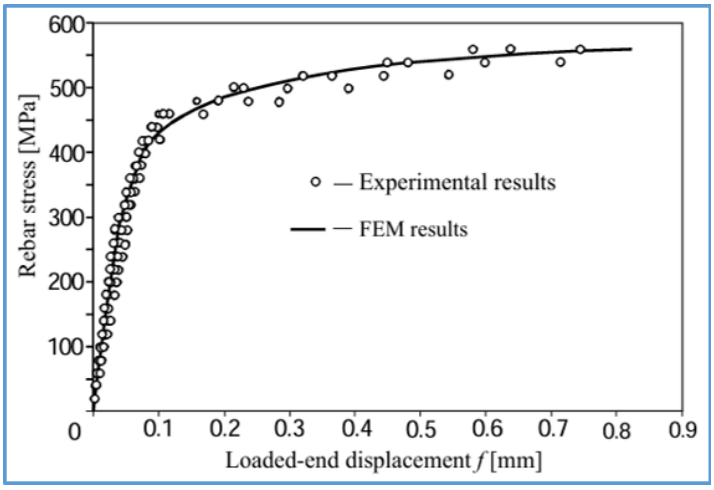

Figure 2.24:Mathematical models illustrating the variation in rebar stress as a function of load and displacement (adapted from Samoshkin and Tikhomirov, 2021)

Similarly, Sultan and Hamza (2023) formulated mathematical models to describe the stress–strain relationship of normal- and high-strength concrete under compression. Two key equations underpin their approach: Equation (2.11) linking experimental and theoretical stresses, and Equation (2.12) defining the stress–strain curve using parameters a, b, and c that depend on concrete strength. These parameters control the degree of nonlinearity and the shape of the ascending and descending branches, including the turning point. The results generated using Equation (2.12) are shown in Figure 2.25, where the stress–strain response displays a peak value of 1 when the applied load reaches its maximum.

$$DR = \frac{\sum_{j=1}^{n} [\sigma_{exp} - \sigma_{th}]}{\sum_{j=1}^{n} \sigma_{exp}} \times 100\% \quad (2.11)$$

$$y = X^{a\left(\frac{1\,x^c}{1+b\,x^c}\right)} \quad (2.12)$$

To clarify this relationship, the additional equations presented in the legend of Figure 2.25 are derived from Equations (2.11) and (2.12) and provide complementary expressions for representing the experimental and theoretical stress–strain responses. They therefore establish a direct link between the mathematical formulation and the curves illustrated in Figure 2.25.

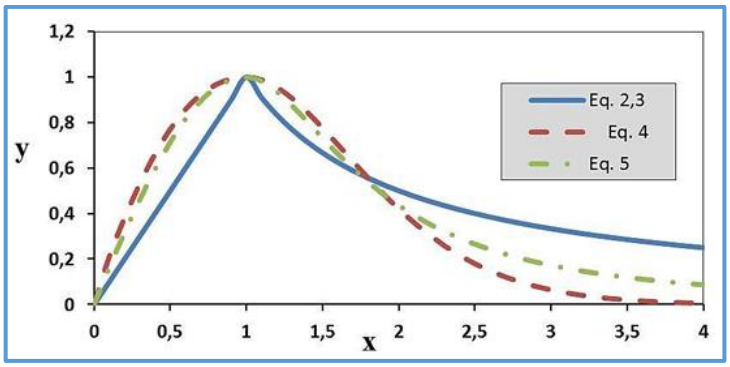

Figure 2.25: Representative form of a developed mathematical model for the stress–strain relationship (after Sultan and Hamza, 2023)

In summary, the three cases presented in this section demonstrate the effectiveness of mathematical formulations in establishing robust models for understanding concrete-related phenomena. The first case highlights modelling of physico-chemical degradation processes, while the latter two show how mechanical parameters such as compressive strength can be accurately predicted through stress–strain relationships. However, these formulations also reveal limitations for the present study. Their applicability to complex microstructural behaviours, particularly those derived from surface imaging of cement-based materials, is restricted. Addressing such challenges requires new types of mathematical expressions capable of capturing microstructural evolution during hydration and corrosion. To bridge the gap between experimental observations and theoretical models, artificial neural networks are employed in this study to capture the intricate patterns of microstructural evolution in cement-based materials.

2.5.2 Framework of mathematical formulations using ANNs

ANNs provide a robust mathematical framework for modelling complex, nonlinear phenomena in concrete materials, including hydration and corrosion under varying physical and chemical conditions (Gurney, 1997; Larsen, 1999; Kriesel, 2005; Hakim *et al*., 2011; Sharma *et al*., 2012). Inspired by the structure and functioning of the human brain, ANNs analyse intricate data patterns and offer

enhanced predictive accuracy compared with traditional mathematical models (Figure 2.26).

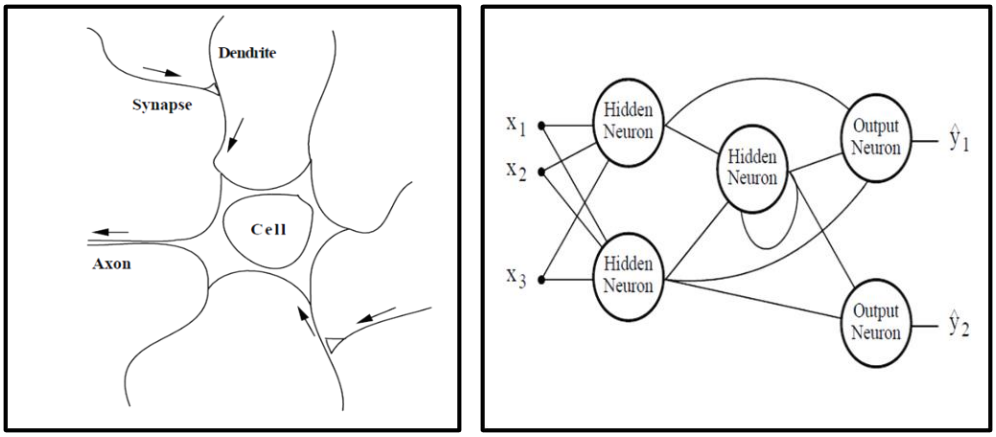

Figure 2.26: Similitude between neuronal architectures with a human neuron on the left and a model of an artificial neuron on the right (Larsen, 1999)

The design of ANN architecture is a critical preliminary step and typically comprises input and output neurons, hidden layers, and weight parameters operating within activation functions. Training enables the network to learn behavioural patterns by linking input parameters with predefined outputs through iterative trial-and-error adjustments. This process involves selecting a suitable learning algorithm, defining the prediction system (linear or nonlinear), and optimising the network structure (Cheng and Titterington, 1994; Kriesel, 2005; Khadeni *et al*., 2016; Boukhatem *et al*., 2011; Basheer and Hajmeer, 2000; Hakim *et al*., 2011). The datasets used during training provide the foundation for model calibration and subsequent analysis (Kriesel, 2005; Basheer and Hajmeer, 2000).

The performance of an ANN depends both on the architecture's ability to handle input–output relationships and the effectiveness of the employed algorithms (Basheer and Hajmeer, 2000; Hakim *et al*., 2011). A common approach is the sigmoidal error back-propagation method used in concrete material, which adjusts the weights between neuronal layers to minimise the error gradient (Ukrainczyk and Ukrainczyk, 2018; Hewayde *et al*., 2007; Onyari and Ikotun, 2018):

$$\Delta E_{m/w} = \frac{\partial E_m}{\partial W} \qquad (2.13)$$

$$W_{m+1} = W_m - u\, E_{m/v} \quad (2.14)$$

where E_m is the error gradient; W represents the weight matrix; m is the initial training step; u is the learning rate; and v represents a variable value to be transferred between two neuronal layers.

This algorithm (i.e., Equations 2.13 and 2.14) allows iterative refinement of predictions, providing a reliable tool for modelling concrete behaviour. Hewayde *et al*. (2007) demonstrated the practical application of ANNs to concrete corrosion under sulphuric acid attack, successfully predicting weight loss (RMSE = 0.013, AAE = 8.45%) and compressive strength deterioration (RMSE = 2.35 MPa, AAE = 4.49%). Their findings confirm that ANN-based formulations can effectively capture complex degradation patterns.

Figure 2.28 shows an example of an ANN architecture in predicting both models of weight loss and compressive strength using the backpropagation algorithm (Hewade *et al*. 2007).

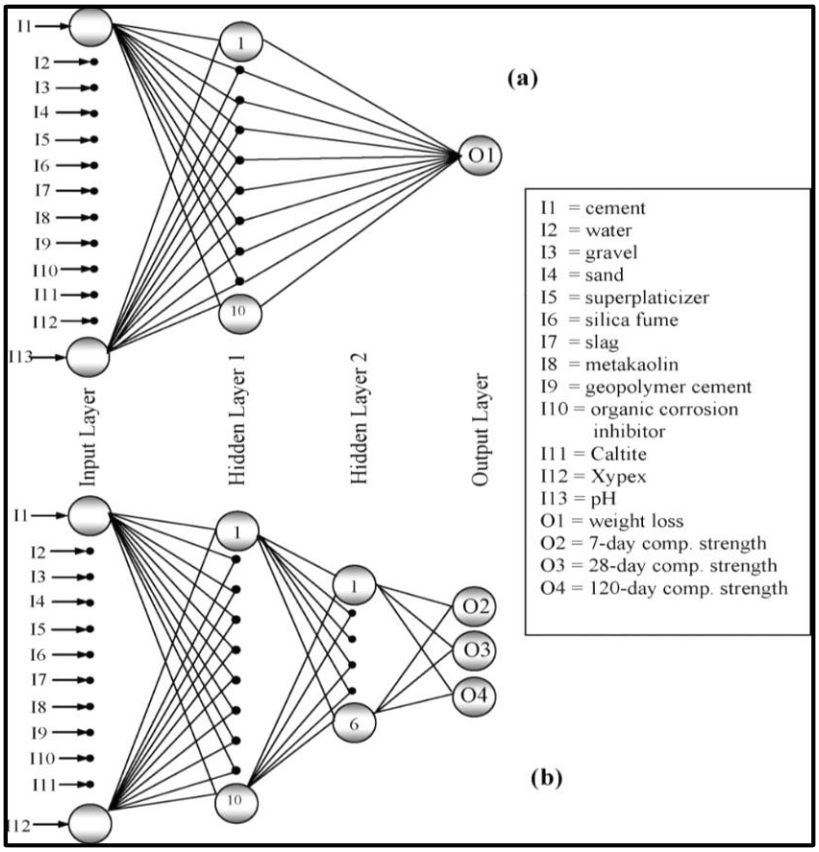

Figure 2.27: Two ANN architectures using each one multiple-input of factors to predict concrete corrosion due to H_2SO_4 (Hewayde *et al*., 2007): (a) The output layer is the weight loss; (b) The output layer is the compressive strength

Figure 2.27 illustrates representative ANN architectures employed for modelling concrete degradation. In Figure 2.27(a), the network incorporates thirteen input factors, including cement, water, gravel, sand, and acid concentration, among the most influential. This multi-layer perceptron (MLP) consists of three layers (i.e., input, hidden, and output) where the output layer predicts concrete corrosion in terms of weight loss. Conversely, Figure 2.27(b) presents a similar framework, with the key difference that the ANN comprises four layers, allowing the prediction of concrete degradation based on compressive strength. The selection of three layers for the weight-loss model and four layers for the compressive-strength model was guided by the accuracy achieved in predicting concrete degradation (Hewayde *et al*., 2007).

In summary, ANNs extend the capabilities of traditional mathematical models, offering a flexible and precise method for analysing microstructural and mechanical behaviours in cement-based materials, particularly when combined with image-derived datasets. However, existing algorithms still exhibit limitations in handling highly complex ANN frameworks and training patterns, as required for this study (see Section 5.3). Consequently, the implementation of novel algorithms is proposed to overcome these limitations and enhance the predictive and analytical power of ANN-based formulations.

2.6 Summary

The review of the existing literature highlights several key findings, alongside notable gaps that are pertinent to the present study.

The evidence underscores the predominant role of C_3S in early heat generation during cement hydration, in contrast to the delayed thermal contribution of C_2S, which becomes increasingly significant at later stages (Bye, 1999; Huang *et al*., 2025). This temporal distinction is further influenced by external physical factors affecting the microstructure of hydrating cement particles. Specifically, C_3S triggers a rapid release of heat in the initial hydration phase, whereas C_2S exhibits a slower and less pronounced thermal effect (Bye, 1999; Jansen *et al*., 2012; Semugaza *et al*., 2023; Huang *et al*., 2025). Over time, C_3S drives higher degrees of hydration, while C_2S remains associated with lower hydration levels. The pronounced early heat peak is consistently attributed to the kinetics of C_3S, a process further enhanced by the intrinsic alkalinity of Portland cement (Bye, 1999; Allahverdi *et al*., 2020).

External factors (including cement type, curing temperature, and curing duration) also exert a substantial influence on hydration kinetics, microstructural development, and the mechanical performance of cementitious materials at later hydration stages (Bye, 1999; Bentz *et al*., 1997; Elkhadiri *et al*., 2023; Huang *et al*., 2025).

Regarding durability, the concentration of acids has been identified as a critical factor accelerating concrete corrosion. It facilitates the mobility of sulphur ions and the formation of salts such as ettringite, which progressively deteriorate the cementitious matrix at the microstructural level (Attiogbe and Rizkalla, 1988; Shengyuan *et al*., 2012; Taheri *et al*., 2020; Allahverdi *et al*., 2020; Devi *et al*., 2022). Key influencing parameters include pH, water-to-cement (w/c) ratio, exposure duration, and sulphur ion mobility, all of which significantly contribute to corrosion and observable colour changes in cement microstructures (Shengyuan *et al*., 2012; Taheri *et al*., 2020).

The scanned point method offers the advantage of accurately defining scanning areas via circular markers (Jonawski *et al*., 2016). This non-destructive technique is well-suited for laboratory-scale monitoring of both hydration and corrosion processes in cement grains, particularly through the analysis of colour variations.

Current mathematical formulations applied to concrete materials reveal limitations when addressing complex microstructural behaviours, particularly those derived from surface imaging of cement-based materials. ANNs extend the capabilities of conventional models, providing a flexible and precise approach for analysing microstructural and mechanical behaviours, especially when integrated with image-based datasets. Nevertheless, existing ANN algorithms still encounter challenges in managing highly complex network architectures and training patterns, as required for this study. Therefore, the development of novel algorithms is proposed to overcome these constraints and enhance the predictive and analytical power of ANN-based formulations.

CHAPTER 3: EXPERIMENTAL PROGRAM AND EQUIPMENT

3.1 Introduction

The present chapter introduces the experimental investigations conducted to monitor the evolution of cement grain colouration. The work is centred on the collection of scanned surface images of concrete cubes subjected to both curing and corrosion conditions. The objective of the endeavour is to measure the microstructural behaviour of hydrating cement grains during the later stages of hydration (Elkhadiri *et al*., 2009; Jansen *et al*., 2012; Vasconcellos *et al*., 2023; Semugaza *et al*., 2023; Huang *et al*., 2025). Particular attention is given to examining the influence of corrosion on the durability and integrity of concrete mixtures exposed to sulphuric acid solutions.

In terms of laboratory test work, two concrete mixtures (M1 and M2) were prepared using Portland cement and locally sourced aggregates. The colouration of cement grains, the mechanical resistance of concrete and the corresponding temperature profile were monitored under both curing and corrosive conditions. A low-concentration sulphuric acid solution (30 g/ℓ) was used to simulate the corrosive environment while the response of the cement surface was measured by scanned point analysis during the acid attack. Details of the experimental programme and equipment employed are provided in the three main sections that follow.

3.2 Preparation of concrete samples

In this section, the main components of the concrete mixtures are identified. The preparation of mixtures is then covered following the required standards. Protocols for the curing of concrete specimens are described next. Lastly, the compressive strength testing program is presented.

3.2.1 Components of concrete used

Two concrete mixtures were prepared following the ASTM C150-07 standard (American Society for Testing and Materials, 2007). This standard requires the use of a Portland cement classified as Type I. This means that the cement can be used without any restrictions and that the incorporation of additional constituents inducing high initial mechanical strength during the preparation of concrete is not recommended. In addition to this, Portland cement is required as per the ASTM C150-07 standard because of its ability to withstand sulphuric acid attack. The latter motivated the choice since Türkel *et al*. (2007) confirmed experimentally the acid resistance of Portland cements compared to pozzolanic cements (see Section 2.3.2.1 of Chapter 2).

Coarse and fine aggregates were the next components used. Their preparation was done in accordance with the SANS 1083 specifications (South African Bureau of Standards, 2014a). This standard provides guidelines in the choice of aggregate properties as well as their ratios for enhanced properties of concrete. The aggregate was collected from the Mofia quarry located at 12 km North-East of Tenke Fungurume Mining plant. The aggregates employed in the present study was from a calcareous rock.

A large batch of approximately 3650 kg of aggregates was obtained from the quarry and prepared in the laboratory for testing. Initially, the aggregates were weighed using a 100 kg scale and subsequently characterised through preliminary tests to determine their calcareous properties before concrete mixture preparation.

Two primary tests were conducted. The first, the Aggregate Crushing Value (ACV), evaluated the hardness of the aggregates. The measured ACV was 26.7%, exceeding the SANS 1083 standard requirement of 25% (South African Bureau of Standards, 2014a), confirming the suitability of the aggregates as a calcareous rock for concrete production. The second test, sieve analysis, assessed the particle size distribution within the batch. Aggregates were sieved through screens of 19 mm, 12.5 mm, 9.5 mm, 4.75 mm, 600 µm, 75 µm, and the pan. Approximately 90% of

the aggregate weight was retained on the 4.75 mm sieve, indicating that the particle sizes predominantly fell within the standard 4.75–19 mm range, which is critical for optimising the mechanical strength of the concrete.

These characterisation tests were essential for designing the concrete mixtures used in all planned laboratory experiments. Moreover, they provide a reliable indication of the expected compressive strength performance of the concrete cubes (see Section 3.2.4 below).

3.2.2 Preparation of concrete mixtures

The concrete mixtures were prepared following the SANS 5861-1:2006 standards while the temperatures of the mixes were monitored during the production phase as guided by the ASTM 1064-05 standards. These two standards provide the prescriptions for freshly mixed concrete and for the controlling temperature during the casting of concrete (American Society for Testing and Materials, 2005; South African Bureau of Standards, 2014b).

In the present study, the concrete mixer in Figure 3.1 was used to produce fresh pastes. This mixer has a batching capacity of 0.3 m^3 per casting. In line with the SANS 5861-1:2006, each batch of concrete was mixed in two steps for 180 s. The dry components (i.e., cement and aggregate) were mixed first before water was added. Also, the temperature of concrete was recorded during production using an infra-red thermometer. Details about the thermometer are covered later in Section 3.3.4.



Figure 3.1: The concrete mixer used for casting

In this study, two concrete mix designs were selected to achieve target compressive strengths of 30 MPa and 40 MPa at 28 days. Their selection was informed by the work of Semugaza *et al*. (2023), who investigated a range of cement paste compositions to assess heat release and heat transfer during the early stages of hydration. Building on their findings, the present research extends this approach to concrete mixtures by examining how variations in mix design may influence both compressive strength development and temperature evolution. On this basis, it is hypothesised that concrete mixtures designed for different strength classes will exhibit distinct thermal and mechanical behaviours. Specifically, the differences in composition are expected to result in measurable variations in heat generation during hydration, which, in turn, will affect the rate and magnitude of strength development as the microstructure evolves (see Section 7.3 of Chapter 7).

The SANS 5861-1:2006 standard provides guidelines for determining the required mix design for the chosen compressive strength to be expected of the concrete at 28 days of age. It is based on this standard that the compositions of two concrete mixtures were estimated.

Table 3.1 Mix compositions for M1 (30 MPa) and M2 (40 MPa) concrete cubes

	Compositions	
Ingredients	**M1**	**M2**
Coarse aggregate (kg)	900	950
Fine aggregate (kg)	900	900
Cement (kg)	500	500
Water (ℓ)	225	200
Admixture (kg)	0	0
Water-to-cement ratio	0.45	0.40

Note in Table 3.1 that the compressive strength of the Portland cement used is quoted in the Manufacturer's Specification Data Sheet to be 42.5 MPa at 28 days.

One important aspect in the preparation of concrete was the regular monitoring of the temperature of the mix at each step along the production line. Furthermore, the temperature was recorded inside the mixer as exemplified in Figure 3.2. Average, minimum, and maximum temperatures are displayed for the batch.

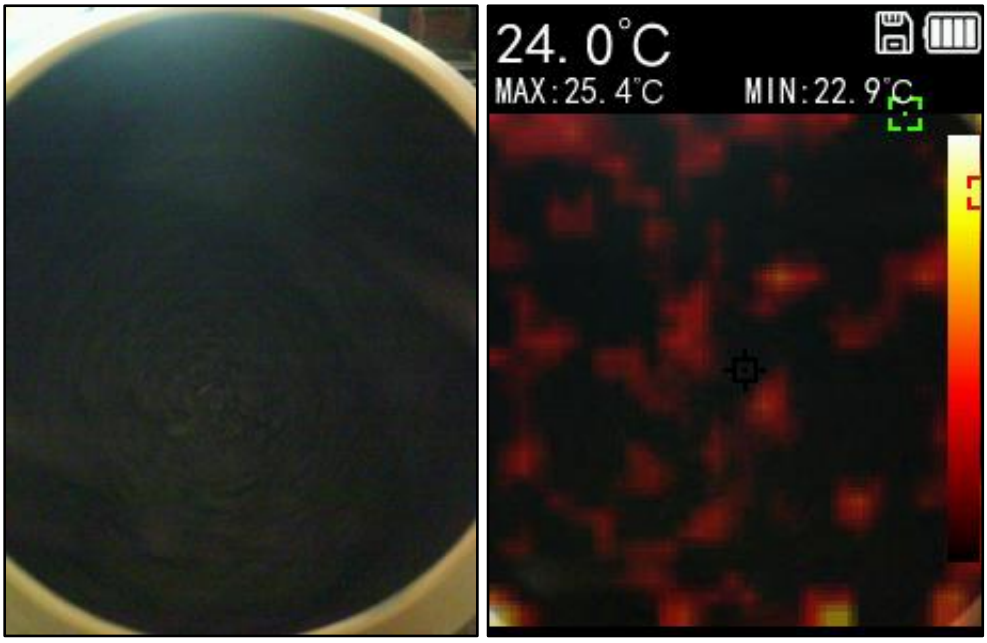

Figure 3.2: (Left) Content of the concrete mixer and (Right) recording of the temperature inside the mixer during production

After 180 s of mixing, the batch was then poured into a wheelbarrow and tested for temperature as shown in Figure 3.3.

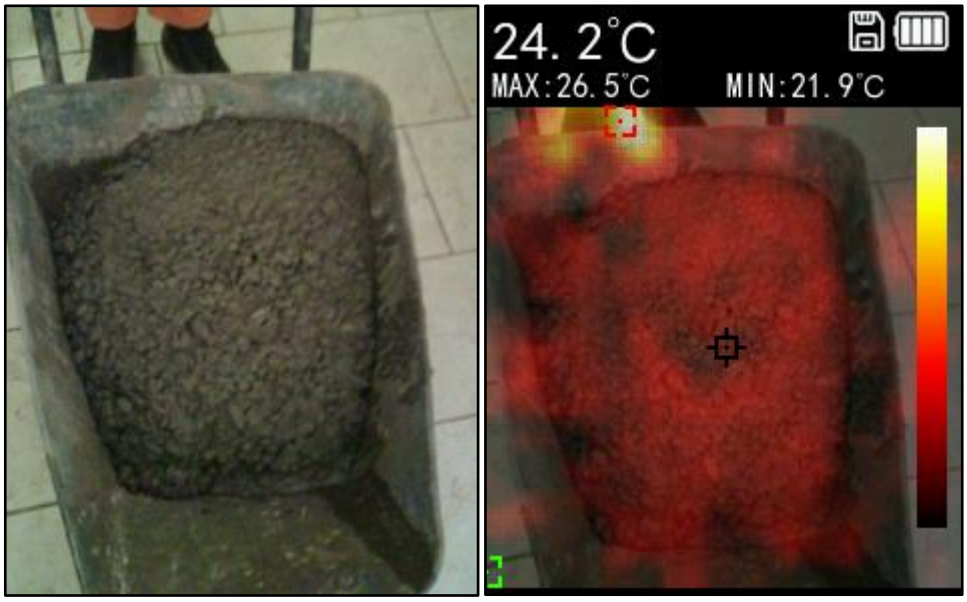

Figure 3.3: (Left) Concrete sample in the wheelbarrow and (Right) recording of temperature

Finally, at the end of the production line, concrete cubes were cast in 150 x 150 x 150 mm moulds. Here also, temperature was measured (see Figure 3.4).

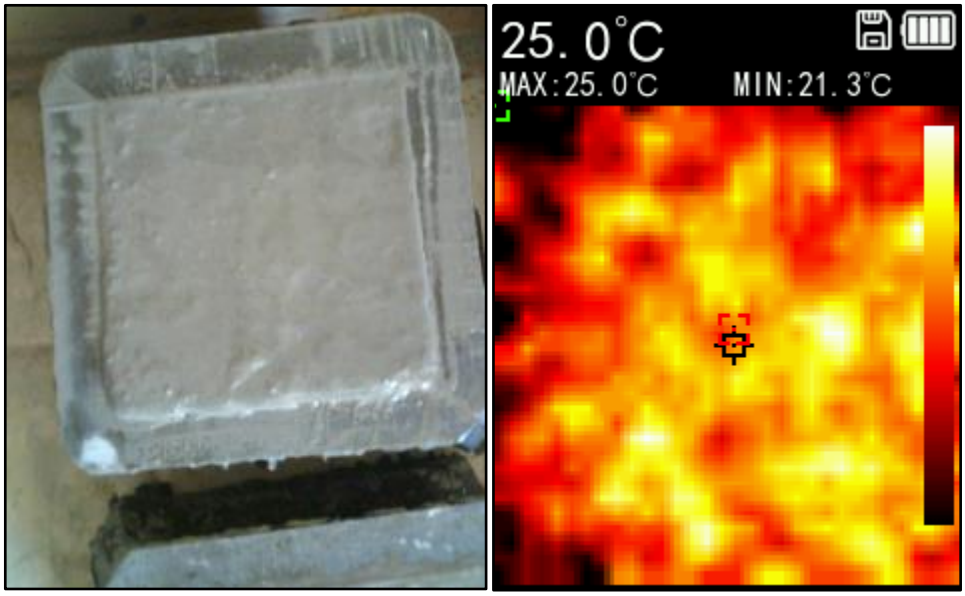

Figure 3.4: (Left) Casting of a 150 x 150 x 150 mm concrete cube and (Right) measurement of the surface temperature of the cast concrete

It is important to note that the temperature of the different batches of fresh concrete cubes was monitored throughout the production stage. This monitoring approach was informed by the work of Shokravi and Shaghaghi (2019) in which a methodology for recording the temperatures of individual constituents (i.e., cement, water, and aggregates) directly within a batching plant was outlined. According to these authors, such temperature control offers a clear advantage in regulating key physical parameters of concrete, particularly shrinkage associated with temperature fluctuations, which may otherwise lead to early-age cracking.

3.2.3 Curing of concrete samples

Once the concrete samples were cast and deemed firm after 24 h of casting, they were then cured by submerging them into water (see Figure 3.5). Curing was aimed to improve the physical and mechanical properties of concrete such as compressive strength and hardness (American Society for Testing and Materials, 2001). Curing also protects the concrete material against shrinkage and cracking under service conditions. All the experimental protocols associated with curing including the monitoring programme of the cement grain hydration are detailed in Section 3.3.2.

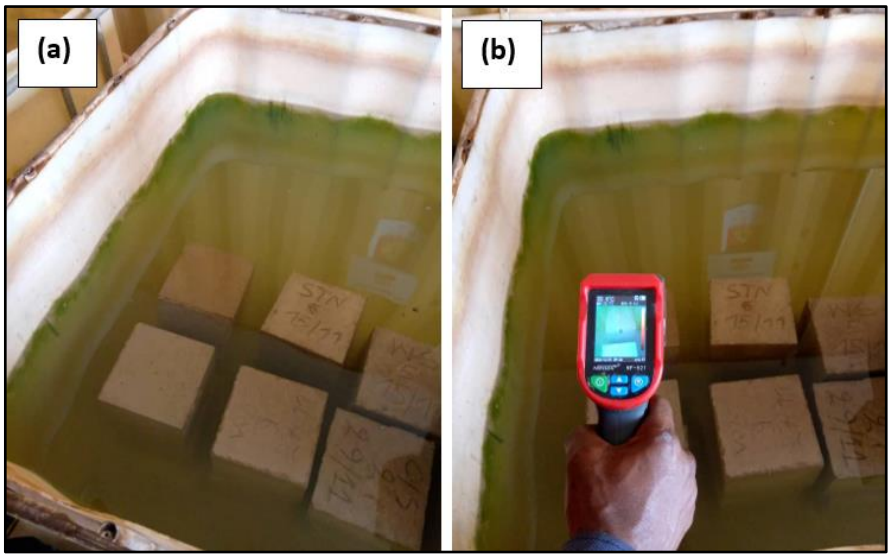

Figure 3.5: (a) Curing tank with partial view of concrete cubes and (b) monitoring of water temperature using a thermometer

The testing of moist-cured concrete cubes varied from a period of 0 to 28 days of age. As shown in Figure 3.5, water temperature was measured every day and recorded until the end of the curing period. For quality control, a thermometer and a pH-meter were both used to verify that the water temperature and pH were around 20°C and 7.0 ± 0.5 respectively. In case of a drastic change of any of the two parameters, all the water was slowly drained and gradually replaced with fresh water until the set point was reached. Note here that the main reason for controlling the pH of water is to avoid any phenomenon of concrete salinization, which can contribute to the reduction of the concrete strength (American Society for Testing and Materials, 2001).

3.2.4 Compressive strength testing

Compressive strength tests were performed on the concrete cubes of size 150 x 150 x 150 mm prepared in Section 3.2.2 above. Tests were done after 3, 7, 14, 21 and 28 days of curing. These tests were conducted in accordance with the SANS 5863:2006 standard (see Section 3.2.2). The standard provides relevant information on how to conduct a compressive strength test in the laboratory. The specifications associated with the standard outline the procedure to follow in the application of loads on the surface of concrete cubes. Furthermore, the standard gives the formula for the calculation of compressive strength after a curing period (South African Bureau of Standards, 2006).

In terms of the actual compressive tests, a laboratory press was used to crush each concrete cube as recommended by the South African Bureau of Standards (2006). A load was progressively applied to each concrete cube at a rate of 350 kN/min. This rate provides from the service-standard of equipment itself as displayed on screen as can be seen in Figure 3.6.



Figure 3.6: (Left) Testing of concrete cube under a cube-press equipment and (Right) Display of the rate of compression

The load recorded immediately after the concrete cube failed was displayed on the screen of the cube-press for the corresponding curing age. The compressive strength was then calculated for concrete sample as follows (South African Bureau of Standards, 2006):

$$C_{d,n} = \frac{P}{S} \tag{3.1}$$

Where $C_{d,n}$ is the compressive strength [in MPa] corresponding to the day d_n when testing is conducted. In this research, n = 3, 7, 14, 21 and 28 days

P is the load measured by cube-press equipment in kN

S represents the surface of concrete sample in mm^2. In this work, S is equal to 225 mm^2.

The estimated compressive strengths for the two concrete mixtures (M1 and M2) are given in Table 3.2. As stated in Section 3.2.2, both mixtures in Table 3.1 were designed to produce concretes of compressive strengths 30 ± 1 MPa for M1 and 40 ± 1 MPa for M2 after 28 days of curing. Values reported in Table 3.2 satisfy the requirements.

Table 3.2: Compressive strengths measured during the curing of concrete cubes prepared following M1 and M2 designs

	Compressive strength recorded [in MPa]	
Curing period [in days]	**M1**	**M2**
3	15.0	20.6
7	19.1	28.5
14	25.1	32.0
21	27.2	35.5
28	29.2	39.6

Indeed, with reference to Table 3.2, the measured compressive strength for M1 (29.2 MPa) tested at 28 days falls with the confidence interval, i.e., 30 ± 1 MPa or 29 – 31 MPa. A similar conclusion is reached for M2, that is, the compressive strength of 39.6 MPa measured at 28 days is acceptable for 40 ± 1 MPa target.

3.3 Protocols used to monitor the colouration of cement grains

This section presents the experimental methodologies used to monitor cement grain colouration (CGC) in concrete mixtures under both curing and corrosion conditions, along with the procedures and laboratory equipment employed for dataset collection. It also introduces the experimental programme designed to capture CGC and temperature variations during moist-curing period. The subsequent section then describes the equipment and data-collection methods applied throughout the various stages of the experimental campaign.

3.3.1 Preparation of concrete samples used for experimentation

In terms of the experimental programme associated with the CGC of concrete mixtures, 17 concrete cubes were prepared beforehand per mixture as described previously in Section 3.2.2. A total of 34 concrete cubes was therefore cast for both mixtures (M1 and M2). The 17 cubes prepared with the M1 mixture were

split as follows: 15 cubes for the compressive testing of M1 and 2 cubes for the non-destructive tests aimed at monitoring of the CGC after every curing period. A similar split was done for the M2 mixture.

Talking about the non-destructive CGC tests, each of the 4 concrete cubes retained for the purpose was marked with appropriately laid out circles referred to here as experimental or marked points. Janowski *et al*. (2016) advocated for the point marking technique and demonstrated that the image scanning of these marked points could be utilized in the diagnosis of failed reinforced concrete. So, based on the recommendations by Jonawski *et al.* (2016), 9 circular points were marked respectively on four lateral faces of the concrete cubes as shown in Figure 3.7. A total of 36 points were tagged per each concrete cube for CGC testing.

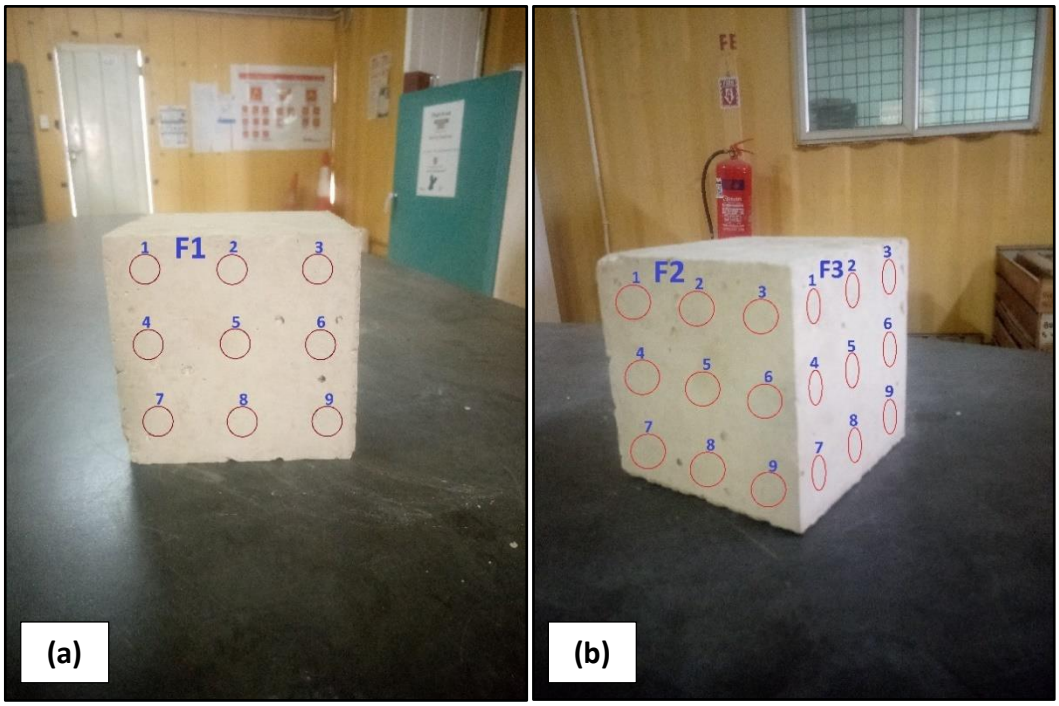

Figure 3.7: A concrete cube marked with experimental points for the CGC test with 3 faces presented: (a) Face 1 and (b) both Face 2 and Face 3

The circular points in Figure 3.7 are 24 mm in diameter. This diameter is informed by the size of the scanner-microscope. It enabled the correct focus of the equipment to take images within the perimeter of the tested experimental point. The scanning microscopy and the collection of scanned images are covered next.

3.3.2 Equipment used and experimental tests considered

Section 2.4.2 of Chapter 2 reviewed cases where microscopic scanners have been used to collect images with colour variations in the study of concrete. In this study, the scanning device used for the purpose is presented in Figures 3.8 and 3.9 with identifying labels. The labels indicate the main components of the device as follows: A – the focus adjustment wheel, which allows magnification of images up to 1000×; B – the power button; C – the bracket for adjusting the LED brightness; D – a U-shaped device for scanner adjustment; E – the handle used to modify the scanner's height and angle; F – the metal base; G – the USB interface port; H – the smart camera integrated into the equipment casing; I – the LED light; and J – the equipment focus.

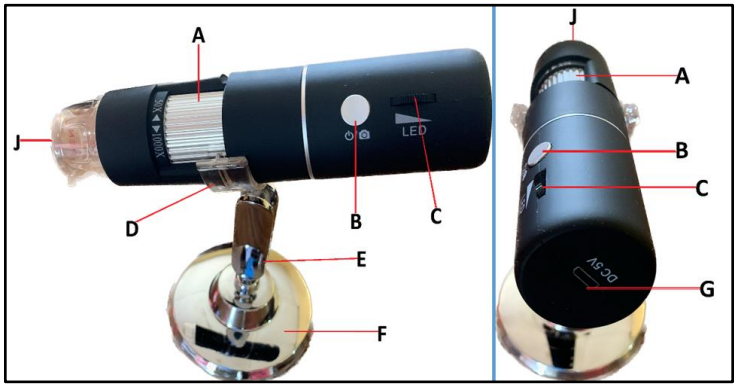

Figure 3.8: (Left) Lateral and (right) front view of the microscopic scanner

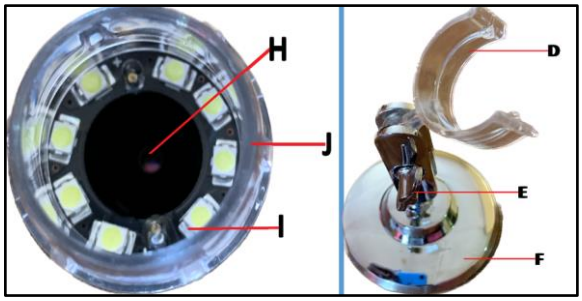

Figure 3.9: (Left) Overall view of focus and (Right) support accessory

Figure 3.10 presents the thermometer that was used to measure the temperature of concrete samples during preparation and curing.

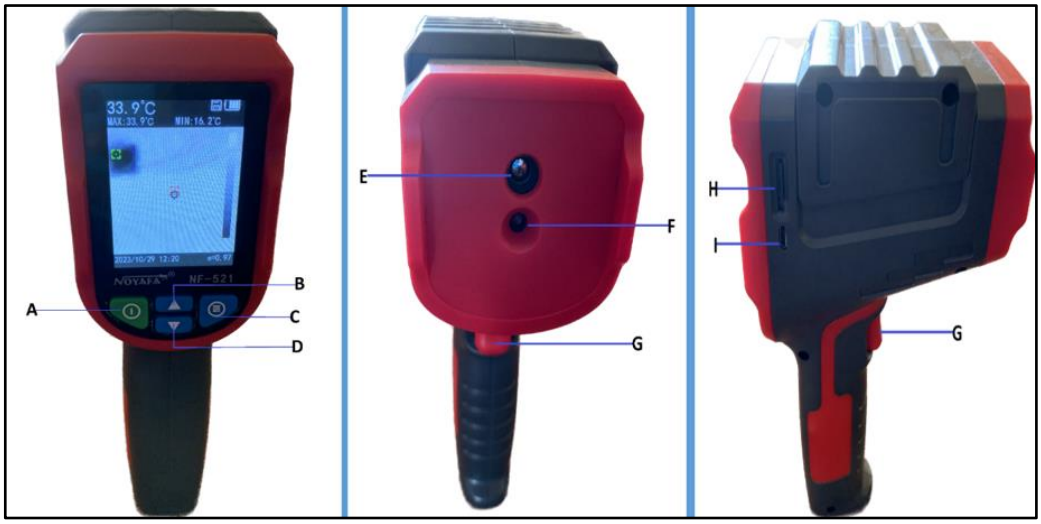

Figure 3.10: (Left) Front view of the thermometer showing the display screen; (Centre) Rear view and (Right) Lateral view of the thermometer

In Figure 3.10, the following labels should be noted: A identifies the Return button; B is the Up button; C is the OK and Menu button; D is the Down button; E is the thermometer lens; F is the Infra-red camera; H is where the SD card slot is located; I is USB interface port; and G is the Trigger button.

Once the microscopic scanner was set up, images were collected following the procedure in Figure 3.11. The workflow ensured that appropriate images of the marked points were taken and stored on a dedicated computer for the later analysis presented in Chapter 4.

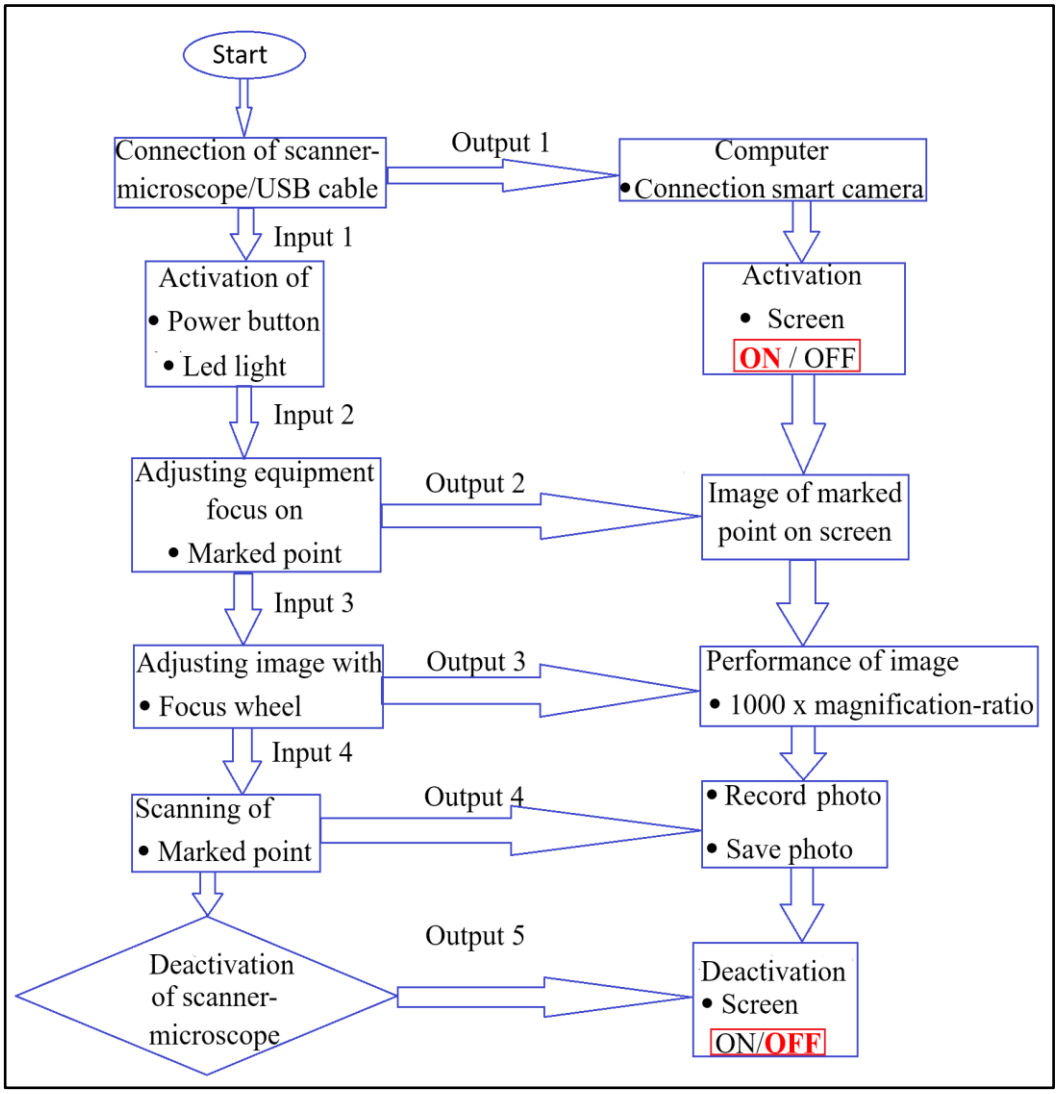

Figure 3.11: Flowchart for collecting images of marked points with the microscopic scanner set at 1000x magnification

3.3.3 Measurement of cement grain colouration under curing conditions

In Section 2.3.2, a limitation was noted in the protocols used to collect image data from concrete surfaces using a microscopic device. To address this, the present study implemented a laboratory protocol for monitoring scanned concrete surfaces, aimed at capturing image data to assess colour changes. This novel protocol involved two main steps. First, after three days of immersion, ten concrete cubes (five from each mixture) were removed from the water tank shown in Figure 3.5. Six of these cubes were used to measure surface temperature prior

to compressive testing, using an infrared thermometer as illustrated in Figures 3.12 and 3.13. The remaining four cubes underwent non-destructive scanning to evaluate cement grain colouration. For the two mixtures, a total of 144 experimental points were scanned using the microscope-scanner after three days of curing.

The scanning procedure was carried out as follows: the cubes were removed from the water tank, surface images were captured at predetermined points, and the cubes were then returned to the tank until the next testing day. This procedure was repeated at 7, 14, 21, and 28 days of curing, providing a comprehensive image dataset for both mixtures, M1 (30 MPa) and M2 (40 MPa), which was subsequently analysed in Section 4.2 of Chapter 4. Through this approach, the laboratory monitoring protocol generated a robust dataset of scanned concrete surface images to support the assessment of cement microstructure evolution.

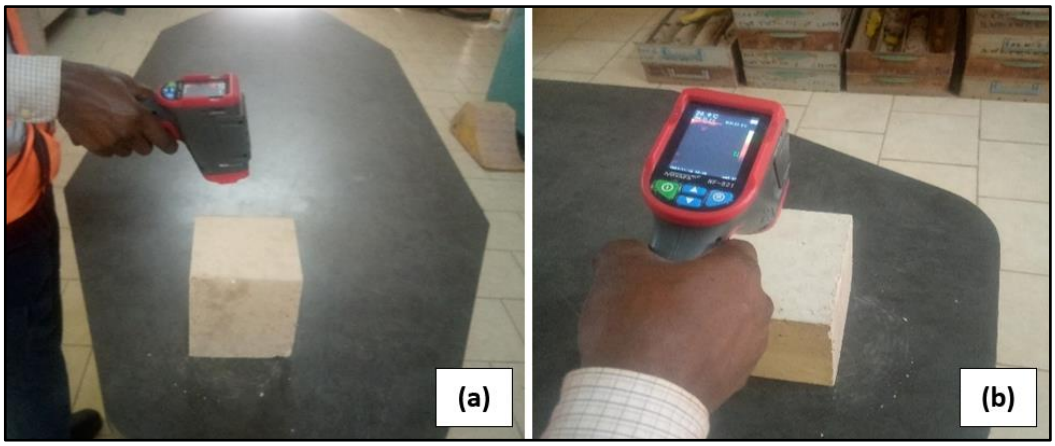

Figure 3.12: (a) Collection of concrete temperature with an infra-red thermometer and (b) overall view showing the device screen

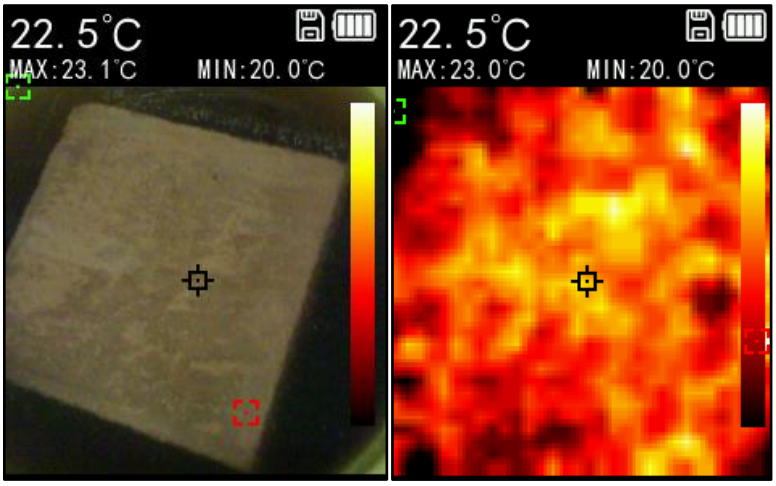

Figure 3.13: Image of concrete aimed at with an infra-red thermometer (left) and recording of the temperature (right)

In Figure 3.13 the main target is represented by a black pointer while secondary targets in red and green show respectively the points of maximal and minimal temperatures recorded. These temperatures measured on concrete samples as illustrated in Figure 3.9 are listed in Table 3.3 for mixture M1 and Table 3.4 for M2.

Table 3.3: Temperatures recorded for concrete cubes of mix design M1 for different curing ages

	Temperature measured [in °C]		
Curing age	**Average**	**Minimum**	**Maximum**
3 days	21.75	20.0	23.5
7 days	22.35	21.0	23.7
14 days	24.60	21.8	27.4
21 days	23.45	22.7	24.2
28 days	22.95	21.5	24.4

Table 3.3 presents the average minimum and maximum temperatures measured during the curing period. For instance, the temperature at 3 days reaches 21.75°C, increasing to 22.35°C at 7 days. These values correspond to concrete cubes prepared with mix M1 (30 MPa).

Table 3.4: Temperatures recorded for concrete cubes of mix design M2 for different curing ages

	Temperature measured [in °C]		
Curing age	**Average**	**Minimum**	**Maximum**
3 days	20.45	18.6	22.3
7 days	20.95	18.7	23.2
14 days	21.50	19.0	24.0
21 days	24.20	21.5	26.9
28 days	22.80	21.2	24.4

Table 3.4 shows the corresponding average temperatures for mix M2 (40 MPa). A comparison between Tables 3.3 and 3.4 indicates that the peak average temperature for M1 occurs at 14 days (24.60°C), whereas for M2 it is reached at 21 days (24.20°C).

Now, after temperatures were taken, the cubes were then scanned for cement grain colouration. Figures 3.14 and 3.15 show how the marked points were scanned. Figure 3.14 illustrates the data collection of point P8, i.e., middle point of the row of the first face of the concrete cube. Also note in Figure 3.14 that J represents the tested area around point P8; K is the USB cable connecting the device to the computer; and L in Figures 3.15 – 3.16 is the computer screen.

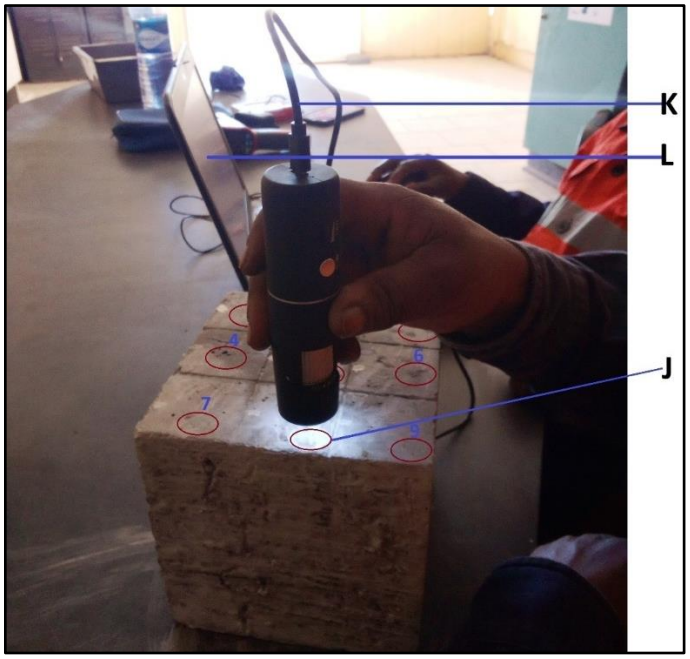

Figure 3.14: Sweeping of marked points with a microscopic scanner



Figure 3.15: Illustration of both scanning of marked point and indication on screen of the CGC image

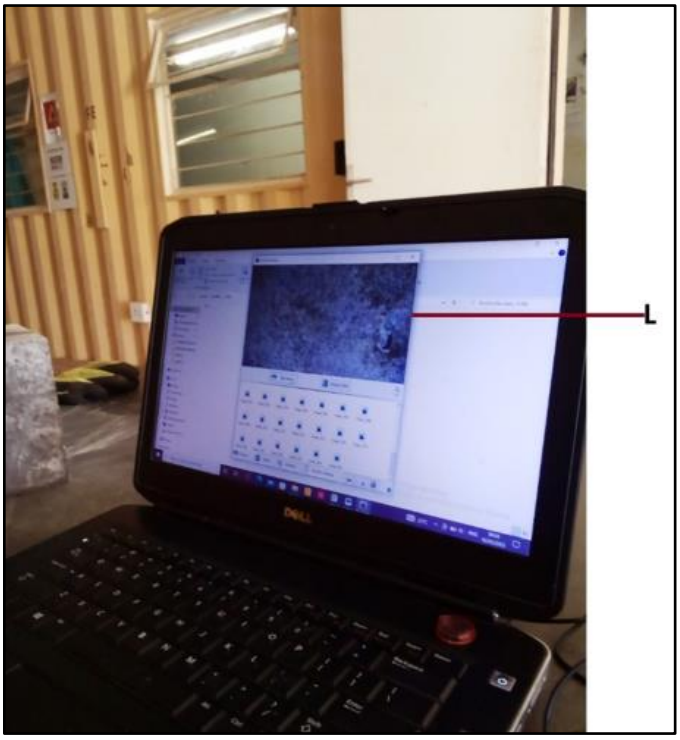

Figure 3.16: Overall view of the computer screen showing the CGC image

The experimental procedure of immersion tests under curing conditions is summarized in Tables 3.5

Table 3.5: Experimental procedure of immersion tests under curing conditions

Material	Immersion solution	Immersion time	Test measurement		Testing frequency
150 x 150 x 150 mm concrete cubes	Water	3 days	Temperature	x	3 days from production day
			Scanning	x	
		7 days	Temperature	x	4 days from the third day of immersion
			Scanning	x	
		14 days	Temperature	x	Every 7 days
			Scanning	x	
		21 days	Temperature	x	
			Scanning	x	
		28 days	Temperature	x	
			Scanning	x	

3.3.4 Monitoring of concrete surface colour changes under corrosion conditions

To extend the study CGC beyond curing, a laboratory protocol was developed to monitor concrete surfaces under corrosive conditions, providing a comprehensive dataset on the effects of sulphuric acid over time.

Concrete mixtures of composition M1 (30 MPa) were immersed in a 30 g/ℓ sulphuric acid solution. This composition was chosen to allow long-term testing, as lower acid concentrations enable concrete samples with calcareous aggregates to remain submerged for extended periods. One cube, previously used for curing tests and containing 36 experimental points, was retained for corrosion assessment (Figure 3.17). After three days of immersion, the cube was removed, drained, rinsed with tap water for one minute in order to get rid of insoluble salts, and then scanned using the scanner-microscope to capture CGC images. Following scanning, the cube was returned to the solution, and the procedure was repeated at 6, 9, 12, 18, 24, and 27 days (see Table 3.6). Between measurements, the sulphuric acid solution was monitored with a portable pH meter to maintain a concentration of 30 g/ℓ, with pH stability within ±0.1%. Any deviations were corrected by replacing the solution. The intervals between testing days (e.g., between days 6 and 9, or 12 and 18) were required to allow sufficient time for solution replacement between consecutive tests.



Figure 3.17: (a) Concrete cube in a container filled with sulphuric acid solution and (b) water-washed concrete cube after 3 days of acid immersion

Table 3.6: Adopted experimental procedure for immersion tests under corrosion conditions

Material	Immersion solution	Immersion time	Test measurement		Testing frequency
150 x 150 x 150 mm concrete cubes	Water	3 days	Temperature	x	3 days from production day
			Scanning	x	
		7 days	Temperature	x	4 days from the third day of immersion
			Scanning	x	
		14 days	Temperature	x	Every 7 days
			Scanning	x	
		21 days	Temperature	x	
			Scanning	x	
		28 days	Temperature	x	
			Scanning	x	

Tables 3.6 and 3.7 summarise experimental procedures of immersion test for concrete mixtures in the laboratory. This shows how often the concrete cubes were primarily monitored and tested during the curing condition prior to a

continuous immersion in sulphuric acid solution. Data collected experimentally in both conditions were firstly recorded in a spread sheet and then prepared for further statistical analysis in the next chapters. This analysis programme served to the training process under the ANNs for generating mathematical models regarding concrete mixtures.

3.4 Challenges encountered during the experimental work

The experimental programme in this chapter aimed to collect clear and useful data in line with the research objectives (see Section 1.4 of Chapter 1). However, some limitations prevented it from being fully carried out.

The absence of suitable non-destructive testing equipment meant that mechanical stresses in corroded specimens could not be measured, which also limited the analysis of compressive strength and the study of cement microstructures.

Time limitations also affected the immersion tests, preventing data collection beyond 27 days and making it impossible to monitor specimens in low-concentration sulphuric acid (30 g/ℓ) until they were fully degraded. Consequently, the M2 mixture (40 MPa) was not tested for corrosion. The irregular schedule for replacing the acid solutions—first every 3 days, then up to 6 days, before returning to 3 days—also reduced consistency, probably due to variations in acid quality.

Limited availability of acid solutions additionally restricted testing across multiple specimens and mixture types (M1 and M2). Despite these limitations, the data obtained provided a sufficient basis for the experimental procedures that follow, which have been carefully adapted to address the challenges identified.

CHAPTER 4: ANALYSIS OF SCANNED IMAGE DATA

4.1 Introduction

It is hypothesised that systematic variations in the colour patterns of scanned concrete images reflect the evolving microstructures of cement. As outlined in Section 2.3.2.2 of Chapter 2, quantitatively tracking these variations offers a means of assessing microstructural responses to hydration and to corrosion induced by sulphuric acid. This approach therefore provides a non-invasive and reliable basis for characterising cement behaviour. The present chapter examines this hypothesis for the first time.

The first part compiles the raw images scanned at selected points on the concrete surfaces, arranged chronologically and separated according to curing or corrosion conditions. These images are accompanied by preliminary observations that highlight the dominant colour features, with the aim of identifying visual indicators of hydration or corrosion progression.

The second part describes the methodological framework used to convert colour images into black-and-white representations at the scale of cement grains. This step enables a pixel-based quantification of the scanned data, establishing an initial and robust dataset from which the subsequent chapters evaluate the development of both hydration and corrosion mechanisms.

4.2 Scanned images under curing and corrosion conditions

This section presents the scanned images obtained during the laboratory programme, grouped according to curing or corrosion exposure. For each condition, the images are organised by concrete mixture type and by the corresponding testing times at which they were captured.

4.2.1 Scanned images under curing conditions

This subsection presents scanned images from three surface points on a 150 × 150 × 150 mm specimen of mixture M1 (30 MPa). Table 4.1 compiles images from points 1, 2, and 3 (layer 1) at 3, 7, 14, 21, and 28 days of curing, clearly illustrating the progressive colour changes and providing a foundation for the comparative analyses in the following sections.

Table 4.1: Scanned images under curing conditions for concrete mixture (M1/30MPa)

Scanned images of 3 points (M1/30MPa) under curing conditions		
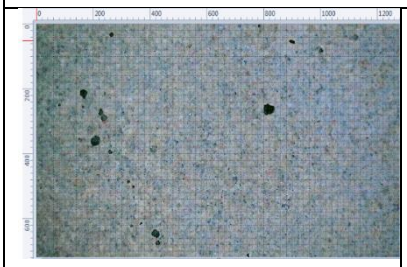	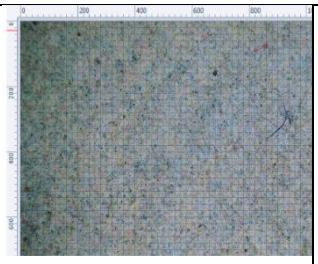	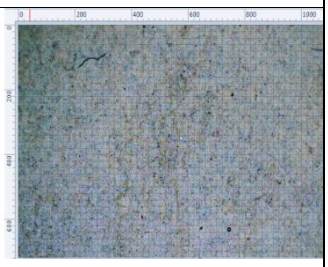
Scanned image of Point1 @ 3days	Scanned image of Point2 @ 3days	Scanned image of Point3 @ 3days
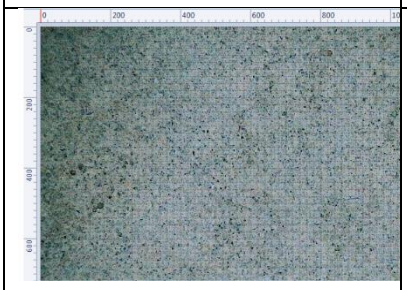	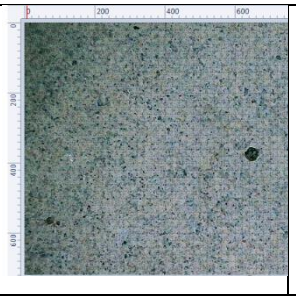	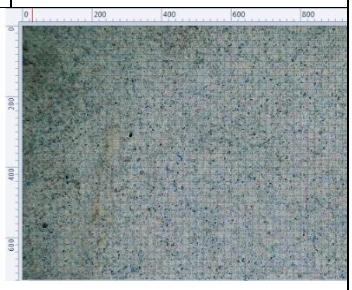
Scanned image of Point1 @ 7days	Scanned image of Point2 @ 7days	Scanned image of Point3 @ 7days
	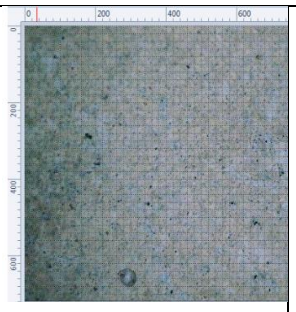	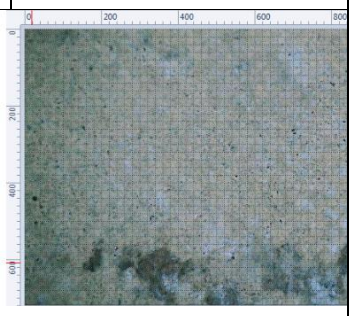
Scanned image of Point1 @ 14days	Scanned image of Point 2 @ 14days	Scanned image of Point3@ 14days

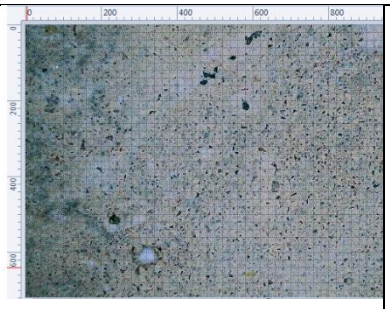	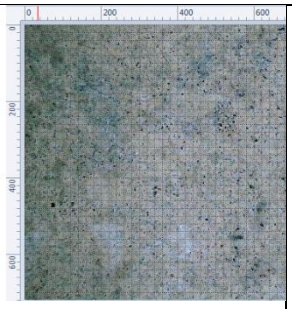	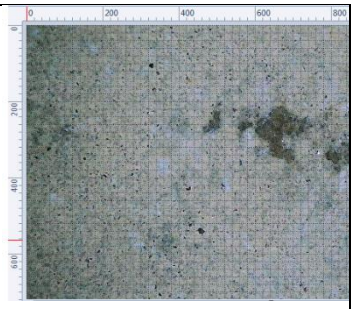
Scanned image of Point1 @ 21days	Scanned image of Point 2 @ 21days	Scanned image of Poimt3@ 21days
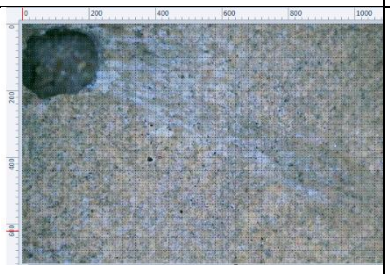	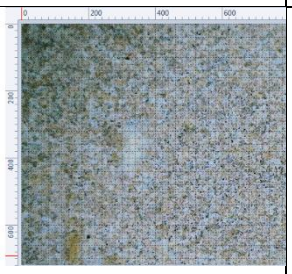	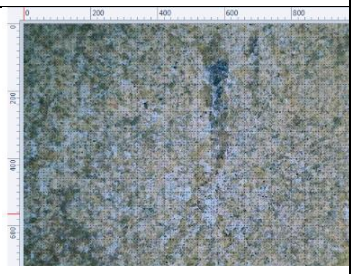
Scanned image of Point 1 @ 28days	Scanned image of Point 2 @ 28days	Scanned image of Point3 @ 28days

Table 4.1 presents a series of images captured at three selected points (P1, P2 and P3) on the surface of a 150 × 150 × 150 mm concrete cube. These images were obtained at different curing times in order to monitor surface changes. The data correspond to the concrete mixture identified as M1 (30 MPa). Preliminary observations from scanned images suggest three ranges of CGC. Firstly, from 3 to 7 days of curing, the colouration of the cement grain occurs in three colours: pink, brown and blue. Sometimes, occurrence of forms resembling to clouds. The light blue stains indicate an early phase of the cement hydration. Secondly, predominance of two colours (pink and blue) occurring between 14 and 21 days. Light blue indicating the cement hydration in its intermediary phase, occurrence of some forms resembling either to a river or a lake. Third, at 28 days of curing, again cement grains turn into three distinct colours: pink, brown and blue. By contrast, during this last phase a large spectrum with light blue colour is concentrated on the middle area, thus indicating the evolving of cement grain hydration.

For the reason of similarity, other representative tables regarding images of scanned points for M1 (30MPa @28days) and M2 (20MPa @28days) are reported in Appendix A.

4.2.2 Scanned images under corrosion conditions

This subsection presents the scanned images collected from three surface points on a 150 × 150 × 150 mm specimen exposed to sulphuric-acid-induced corrosion. The corresponding table compiles images from points P1, P2, and P3 at the designated testing intervals, clearly illustrating the progressive colour transformations resulting from corrosion and providing a basis for the quantitative analyses developed later in this chapter.

Table 4.2 presents scanned images under corrosion conditions for the M1 / 30 MPa concrete mix.

Table 4.2: Scanned images under corrosion conditions for concrete mixture (M1/30MPa)

Scanned images of 3 points (M1/30MPa) under corrosion conditions		
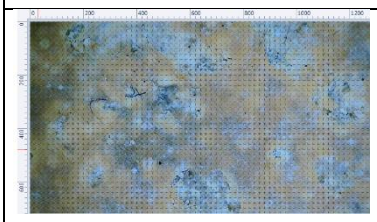	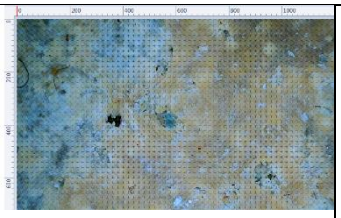	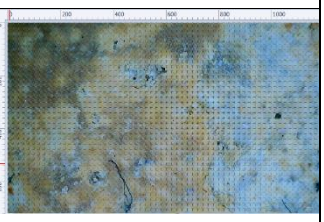
Scanned image of Point1 @ 3days	Scanned image of Point2 @ 3days	Scanned image of Point3 @ 3days
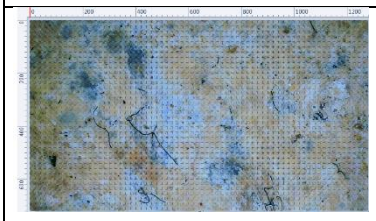	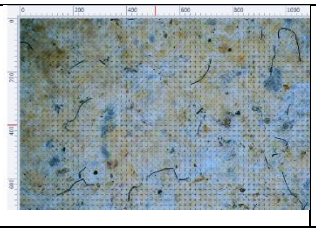	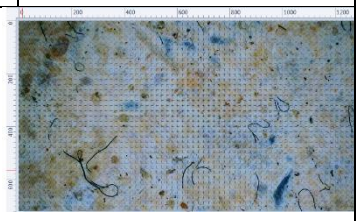
Scanned image of Point 1 @ 6days	Scanned image of Point2 @ 6days	Scanned image of Point3 @ 6days

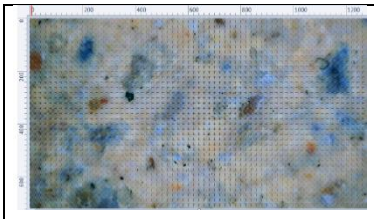	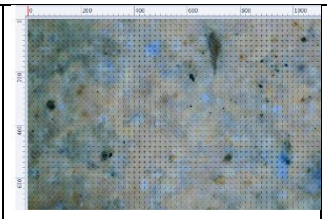	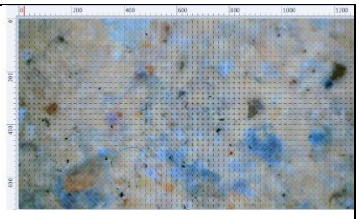
Scanned image of Point 1 @ 9days	Scanned image of Point 2 @ 9 days	Scanned image of Point3 @ 9days
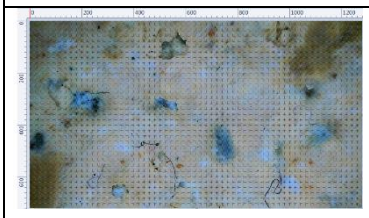	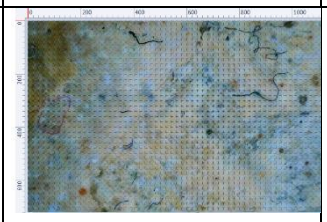	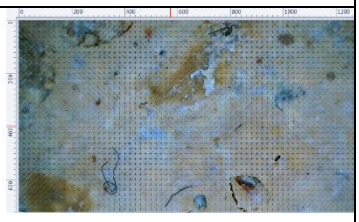
Scanned image of Point1 @ 12days	Scanned image of Point2 @ 12days	Scanned image of Point3 @ 12days
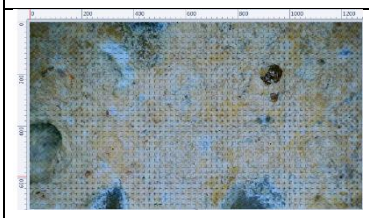	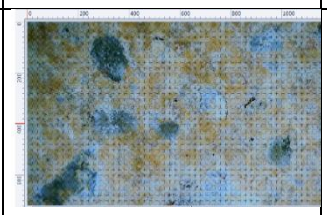	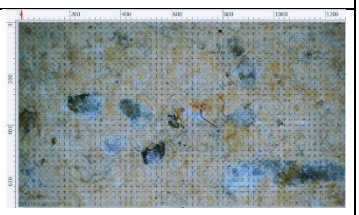
Scanned image of Point1 @ 18days	Scanned image of Point2 @ 18days	Scanned image of Point3 @ 18days
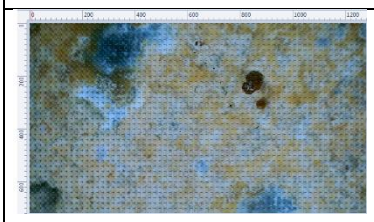	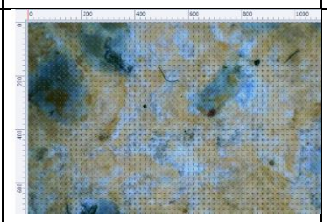	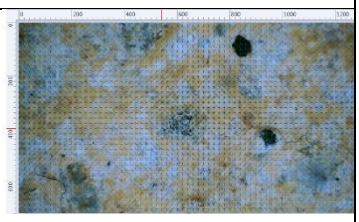
Scanned image of Point1 @ 24days	Scanned image of Point2 @ 24days	Scanned image of Point3 @ 24days
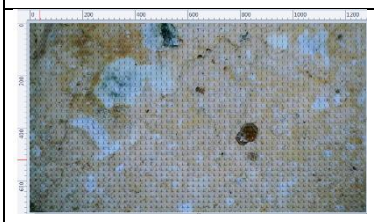	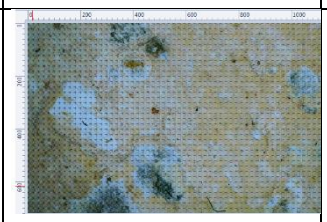	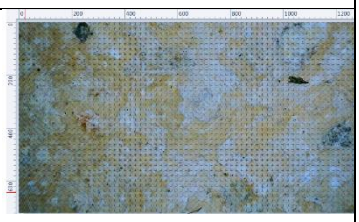
Scanned image of Point1 @ 27days	Scanned image of Point2 @ 27days	Scanned image of Point 3@ 27days

Table 4.2 relates to a case of images of three scanned points (P1, P2 and P3) under corrosion conditions. In addition, concrete mixtures (M1 / 30 MPa) are tested at a

concentration of sulphuric acid of 30g/ℓ (refer to Section 3.3.4 of Chapter 3). Here again, preliminary observations regarding colour changes of images as functions of corrosion time suggest two main ranges of CGC. Firstly, an almost equal distribution of the surface between the brown and blue colours occurring at 3 – 9 days of immersion. Similarity with a map showing respectively the earth in brown colour and the lake in blue ones. The blue colour represents probably a sign of cement hydration. By contrast, the presence of the brown colour is may be the beginning of concrete corrosion with a salt formation inducing to ettringite (Allahverdi and Škvára, 2000). Secondly, from 12 to 27 days, a predominance of the light brown area versus the blue ones can be observed. The images associated with the remaining scanned points are included in Appendix B.

In the next section, the images presented in Tables 4.1 and 4.2 are used as a reference framework. They guide the conversion of coloured images into black and white pixel values during the image processing procedure under curing and corrosion conditions.

4.3 Methodology for converting coloured images into grey pixel images

The present section covers the processing methodology with regards to how to convert coloured images of cement grains to black and white pixel images. Then, how to convert the obtained black and white image to a describable pixel framework. In this technique, the objective was to compile a numerical database of the rate of black-and-white pixel concentrated into the scanned images. For the case of the current study, the rate evaluation of black-and-white pixel concentrated into the scanned points was developed using Python (version 3.12).

Python is widely used programming language known for its simplicity, readability, and efficiency. This software is also used to design image processing and provide statistical analysis of black and white pixels. The main advantage of employing Python is its capability to efficiently process image data derived from predefined

Microsoft® Excel® spreadsheets. Also, its capacity to compute percentage of black and white pixels, and to generate visual plots that include respectively the original-coloured image, the binary (black-and-white) version of the converted image, and a table displaying relevant statistical information.

4.3.1 Images processing under curing and corrosion conditions

This section presents the methodology adopted for image processing, together with the results obtained under both curing and corrosion conditions. Coloured images were first acquired from 144 experimental points associated with the two concrete mixtures. These images were collected prior to the casting of the concrete specimens; namely, M1 (30 MPa at 28 days) and M2 (40 MPa at 28 days). The specimens were subsequently subjected to curing conditions (see Section 3.3.3 of Chapter 3).

The next stage involved acquiring images from 36 experimental points on an M1 cube subjected to the corrosion test (see Section 3.3.4 of Chapter 3). Finally, these images were processed using Python, allowing the design of the image processing workflow and the statistical analysis of black-and-white pixel distribution across the scanned points. The responses obtained from image processing and analysis under curing conditions, with respect to the black-and-white pixel rates at scanned point 1 (including layer 1 and Face 1), are illustrated in Figures 4.1 to 4.5.

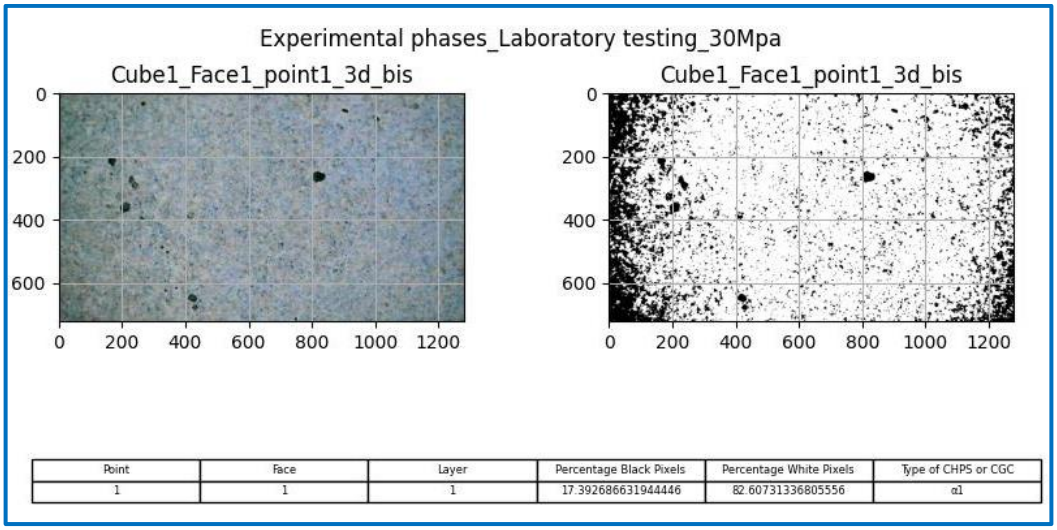

Point	Face	Layer	Percentage Black Pixels	Percentage White Pixels	Type of CHPS or CGC
1	1	1	17.392686631944446	82.60731336805556	α1

Figure 4.1: Image processing of cement grain colouration for the scanned point 1 for concrete M1 under curing conditions at 3 days (left) and converted black-and-white pixel image (right)

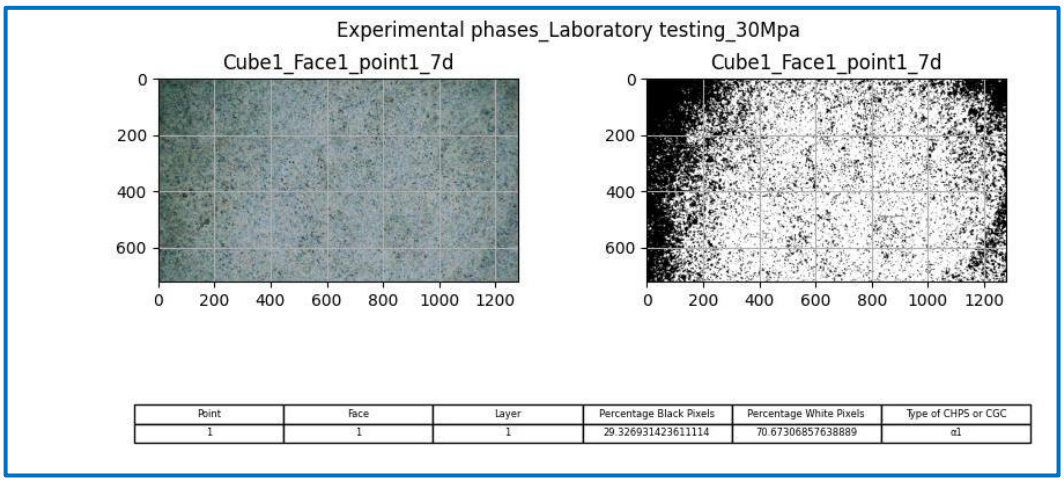

Point	Face	Layer	Percentage Black Pixels	Percentage White Pixels	Type of CHPS or CGC
1	1	1	29.326931423611114	70.67306857638889	α1

Figure 4.2: Image processing of cement grain colouration for the scanned point 1 for concrete M1 under curing conditions at 7 days (left) and converted black-and-white pixel image (right)

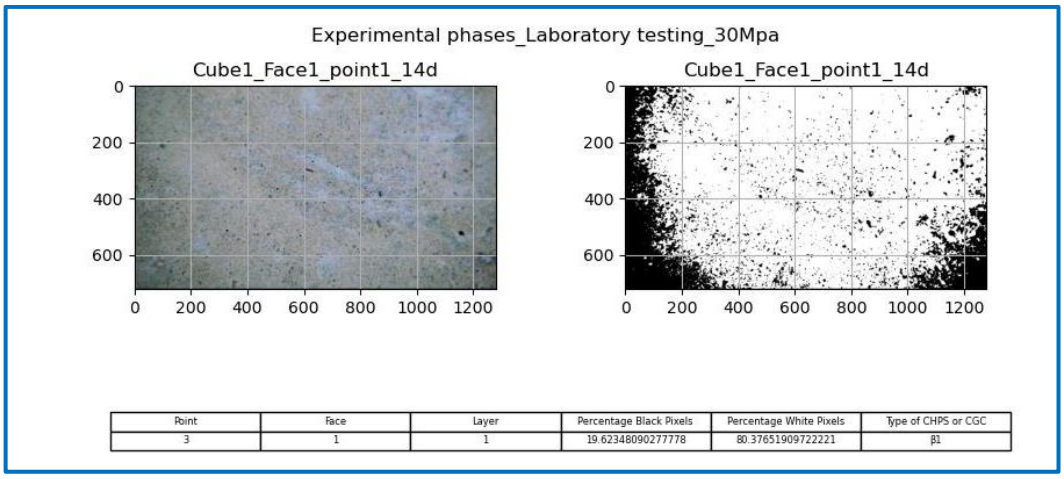

Point	Face	Layer	Percentage Black Pixels	Percentage White Pixels	Type of CHPS or CGC
3	1	1	19.62348090277778	80.37651909722221	β1

Figure 4.3: Image processing of cement grain colouration for the scanned point 1 for concrete M1 under curing conditions at 14 days (left) and converted black-and-white pixel image (right)

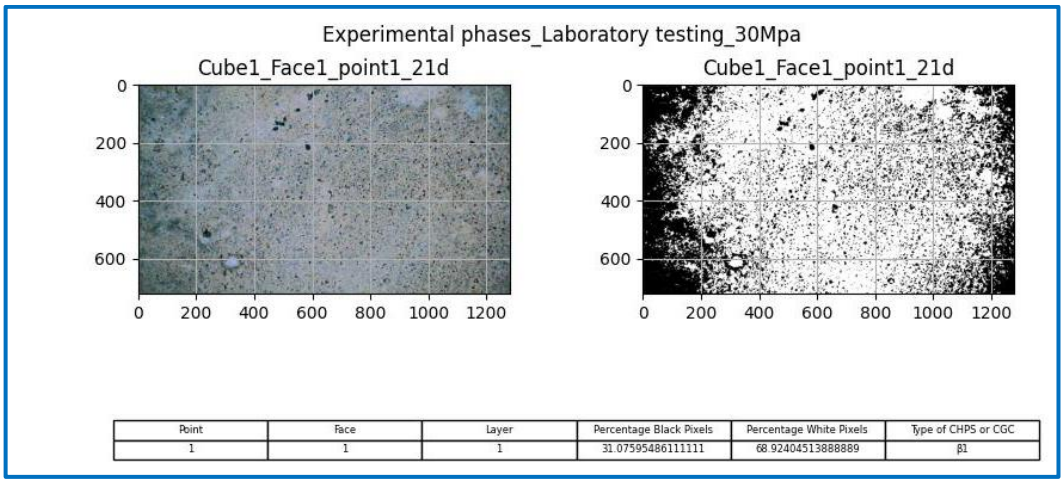

Point	Face	Layer	Percentage Black Pixels	Percentage White Pixels	Type of CHPS or CGC
1	1	1	31.07595486111111	68.92404513888889	β1

Figure 4.4: Image processing of cement grain colouration for the scanned point 1 for concrete M1 under curing conditions at 21 days (left) and converted black-and-white pixel image (right)

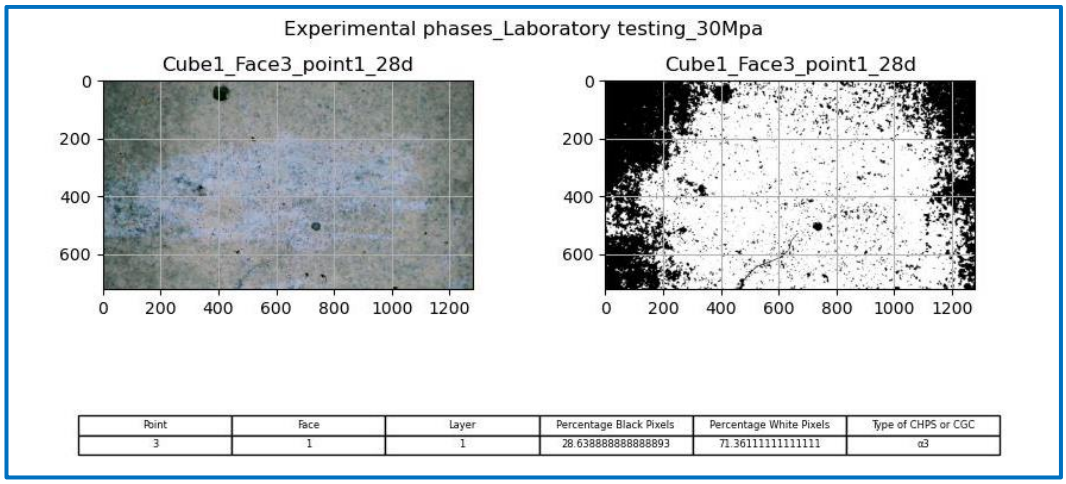

Point	Face	Layer	Percentage Black Pixels	Percentage White Pixels	Type of CHPS or CGC
3	1	1	28.638888888888893	71.36111111111111	α3

Figure 4.5: Image processing of cement grain colouration for the scanned point 1 of concrete M1 under curing conditions at 28 days (left) and converted black-and-white pixel image (right)

Figures 4.1 to 4.5 show a case of results concerning respectively the image processing and the analysis of pixel rates. Through these Figures, the following relevant information are given: the image processing of both coloured and black-and-white pixel image, the pixel-greyscale in which image processes under Python have been performed (800 x 1200 pixel-size), the scanned location (point 1, layer 1 and face 1), the number corresponding to concrete cube (C1), the type of concrete mixture (M1) and the laboratory testing (curing test) as well as the corresponding tested day (3, 7, 14, 21 and 28 days). In addition to this, statistical analysis in respect of the rate of black pixel (OBP1) and white pixel (OWP1) concentrated into the scanned point 1 have been established.

By observing one by one the evolving of image processing between the coloured and the black-and-white pixel image within the curing testing, it seems that light colours in blue, pink and brown occurring throughout the coloured image of cement grain interact with the white-pixel area from the black-and-white pixel image. Also, the size of both white and black pixel area is related to the change in pixel rates. Across 3, 7, and 28 days of curing (Figures 4.1 – 4.5), white pixels consistently occupy a larger area than black pixels. At 3 days, black pixels appear as sparse microscopic dots along the edges, while by 7 days they form a more continuous band and increase in density. At 28 days, black pixels are denser and

migrate further toward the perimeter, though the white/light-coloured area remains dominant. This persistence of white pixels likely reflects ongoing cement hydration observed in laboratory tests (see Table 4.1).

The following paragraph focuses on the image processing and analysis of pixel rates for scanned point 1 on concrete M1 subjected to an acid attack of 30 g/ℓ. As before, Python was used to design the image processing workflow and to determine the distribution of black-and-white pixels across nine scanned points. The results of this analysis are shown in Figures 4.6 to 4.12.

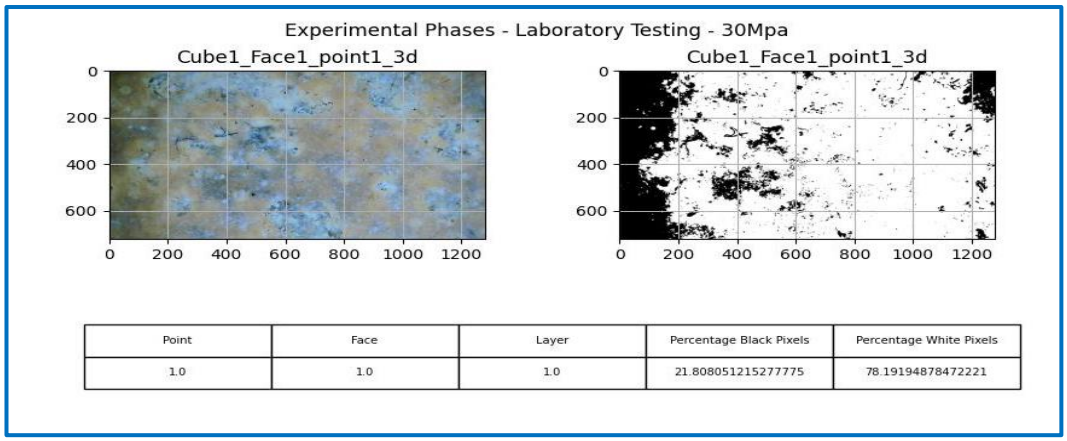

Point	Face	Layer	Percentage Black Pixels	Percentage White Pixels
1.0	1.0	1.0	21.808051215277775	78.19194878472221

Figure 4.6: Image processing of cement grain colouration at scanned point 1 of concrete M1 under corrosion conditions at 3 days (left), alongside the corresponding black-and-white pixel image (right)

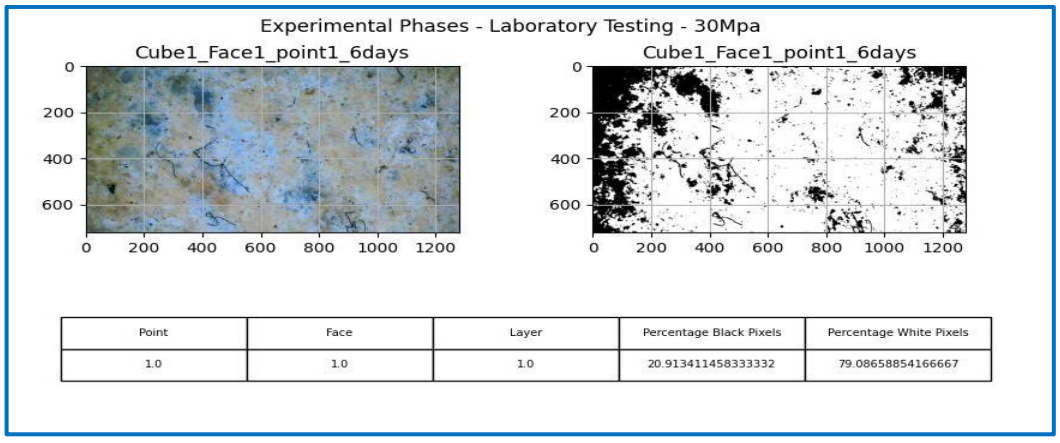

Point	Face	Layer	Percentage Black Pixels	Percentage White Pixels
1.0	1.0	1.0	20.913411458333332	79.08658854166667

Figure 4.7: Image processing of cement grain colouration at scanned point 1 of concrete M1 under corrosion conditions at 6 days (left), alongside the corresponding black-and-white pixel image (right)

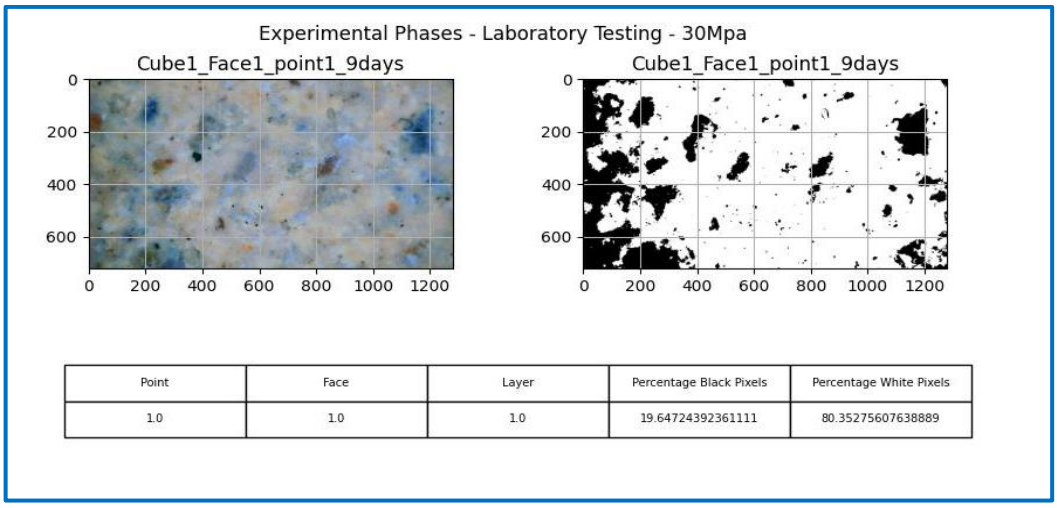

Point	Face	Layer	Percentage Black Pixels	Percentage White Pixels
1.0	1.0	1.0	19.64724392361111	80.35275607638889

Figure 4.8: Image processing of cement grain colouration at scanned point 1 of concrete M1 under corrosion conditions at 9 days (left), alongside the corresponding black-and-white pixel image (right)

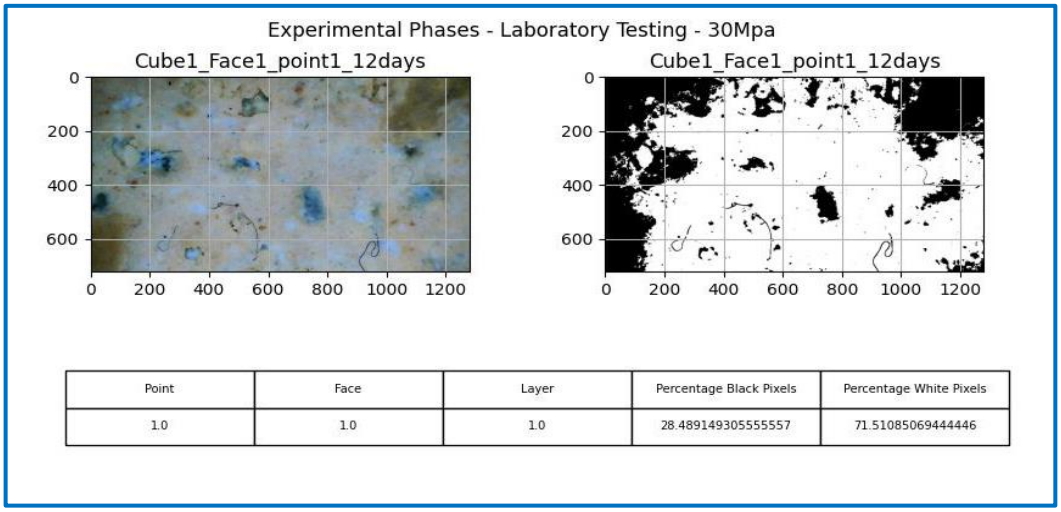

Point	Face	Layer	Percentage Black Pixels	Percentage White Pixels
1.0	1.0	1.0	28.489149305555557	71.51085069444446

Figure 4.9: Image processing of cement grain colouration at scanned point 1 of concrete M1 under corrosion conditions at 12 days (left), alongside the corresponding black-and-white pixel image (right)

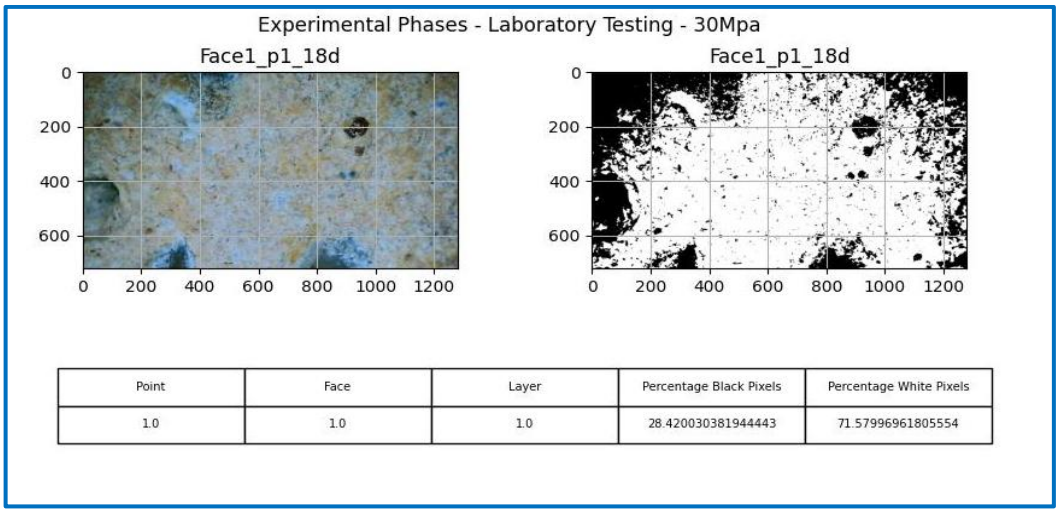

Figure 4.10: Image processing of cement grain colouration at scanned point 1 of concrete M1 under corrosion conditions at 18 days (left), alongside the corresponding black-and-white pixel image (right)

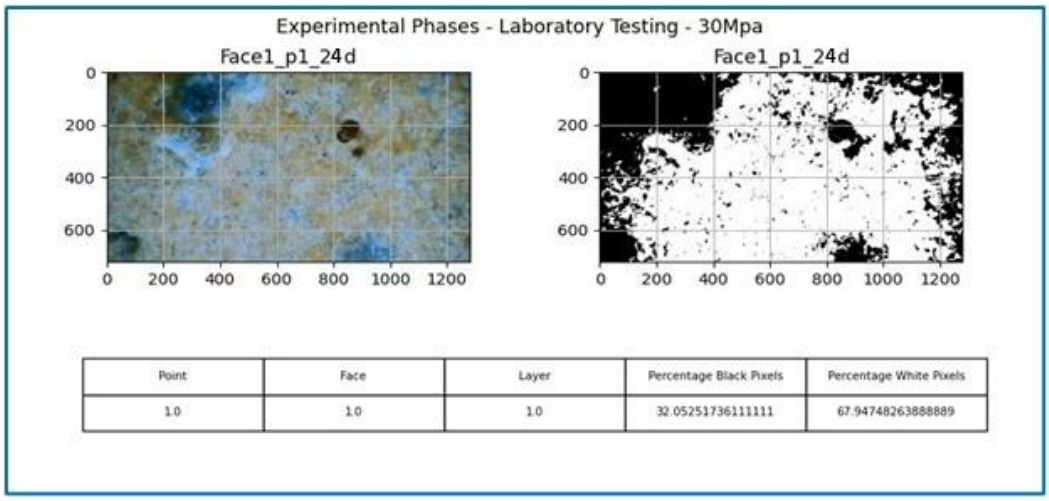

Figure 4.11: Image processing of cement grain colouration at scanned point 1 of concrete M1 under corrosion conditions at 24 days (left), alongside the corresponding black-and-white pixel image (right)

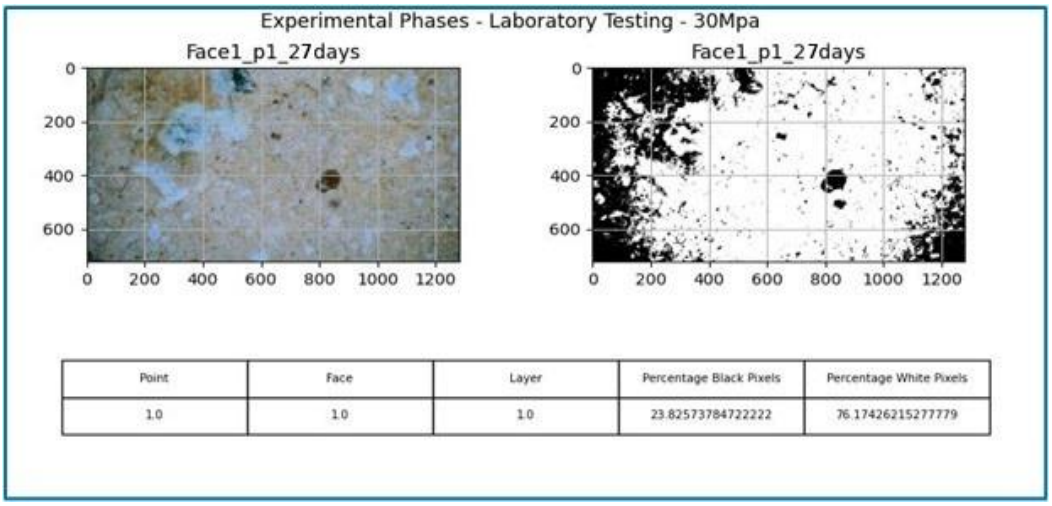

Figure 4.12: Image processing of cement grain colouration at scanned point 1 of concrete M1 under corrosion conditions at 27 days (left), alongside the corresponding black-and-white pixel image (right)

Figures 4.6 – 4.12 present the results of image processing and statistical analysis of pixel distribution at scanned point 1 under corrosion conditions. As observed, white/light-coloured pixels consistently occupy a larger area than black/dark-coloured pixels throughout the corrosion period. Initially, black pixels appear sparsely across the image, gradually becoming more concentrated along the image boundaries as corrosion progresses. By the final stage, white pixels remain dominant, reflecting the combined effects of cement hydration and sulphuric acid exposure. The presence of light colours, such as blue and brown, which are converted to white in the processed images, is probably due to the presence of both calcium and sulphur ions within the concrete matrix, as previously reported by Taheri *et al*. (2020).

To summarise, the results obtained under both curing and corrosion conditions indicate that blue and brown colours play a crucial role in characterising the evolution of hydration and corrosion mechanisms. Moreover, the proportion of white pixel areas (WAP) consistently remains higher than that of black pixel areas (BAP). The observed colour transitions further suggest a clear correlation between light colours and white pixels, and between dark colours and black pixels. These

relationships are further examined later in Section 6.3 to extract relevant colour features and strengthen the interpretation of image-based analysis.

4.3.2 Black and white pixel values within image processing

This section provides an analysis of the black and white pixel values obtained through the image processing procedure (see Section 4.3.1). These values are derived from the processed images corresponding to 144 scanned points distributed over the 16 faces of four concrete cubes, i.e., eight faces from two M1 cubes and eight faces from two M2 cubes. The results for nine selected scanned points (M1 / 30 MPa), analysed as a function of curing time, are summarised in Tables 4.3 and 4.4, while the corresponding data under corrosion conditions are presented in Tables 4.5 and 4.6. This analysis provides a quantitative basis for evaluating the evolution of pixel distribution under both curing and corrosion scenarios. For reasons of consistency, the remaining results for M1/30 MPa and M2/40 MPa are provided in Appendix C.

Table 4.3: Analysis of the distribution of black and white pixel rates for nine scanned points on Face 1 of the M1 concrete cube (30 MPa) under curing conditions after 3 days

Output Point 1 (Face 1)		**Output Point 2 (Face 1)**		**Output Point 3 (Face 1)**	
Black pixel	White pixel	Black pixel	White pixel	Black pixel	White pixel
17.40%	82.60%	24.50%	75.50%	19.70%	80.30%
Output Point 4 (Face 1)		**Output Point 5 (Face 1)**		**Output Point 6 (Face 1)**	
Black pixel	White pixel	Black pixel	White pixel	Black pixel	White pixel
24.50%	75.50%	35.10%	64.90%	30.30%	69.70%
Output Point 7 (Face 1)		**Output Point 8 (Face 1)**		**Output Point 9 (Face 1)**	
Black pixel	White pixel	Black pixel	White pixel	Black pixel	White pixel
30.20%	69.80%	22.10%	77.90%	30.00%	70.00%

Table 4.4: Analysis of the distribution of black and white pixel rates for nine scanned points on Face 1 of the M1 concrete cube (30 MPa) under curing conditions after 28 days

Output Point 1 (Face 1)		**Output Point 2 (Face 1)**		**Output Point 3 (Face 1)**	
Black pixel	White pixel	Black pixel	White pixel	Black pixel	White pixel
25.00%	75.00%	21.30%	78.70%	33.10%	66.90%
Output Point 4 (Face 1)		**Output Point 5 (Face 1)**		**Output Point 6 (Face 1)**	
Black pixel	White pixel	Black pixel	White pixel	Black pixel	White pixel
28.90%	71.10%	31.00%	69.00%	31.00%	69.00%
Output Point 4 (Face 1)		**Output Point 5 (Face 1)**		**Output Point 6 (Face 1)**	
Black pixel	White pixel	Black pixel	White pixel	Black pixel	White pixel
33.20%	66.80%	20.90%	79.10%	21.50%	78.50%

Table 4.5: Analysis of the distribution of black and white pixel rates for nine scanned points on Face 1 of the M1 concrete cube (30 MPa) under corrosion conditions after 3 days

Output Point 1 (Face 1)		**Output Point 2 (Face 1)**		**Output Point 3 (Face 1)**	
Black pixel	White pixel	Black pixel	White pixel	Black pixel	White pixel
21.80%	78.20%	28.70%	71.30%	31.50%	68.50%
Output Point 4 (Face 1)		**Output Point 5 (Face 1)**		**Output Point 6 (Face 1)**	
Black pixel	White pixel	Black pixel	White pixel	Black pixel	White pixel
27.60%	72.40%	25.80%	74.20%	32.20%	67.80%
Output Point 7 (Face 1)		**Output Point 8 (Face 1)**		**Output Point 9 (Face 1)**	
Black pixel	White pixel	Black pixel	White pixel	Black pixel	White pixel
41.90%	58.10%	29.00%	71.00%	36.60%	63.40%

Table 4.6: Analysis of the distribution of black and white pixel rates for nine scanned points on Face 1 of the M1 concrete cube (30 MPa) under corrosion conditions after 27 days

Output Point 1 (Face 1)		**Output Point 2 (Face 1)**		**Output Point 3 (Face 1)**	
Black pixel	White pixel	Black pixel	White pixel	Black pixel	White pixel
23.80%	76.20%	27.20%	72.80%	26.30%	73.70%
Output Point 4 (Face 1)		**Output Point 5 (Face 1)**		**Output Point 6 (Face 1)**	
Black pixel	White pixel	Black pixel	White pixel	Black pixel	White pixel
19.90	80.10	19.50	80.50	22.50	77.50
Output Point 7 (Face 1)		**Output Point 8 (Face 1)**		**Output Point 9 (Face 1)**	
Black pixel	White pixel	Black pixel	White pixel	Black pixel	White pixel
23.20%	76.80%	16.80	83.20	19.40	80.60

Tables 4.3 to 4.6 present two sets of image processing results obtained under different testing scenarios: curing conditions as a function of time (Tables 4.3 and 4.4) and corrosion conditions (Tables 4.5 and 4.6). These results correspond to the concrete mixture M1. They provide further insight into how the proportions of black and white pixels vary under both conditions. In general, the output values for black pixels remain relatively low, ranging between 10% and 30% (OBP), while those for white pixels are higher, ranging between 60% and 90% (OWP). The marked increase observed in the white pixel distribution is probably influenced by colour kinetics, suggesting that the dominance of white or light-coloured areas has a significant impact on pixel variation compared with darker regions. The remaining tables are reported in Appendix B.

In brief, the results indicate two distinct image processing scenarios corresponding to curing and corrosion conditions for mixture M1. Across both conditions, black pixel values remain relatively low, while white pixels dominate. This predominance of white or light-coloured areas suggests that colour kinetics play a key role in influencing pixel variation during both testing phases. In addition to this, the results reveal two distinct patterns of pixel distribution under curing and corrosion

conditions, with white pixels consistently prevailing over black ones. These findings serve as essential output data for the subsequent in-depth analysis using the ANN model (see Section 5.3 later in Chapter 5).

4.4 Concluding remarks

The study validates the hypothesis that colour-pattern variations in scanned concrete images provide a direct reflection of microstructural change under both hydration and sulphuric-acid corrosion. Across all testing stages, white pixels consistently dominated over black ones, highlighting the white area proportion (WAP) as a sensitive and reliable indicator of microstructural activity.

This dominance is driven by hydration during curing and by corrosion-induced cement grain colouration. Two distinct image-response regimes were identified—one for curing and one for corrosion—yet both exhibit low black-pixel levels and strong white-pixel prevalence. These consolidated findings supply the essential dataset required for the subsequent ANN-based analysis of microstructural behaviour.

CHAPTER 5: MODELS OF SCANNED POINTS AT CEMENT GRAIN SCALE

5.1 Introduction

The present chapter addresses the modelling of scanned points at the cement-grain scale and is organised in two parts. The first part outlines the matrix equations developed to compute these points and introduces a tailored procedure for generating numerical values that incorporate both the experimental parameters and their precise geometrical positions.

The second part formalises the mathematical ANN framework used to evaluate black- and white-pixel rates and to train the corresponding input–output patterns, concluding with a predictive scheme that links scanned-point locations to pixel-distribution behaviour.

Taken together, these elements provide a coherent pathway from numerical formulation to computational interpretation. They also establish a clear foundation for the analytical developments explored in the sections that follow.

5.2 Computation of scanned points using matrix functions

The present section introduces the matrix-based procedure developed to compute the scanned points. Drawing on the hypothesis presented in Section 2.5.3 (of Chapter 2), it proposes a tailored method for producing numerical values capable of capturing both the experimental parameters and the precise geometrical positions of the scanned points.

The resulting values, assigned to the nine scanned points (P1 – P9) on the concrete surface, are referred to as the Indices of Black-and-White Pixels (IBWP). These serve as the input dataset for the ANN framework, supporting a detailed assessment of black- and white-pixel rate distributions previously reported in Tables 4.3 – 4.6.

To support this process, Equation (5.1) formalises the matrix structure used to generate the numerical values, providing a direct connection between the experimental conditions, the spatial arrangement of the scanned points, the pixel information, and the hypothesis outlined in Section 2.5.2 of Chapter 2:

$$\mathrm{I_{i,j}BWP(P_{1\ldots n})} = \left(\mathrm{X_i; X_j}\right)\tilde{\omega}_{1\ldots n} \tag{5.1}$$

In Equation (5.1), $\mathrm{I_{i,J}BWP}$ denotes the network of input parameters corresponding to the black- and white-pixel rates of the scanned points, while $\mathrm{P_{1\ldots n}}$, expressed as $\tilde{\omega}_{1\ldots n}$, represents the positions of the points scanned on the surface of a concrete cube to which the input pairs $\left(\mathrm{X_i; X_j}\right)$ refer.

The matrix formulation of these input pairs, used to evaluate pixel rates, is also shown in Equation (5.2). Here, $\left(\mathrm{X_i; X_j}\right)\tilde{\omega}_{1\ldots n}$ indicates the assignment of input parameters to specific scanned points. The indices $\mathrm{i\ and\ j}$ correspond to the number of input variables within the ANN architecture (see Section 5.3.1 below), while n represents the total number of scanned points. In the present study, n = 9, such that $\mathrm{I_{i,j}BWP(P_{1\ldots n})}$ simplifies to $\mathrm{I_{i,j}BWP(P_{1\ldots 9})}$, as given in Equation (5.3).

Thus, Equation (5.2) and (5.3) can be written as follows:

$$\left(\mathrm{X_i; X_j}\right)\tilde{\omega}_{1\ldots n} = \begin{vmatrix} (\mathrm{X_1; X_2})\tilde{\omega}_1 & (\mathrm{X_3; X_4})\tilde{\omega}_2 & (\mathrm{X_5; X_6})\tilde{\omega}_3 \\ \vdots & \vdots & \vdots \\ (\mathrm{X_7; Y_8})\tilde{\omega}_4 & (\mathrm{X_9; X_{10}})\tilde{\omega}_5 & (\mathrm{X_{11}; X_{12}})\tilde{\omega}_6 \\ \vdots & \vdots & \vdots \\ (\mathrm{X_{i-4}; X_{j-4}})\tilde{\omega}_{n-2,} & (\mathrm{X_{i-2}; X_{j-2}})\tilde{\omega}_{n-1} & (\mathrm{X_i; X_j})\tilde{\omega}_n \end{vmatrix} \tag{5.2}$$

$$\left(\mathrm{X_i; X_j}\right)\tilde{\omega}_{1\ldots 9} = \begin{vmatrix} (\mathrm{X_1; X_2})\tilde{\omega}_1 & (\mathrm{X_3; Y_4})\tilde{\omega}_2 & (\mathrm{X_5; X_6})\tilde{\omega}_3 \\ \vdots & \vdots & \vdots \\ (\mathrm{X_7; X_8})\ \tilde{\omega}_4 & (\mathrm{X_9; X_{10}})\tilde{\omega}_5 & (\mathrm{X_{11}; X_{12}})\tilde{\omega}_6 \\ \vdots & \vdots & \vdots \\ (\mathrm{X_{13}; X_{14}})\tilde{\omega}_7 & (\mathrm{X_{15}; X_{16}})\tilde{\omega}_8 & (\mathrm{X_{17}; X_{18}})\tilde{\omega}_9 \end{vmatrix} \tag{5.3}$$

Equation (5.4) presents the matrix of numerical values for the input variable pairs $\left(\mathrm{X_i; X_j}\right)$ used to evaluate black- and white-pixel rates at the scanned points, calculated in MATLAB R2022b:

$$(X_i; X_j)\tilde{\omega}_{1\ldots n} = \begin{vmatrix} (40.36; 59.64)\tilde{\omega}_1 & (0.00; 100.00)\tilde{\omega}_2 & (12.54; 98.46)\tilde{\omega}_3 \\ \vdots & \vdots & \vdots \\ (40.56; 59.44)\tilde{\omega}_4 & (31.17; 68.83)\tilde{\omega}_5 & (19.04; 80.96)\tilde{\omega}_6 \\ \vdots & \vdots & \vdots \\ (40.36; 59.64)\tilde{\omega}_7 & (35.38; 64.62)\tilde{\omega}_8 & (15.90; 84.10)\tilde{\omega}_9 \end{vmatrix} \quad (5.4)$$

In this matrix, the first row corresponds to points P1, P2, and P3, with respective values of 40.35 % (IBP1) and 59.64 % (IWP1); 0.00 % (IBP2) and 100 % (IWP2); and 12.54 % (IBP3) and 98.46 % (IWP3). The second row represents P4 to P6, with 40.56 % (IBP4) and 59.44 % (IWP4), 31.17 % (IBP5) and 68.83 % (IWP5), 19.04 % (IBP6) and 80.96 % (IWP6), and so forth.

In this study, the input values are treated as representative of all four faces of a 150 × 150 × 150 mm concrete cube, ensuring a consistent dataset for subsequent ANN-based analyses. The matrix equations implemented in this section, founded on a tailored approach to accurately capture both the experimental parameters and the precise geometrical positions of the scanned points, have demonstrated robust and reliable results, providing a solid basis for further computational investigations.

5.3 Artificial neural network architecture for black and white pixel rates

The ANN architecture, which is an integral part of artificial intelligence, is widely used as a graphical framework to activate mathematical functions through input, hidden and output layers (Larsen, 1999; Kriesel, 2005, Khadeni *et al.*, 2016). This approach allows for the efficient processing and analysis of complex data patterns, making the ANN a versatile tool in various domains. Its adaptability and learning capabilities have positioned the ANN as a cornerstone in advancing predictive modelling and decision-making systems. In the present research, ANNs are employed to formalise a mathematical framework that activates functions across the input, hidden, and output layers to evaluate black and white pixel rates. The architecture defines the mapping between the nine scanned-point inputs and the pixel-based output patterns generated through image processing. This framework

supports the development of predictive models that capture how scanned-point positions influence the distribution of black and white pixels

5.3.1 Implementation of artificial neural network architecture

As part of this study, three key ANN architectures related to the nine scanned points (P) $\{P_1 \dots P_9\}$ were developed for modelling purposes. The design topology illustrated in Figures 5.1 – 5.3 provides the connectivity details between the input and output vectors. In addition to this, the interaction between different neurons and hidden layers is developed throughout the ANN framework.

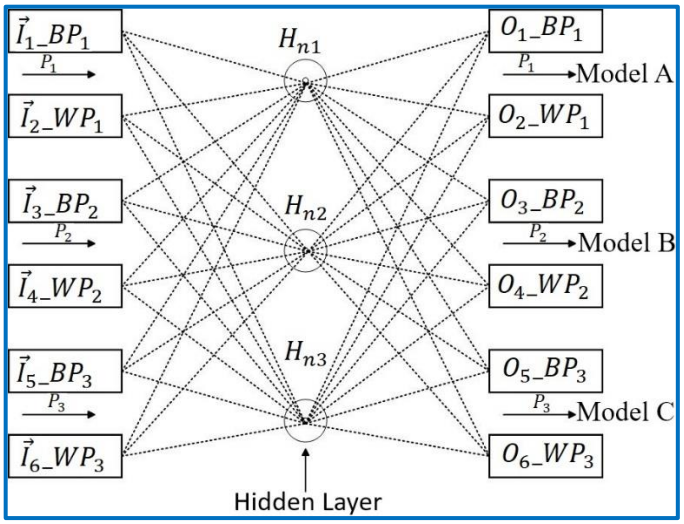

Figure 5.1: ANN architecture for scanned points P_1, P_2, and P_3, illustrating the connections and signal transfer across layers

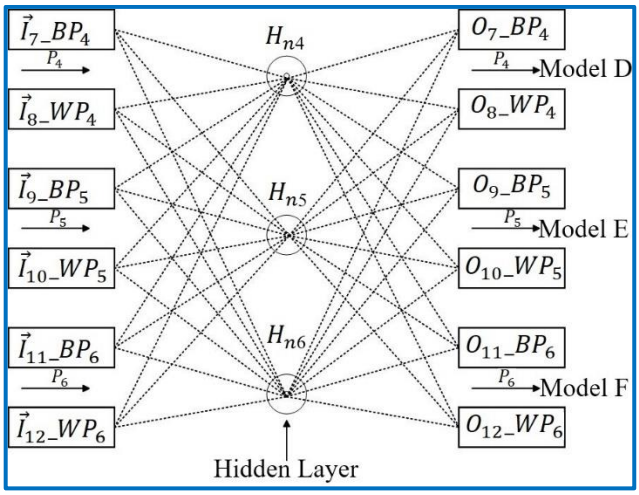

Figure 5.2: ANN architecture for scanned points P_4, P_5, and P_6, illustrating the connections and signal transfer across layers

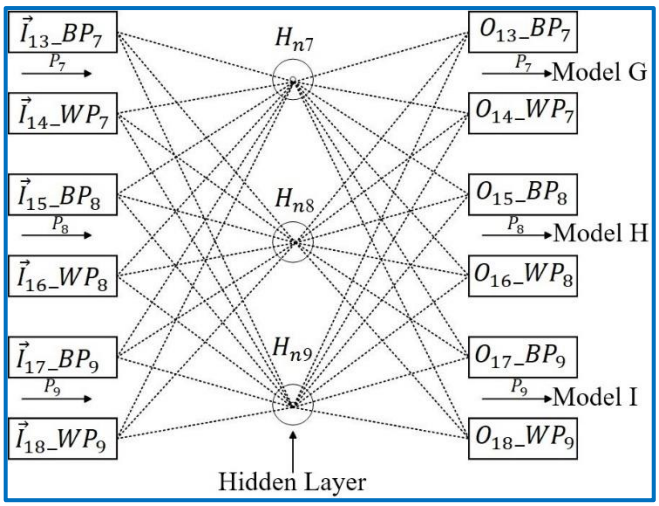

Figure 5.3: ANN architecture for scanned points P_7, P_8, and P_9, illustrating the connections and signal transfer across layers

Figures 5.1 to 5.3 illustrate the architecture of the three Artificial Neural Networks (ANNs) applied to nine scanned points (P_1 – P_9) on the concrete surface. Each network comprises an input, hidden, and output layer, which sequentially manage data transmission and transformation. The output layer contains six neurons representing the interconnection topology between black and white pixel rates, with each point linked to models labelled A to I (Figures 5.1 – 5.3). Figures 5.4 to 5.6 provide a detailed view of the network topology, emphasising the interconnections and the role of weight distributions across hidden and output neurons.

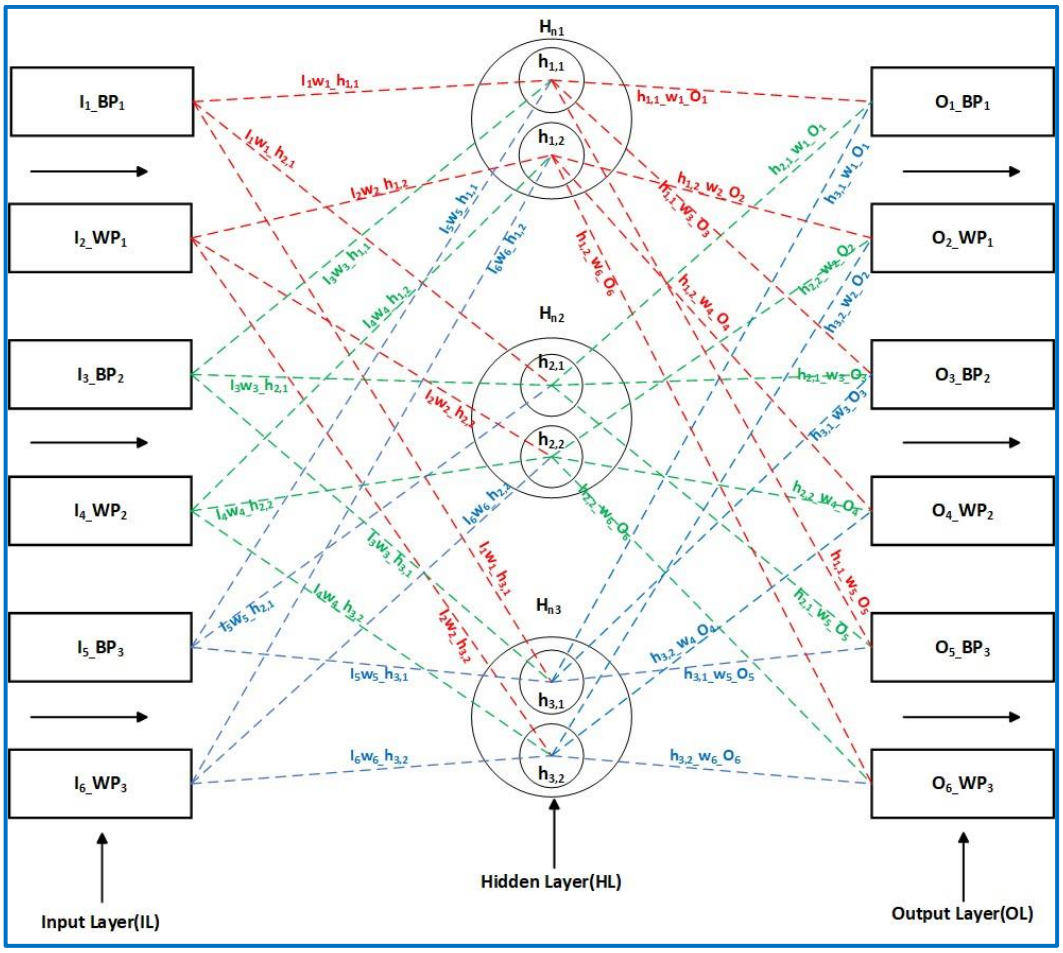

Figure 5.4: Network topology of input, hidden, and output neurons for scanned points P_1, P_2, and P_3, highlighting the interconnections and the associated weight distribution

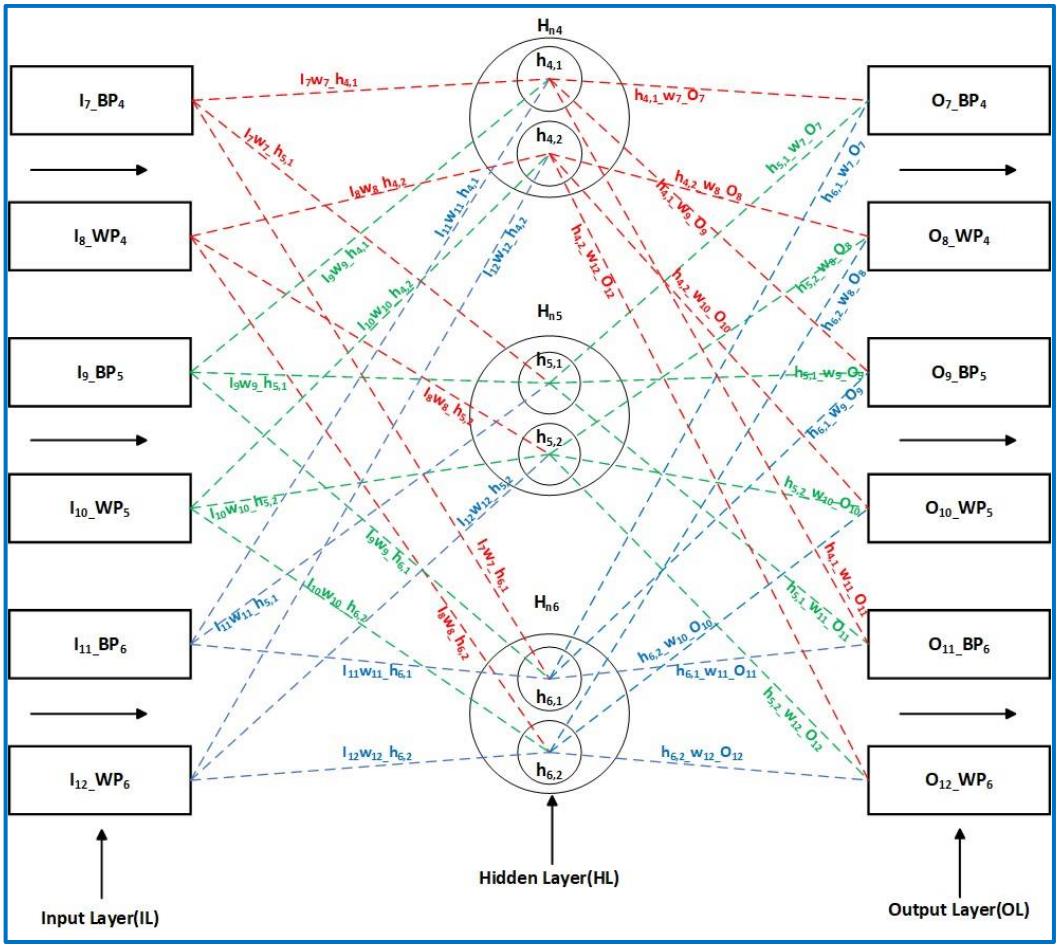

Figure 5.5: Network topology of input, hidden, and output neurons for scanned points P_4, P_5, and P_6, highlighting the interconnections and the associated weight distribution

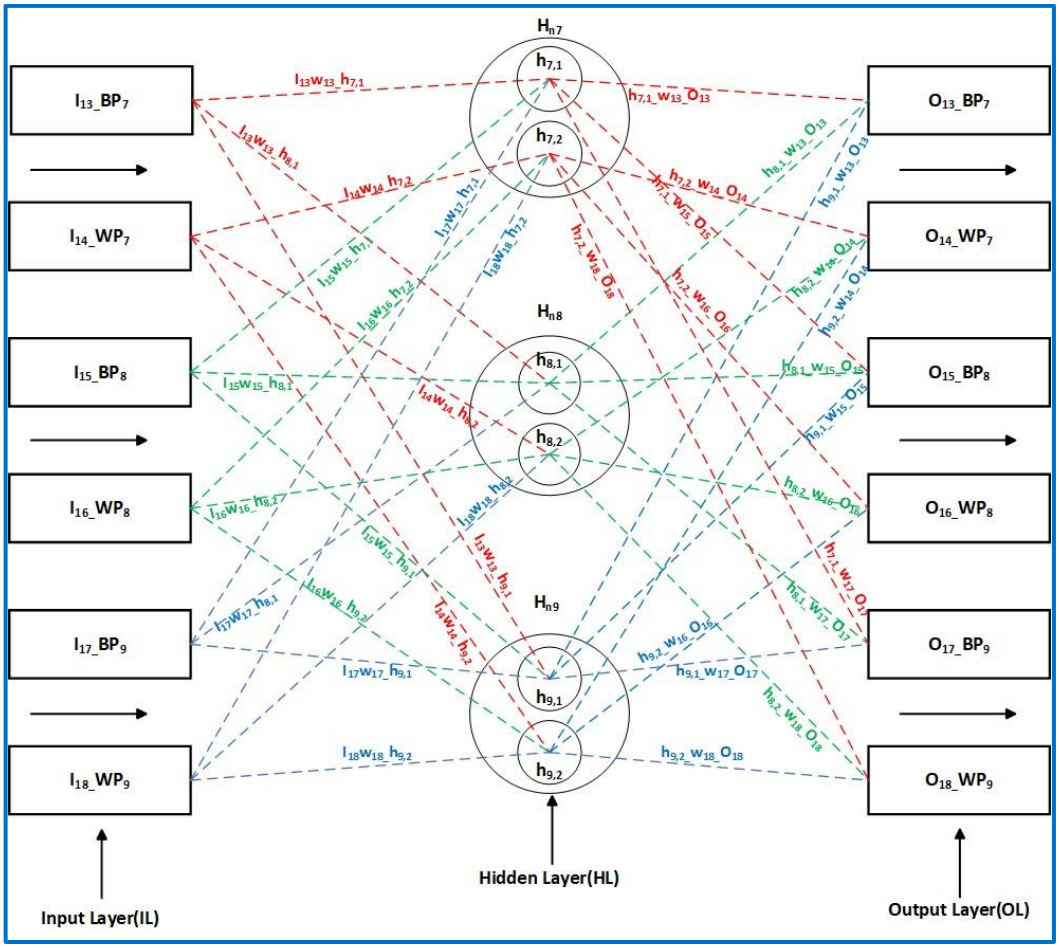

Figure 5.6: Network topology of input, hidden, and output neurons for scanned points P_7, P_8, and P_9, highlighting the interconnections and the associated weight distribution

Figures 5.4 to 5.6 focus on the network topology, highlighting the interconnections among input, hidden, and output neurons as well as the associated weight distributions. Signals representing black and white pixel rates are transmitted through the main and secondary hidden neurons, with each connection scaled by specific weight coefficients. These weighted signals are then propagated to the output neurons, producing the final network outputs. This process emphasises the key role of weight allocation in controlling signal transformation and overall network response. Further details on the evaluation of input–output data and the interconnection procedure are provided in the next section.

5.3.2 Neural network layer computation and functional fit analysis

The computation of neural layers regarding the ANN architecture is widely discussed in the literature. In previous studies based on the performance of the computation of neural network layers, numerous researchers have demonstrated that the successful in predicting or simulating models depend on the choice of appropriate algorithms (Gurney, 1997; Hewayde *et al*., 2007; Boukhatem *et al*., 2011). In the concrete technology as well as concrete corrosion, a sigmoidal type of algorithm called back-propagation of error is commonly used for both transfer functions and training patterns (Guoqiang *et al*., 1998; Basheer and Hajmeer, 2018; Hakim *et al*., 2011). In the current study, this type of algorithm presents limitations when a complex analysis of neural network layers including subordinate hidden neurons are investigated. To solve complex problems, the implementation of news algorithms for computing neural network layers as well as the training of input/output patterns is necessary.

For methodological purposes, the assessment of both activation and transfer functions within the input neurons across the input layer (IL), hidden layer (HL), and output layer (OL) was performed within the framework of the three implemented ANNs, as presented in Figures 5.4 to 5.6. The technique was based on the implementation of learning algorithms according to the specific characteristics of each subordinate hidden neuron. In addition, a particular accent took into account both efficiency and accuracy to evaluate input/output patterns throughout the ANN architecture.

Given the limitations of the current algorithm in processing complex cases addressed in this thesis (see Section 2.5.2 of Chapter 2), supplementary equations were introduced to activate the neural network layers, including the hidden neurons, as follows:

$$I_{X_i} = \left[\frac{1}{\Delta a \log(X_i + Y_i)}\right] \tag{5.5}$$

$$I_{X_j} = \left[\frac{1}{\Delta b \log(X_j + Y_j)}\right] \tag{5.6}$$

In Equations (5.5) and (5.6), Δa and Δb denote the activation variance coefficients governing the learning process between the input and output parameters (X_i; Y_i) and (X_j; Y_j) respectively, both ranging between 6 and 12. The activation of functions within the ANN framework was achieved using the following relations:

$$\mathcal{F}_{Xi} = \sum_{i=9}^{Hn=9} \ln e^{\Delta c}[(X_i - w_i H_{n1}) + \cdots (X_i - w_i H_{n9})] \quad (5.7)$$

$$\mathcal{F}_{Yj} = \sum_{j=9}^{Hn=9} \ln e^{\Delta d}[(Y_j - w_j H_{n1}) + \cdots (Y_j - w_j H_{n9})] \quad (5.8)$$

Equations (5.7) and (5.8) define the activation algorithms $\mathcal{F}_{Xi}$ and $\mathcal{F}_{YJ}$, related to the signal transmission from nine main neurons (H_{n1} … H_{n9}) and 18 subordinate hidden neurons (Figures 5.4 – 5.6). The transmitted signals are weighted by coefficients ($w_i H_{n1} \ldots w_i H_{n9}$) and ($w_j Y_1 \ldots . w_J Y_9$).

The coefficients Δc and Δd correspond to the weight variance factors that influence the input–output pairs (X_i; Y_i) and (X_j; Y_j) respectively. Coefficient Δc varies between 0.1 and 3, while Δd ranges from 0.1 to 6. Hence, these two equations collectively define the activation and transfer mechanisms of the numerical values transmitted through the ANN framework to the output layer. In the present study, the evaluation of the minimised error discrepancy between the computed and the target outputs is accurately determined using Equations (5.9) and (5.10), which are presented below to support the subsequent training phase.

$$E_{Xi} = \frac{X_i}{\Delta a U_i}\left[\frac{1}{\log(X_i + Y_j)}\right] \quad (5.11)$$

$$E_{Yj} = \frac{Y_j}{\Delta b V_J}\left[\frac{1}{\log(X_i + Y_j)}\right] \quad (5.12)$$

Here, $E_{Xi}$and E_{Yj} refer to the cumulative errors associated with the input and output neurons during training.

5.3.3 Training processes of inputs parameters for evaluating output targets

The training phase constitutes a critical stage in which input–output patterns acquire specific behaviours through memorisation and iterative refinement, with training datasets serving to evaluate model performance and enhance prediction accuracy (Gurney, 1997; Larsen, 1999; Kriesel ,2005; Hakim *et al*., 2011; Sharma *et al*., 2012). In this study, a learning framework incorporating 18 subordinate hidden neurons within the ANN is employed to train the inputs to predict outputs derived from black- and white-pixel image processing.

It should be emphasised, however, that the back-propagation algorithm with a non-linear activation function—commonly used in the literature (see Section 2.5.2 of Chapter 2)—faces inherent limitations when applied to more complex ANN architectures, such as those involving the secondary hidden neurons considered here. This highlights the need for careful algorithmic design to ensure robust training outcomes.

For the practical implementation of this framework, a total of 144 test points were analysed for each concrete mixture (M1 and M2) in relation to the curing process, whereas 36 test points were examined for mixture M1 regarding the corrosion process (see Sections 3.3.3 and 3.3.4 of Chapter 3). Consequently, the learning process was trained using the input parameters (IBP and IWP) derived from a total of 180 scanned points in order to predict the corresponding outputs (OBP and OWP). Training was carried out in three steps: first, Equations (5.5) and (5.6) were adjusted using trial-and-error to minimise recognition errors; second, Equations (5.4) to (5.10) were refined to optimise the activation functions of nine primary neurons (H_{n1} … H_{n9}) and 18 subordinate hidden neurons; third, Equations (5.11) to (5.12) were tuned to reduce the residual error between the computed and desired outputs. Each ANN model was trained iteratively until a stable minimum error was achieved, typically after five iterations.

By repeating these operations several times, the learning algorithms effectively trained the neural network to internalise the minimisation functions and to accurately predict the output parameters. In the present study, the training process for each ANN model was terminated after five iterative computations once the error between the computed and target outputs had reached a stable minimum.

The behaviour of the ANN throughout the training phase is reported in Tables 5.1 to 5.4, which detail the activation patterns of the network layers corresponding to the curing progression under 3 – 28 days for the M1 / 30 MPa concrete mix.

Table 5.1: Activation of neural network layers for the rate of black-and-white pixel image under curing conditions at 3 days using M1 / 30 MPa

Activation of input, hidden and output layers across the neural network under curing conditions at 3 days, in percentage					
Input Layer (IL)		Hidden Layer (HL)		Output layer (OL)	
I_1BP(P_1, L_1)	I_2WP(P_1, L_1)	$h_{1,1}/BP_1$	$h_{1,2}/WP_1$	O_1BP(P_1, L_1)	O_2WP(P_1, L_1)
40.36	59.64	13.9740	15.7451	17.40	82.60
I_3BP(P_2, L_1)	I_4WP(P_2, L_1)	$h_{2,1}/BP_2$	$h_{2,2}/WP_2$	O_3BP(P_2, L_1)	O_4WP(P_2, L_1)
100.00	0.00	13.974	15.7451	24.50	75.50
I_5BP(P_3, L_1)	I_6WP(P_3, L_1)	$h_{3,1}/BP_3$	$h_{3,2}/WP_3$	O_5BP(P_3, L_1)	O_6WP(P_3, L_1)
1.54	98.46	13.9740	15.7451	19.70	80.30
I_7BP(P_4, L_2)	I_8WP(P_4, L_2)	$h_{4,1}/BP_4$	$h_{4,2}/WP_4$	O_7BP(P_4, L_2)	O_8WP(P_4, L_2)
40.56	59.44	8.9713	20.7453	24.50	75.50
I_9BP(P_5, L_2)	I_{10}WP(P_5, L_2)	$h_{5,1}/BP_5$	$h_{5,2}/WP_5$	O_9BP(P_5, L_2)	O_{10}WP(P_5, L_2)
31.17	68.83	8.9713	20.7453	35.10	64.90
I_{11}BP(P_6, L_2)	I_{12}WP(P_6, L_2)	$h_{6,1}/BP_6$	$h_{6,2}/WP_6$	O_{11}BP(P_6, L_2)	O_{12}WP(P_6, L_2)
19.04	80.96	8.9713	20.7453	30.30	69.70
I_{13}BP(P_7, L_3)	I_{14}WP(P_7, L_3)	$h_{7,1}/BP_7$	$h_{7,2}/WP_7$	O_{13}BP(P_7, L_3)	O_{14}WP(P_7, L_3)
40.36	59.64	11,9283	17,8283	30.20	69.80
I_{15}BP(P_8, L_3)	I_{16}WP(P_8, L_3)	$h_{8,1}/BP_8$	$h_{8,2}/WP_8$	O_{15}BP(P_8, L_3)	O_{16}WP(P_8, L_3)
64.62	35.38	11.9283	17.8283	22.10	77.90
I_{17}BP(P_9, L_3)	I_{18}WP(P_9, L_3)	$h_{9,1}/BP_9$	$h_{9,2}/WP_9$	O_{17}BP(P_9, L_3)	O_{18}WP(P_9, L_3)
15.90	84.10	11.9283	17.8283	30.00	70.00

Table 5.2: Activation of neural network layers for the rate of black-and-white pixel image under curing conditions at 7 days using M1 / 30 MPa

Activation of input, hidden and output layers across the neural network under curing conditions at 7 days, in percentage					
Input Layer (IL)		Hidden Layer (HL)		Output layer (OL)	
I_1BP(P_1, L_1)	I_2WP(P_1, L_1)	$h_{1,1}/BP_1$	$h_{1,2}/WP_1$	O_1BP(P_1, L_1)	O_2WP(P_1, L_1)
40.36	59.64	14.0363	15.7374	29.30	70.70
I_3BP(P_2, L_1)	I_4WP(P_2, L_1)	$h_{2,1}/BP_2$	$h_{2,2}/WP_2$	O_3BP(P_2, L_1)	O_4WP(P_2, L_1)
100.00	0.00	14.0363	15.7374	31.50	68.50
I_5BP(P_3, L_1)	I_6WP(P_3, L_1)	$h_{3,1}/BP_3$	$h_{3,2}/WP_3$	O_5BP(P_3, L_1)	O_6WP(P_3, L_1)
1.54	98.46	14.0363	15.7374	26.20	73.80
I_7BP(P_4, L_2)	I_8WP(P_4, L_2)	$h_{4,1}/BP_4$	$h_{4,2}/WP_4$	O_7BP(P_4, L_2)	O_8WP(P_4, L_2)
40.56	59.44	8.9292	20.7664	18.40	81.60
I_9BP(P_5, L_2)	I_{10}WP(P_5, L_2)	$h_{5,1}/BP_5$	$h_{5,2}/WP_5$	O_9BP(P_5, L_2)	O_{10}WP(P_5, L_2)
31.17	68.83	8.9292	20.7664	23.70	76.30
I_{11}BP(P_6, L_2)	I_{12}WP(P_6, L_2)	$h_{6,1}/BP_6$	$h_{6,2}/WP_6$	O_{11}BP(P_6, L_2)	O_{12}WP(P_6, L_2)
19.04	80.96	8.9292	20.7664	20.80	79.20
I_{13}BP(P_7, L_3)	I_{14}WP(P_7, L_3)	$h_{7,1}/BP_7$	$h_{7,2}/WP_7$	O_{13}BP(P_7, L_3)	O_{14}WP(P_7, L_3)
40.36	59.64	11.9168	17.8332	17.00	83.00
I_{15}BP(P_8, L_3)	I_{16}WP(P_8, L_3)	$h_{8,1}/BP_8$	$h_{8,2}/WP_8$	O_{15}BP(P_8, L_3)	O_{16}WP(P_8, L_3)
64.62	35.38	11.9168	17.8332	30.00	70.00
I_{17}BP(P_9, L_3)	I_{18}WP(P_9, L_3)	$h_{9,1}/BP_9$	$h_{9,2}/WP_9$	O_{17}BP(P_9, L_3)	O_{18}WP(P_9, L_3)
15.90	84.10	11.9168	17.8332	26.20	73.80

Table 5.3: Activation of neural network layers for the rate of black-and-white pixel image under curing conditions at 21 days using M1 / 30 MPa

Activation of input, hidden and output layers across the neural network under curing conditions at 21 days, in percentage					
Input Layer (IL)		Hidden Layer (HL)		Output layer (OL)	
I_1BP(P_1, L_1)	I_2WP(P_1, L_1)	$h_{1,1}/BP_1$	$h_{1,2}/WP_1$	O_1BP(P_1, L_1)	O_2WP(P_1, L_1)
40.36	59.64	14.0090	15.7386	31.10	68.90
I_3BP(P_2, L_1)	I_4WP(P_2, L_1)	$h_{2,1}/BP_2$	$h_{2,2}/WP_2$	O_3BP(P_2, L_1)	O_4WP(P_2, L_1)
100.00	0.00	14.0090	15.7386	24.60	75.40
I_5BP(P_3, L_1)	I_6WP(P_3, L_1)	$h_{3,1}/BP_3$	$h_{3,2}/WP_3$	O_5BP(P_3, L_1)	O_6WP(P_3, L_1)

1.54	98.46	14.0090	15.7386	22.90	77.10
I_7BP(P_4, L_2)	I_8WP(P_4, L_2)	$h_{4,1}/BP_4$	$h_{4,2}/WP_4$	O_7BP(P_4, L_2)	O_8WP(P_4, L_2)
40.56	59.44	8.9519	20.7547	20.50	79.50
I_9BP(P_5, L_2)	I_{10}WP(P_5, L_2)	$h_{5,1}/BP_5$	$h_{5,2}/WP_5$	O_9BP(P_5, L_2)	O_{10}WP(P_5, L_2)
31.17	68.83	8.9519	20.7547	29.10	70.90
I_{11}BP(P_6, L_2)	I_{12}WP(P_6, L_2)	$h_{6,1}/BP_6$	$h_{6,2}/WP_6$	O_{11}BP(P_6, L_2)	O_{12}WP(P_6, L_2)
19.04	80.96	8.9519	20.7547	27.10	72.90
I_{13}BP(P_7, L_3)	I_{14}WP(P_7, L_3)	$h_{7,1}/BP_7$	$h_{7,2}/WP_7$	O_{13}BP(P_7, L_3)	O_{14}WP(P_7, L_3)
40.36	59.64	11,9247	17,8480	27.20	72.80
I_{15}BP(P_8, L_3)	I_{16}WP(P_8, L_3)	$h_{8,1}/BP_8$	$h_{8,2}/WP_8$	O_{15}BP(P_8, L_3)	O_{16}WP(P_8, L_3)
64.62	35.38	11.9247	17.8480	23.60	76.40
I_{17}BP(P_9, L_3)	I_{18}WP(P_9, L_3)	$h_{9,1}/BP_9$	$h_{9,2}/WP_9$	O_{17}BP(P_9, L_3)	O_{18}WP(P_9, L_3)
15.90	84.10	11.9247	17.8480	23.50	76.50

Table 5.4: Activation of neural network layers for the rate of black-and-white pixel image under curing conditions at 28 days using M1 / 30 MPa

Activation of input, hidden and output layers across the neural network at 28 under curing conditions days, in percentage					
Input Layer (IL)		Hidden Layer (HL)		Output layer (OL)	
I_1BP(P_1, L_1)	I_2WP(P_1, L_1)	$h_{1,1}/BP_1$	$h_{1,2}/WP_1$	O_1BP(P_1, L_1)	O_2WP(P_1, L_1)
40.36	59.64	13.9781	15.7344	25.00	75.00
I_3BP(P_2, L_1)	I_4WP(P_2, L_1)	$h_{2,1}/BP_2$	$h_{2,2}/WP_2$	O_3BP(P_2, L_1)	O_4WP(P_2, L_1)
100.00	0.00	13.9781	15.7344	21.30	78.70
I_5BP(P_3, L_1)	I_6WP(P_3, L_1)	$h_{3,1}/BP_3$	$h_{3,2}/WP_3$	O_5BP(P_3, L_1)	O_6WP(P_3, L_1)
1.54	98.46	13.9781	15.7344	33.10	66.90
I_7BP(P_4, L_2)	I_8WP(P_4, L_2)	$h_{4,1}/BP_4$	$h_{4,2}/WP_4$	O_7BP(P_4, L_2)	O_8WP(P_4, L_2)
40.56	59.44	8.9762	20.7445	28.90	71.10
I_9BP(P_5, L_2)	I_{10}WP(P_5, L_2)	$h_{5,1}/BP_5$	$h_{5,2}/WP_5$	O_9BP(P_5, L_2)	O_{10}WP(P_5, L_2)
31.17	68.83	8.9762	20.7445	31.00	69.00
I_{11}BP(P_6, L_2)	I_{12}WP(P_6, L_2)	$h_{6,1}/BP_6$	$h_{6,2}/WP_6$	O_{11}BP(P_6, L_2)	O_{12}WP(P_6, L_2)
19.04	80.96	8.9762	20.7445	31.00	69.00
I_{13}BP(P_7, L_3)	I_{14}WP(P_7, L_3)	$h_{7,1}/BP_7$	$h_{7,2}/WP_7$	O_{13}BP(P_7, L_3)	O_{14}WP(P_7, L_3)
40.36	59.64	23.6809	5.9342	33.20	66.80
I_{15}BP(P_8, L_3)	I_{16}WP(P_8, L_3)	$h_{8,1}/BP_8$	$h_{8,2}/WP_8$	O_{15}BP(P_8, L_3)	O_{16}WP(P_8, L_3)

64.62	35.38	23.6809	5.9342	20.90	79.10
I_{17}BP(P_9, L_3)	I_{18}WP(P_9, L_3)	$h_{9,1}/BP_9$	$h_{9,2}/WP_9$	O_{17}BP(P_9, L_3)	O_{18}WP(P_9, L_3)
15.90	84.10	23.6809	5.9342	21.50	78.50

Under curing conditions (Tables 5.1 – 5.4), black pixels ranged from 17.40% to 35.10% and white pixels from 64.90% to 82.60% at 3 days, 17.00 – 31.50% and 68.50 – 83.00% at 7 days, 17.20 – 24.30% and 75.70 – 82.80% at 14 days, and 20.90 – 33.20% and 66.80 – 79.10% at 28 days.

These ranges not only illustrate the temporal evolution of the concrete surface under curing conditions but also reflect the ability of the ANN to capture and predict the pixel patterns.

The behaviour of the ANN during training with regards to corrosion progression under 3 – 27 days for the M1/30 MPa is summarised in Tables 5.5 to 5.8.

Table 5.5: Activation of neural network layers for the rate of black-and-white pixel image under corrosion conditions at 3 days using M1 / 30 MPa, tested to sulphuric acid of 30 g/ℓ

Activation of input, hidden and output layers across the neural network under corrosion conditions at 3 days, in percentage					
Input Layer (IL)		Hidden Layer (HL)		Output layer (OL)	
I_1BP(P_1, L_1)	I_2WP(P_1, L_1)	$h_{1,1}/BP_1$	$h_{1,2}/WP_1$	O_1BP(P_1, L_1)	O_2WP(P_1, L_1)
40.36	59.64	14.0105	15.7367	21.80	78.20
I_3BP(P_2, L_1)	I_4WP(P_2, L_1)	$h_{2,1}/BP_2$	$h_{2,2}/WP_2$	O_3BP(P_2, L_1)	O_4WP(P_2, L_1)
100.00	0.00	14.0105	15.7367	28.70	71.30
I_5BP(P_3, L_1)	I_6WP(P_3, L_1)	$h_{3,1}/BP_3$	$h_{3,2}/WP_3$	O_5BP(P_3, L_1)	O_6WP(P_3, L_1)
1.54	98.46	14.0105	15.7367	31.50	68.50
I_7BP(P_4, L_2)	I_8WP(P_4, L_2)	$h_{4,1}/BP_4$	$h_{4,2}/WP_4$	O_7BP(P_4, L_2)	O_8WP(P_4, L_2)
40.56	59.44	8.9680	20.7453	27.60	72.40
I_9BP(P_5, L_2)	I_{10}WP(P_5, L_2)	$h_{5,1}/BP_5$	$h_{5,2}/WP_5$	O_9BP(P_5, L_2)	O_{10}WP(P_5, L_2)
31.17	68.83	8,9680	20,7453	25.80	74.20
I_{11}BP(P_6, L_2)	I_{12}WP(P_6, L_2)	$h_{6,1}/BP_6$	$h_{6,2}/WP_6$	O_{11}BP(P_6, L_2)	O_{12}WP(P_6, L_2)
19.04	80.96	8.9680	20.7453	32.20	67.80
I_{13}BP(P_7, L_3)	I_{14}WP(P_7, L_3)	$h_{7,1}/BP_7$	$h_{7,2}/WP_7$	O_{13}BP(P_7, L_3)	O_{14}WP(P_7, L_3)
40.36	59.64	11.9671	17.8170	41.90	58.10

I_{15}BP(P_8, L_3)	I_{16}WP(P_8, L_3)	$h_{8,1}/BP_8$	$h_{8,2}/WP_8$	O_{15}BP(P_8, L_3)	O_{16}WP(P_8, L_3)
64.62	35.38	11.9671	17.8170	29.00	71.00
I_{17}BP(P_9, L_3)	I_{18}WP(P_9, L_3)	$h_{9,1}/BP_9$	$h_{9,2}/WP_9$	O_{17}BP(P_9, L_3)	O_{18}WP(P_9, L_3)
15.90	84.10	11.9671	17.8170	36.60	63.40

Table 5.6: Activation of neural network layers for the rate of black-and-white pixel image under corrosion conditions at 6 days using M1 / 30 MPa, tested to sulphuric acid of 30 g/ℓ

Activation of input, hidden and output layers across the neural network under corrosion conditions at 6 days, in percentage					
Input Layer (IL)		Hidden Layer (HL)		Output layer (OL)	
I_1BP(P_1, L_1)	I_2WP(P_1, L_1)	$h_{1,1}/BP_1$	$h_{1,2}/WP_1$	O_1BP(P_1, L_1)	O_2WP(P_1, L_1)
40.36	59.64	13.9479	15.7427	20.90	79.10
I_3BP(P_2, L_1)	I_4WP(P_2, L_1)	$h_{2,1}/BP_2$	$h_{2,2}/WP_2$	O_3BP(P_2, L_1)	O_4WP(P_2, L_1)
100.00	0.00	13.9479	15.7427	19.00	81.00
I_5BP(P_3, L_1)	I_6WP(P_3, L_1)	$h_{3,1}/BP_3$	$h_{3,2}/WP_3$	O_5BP(P_3, L_1)	O_6WP(P_3, L_1)
1.54	98.46	13.9479	15.7427	22.20	77.80
I_7BP(P_4, L_2)	I_8WP(P_4, L_2)	$h_{4,1}/BP_4$	$h_{4,2}/WP_4$	O_7BP(P_4, L_2)	O_8WP(P_4, L_2)
40.56	59.44	8.9716	20.7550	33.60	66.40
I_9BP(P_5, L_2)	I_{10}WP(P_5, L_2)	$h_{5,1}/BP_5$	$h_{5,2}/WP_5$	O_9BP(P_5, L_2)	O_{10}WP(P_5, L_2)
31.17	68.83	8.9716	20.7550	26.60	73.40
I_{11}BP(P_6, L_2)	I_{12}WP(P_6, L_2)	$h_{6,1}/BP_6$	$h_{6,2}/WP_6$	O_{11}BP(P_6, L_2)	O_{12}WP(P_6, L_2)
19.04	80.96	8.9716	20.7550	24.30	75.70
I_{13}BP(P_7, L_3)	I_{14}WP(P_7, L_3)	$h_{7,1}/BP_7$	$h_{7,2}/WP_7$	O_{13}BP(P_7, L_3)	O_{14}WP(P_7, L_3)
40.36	59.64	11.9056	17.8333	28.20	71.80
I_{15}BP(P_8, L_3)	I_{16}WP(P_8, L_3)	$h_{8,1}/BP_8$	$h_{8,2}/WP_8$	O_{15}BP(P_8, L_3)	O_{16}WP(P_8, L_3)
64.62	35.38	11.9056	17.8333	19.30	80.70
I_{17}BP(P_9, L_3)	I_{18}WP(P_9, L_3)	$h_{9,1}/BP_9$	$h_{9,2}/WP_9$	O_{17}BP(P_9, L_3)	O_{18}WP(P_9, L_3)
15.90	84.10	11.9056	17.8333	23.00	77.00

Table 5.7: Activation of neural network layers for the rate of black-and-white pixel image under corrosion conditions at 24 days using M1 / 30 MPa, tested to sulphuric acid of 30 g/ℓ

Activation of input, hidden and output layers across the neural network under corrosion conditions at 24 days, in percentage					
Input Layer (IL)		Hidden Layer (HL)		Output layer (OL)	
I_1BP(P_1, L_1)	I_2WP(P_1, L_1)	$h_{1,1}/BP_1$	$h_{1,2}/WP_1$	O_1BP(P_1, L_1)	O_2WP(P_1, L_1)
40.36	59.64	14.0403	15.7334	32.10	67.90
I_3BP(P_2, L_1)	I_4WP(P_2, L_1)	$h_{2,1}/BP_2$	$h_{2,2}/WP_2$	O_3BP(P_2, L_1)	O_4WP(P_2, L_1)
100.00	0.00	14.0403	15.7334	31.40	68.60
I_5BP(P_3, L_1)	I_6WP(P_3, L_1)	$h_{3,1}/BP_3$	$h_{3,2}/WP_3$	O_5BP(P_3, L_1)	O_6WP(P_3, L_1)
1.54	98.46	14.0403	15.7334	30.70	69.30
I_7BP(P_4, L_2)	I_8WP(P_4, L_2)	$h_{4,1}/BP_4$	$h_{4,2}/WP_4$	O_7BP(P_4, L_2)	O_8WP(P_4, L_2)
40.56	59.44	8.9733	20.7463	26.10	73.90
I_9BP(P_5, L_2)	I_{10}WP(P_5, L_2)	$h_{5,1}/BP_5$	$h_{5,2}/WP_5$	O_9BP(P_5, L_2)	O_{10}WP(P_5, L_2)
31.17	68.83	8.9733	20.7463	34.00	66.00
I_{11}BP(P_6, L_2)	I_{12}WP(P_6, L_2)	$h_{6,1}/BP_6$	$h_{6,2}/WP_6$	O_{11}BP(P_6, L_2)	O_{12}WP(P_6, L_2)
19.04	80.96	8,9733	20,7463	29.70	70.30
I_{13}BP(P_7, L_3)	I_{14}WP(P_7, L_3)	$h_{7,1}/BP_7$	$h_{7,2}/WP_7$	O_{13}BP(P_7, L_3)	O_{14}WP(P_7, L_3)
40.36	59.64	11.9361	17.8262	35.00	65.00
I_{15}BP(P_8, L_3)	I_{16}WP(P_8, L_3)	$h_{8,1}/BP_8$	$h_{8,2}/WP_8$	O_{15}BP(P_8, L_3)	O_{16}WP(P_8, L_3)
64.62	35.38	11.9361	17.8262	22.50	77.50
I_{17}BP(P_9, L_3)	I_{18}WP(P_9, L_3)	$h_{9,1}/BP_9$	$h_{9,2}/WP_9$	O_{17}BP(P_9, L_3)	O_{18}WP(P_9, L_3)
15.90	84.10	11.9361	17.8262	29.90	70.10

Table 5.8: Activation of neural network layers for the rate of black-and-white pixel image under corrosion conditions at 27 days using M1 / 30 MPa, tested to sulphuric acid of 30 g/ℓ

Activation of input, hidden and output layers across the neural network under corrosion conditions at 27 days, in percentage					
Input Layer (IL)		Hidden Layer (HL)		Output layer (OL)	
I_1BP(P_1, L_1)	I_2WP(P_1, L_1)	$h_{1,1}/BP_1$	$h_{1,2}/WP_1$	O_1BP(P_1, L_1)	O_2WP(P_1, L_1)
40.36	59.64	14,0090	15,7394	23.80	76.20
I_3BP(P_2, L_1)	I_4WP(P_2, L_1)	$h_{2,1}/BP_2$	$h_{2,2}/WP_2$	O_3BP(P_2, L_1)	O_4WP(P_2, L_1)

100.00	0.00	14.0090	15.7394	27.20	72.80
I_5BP(P_3, L_1)	I_6WP(P_3, L_1)	$h_{3,1}/BP_3$	$h_{3,2}/WP_3$	O_5BP(P_3, L_1)	O_6WP(P_3, L_1)
1.54	98.46	14.0090	15.7394	26.30	73.70
I_7BP(P_4, L_2)	I_8WP(P_4, L_2)	$h_{4,1}/BP_4$	$h_{4,2}/WP_4$	O_7BP(P_4, L_2)	O_8WP(P_4, L_2)
40.56	59.44	8.9276	20.7653	19.90	80.10
I_9BP(P_5, L_2)	I_{10}WP(P_5, L_2)	$h_{5,1}/BP_5$	$h_{5,2}/WP_5$	O_9BP(P_5, L_2)	O_{10}WP(P_5, L_2)
31.17	68.83	8.9276	20.7653	19.50	80.50
I_{11}BP(P_6, L_2)	I_{12}WP(P_6, L_2)	$h_{6,1}/BP_6$	$h_{6,2}/WP_6$	O_{11}BP(P_6, L_2)	O_{12}WP(P_6, L_2)
19.04	80.96	8.9276	20.7653	22.50	77.50
I_{13}BP(P_7, L_3)	I_{14}WP(P_7, L_3)	$h_{7,1}/BP_7$	$h_{7,2}/WP_7$	O_{13}BP(P_7, L_3)	O_{14}WP(P_7, L_3)
40.36	59.64	11.8745	17.8372	23.20	76.80
I_{15}BP(P_8, L_3)	I_{16}WP(P_8, L_3)	$h_{8,1}/BP_8$	$h_{8,2}/WP_8$	O_{15}BP(P_8, L_3)	O_{16}WP(P_8, L_3)
64.62	35.38	11.8745	17.8372	16.80	83.20
I_{17}BP(P_9, L_3)	I_{18}WP(P_9, L_3)	$h_{9,1}/BP_9$	$h_{9,2}/WP_9$	O_{17}BP(P_9, L_3)	O_{18}WP(P_9, L_3)
15.90	84.10	11.8745	17.8372	19.40	80.60

Under corrosion conditions with sulphuric acid (Tables 5.5 – 5.8), black pixels ranged from 21.80 – 41.90% and white pixels 58.10 – 78.20% at 3 days, 19.00 – 33.60% and 66.40 – 80.70% at 6 days, 22.50 – 35.00% and 65.00 – 77.50% at 24 days, as well as 16.80 – 27.20% and 72.80 – 83.20% at 27 days.

These results illustrate the progression of black-and-white pixel patterns under sulphuric acid exposure and provide the basis for the mathematical models implemented in Section 5.4.2 to analyse pixel rates and corrosion effects. The ANN demonstrates its capability to capture these evolving patterns over time, reflecting the combined influence of concrete properties and aggressive environmental conditions. All the remaining tables associated with M1 / 30MPa including M2 / 40 MPa are presented in Appendix C.

To summarise, the mathematical formulations implemented in this doctoral study provided a solid and systematic framework for the activation of functions and the training of the ANN. By applying these equations to 180 scanned points, the network was progressively guided to minimise errors and accurately capture the relationships between input and output parameters. This approach not only

ensured reliable predictions of black- and white-pixel patterns on the concrete surface but also demonstrated the critical role of tailored mathematical modelling in enhancing both the learning process and the overall predictive performance of the network.

5.4 Models of scanned points using artificial neural networks

This section presents the main steps that contributed to modelling the scanned points based on the black-and-white pixel rates of the two mixtures (M1 and M2).

In this study, nine scanned point models were developed to evaluate the distribution of black and white pixels within the ANN framework (see Section 5.3). The experimental output data obtained from black-and-white pixel images were applied to design the scanned point models representing the influence of pixel variation on cement grains during the curing and corrosion phases. Furthermore, the identification indices (IBP and OWP) of black-and-white pixels affecting cement grains were used as input parameters for estimating the pixel rates of the scanned points throughout the ANN framework (refer to Section 5.3.1). The integration of OBWP output data was also carried out for both concrete mixtures (M1 and M2) to enhance the evaluation of the scanned point models.

Two investigation scenarios are examined in this section. The first concerns the assessment of black-and-white pixel rates under curing conditions for both concrete mixtures, while the second addresses their evolution under corrosion conditions, in which a M1 cube was exposed to a sulphuric acid solution of 30 g/ℓ. All graphical analyses were performed in MATLAB R2022b. These analyses form the basis for the detailed presentation of results in the following sections.

5.4.1 Assessment of black and white pixel rates under curing conditions

This section provides a detailed examination of the ANN models developed to assess black-and-white pixel rates. The analysis begins with the behaviour of the

scanned point models under curing conditions, as illustrated in Figures 5.7 to 5.10 below.

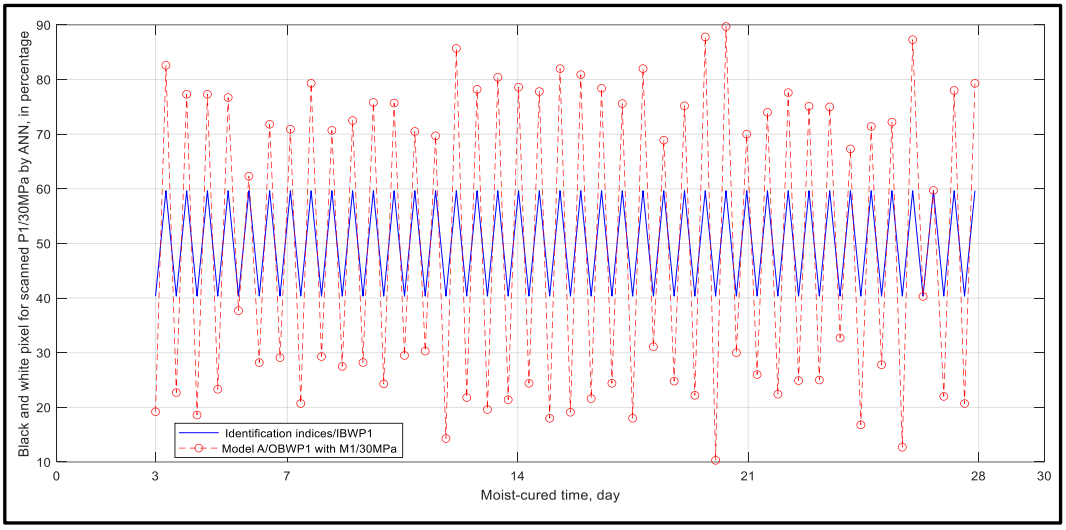

Figure 5.7: Model A/OBWP1 with M1 / 30 MPa and IBWP1 for evaluating the black and white pixel rates into scanned point 1 under curing conditions

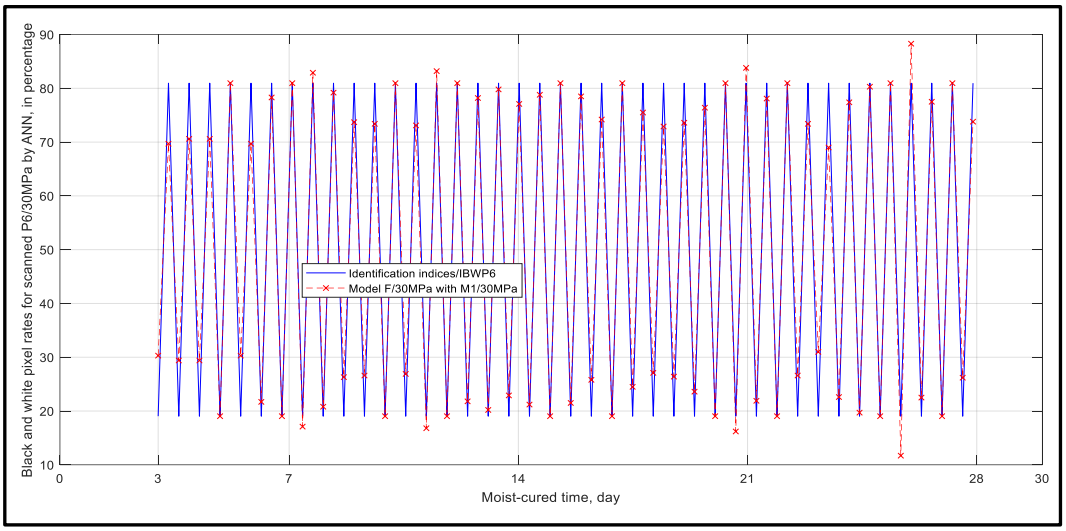

Figure 5.8: Model F/OBWP6 with M1 / 30 MPa and IBWP6 for evaluating the black and white pixel rates into scanned point 6 under curing conditions

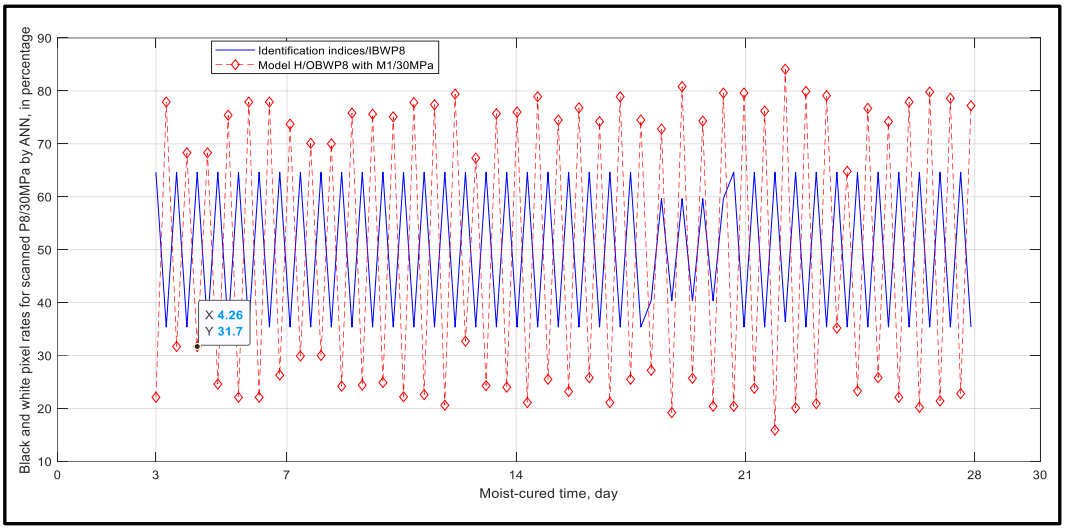

Figure 5.9: Model H/OBWP8 with M1 / 30 MPa and IBWP8 for evaluating the black and white pixel rates into scanned point 8 under curing conditions

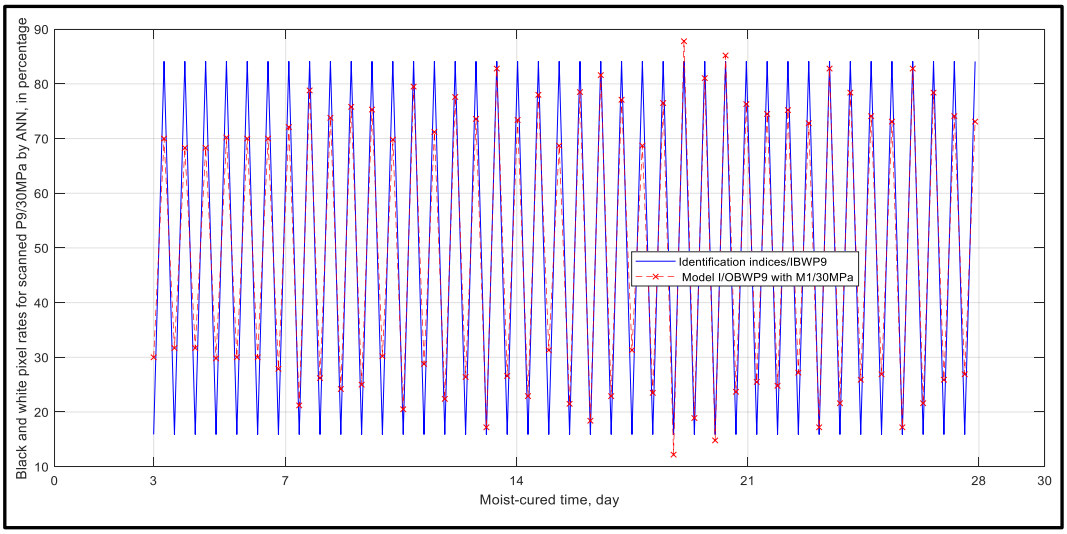

Figure 5.10: Model I/OBWP9 with M1 / 30 MPa and IBWP9 for evaluating the black and white pixel rates into scanned point 9 under curing conditions

Figures 5.7 – 5.10 present models (M1 / 30 MPa) based on 800 × 1200 greyscale images used to analyse black-and-white pixel rates at scanned points P1 (Model A), P6 (Model F), P8 (Model H), and P9 (Model I) under curing conditions. Experimental results are shown as red dotted lines while ANN-based identification indices are displayed as solid blue lines. The variation in black and white pixel rates for the nine models (Mi1/30 MPa) was assessed as a function of curing time. The remaining models (P2, P3, P4, P5, P7) are provided in Appendix C.

Overall, Figures 5.7 – 5.10 reveal a clear inverse relationship between black and white pixel rates during curing: as black pixels decrease, white pixels increase. Model I (scanned point 9) exhibited the most consistent and accurate response, recording the highest white pixel rate of 82.80% and the lowest black pixel rate of 17.20% at 14 days (Figure 5.10). Corresponding ANN identification indices reached 84.10% (white) and 15.90% (black). Throughout the curing period, white pixel rates began at 82.60% (3 days) and gradually declined to 79.50% (28 days). Figure 5.11 illustrates the performance of Model I, highlighting its accuracy in representing the pixel rate evolution, as generated using Visio 2019.

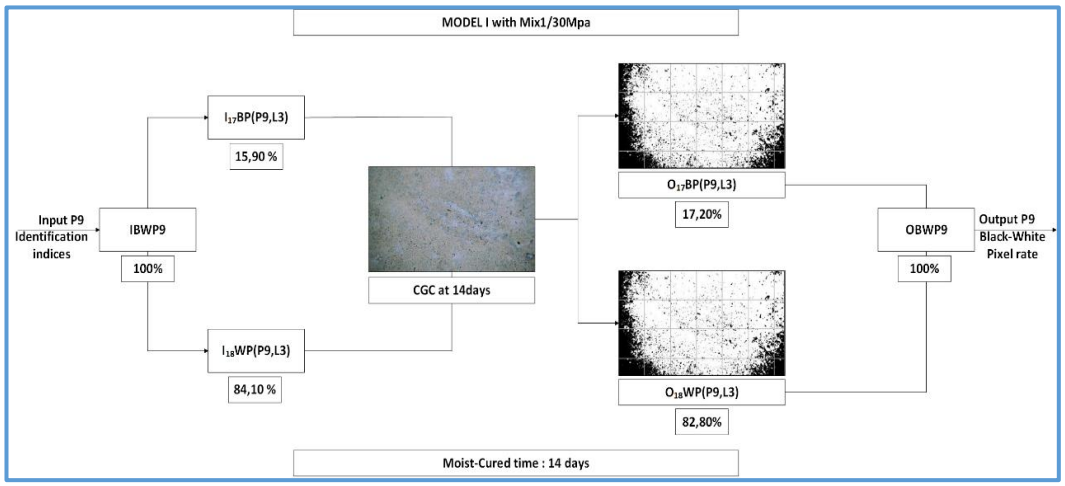

Figure 5.11: Schematic representation of Model I/scanned point 9 with M1 / 30 MPa in recording at 14 days both the highest and lowest pixel rate under curing conditions

Figure 5.11 illustrates Model I for M1 (30 MPa) after 14 days of curing. The white area proportion (WAP) and black area proportion (BAP) indicate the distribution of light and dark pixels within the greyscale image. A crown-shaped black band can be observed encircling the white perimeter. At 14 days, WAP reached 82.80%, while BAP decreased to 17.20%, reflecting hydration effects acting on cement grains during curing. Following this analysis, further models were developed to evaluate the performance of M2 (40 MPa) under similar curing conditions. The next section presents the results of these scanned point models, highlighting how pixel distribution patterns evolve with increased compressive strength.

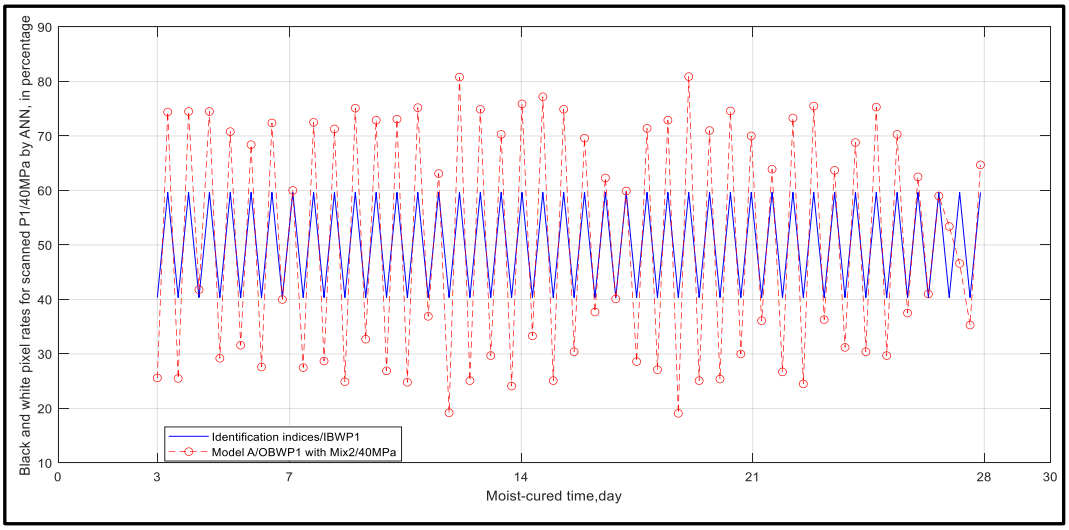

Figure 5.12: Model A/OBWP1 with M2 / 40 MPa and IBWP1 for evaluating the black and white pixel rates into scanned point 1 under curing conditions

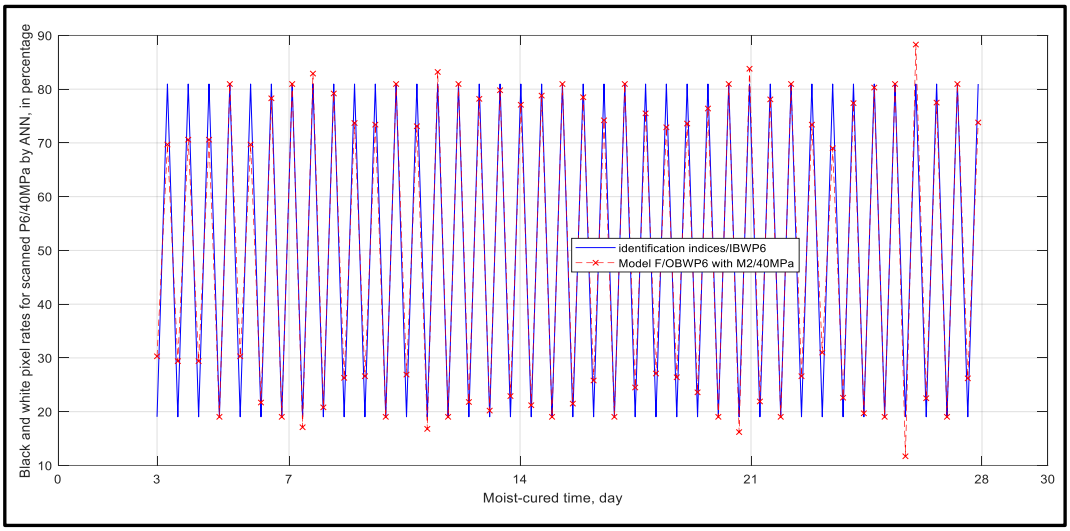

Figure 5.13: Model F/OBWP6 with M2 / 40 MPa and IBWP6 for evaluating the black and white pixel rates into scanned point 6 under curing conditions

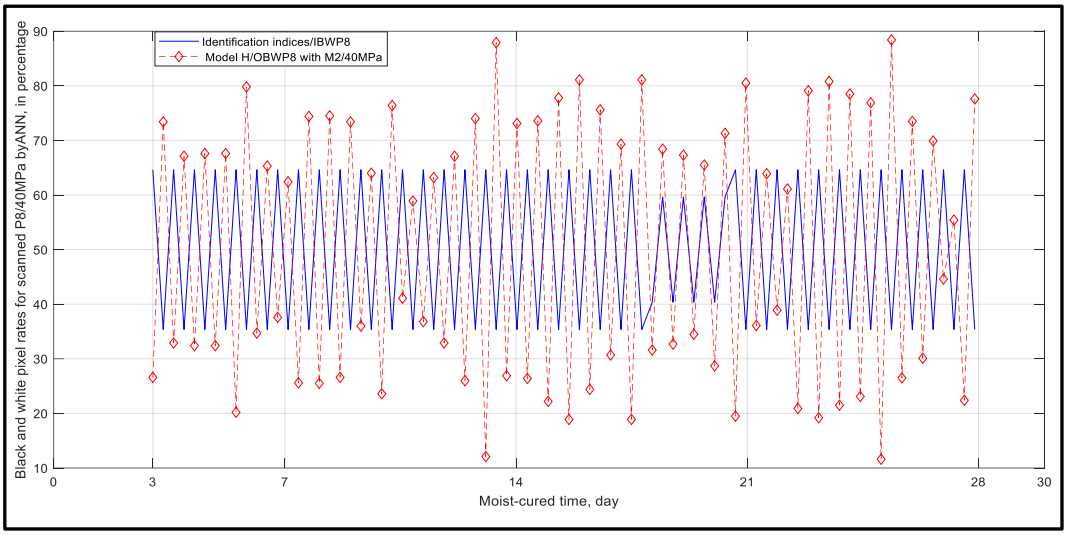

Figure 5.14: Model H/OBWP8 with M2 / 40 MPa and IBWP8 for evaluating the black and white pixel rates into scanned point 8 under curing conditions

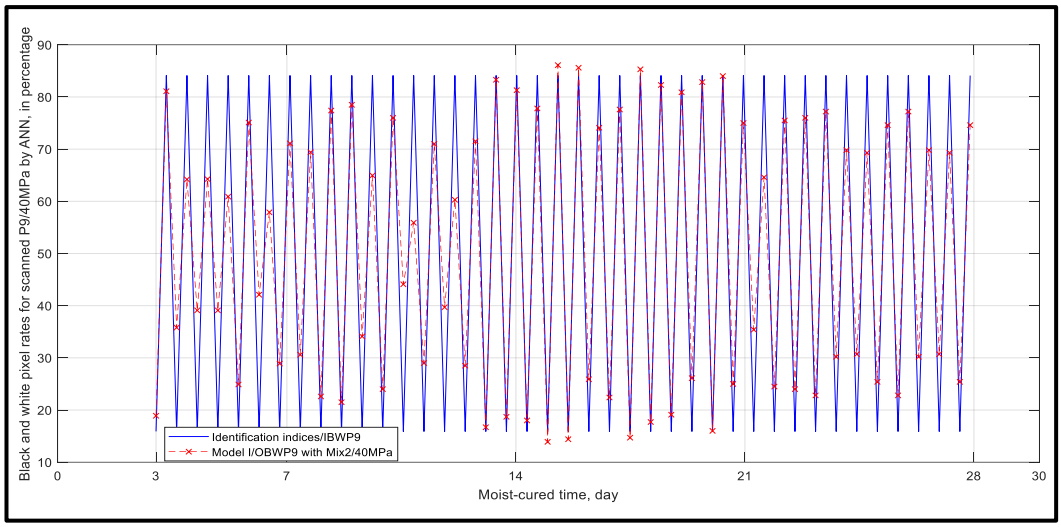

Figure 5.15: Model I/OBWP9 with M2 / 40 MPa and IBWP9 for evaluating the black and white pixel rates into scanned point 9 under curing conditions

Figures 5.12 – 5.15 present four representative models (A, F, H, and I) for mixture M2 (40 MPa) under curing conditions. As observed for M1, both minimum and maximum pixel rates were evaluated across all scanned points. The comparison shows that M2 follows a similar overall pattern, with black pixel proportions ranging from 16.70% to 30% and white pixel proportions from 70% to 83.30%. Model I (scanned point 9) recorded the highest white pixel rate of 83.30% and the lowest black pixel rate of 16.70% at 14 days. These results indicate that M2 achieves slightly higher white pixel values than M1, with the performance of

Model I shown in Figure 5.16. This modest difference in white pixel proportions between M1 and M2 is probably due to the influence of their respective mixture compositions (see Table 3.1). The remaining figures are provided in Appendix C.

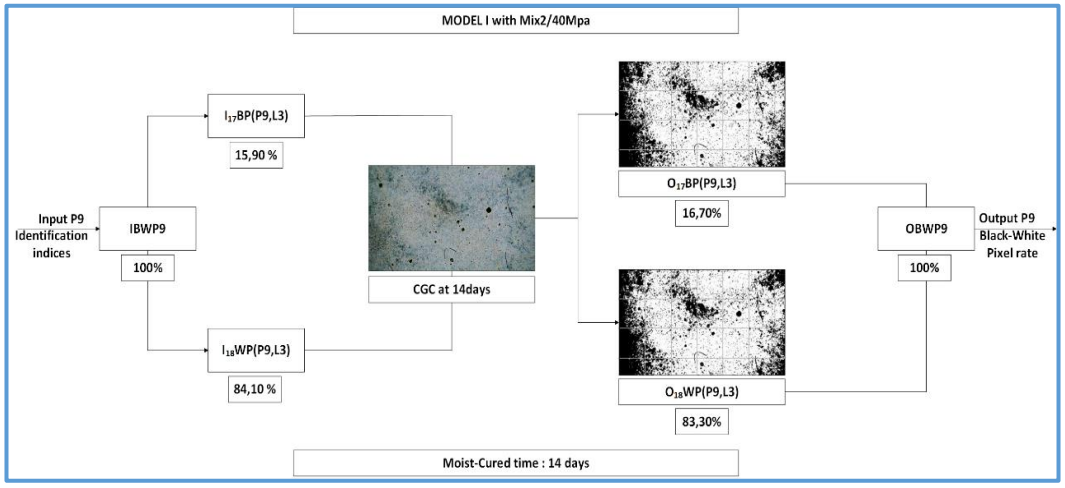

Figure 5.16: Schematic representation of Model I/scanned point 9 with M2 / 40MPa in recording at 14 days both the highest and lowest pixel rate under curing conditions

Figure 5.16 illustrates Model I for M2 (40 MPa) at 14 days, showing the highest and lowest pixel rates under curing conditions. Comparison of the three images highlights interactions between light and dark colours, pixel rates, and WAP/BAP. The white pixel rate (WAP) reached 83.30%, while the black pixel rate (BAP) was 16.70%, reflecting hydration effects on cement grains.

The observations under curing conditions demonstrated the progressive hydration of cement grains, characterised by a predominance of white pixels and a gradual reduction in dark areas. These findings provided valuable insights into the evolution of microstructural changes associated with matrix densification. However, to fully assess the durability behaviour of the material, it was necessary to extend the investigation to more aggressive environments. The next section therefore focuses on the modelling of scanned points used to evaluate the evolution of black-and-white pixel rates under corrosion conditions.

5.4.2 Assessment of black and white pixel rates under corrosion conditions

This section addresses the modelling of scanned points used to assess the evolution of black-and-white pixel rates under corrosion conditions. The analysis is based on a concrete cube produced with mixture M1 (30 MPa) and exposed to a 30 g/ℓ sulphuric acid solution. Through the ANN framework, the interplay between image-based pixel variations and the corrosion-induced degradation of cement grains is examined in detail. These results provide the basis for the subsequent analysis, in which the ANN is used to interpret how corrosion-driven colour changes influence the distribution and progression of pixel values across the scanned points.

Figures 5.17 – 5.20 present the black- and white-pixel rates obtained under these corrosion conditions for a M1 concrete cube exposed to the 30 g/ℓ sulphuric acid solution.

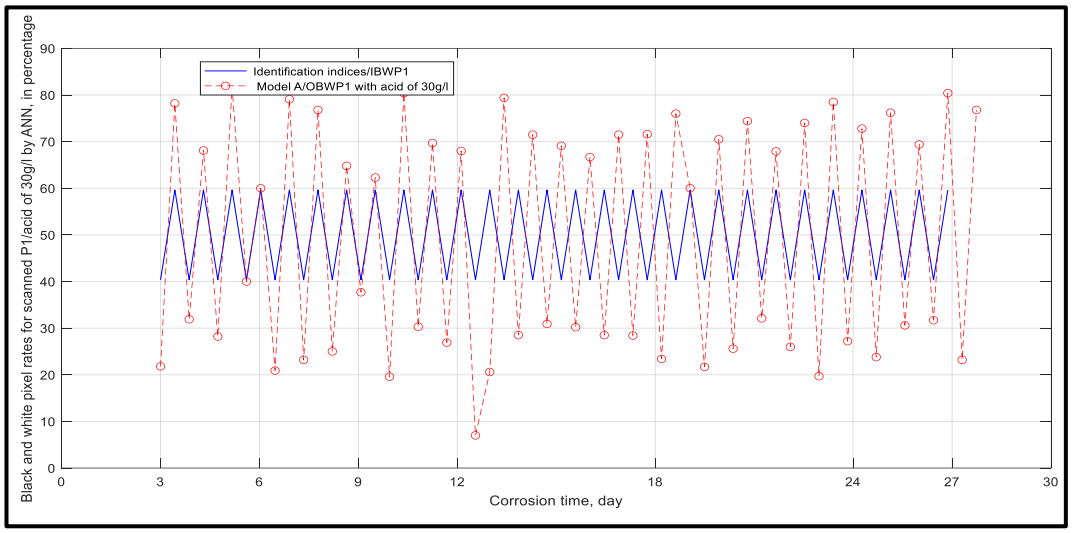

Figure 5.17: Model A/OBWP1 with M1 / 30 MPa and IBWP1, tested to sulphuric acid of 30 g/ℓ, for evaluating the black and white pixel rates into scanned point 1 under corrosion conditions

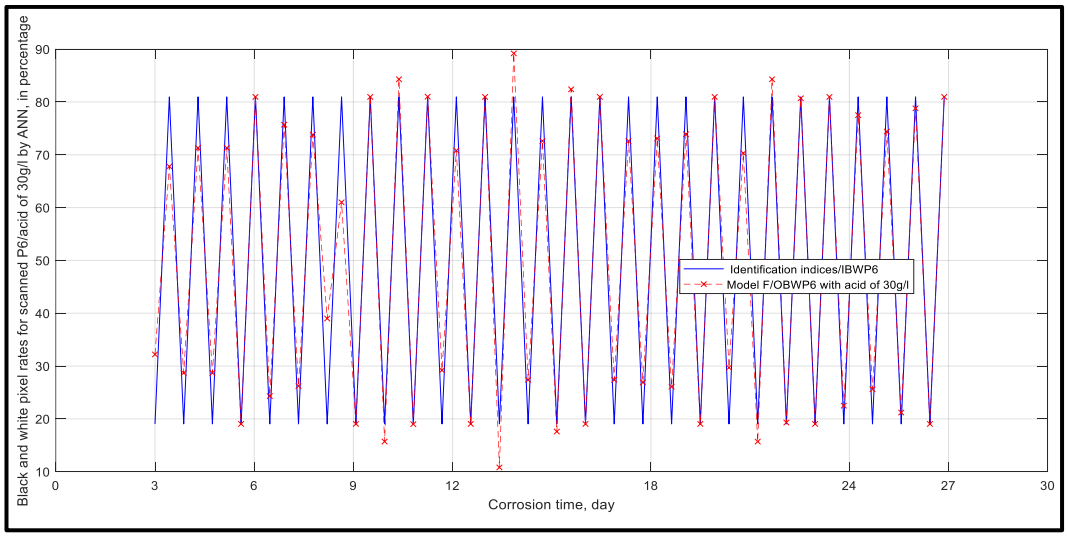

Figure 5.18: Model F/OBWP6 with Mix 1 / 30 MPa and IBWP6, tested to sulphuric acid of 30 g/ℓ, for evaluating the black and white pixel rates into scanned point 6 under corrosion conditions

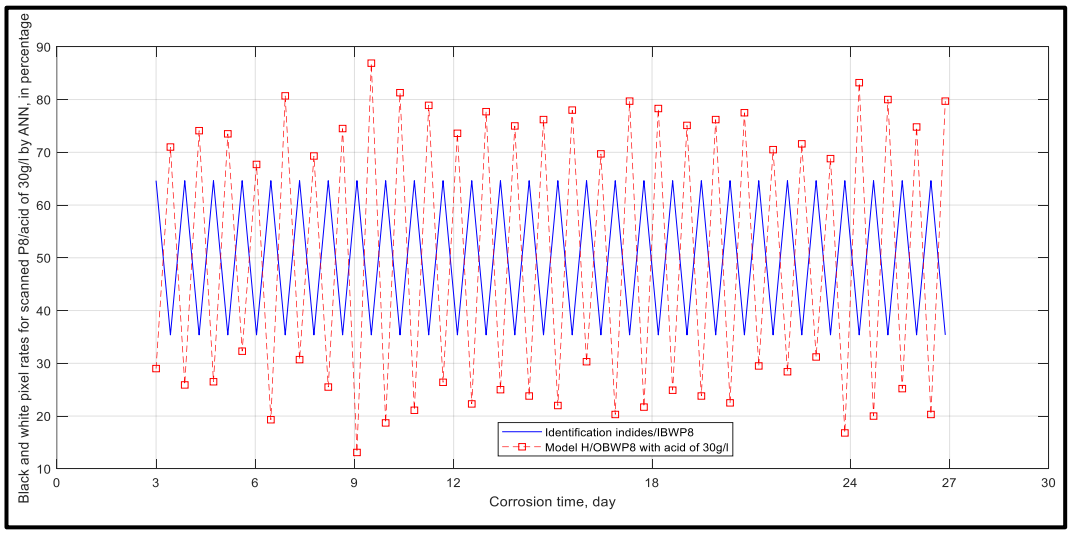

Figure 5.19: Model H/OBWP8 with M1 / 30 MPa and IBWP8, tested to sulphuric acid of 30 g/ℓ, for evaluating the black and white pixel rates into scanned point 8 under corrosion conditions

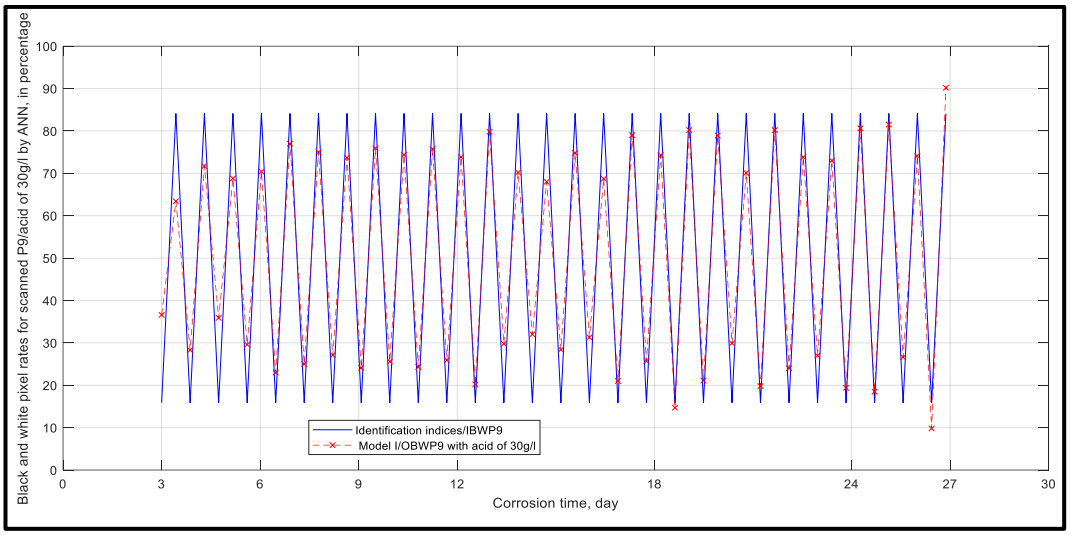

Figure 5.20: Model I/OBWP9 with M1 / 30 MPa and IBWP9, tested to sulphuric acid of 30 g/ℓ, for evaluating the black and white pixel rates into scanned point 9 under corrosion conditions

Figures 5.17 – 5.20 present four representative models (A, F, H, and I) developed using M1 (30 MPa) and exposed to a 30 g/ℓ sulphuric acid solution under corrosion conditions. These models analyse the black-and-white pixel rates derived from image outputs to evaluate the corrosion effects on the concrete surface. Additional scanned point models are provided in Appendix C.

Among the evaluated models, Model F (scanned point 6) at 12 days recorded the highest white pixel rate and the lowest black pixel rate within the ANN framework, at 89.20% and 10.80%, respectively. Compared with the curing phase for both M1 and M2, the variation in pixel rates under corrosion conditions was more pronounced for M1 exposed to sulphuric acid. This increase in the white pixel rate is mainly attributed to the mobility of sulphur ions within the concrete matrix, accelerating corrosion over time (see Section 2.3.1 of Chapter 2). Figure 5.21 illustrates Model F, highlighting the pixel rate variations across both colour and greyscale images.

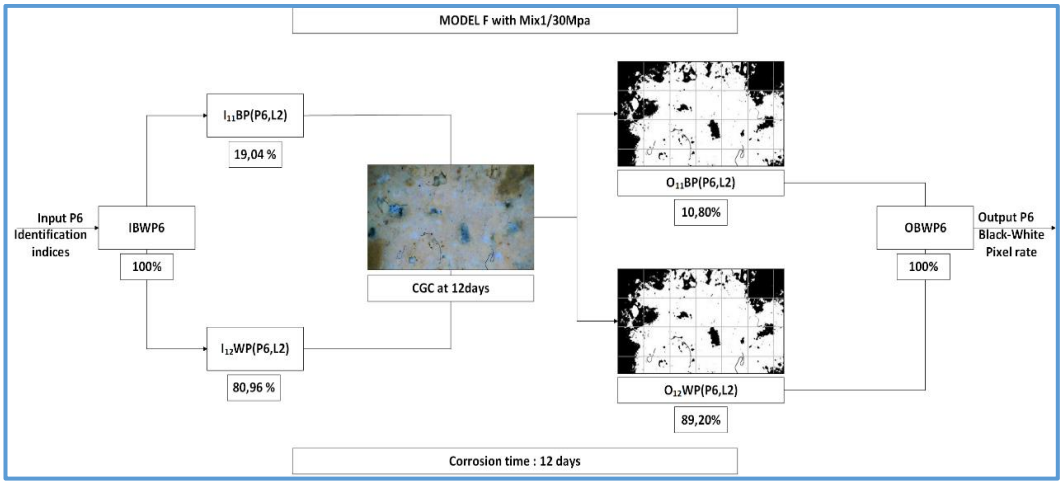

Figure 5.21: Schematic representation of Model F (scanned point 6)

Figure 5.21 presents a schematic representation of Model F (scanned point 6) using M1 (30 MPa), tested with a 30 g/ℓ sulphuric acid solution, showing the highest and lowest pixel rates recorded by the ANN under corrosion conditions at 12 days. In this model, interactions between light and dark colours are evident, reflecting changes in both white and black pixel rates as well as in the WAP and BAP. Under these corrosion conditions, the white pixel rate reached 89.20**%** (WAP/12 days), while the black pixel rate decreased to 10.80**%** (BAP/12 days). This pronounced increase in white pixel rate is likely attributable to the kinetic effects of sulphuric acid on the concrete matrix during the exposure period.

In summary, under corrosion conditions, the scanned-point models show a clear rise in white pixel rates and a decrease in black pixel rates compared with curing conditions. This effect is particularly evident in Model F (scanned point 6, M1 / 30 MPa) at 12 days, emphasising the strong impact of sulphuric acid on the concrete matrix. The findings confirm that variations in pixel rates reliably capture the progression of microstructural degradation, offering both visual and quantitative evidence of corrosion over time. The consistent increase in white pixel rates, in line with the white area proportion (WAP) observed in both curing and corrosion regimes, supports the conclusion that pixel rates may serve as a physical indicator of hydration and corrosion processes.

In the present research, these observations suggest that changes in white pixel rates could be used as a physical indicator for identifying the prevailing hydration and corrosion mechanisms. This perspective directly informs the first research question introduced in Section 1.4 of Chapter 1. Accordingly, the working hypothesis is that white pixel rates can effectively be used to assess the evolution of microstructural changes and thereby distinguish between different hydration and corrosion regimes during the slower phases. Section 6.2 of the next chapter attempts to address this question by testing the validity of this hypothesis.

5.5 Significance of the research findings

In line with the hypothesis formulated in Section 2.5.3 of the literature review, it was proposed that, in the absence of a suitable matrix for directly calculating the input values, a customised set of matrix equations could be developed to generate numerical values that reflect both the experimental parameters and the precise geometrical positions of the scanned points. The matrix equations implemented in this study successfully produced these numerical values for the scanned points on the surface of a 150 × 150 × 150 mm concrete cube, which then served as the input parameters for analysing the output targets within the ANN architecture. This approach also enabled verification of the effectiveness of the implemented matrix equations in providing reliable input–output relationships for the modelling process.

The ANN models successfully captured the evolution of black-and-white pixel patterns under both curing and corrosion conditions. During curing, black pixel values generally decreased while white pixel values remained high, reflecting ongoing hydration. Under sulphuric acid exposure, however, pixel rates varied more sharply, indicating progressive surface degradation. These findings confirm the capacity of the ANN to predict changes in concrete surface conditions, establishing it as a reliable tool for monitoring material behaviour under different environmental regimes.

The scanned-point models further allowed for a detailed assessment of black and white pixel distributions within the ANN framework. Under curing conditions, both mixtures (M1 / 30 MPa and M2) exhibited their highest white pixel rates in Model I, corresponding to scanned point 9 at 14 days (see Section 5.4.1 of Chapter 5). The recorded white pixel proportions were 82.80% for M1 and 83.30% for M2, showing that mixture M2 achieved slightly higher whiteness levels than M1.

By contrast, under corrosion conditions, the highest white pixel rate and lowest black pixel rate within the ANN framework were found in Model F, associated with scanned point 6 at 12 days, where the white pixel rate reached 89.20%. This marked increase in white pixel rates under corrosion is likely attributable to the strong influence of sulphuric acid on the concrete matrix and mixture design, compared with the responses observed under hydration conditions.

Overall, these findings demonstrate the robustness of the proposed methodological framework and confirm that the integration of matrix-based inputs and ANN modelling offers a reliable and insightful approach for characterising concrete behaviour under both hydration and corrosion regimes.

Building on these results, the next chapter investigates the specific hydration and corrosion regimes that may develop over time, using the white pixel rate as a physical indicator to trace and characterise their progression.

CHAPTER 6: INVESTIGATION OF HYDRATION AND CORROSION REGIMES WITHIN CONCRETE MIXTURES

6.1 Introduction

This chapter investigates the hydration and corrosion regimes influencing cement grains in concrete mixtures, addressing the first research question regarding the dominant mechanisms during the slow phases (Section 1.4, Chapter 1). It is structured into two parts.

The first part examines these mechanisms using the hypothesis that changes in white pixel rates act as physical indicators of the prevailing hydration and corrosion processes. The second part applies matrix-based analytical formulations and dedicated algorithms to process the colorimetric properties of cement grains, providing quantitative and visual insights into the underlying physical and chemical transformations.

6.2 Hydration and corrosion mechanisms of cement grains

Building on the hypothesis outlined in Section 5.4 (Chapter 5) that variations in white pixel rates can serve as a physical indicator of microstructural evolution and help distinguish between hydration and corrosion regimes during the slower phases, this section develops a concise analytical approach to address the first research question introduced in Section 1.4 of Chapter 1.

The first part of the section presents a methodological framework that integrates image-based experimental data with theoretical modelling to assess hydration and corrosion mechanisms within concrete mixtures. White pixel rates extracted from scanned images are used as a non-destructive indicator of hydration progression (see Section 5.5, Chapter 5). These experimental datasets, generated through the ANN-based framework described in Section 5.3.3 and summarised in Tables 5.1 – 5.8 (Chapter 5), are employed to inform and calibrate mathematical

models, enabling a theoretical interpretation of hydration and corrosion dynamics grounded in pixel-level analysis. The second part then introduces the resulting theoretical models for cement grain hydration and corrosion as functions of curing and corrosion time.

6.2.1 Theoretical and methodological foundations of mathematical models for slow-phase hydration and corrosion of cement grains

The method used to generate progression curves for theoretical models of cement grain hydration and corrosion, based on experimental white-pixel data, relies on two main elements.

Firstly, it incorporates the correlation between white pixels and the colour images, which highlights similarities in hydrated or corroded regions. This information is obtained through the experimental processing of scanned images (see Section 4.3 of Chapter 4).

Secondly, it recognises that these processes follow distinct trajectories, shaped by the structural behaviour of specific subnetworks (SNs). These SNs form part of the broader networks for CGH and cement corrosion (CC), respectively. Within the CGH network, four subnetworks are identified and temporally defined, whereas the CC network comprises six subnetworks. Tables 6.1 and 6.2 summarise these subnetworks for CGH and CC respectively.

Table 6.1: Distribution of subnetworks according to curing time

CGH Subnetworks	**Curing time**
SN1/CGH	3 – 7 days
SN2/CGH	7 – 14 days
SN3/CGH	14 – 21 days
SN4/CGH	21 – 28 days

Table 6.2: Distribution of subnetworks according to corrosion time

CC Subnetworks	Corrosion time
SN1/CC	3 – 6 days
SN2/CC	6 – 9 days
SN3/CC	9 – 12 days
SN4/CC	12 – 18 days
SN5/CC	18 – 24 days
SN6/CC	24 – 27 days

Tables 6.1 and 6.2 summarise the subnetworks defined by their respective time ranges. For the CGH network, SN1 covers 3 – 7 days, SN2 covers 7 – 14 days, SN3 covers 14 – 21 days, and SN4 covers 21 – 28 days (see Section 4.3.4 of Chapter 4), while the CC network comprises six subnetworks spanning 3 – 27 days of corrosion exposure.

Building on this temporal framework, the second stage of the methodology treats the subnetworks as controlling the independent parameters (inputs), with the dependent parameters (outputs) represented by the white pixel rates obtained from image processing (see Tables 4.3 – 4.6, Chapter 4). These datasets were then compiled to generate the progression curves, with hydration and corrosion regime data as presented for three represented scanned points P1 – P3 in Tables 6.3 and 6.4 respectively.

Table 6.3: Input and output data for assessing the hydration regime

Input data (days)	Output data: White pixel rates (%)		
	Point 1	Point 2	Point 3
3 – 7	82.6 – 70.7	75.5 – 68.5	80.3 – 73.8
7 – 14	70.7 – 80.4	68.5 – 79.8	73.8 – 77.9
14 – 21	80.4 – 68.9	79.8 – 75.4	77.9 – 77.1
21 – 28	68.9 – 75.0	75.4 – 78.7	77.1 – 66.9

Table 6.4: Input and output data for assessing the corrosion regime

Input data (days)	Output data: White pixel rates (%)		
	Point 1	Point 2	Point 3
3 – 6 days	78.2–79.1	71.3–81	68.5–77.8
6 – 9 days	79.1–80.4	81–74.6	77.8–87.1
9 – 12 days	80.4–71.5	74.6–72.9	87.1–71.6
12 – 18 days	71.5–71.6	72.9–70.3	71.6–74.5
18 – 24 days	71.6–67.9	70.3–68.6	74.5–69.3
24 – 27 days	67.9–76.2	68.6–72.8	69.3–73.7

Both Tables 6.3 and 6.4 provide a summary of range values of the input and output parameters employed to assess the behaviour of concrete under hydration and corrosion conditions. In order to generate the progression curves for hydration and corrosion during the slow phases, and to address the inherent complexity of the problem, the input and output datasets (Tables 6.3 and 6.4) were processed and plotted using MATLAB R2022b. The resulting graphs, which visualise the evolution of these processes, are presented in the following sections.

6.2.2 Assessment of theoretical models of cement hydration mechanisms under curing time

Based on the methodology described in Section 6.2.1, this subsection reports the results from the simulation and interpretation of hydration mechanisms using the theoretical models. This allows for a clear comparison between predicted and observed hydration trends.

Figures 6.1 – 6.8 depict the way the OWP models respond to local variations in the theoretical CGH models. For mixture M1, four representative scanned points (P1, P3, P6 and P9) are considered (Figures 6.1 – 6.4), while for mixture M2 the analysis

examines four representative scanned points (P1, P3, P7 and P8) (refer to Figures 6.5 – 6.8). In each case, the results are expressed as a function of curing time.

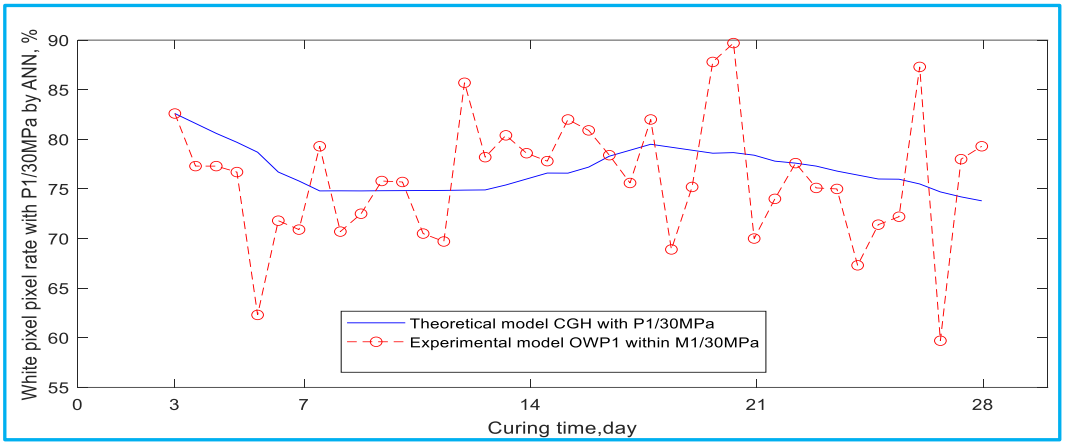

Figure 6.1: Sensitivity of the OWP1 model at scanned point P1 within M1 (30 MPa) in capturing the variation of the theoretical CGH model

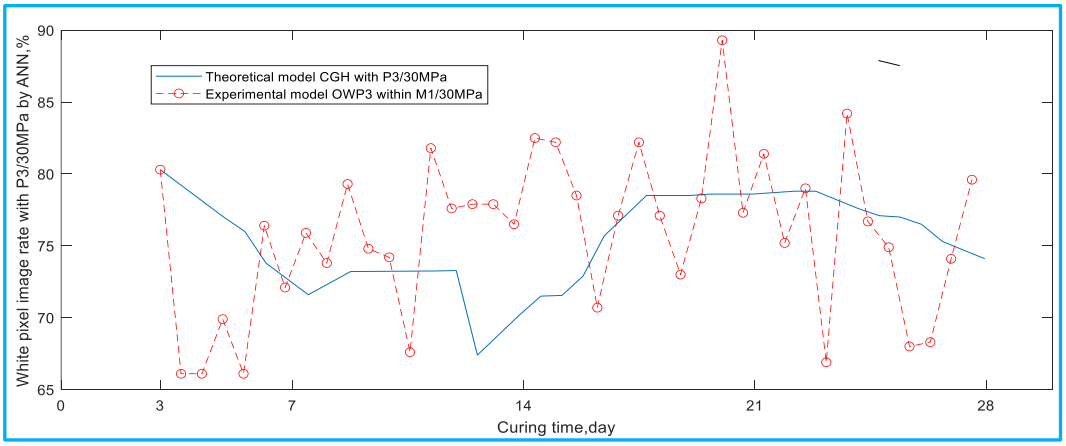

Figure 6.2: Sensitivity of the OWP3 model at scanned point P3 within M1 (30 MPa) in capturing the variation of the theoretical CGH model

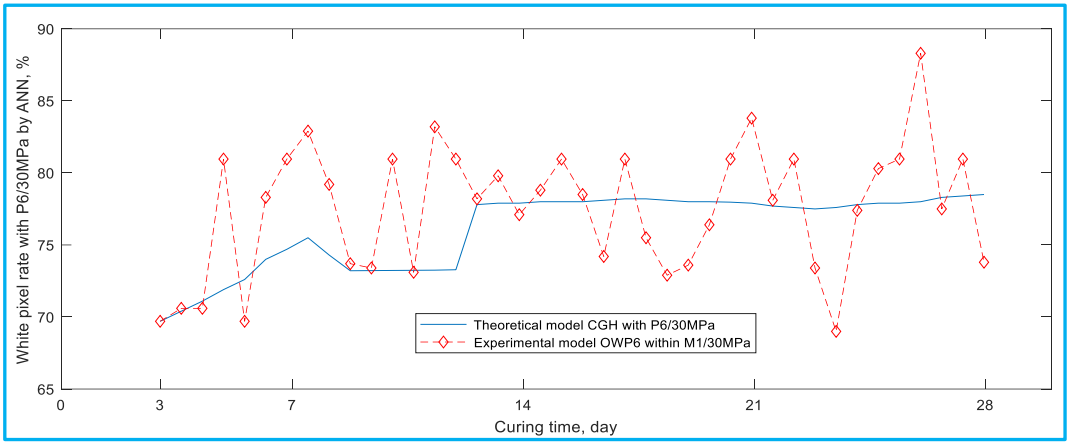

Figure 6.3: Sensitivity of the OWP6 model at scanned point P6 within M1 (30 MPa) in capturing the variation of the theoretical CGH model

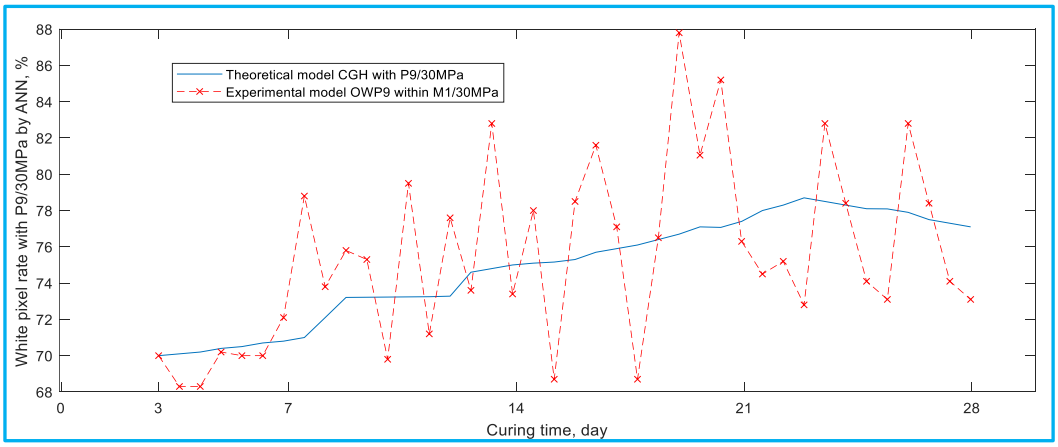

Figure 6.4: Sensitivity of the OWP9 model at scanned point P9 within M1 (30 MPa) in capturing the variation of the theoretical CGH model

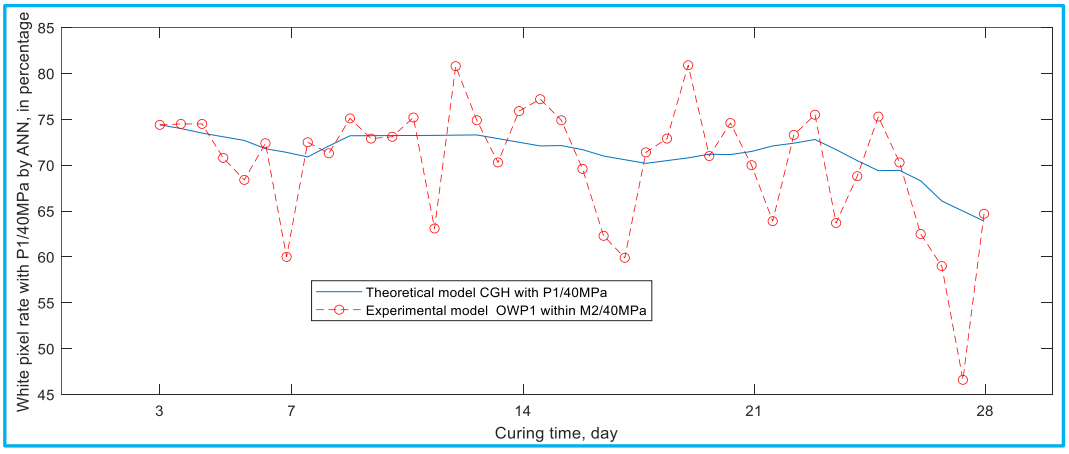

Figure 6.5: Sensitivity of the OWP1 model at scanned point P1 within M2 (40 MPa) in capturing the variation of the theoretical CGH model

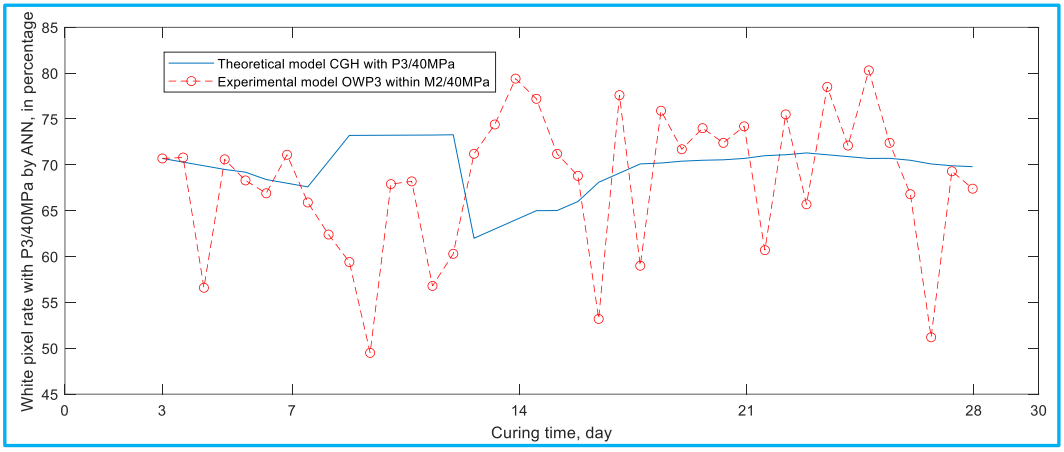

Figure 6.6: Sensitivity of the OWP3 model at scanned point P3 within M2 (40 MPa) in capturing the variation of the theoretical CGH model

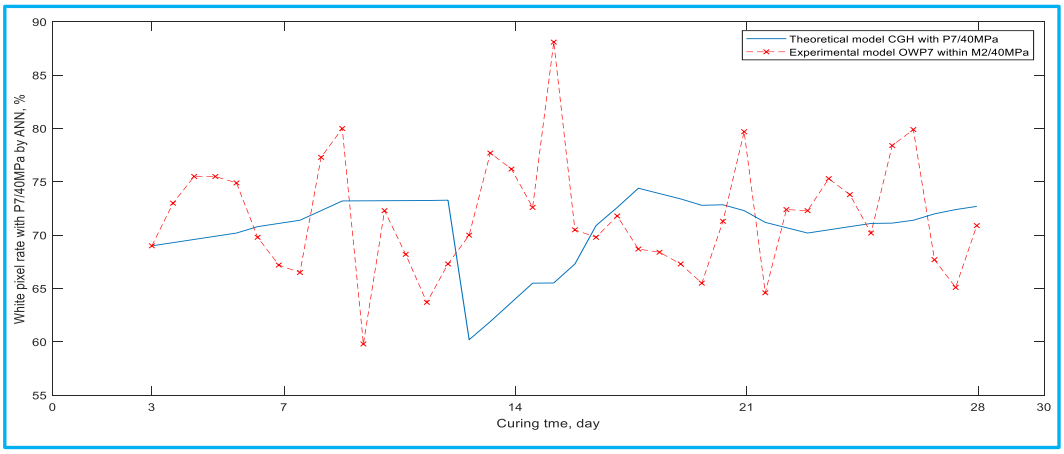

Figure 6.7: Sensitivity of the OWP7 model at scanned point P7 within M2 (40 MPa) in capturing the variation of the theoretical CGH model.

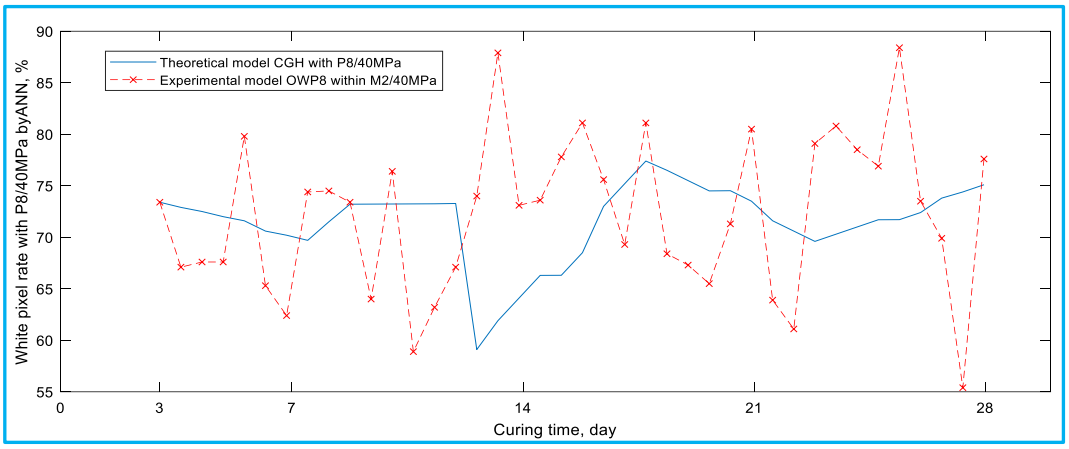

Figure 6.8: Sensitivity of the OWP8 model at scanned point P8 within M2 (40 MPa) in capturing the variation of the theoretical CGH model

Two distinct hydration regimes were identified through theoretical modelling within the CGH network (Figures 6.1 – 6.8). The first regime exhibits a descending trend between 3 and 7 days of curing, representing a retrogressive hydration phase that reaches a stagnation point at day 7 (see Figures 6.1, 6.2, 6.5, and 6.6). This is typically expressed as either a sharp crevasse or a broader depression resembling a basin or valley. Following this phase, the hydration rate increases, approaching a stabilisation plateau observed between 7 and 14 days (SN2/CGH).

The second regime shows an accelerating hydration trend over the same early period, peaking at 7 days before temporarily declining into a basin-shaped crevasse and subsequently rising again toward the stabilization plateau at the end of SN2/CGH. Image analysis in Figure 4.2 confirms that this early stagnation coincides with an increase in black pixel density and a decrease in white pixel proportion, ranging from 60 – 65% for M1/30 MPa and 55 – 60% for M2/40 MPa (see Figures 6.3, 6.4, 6.7, and 6.8).

At later stages (21 – 28 days, SN4/CGH), hydration regimes diverge, either following a descending trajectory or exhibiting accelerating dynamics. In both mixtures, scanned point cloud images show a higher density of white or light-coloured pixels in central regions, reflecting a significant increase in cement grain hydration (refer to Figures 4.4 – 4.5). Analysis of intermediate subnetworks (SN2 and SN3) reveals transitional behaviours bridging early and late hydration, providing insights into the mechanisms underlying differences between mixtures. Appendix F contains the remaining figures.

A comparison between the mixtures indicates that M2/40 MPa predominantly demonstrated retrogressive hydration across scanned points P1 – P8 during the early subnetwork (SN1, 3 – 7 days), with P7 (Figure 6.7) constituting the only exception. By contrast, M1/30 MPa exhibited a more evenly distributed behaviour, with two instances of retrogressive hydration (Figures 6.1 and 6.2) and two instances of accelerating hydration (Figures 6.3 and 6.4). This suggests that early retrogressive behaviour in M2 may result from a limited number of hydrated

cement grains at the onset of late hydration, in line with observations by Elkhadiri *et al*. (2023).

Overall, these findings highlight the influence of mix composition, curing duration, and microstructural dynamics on hydration patterns. While the CGH framework provides refined characterisation of individual hydration trajectories, it shows limitations in capturing the evolution of specific cement microstructures, such as C_3S and C_2S, over the full hydration period (3 – 28 days). To address this, Section 6.3.2 introduces a matrix-based methodology for a more detailed and quantitative assessment of late-stage hydration developments.

6.2.3 Assessment of theoretical models of cement hydration mechanisms under exposure time

As with the hydration mechanisms discussed in Section 6.2.2, the present section examines the behaviour of the theoretical corrosion models. This evaluation builds upon the same methodological principles, extending the analysis to the degradation processes induced under acidic conditions.

The following subsection therefore details the corrosion response derived from model simulations using the extracted white pixel rates. Figures 6.9 to 6.11 illustrate the sensitivity of the experimental white pixel (OWP) models in detecting local variations within the theoretical cement grain corrosion (CC) models for representative scanned points (P1, P2, and P6). The results correspond to concrete mixture M1 (30 MPa) exposed to a low sulphuric acid concentration of 30 g/ℓ, plotted as a function of corrosion time. The other figures are presented in Appendix F.

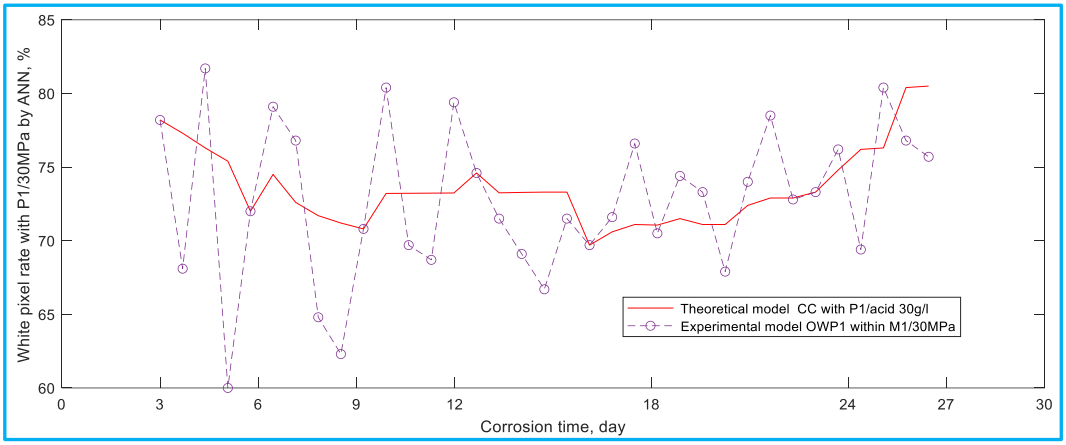

Figure 6.9: Sensitivity of the OWP1 model at scanned point P1 within M1 (30 MPa) in capturing the variation of the theoretical CC model tested to sulphuric acid concentration of 30 g/ℓ

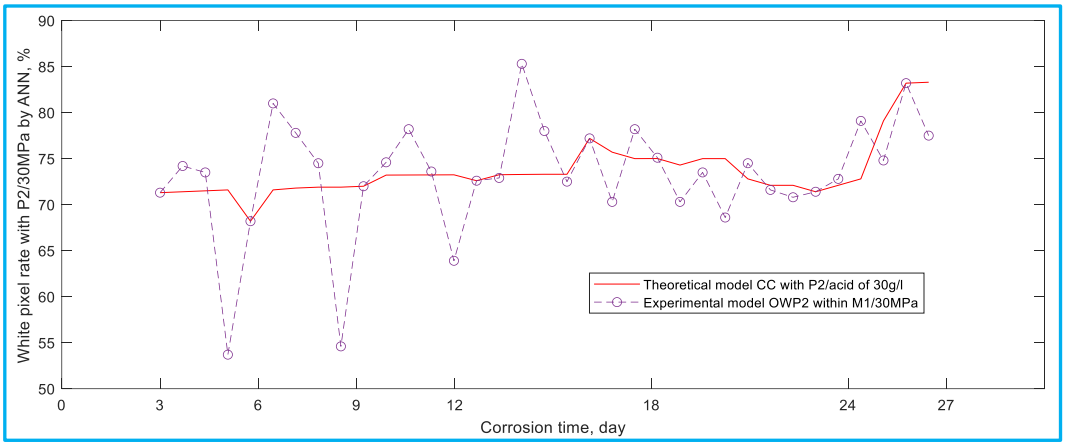

Figure 6.10: Sensitivity of the OWP2 model at scanned point P2 within M1 (30 MPa) in capturing the variation of the theoretical CC model tested to sulphuric acid concentration of 30 g/ℓ

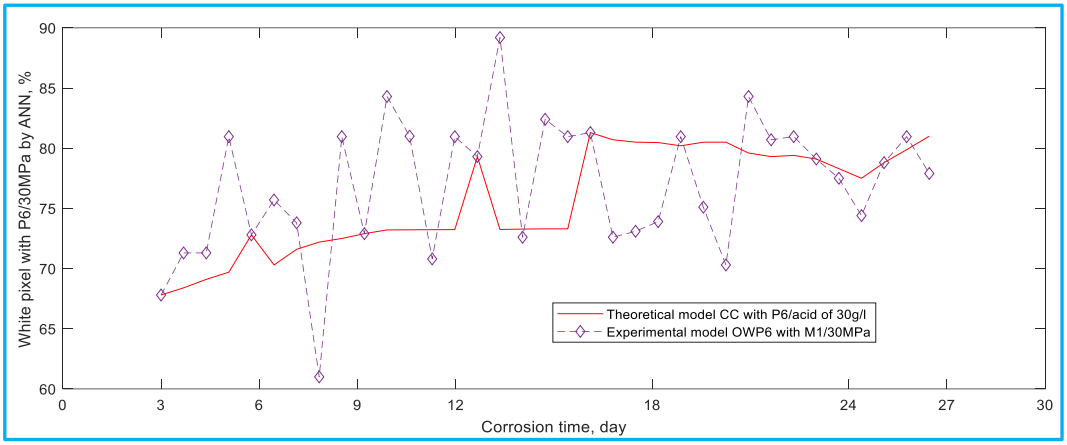

Figure 6.11: Sensitivity of the OWP6 model at scanned point P6 within M1 (30 MPa) in capturing the variation of the theoretical CC model tested to sulphuric acid concentration of 30 g/ℓ

The analysis of Figures 6.9 – 6.11 reveals three distinct corrosion regimes over the 27-day test: retrogressive, stagnant, and accelerating. The retrogressive regime shows an initial decline in corrosion activity, stabilising mid-test, while the stagnant regime maintains nearly constant rates with minor fluctuations. The accelerating regime dominates the later stages, producing the highest corrosion rates, reaching up to 90% at 27 days, primarily due to concrete swelling under sulphuric acid exposure. These regimes demonstrate clear temporal and geometric patterns, closely linked to CGC, offering insights into the mechanisms governing corrosion progression in concrete.

To summarise Section 6.2, the working hypothesis proposed that white pixel rates could serve as a reliable indicator for tracking the evolution of microstructural changes and, in turn, differentiating between hydration and corrosion regimes during their slower phases. The observed variations in white pixel rates have indeed highlighted the dominant mechanisms driving both hydration and corrosion. This finding directly supports the first research question outlined in Section 1.4 of Chapter 1.

Refining this perspective, the working hypothesis affirms that white pixel rates provide a meaningful means of assessing microstructural development and distinguishing between the regimes associated with gradual hydration and

corrosion. However, while white pixel rates offer a valuable overview of these phenomena, they remain limited in capturing the specific evolution of the key cement microstructures, C_2S and C_3S, under such slow processes.

For this reason, the next section introduces cement grain colouration features, which enable a deeper and more detailed examination of the underlying mechanisms governing hydration and corrosion.

6.3 Advanced analysis of cement grain hydration and corrosion behaviour using colouration features

This section applies the developed mathematical models to colour-image data in order to quantify the effects of hydration and corrosion on cement grains. The analysis builds upon the preceding theoretical developments and focuses on extracting meaningful trends from observable colour variations.

To achieve this, the section is organised into two parts. The first outlines the methodology employed to collect and analyse experimental data on CGH and CC, using colorimetric features as diagnostic indicators. The second presents the mathematical framework designed to convert these qualitative image characteristics into quantitative measures, thereby enabling a clearer understanding of the temporal evolution of hydration and corrosion processes through colorimetric analysis.

6.3.1 Analytical approach to cement grain hydration and corrosion using colour indicators

This study uses colour-based image data to quantify CGH and corrosion CC, building on the descriptive assessment of cement grain coloration under curing and corrosion conditions (Tables 4.1 and 4.2). A dataset of scanned points was analysed through a four-stage protocol: compiling all colour descriptors, selecting consistent and informative features, classifying them into hydration- or corrosion-

related types, and integrating these into a matrix-based framework to model the dynamic behaviour of cement grains. From this process, seven representative colour types were identified: α_1, α_2, α_3 and β_1 for curing (Table 6.5) and γ_1, γ_2 and γ_3 for corrosion (Table 6.6), systematically clustered based on visual similarity and functional correspondence within the CGC dataset (Section 4.2).

Table 6.5: Description of colours observed in CGC images during curing of concrete samples: M1 (30 MPa) and M2 (40 MPa) at 28 days

Features of colours regarding four types under curing conditions		
Type	**Description**	**View on the scan**
α1	The base layer consists of three dominant colours: pink, brown, and blue. Small light blue points are dispersed throughout the image, indicating areas of active cement hydration.	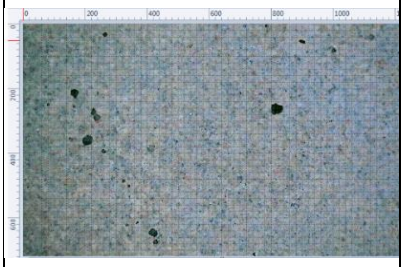
α2	The base layer presents two main colours: pink and blue. As with type α1, small light blue points are visible and serve as indicators of ongoing cement hydration	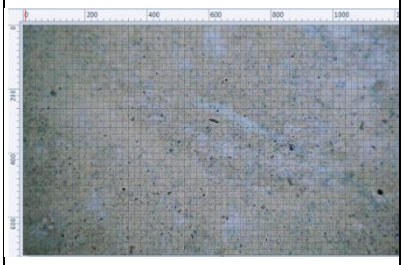
α3	The base layer is characterized by two primary colours: pink and blue. It also displays small light blue points marking zones of hydration. Additionally, the presence of faint, lake-like forms in light hues suggests localized accumulations or spatial differentiation of hydration zones.	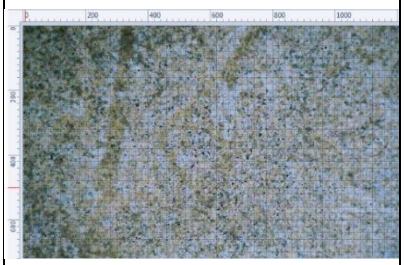

β1	The base layer combines pink, brown, and blue tones. Linear features in light pink and light blue are observed, clearly illustrating hydration progression. Furthermore, broad spectrums in light blue—resembling lake-like patterns—are visible, potentially indicating advanced stages or clustering of hydration activity	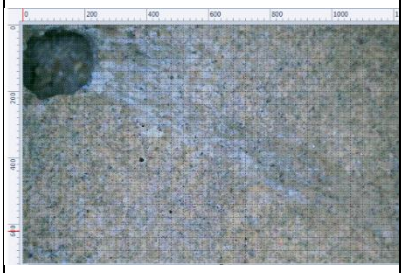

Table 6.6: Description of colours observed in CGC images during corrosion of concrete M1 (30 MPa @ 28 days) in 30 g/ℓ sulfuric acid

Features of colours regarding three types under corrosion conditions		
Type	**Description**	**View on the scan**
ɣ1	The base layer is composed of four distinct colours: dark brown, light brown, dark blue, and light blue. The areas occupied by brown and blue tones are almost equally distributed. The overall visual pattern bears a strong resemblance to a geographical map, with brown regions representing landmasses and blue areas suggesting the presence of water bodies or lakes	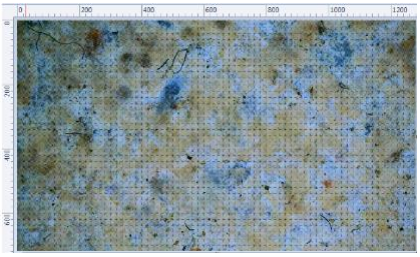
ɣ2	The base layer also includes dark and light shades of both brown and blue. However, in this case, light brown areas are more predominant than the blue ones. As with type ɣ1, the image evokes a map-like distribution, where the brown zones resemble terrestrial surfaces, and the blue tones represent aquatic regions	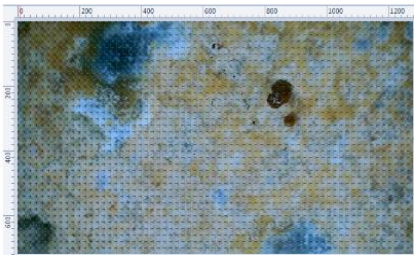

ɣ3	The base layer maintains the same four-colour scheme—dark and light brown, dark and light blue. A marked predominance of light brown areas is observed over both dark hues and blue regions. There is also a noticeable reduction in the presence of light blue tones. The visual similarity with a land–water map remains, with brown indicating the "earth" and blue reflecting diminished "lake" areas, possibly suggesting advanced corrosion or material degradation.	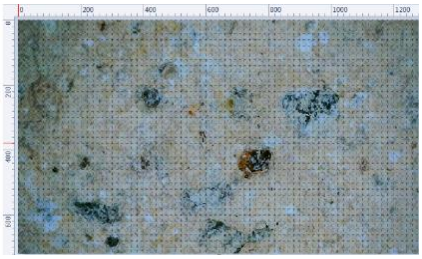

The comparison of Tables 6.5 and 6.6 reveals notable differences in the colorimetric features associated with cement grain behaviour under curing and corrosion conditions, as captured through CGC imaging (see Section 4.1, Chapter 4). These differences are indicative of the underlying physicochemical processes and can be interpreted through both spatial distribution and tonal composition.

Under curing conditions (Table 6.5), the CGC image with colour types (α1 through β1) are largely characterized by the presence of light blue points or zones, which consistently indicate ongoing hydration. The base layers typically exhibit combinations of pink, brown, and blue, with varying degrees of complexity. In more advanced curing stages (e.g., β1), broader light blue spectrums emerge, suggesting more extensive hydration activity and material structuring. The progressive appearance of lake-like formations in α3 and β1 points to localized clustering of hydrated compounds, reflecting the evolution of the microstructure.

In contrast, corrosion conditions (Table 6.6) are represented by CGC image with colour types (ɣ1 through ɣ3) featuring darker tonal ranges and a greater dominance of brown hues, particularly in the light brown spectrum. The balanced distribution of brown and blue in ɣ1 gradually shifts towards predominant brown

regions in ɣ2 and ɣ3. This evolution suggests a loss or suppression of hydration markers (light blue), replaced by colouration associated with material degradation. The cartographic resemblance noted in all three types — where brown signifies "land" and blue suggests "lakes" — serves as a visual metaphor for the shift from hydrated microstructures toward corroded and desaturated cement grains. The subsequent section details the matrix-based formulations used to correlate specific colour typologies with the temporal evolution of cement grain hydration and corrosion mechanisms.

6.3.2 Framework of mathematical expression for computing the similarity frequencies of cement grain colouration

Understanding the evolution of cement grain hydration and corrosion through colorimetric data requires both qualitative insight and a robust quantitative framework. To this end, a methodological approach was developed to analyse similarity frequencies in CGC image descriptions (SCFr_CGC), where recurring colour patterns indicate underlying physical and chemical changes in the cement matrix.

This section presents the mathematical and algorithmic foundations enabling this analysis. It details the transformation of visual data into computable formats, and introduces equations designed to detect, classify, and quantify similarity frequencies within the experimental dataset. Algorithms were used to interpret colour features accurately, while mathematical rules converted these features into binary and matrix representations for precise digital comparison.

Overall, the integrated framework of algorithms and equations allows the systematic identification and measurement of similarity frequency patterns in CGC images, providing a quantitative understanding of cement grain behaviour under both curing and corrosion conditions. The specific equations applied in this study are presented below:

$$\mathrm{SCFr_CGC}_{(\alpha 1-3,\beta 1)} = \log c\,[\frac{\sqrt[s]{k}}{S}] \quad (6.1)$$

$$\mu_{(\alpha 1-3,\beta 1)} = \log c\,[\frac{\sqrt[s]{k}}{S}] \quad (6.2)$$

$$\mathrm{SCFr_CGC}_{(\gamma 1-3)} = \log c\,[\frac{\sqrt[s]{k}}{S}] \quad (6.3)$$

$$\mu_{(\gamma 1-3)} = \log c\,[\frac{\sqrt[s]{k}}{S}] \quad (6.4)$$

From Equations (6.1) – (6.4), $\mathrm{SCFr_CGC}_{(\alpha 1\text{-}3,\ \beta 1)}$ and $\mathrm{SCFr_CGC}_{(\gamma 1\text{-}3)}$ denote the similarity-frequency determinants derived from the matrix networks used to describe the colour frequencies identified in the CGC images, with reference to Tables 6.5 and 6.6. These determinants represent the colour-frequency relationships established from the scanned images during the hydration and corrosion phases, respectively.

The terms $_{(\alpha 1\text{-}3,\ \beta 1)}$ and $_{(\gamma 1\text{-}3)}$ denote the matrix determinants used to assess the 36 scanned points (P) distributed over 4 concrete faces (f) and 3 layers (l). Their function is to convert the identified colour-frequency similarities in the CGC images into binary signals, namely 1 (positive occurrence) or 0 (non-occurrence). Within the present study, a binary value of 1 indicates the presence of a given colour similarity, whereas 0 indicates its absence. Practical examples of this conversion are provided in Equations (6.14) – (6.20).

The parameter k denotes the number of occurrences of a recurrent colour pattern, while C denotes the specific concrete composition associated with that recurrence, namely Mix 1 (M1) or Mix 2 (M2). Accordingly, Equations (6.1) – (6.4) define ($\log c$) as an algorithm for quantifying the frequency of similarity for each identified colour type according to its temporal distribution within the experimental period.

Taken together, these definitions establish the relationship between the scanned colorimetric data, their conversion into binary signals, the cumulative matrix values, and the temporal frequency of the identified colour patterns. This formulation therefore provides the mathematical basis for quantifying the

evolution of colour similarity in CGC images during the hydration and corrosion processes.

Equations (6.1) to (6.4) establish a more rigorous framework for computing colour–frequency similarities from CGC images. These equations underpin the algorithms that will later be integrated into the matrix functions used to analyse the progression of hydration and corrosion mechanisms.

For the purpose of reliably computing colour–frequency similarities using matrix functions, it is further hypothesised that the matrix equations developed for quantifying colour features can offer a more robust assessment of microstructural development, thereby distinguishing between the regimes associated with gradual hydration and corrosion. This assumption arises from the demonstrated limitations of white pixel rates, which are unable to capture the detailed evolution of the key cement microstructures, C_2S and C_3S, during slow hydration and corrosion (refer to Section 6.2).

Building on this rationale, a series of matrix equations is therefore implemented to address this challenge and provide a more precise characterisation of the underlying microstructural processes. These equations are presented below as follows:

$$M_{x1} = \begin{vmatrix} \mu\,(\alpha1,1)_{f_1,l_1} & \mu\,(\alpha1,2)_{f_1,l_1} & \mu\,(\alpha1,3)_{f_1,l_1} \\ \mu\,(\alpha2,1)_{f_1,l_1} & \mu\,(\alpha2,2)_{f_1,l_1} & \mu\,(\alpha2,3)_{f_1,l_1} \\ \mu\,(\alpha3,1)_{f_1,l_1} & \mu\,(\alpha3,2)_{f_1,l_1} & \mu\,(\alpha3,3)_{f_1,l_1} \\ \mu\,(\beta1,1)_{f_1 l_1} & \mu\,(\beta1,2)_{f_1,l_1} & \mu\,(\beta1,3)_{f_1,l_1} \end{vmatrix} \quad (6.6)$$

$$M_{x2} = \begin{vmatrix} \mu\,(\alpha1,1)_{f_2,l_1} & \mu\,(\alpha1,2)_{f_2,l_1} & \mu\,(\alpha1,3)_{f_2,l_1} \\ \mu\,(\alpha2,1)_{f_2,l_1} & \mu\,(\alpha2,2)_{f_2,l_1} & \mu\,(\alpha2,3)_{f_2,l_1} \\ \mu\,(\alpha3,1)_{f_2,l_1} & \mu\,(\alpha3,2)_{f_2,l_1} & \mu\,(\alpha3,3)_{f_2,l_1} \\ \mu\,(\beta1,1)_{f_2 l_1} & \mu\,(\beta1,2)_{f_2,l_1} & \mu\,(\beta1,3)_{f_2,l_1} \end{vmatrix} \quad (6.7)$$

$$M_{x3} = \begin{vmatrix} \mu\,(\alpha1,1)_{f_3,l_1} & \mu\,(\alpha1,2)_{f_3,l_1} & \mu\,(\alpha1,3)_{f_3,l_1} \\ \mu\,(\alpha2,1)_{f_3,l_1} & \mu\,(\alpha2,2)_{f_3,l_1} & \mu\,(\alpha2,3)_{f_3,l_1} \\ \mu\,(\alpha3,1)_{f_3,l_1} & \mu\,(\alpha3,2)_{f_3,l_1} & \mu\,(\alpha3,3)_{f_3,l_1} \\ \mu\,(\beta1,1)_{f_3,l_1} & \mu\,(\beta1,2)_{f_3,l_1} & \mu\,(\beta1,3)_{f_3,l_1} \end{vmatrix} \quad (6.8)$$

$$M_{x4} = \begin{vmatrix} \mu\,(\alpha 1,1)_{f_4,l_1} & \mu\,(\alpha 1,2)_{f_4,l_1} & \mu\,(\alpha 1,3)_{f_4,l_1} \\ \mu\,(\alpha 2,1)_{f_4,l_1} & \mu\,(\alpha 2,2)_{f_4,l_1} & \mu\,(\alpha 2,3)_{f_4,l_1} \\ \mu\,(\alpha 3,1)_{f_4,l_1} & \mu\,(\alpha 3,2)_{f_4,l_1} & \mu\,(\alpha 3,3)_{f_4,l_1} \\ \mu\,(\beta 1,1)_{f_4,l_1} & \mu\,(\beta 1,2)_{f_4,l_1} & \mu\,(\beta 1,3)_{f_4,l_1} \end{vmatrix} \quad (6.9)$$

Each of the four matrices derived from Equations (6.6) – (6.9) comprises three columns and four rows, within which the matrix-based algorithms (MBA) encode the experimental data describing the colour-frequency similarities observed in the CGC images. Within this initial range, $\mu\,(\alpha 1,1)_{f_1,l_1}$; $\mu\,(\alpha 1,2)_{f_1,l_1}$; and $\mu\,(\alpha 1,3)_{f_1,l_1}$ denote the α_1 colour-frequency similarities identified in the CGC images, corresponding respectively to points P1, P2, and P3 on face 1 (f_1) within layer 1 (l_1) (Equation 6.6). The three columns therefore provide a structured numerical space for encoding the experimental behaviour of the four colour types, α1, α2, α3 and β1, in accordance with the analytical treatment developed throughout this chapter.

Additional equations of comparable formulation, established to compute the colour-frequency similarities in CGC images under corrosion conditions, are also implemented. These equations support the gradual transition from the hydration-dominated regime to the corrosion-dominated regime, enabling a more refined assessment of how colour patterns evolve within the CGC structure. Three examples representative of this extended framework are presented below:

$$M_{x5} = \begin{vmatrix} \mu\,(\gamma 1,1)_{f_1,l_1} & \mu\,(\gamma 1,2)_{f_1,l_1} & \mu\,(\gamma 1,3)_{f_1,l_1} \\ \mu\,(\gamma 2,1)_{f_1,l_1} & \mu\,(\gamma 2,2)_{f_1,l_1} & \mu\,(\gamma 2,3)_{f_1,l_1} \\ \mu\,(\gamma 3,1)_{f_1,l_1} & \mu\,(\gamma 3,2)_{f_1,l_1} & \mu\,(\gamma 3,3)_{f_1,l_1} \end{vmatrix} \quad (6.10)$$

$$M_{x6} = \begin{vmatrix} \mu\,(\gamma 1,1)_{f_2,l_1} & \mu\,(\gamma 1,2)_{f_2,l_1} & \mu\,(\gamma 1,3)_{f_2,l_1} \\ \mu\,(\gamma 2,1)_{f_2,l_1} & \mu\,(\gamma 2,2)_{f_2,l_1} & \mu\,(\gamma 2,3)_{f_2,l_1} \\ \mu\,(\gamma 3,1)_{f_2,l_1} & \mu\,(\gamma 3,2)_{f_2,l_1} & \mu\,(\gamma 3,3)_{f_2,l_1} \end{vmatrix} \quad (6.11)$$

$$M_{x7} = \begin{vmatrix} \mu\,(\gamma 1,1)_{f_3,l_1} & \mu\,(\gamma 1,2)_{f_3,l_1} & \mu\,(\gamma 1,3)_{f_3,l_1} \\ \mu\,(\gamma 2,1)_{f_3,l_1} & \mu\,(\gamma 2,2)_{f_3,l_1} & \mu\,(\gamma 2,3)_{f_3,l_1} \\ \mu\,(\gamma 3,1)_{f_3,l_1} & \mu\,(\gamma 3,2)_{f_3,l_1} & \mu\,(\gamma 3,3)_{f_3,l_1} \end{vmatrix} \quad (6.12)$$

$$M_{x8} = \begin{vmatrix} \mu\,(\gamma 1,1)_{f_4,l_1} & \mu\,(\gamma 1,2)_{f_4,l_1} & \mu\,(\gamma 1,3)_{f_4,l_1} \\ \mu\,(\gamma 2,1)_{f_4,l_1} & \mu\,(\gamma 2,2)_{f_4,l_1} & \mu\,(\gamma 2,3)_{f_4,l_1} \\ \mu\,(\gamma 3,1)_{f_4,l_1} & \mu\,(\gamma 3,2)_{f_4,l_1} & \mu\,(\gamma 3,3)_{f_4,l_1} \end{vmatrix} \quad (6.13)$$

In Equations (6.10) to (6.13), four matrix algorithms are applied to three points (P1, P2, P3) located in layer 1 of faces 1, 2, 3, and 4. Supplementary equations involving six further points (P4 to P9), which expand the spatial resolution of the analysis, are presented in Appendix E.

By computing Equations (6.10) – (6.13) individually using a Microsoft® Excel® spreadsheet, the MBA outputs for the colour-frequency similarities in the CGC images are obtained as binary values through matrix Equations (6.14) to (6.20). As described previously (see Equations 6.1 to 6.4), these binary outputs constitute the logical variables used to track the emergence or absence of colour transitions, expressed through binary signals of 1 (positive) or 0 (empty). Within the context of Chapter 6, these signals characterise the structural response of the CGC material, where hydration and corrosion processes are assessed through shifts in colour-feature frequency. The following Equations illustrate the response of binary signals with regards to both processes.

$$M_{x1} = \begin{vmatrix} 1 & 1 & 1 \\ 0 & 0 & 0 \\ 0 & 0 & 0 \\ 0 & 0 & 0 \end{vmatrix} \quad (6.14)$$

$$M_{x2} = \begin{vmatrix} 1 & 0 & 1 \\ 0 & 0 & 0 \\ 0 & 1 & 0 \\ 0 & 0 & 0 \end{vmatrix} \quad (6.15)$$

$$M_{x3} = \begin{vmatrix} 1 & 1 & 1 \\ 0 & 0 & 0 \\ 0 & 0 & 0 \\ 0 & 0 & 0 \end{vmatrix} \quad (6.16)$$

$$M_{x4} = \begin{vmatrix} 0 & 0 & 0 \\ 1 & 1 & 1 \\ 0 & 0 & 0 \\ 0 & 0 & 0 \end{vmatrix} \quad (6.17)$$

$$M_{x5} = \begin{vmatrix} 1 & 0 & 0 \\ 0 & 1 & 1 \\ 0 & 0 & 0 \end{vmatrix} \quad (6.18)$$

$$M_{x6} = \begin{vmatrix} 1 & 1 & 1 \\ 0 & 0 & 0 \\ 0 & 0 & 0 \end{vmatrix} \quad (6.19)$$

$$M_{x7} = \begin{vmatrix} 1 & 1 & 1 \\ 0 & 0 & 0 \\ 0 & 0 & 0 \end{vmatrix} \quad (6.20)$$

Equations (6.14) to (6.20) present the binary frequency values of colour similarity (α_1–α_3 to β_1) and (γ_1 to γ_3) derived from CGC images captured after three days under both curing and corrosion conditions. These scenarios correspond to the four faces of M1 concrete (30 MPa). On Face 1, similarity frequencies are predominantly positive for colour type α_1 across the nine scanned points (Equations 6.14 – 6.17), while a lower frequency of α_2 is observed on Face 2. Conversely, Equations (6.18) to (6.20) summarise the binary similarity values obtained from CGC images captured after three days of corrosion exposure for M1 / 30 MPa concrete. The preliminary data indicate a dominant presence of colour type γ_1 across all nine scanned points on the four faces of the specimen.

The data structured through Equations (6.14) to (6.17) provide an initial characterisation of hydration behaviour, while the extended matrix formulations in Appendix E offer comparative insights for longer curing periods (7 to 28 days). Binary frequency distributions of colour similarity for γ_1 to γ_3 under corrosion exposure are also presented in Appendix D.

To support the development of mathematical models assessing the evolution of cement microstructures under curing and corrosion conditions, numerical values of the colour-similarity frequencies for the four curing-related categories (α_1, α_2, α_3, β_1) and the three corrosion-related categories ($\gamma_1 - \gamma_3$) were computed using an Excel spreadsheet (see Tables 6.7 – 6.12). These values represent the cumulative dataset derived from 72 scanned points distributed across the eight faces of the M1/30 MPa concrete cubes under curing conditions, and from 36 scanned points collected across the four faces under corrosion exposure. The corresponding

dataset for the 72 scanned points recorded on the eight faces of the M2 / 40 MPa specimens is presented in Appendix E.

Tables 6.7 to 6.9 present a selection of the computed results for the colour-similarity frequencies under curing conditions at 3, 7, and 28 days.

Table 6.7: Colour frequency similarity values associated with CGH on Faces 1 – 8 after 3 days of curing (M1 / 30 MPa)

Reference to layers of concrete cubes	**Rate of cement grain hydration within CGC images at 3 days, in percentage**			
	α1	**α2**	**α3**	**β1**
L_1	18.06	8.33	6.94	0.00
L_2	27.78	4.17	1.39	0.00
L_3	23.61	4.17	5.56	0.00

Table 6.8: Colour frequency similarity values associated with CGH on Faces 1 – 8 after 14 days of curing (M1 / 30 MPa)

Reference to layers of concrete cubes	**Rate of cement grain hydration within CGC images at 14 days, in percentage**			
	α1	**α2**	**α3**	**β1**
L_1	15.28	1.39	0.00	16.67
L_2	29.17	0.00	0.00	4.17
L_3	16.67	1.39	0.00	15.28

Table 6.9: Colour frequency similarity values associated with CGH on Faces 1 – 8 after 28 days of curing (M1 / 30 MPa)

Reference to layers of concrete cubes	**Rate of cement grain hydration within CGC images at 28 days, in percentage**			
	α1	α2	α3	β1
L_1	0.00	0.00	25.00	8.33
L_2	4.17	1.39	26.39	1.39
L_3	4.17	0.00	20.83	8.33

Table 6.10: Colour frequency similarity values associated with CC on Faces 1 – 4 after 3 days of exposure

Reference to layers of concrete cubes	Rate of cement grain corrosion within CGC images at 3 days, in percentage		
	ɣ1	**ɣ2**	**ɣ3**
L_1	16.67	16.67	0.00
L_2	30.56	2.78	0.00
L_3	19.44	2.78	11.11

Table 6.11: Colour frequency similarity values associated with CC on Faces 1 – 4 after 12 days of exposure

Reference to layers of concrete cubes	Rate of cement grain corrosion within CGC images at 12 days, in percentage		
	ɣ1	**ɣ2**	**ɣ3**
L_1	8.33	8.33	16.67
L_2	2.78	0.00	30.56
L_3	2.78	0.00	30.56

Table 6.12: Colour frequency similarity values associated with CC on Faces 1 – 4 after 27 days of exposure

Reference to layers of concrete cubes	Rate of cement grain corrosion within CGC images at 27 days, in percentage		
	ɣ1	**ɣ2**	**ɣ3**
L_1	2.78	0.00	30.56
L_2	0.00	0.00	33.33
L_3	0.00	0.00	33.33

The preliminary findings reported in Tables 6.7 – 6.9 for concrete mixture M1 (30 MPa) reveal a clear predominance of colour type α_1 in terms of similarity

frequency. Although α_1 remains the dominant category throughout the early curing stage, its frequency progressively decreases from 69.44% at 3 days to 61.11% at 14 days, relative to α_2, α_3, and β_1. Colour type α_2 follows a similar downward trajectory over the same period, declining from 16.67% to 2.78%, albeit at significantly lower levels. In contrast, between 14 and 28 days of curing, α_3 and β_1 exhibit a pronounced increase in frequency, indicating a transition in the microstructural configuration as hydration progresses.

Under corrosion conditions (Tables 6.10 – 6.12), a distinct behavioural shift is observed. At 3 days of exposure, γ_1 predominates (19.44%) compared with γ_2 (2.78%) and γ_3 (11.11%) across the nine scanned points distributed over the four specimen faces. However, by 27 days of corrosion, the distribution pattern changes substantially: γ_3 rises sharply to 33.33%, while γ_1 and γ_2 decrease to 0%.

This marked predominance of γ_3 at the advanced stage of corrosion likely reflects intensified corrosive activity and associated material degradation, consistent with the observations summarised in Table 6.6.

The matrices presented in Tables 6.7 to 6.12 form the numerical foundation for analysing both the spatial and temporal variations in cement grain behaviour under hydration and corrosion conditions. They allow for the quantification of colour-frequency similarities across the specimen faces and reveal the progression of microstructural changes over time. In Section 6.3.3, these matrices are employed in preliminary mathematical models to examine the evolution of hydration efficiency and the propagation of corrosion as functions of CGC.

Integrating algorithm-based equations for frequency-pattern recognition in CGC images enables a precise quantification of microstructural development. This matrix-driven approach ensures a consistent transition from descriptive colour data to numerical analysis, providing a solid basis for advanced modelling of cement hydration and corrosion processes. Furthermore, the results support the hypothesis that the matrix equations developed for quantifying colour features

offer a reliable assessment of microstructural evolution, effectively distinguishing between regimes of gradual hydration and corrosion.

6.3.3 Quantitative modelling of cement hydration and corrosion using colour similarity matrices

This section presents a mathematical modelling framework for cement hydration and corrosion, developed through the analysis of colour similarity matrices extracted from CGC images (see Equations 6.6 – 6.20 and Tables 6.7 – 6.12).

For the purpose of modelling, the numerical values of GCH (Tables 6.7 to 6.12) were plotted using MATLAB R2022b. This procedure enabled the generation of mathematical models describing cement grain hydration as a function of cement grain colouration, providing a quantitative representation of microstructural evolution under both curing and corrosion conditions. Figures 6.12 to 6.15 illustrate the modelled responses of colour-frequency patterns in hydrated cement grains (M1 / 30 MPa), with particular reference to colour types α_1, α_2, α_3, and β_1.

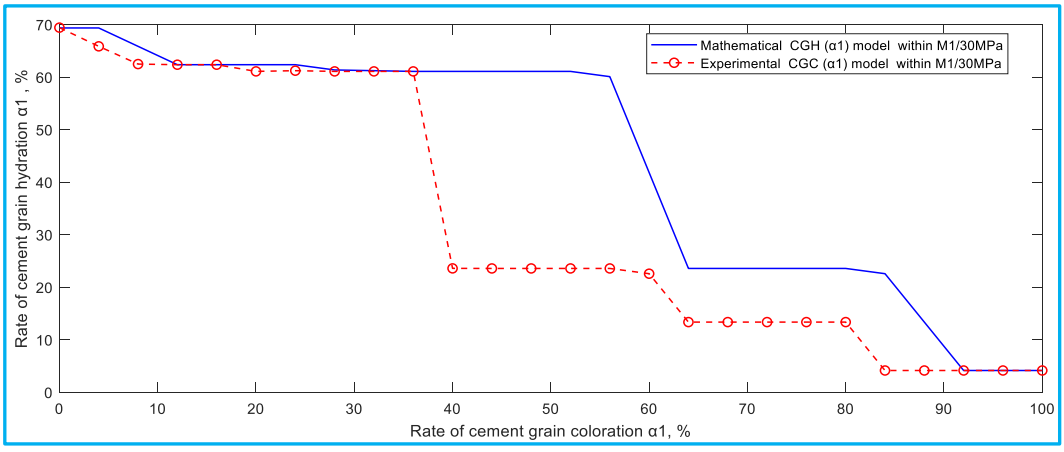

Figure 6.12: Modelling of α1-type colour frequency patterns in hydrated cement grains (M1 / 30 MPa)

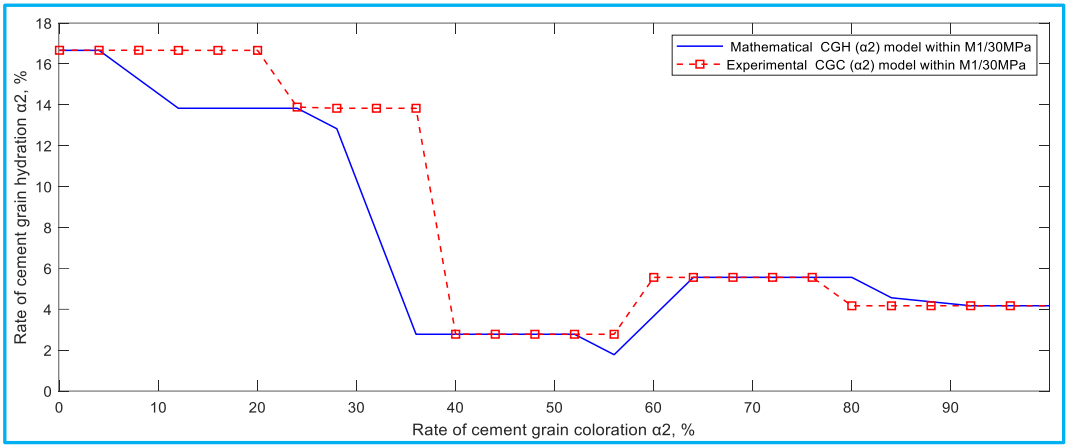

Figure 6.13: Modelling of α2-type colour frequency patterns in hydrated cement grains (M1 / 30 MPa)

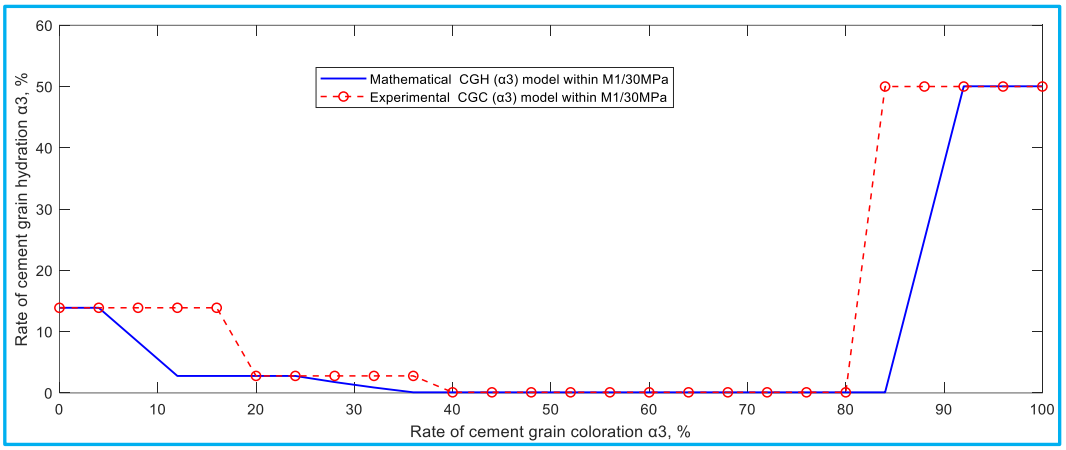

Figure 6.14: Modelling of α3-type colour frequency patterns in hydrated cement grains (M1 / 30 MPa)

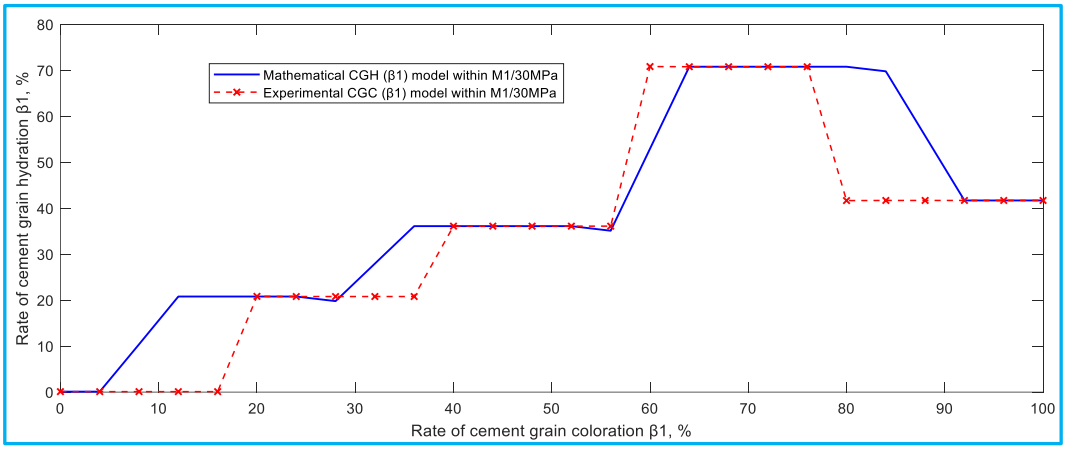

Figure 6.15: Modelling of β_1-type colour frequency patterns in hydrated cement grains (M1 / 30 MPa)

Figures 6.12 to 6.15 show the experimental cement grain coloration models (α1 to β1) developed for M1 (30 MPa), design to follow the evolution of CGH within colour frequency distributions (CFD). As discussed earlier in Section 6.2.2, and in alignment with the observations from the experimental white pixel (OWP) model, the colouration models reveal two main hydration regimes — retrogressive and accelerating — also observed in the theoretical CGH model.

Figures 6.12 and 6.13 highlight two distinct retrogressive regimes associated with the cement grain colouration types α1 and α2. In Figure 6.12, the α1 coloration reflects a high-entry retrogressive regime, with the hydration rate reaching up to 70%, indicating substantial integration into the CGH network. In contrast, Figure 6.13 shows a low-entry retrogressive regime, where the α2 hydration rate remains between 16% and 18%, suggesting more limited CGH activity.

For the α1 regime (Figure 6.12), the descending hydration trajectory eventually reaches a stagnation plateau where cement grain colouration peaks between 90% and 100%, while hydration levels fall to 0 – 10%. Conversely, in the α2 regime (Figure 6.13). The stagnation plateau presents a trough, with colouration values between 50% and 60% for hydration rates as low as 0 – 2%. These two regimes are visually distinguished by their respective colour features (α1 and α2) both marked by the presence of small light blue points—interpreted as indicators of ongoing hydration (see Table 6.5).

Figures 6.14 and 6.15, by comparison, introduce two additional hydration regimes associated with colour types α3 and β1. Figure 6.14 represents a retrogressive regime with a low initial hydration rate (10 – 20%), where the trajectory stagnates with colouration values ranging from 30% to 90%, despite CGH rates remaining at 0%. In contrast, Figure 6.15 illustrates an accelerating hydration regime governed by the β1 coloration model. This regime is characterized by the lowest initial CGH level observed (0%) and suggests a transition toward increasing hydration activity — marking a clear departure from the retrogressive patterns described earlier. In this second case, the hydration trajectory follows a stepwise upward pattern and reaches a high stagnation plateau, with a cement grain colouration (β1) rate

between 60% and 90%, corresponding to a cement grain hydration (β1) rate ranging from 70% to 80%.

Despite the differences between retrogressive and accelerating regimes, both types of cement grain hydration (α3 and β1) share a common feature: a predominance of light blue colourations indicating zones that suggest advanced stages of hydration activity (see Table 6.5).

Figures 6.16 – 6.19 extend the analysis of cement grain hydration dynamics to M2 (40 MPa), allowing for a comparative assessment of the same phenomena observed previously in M1.

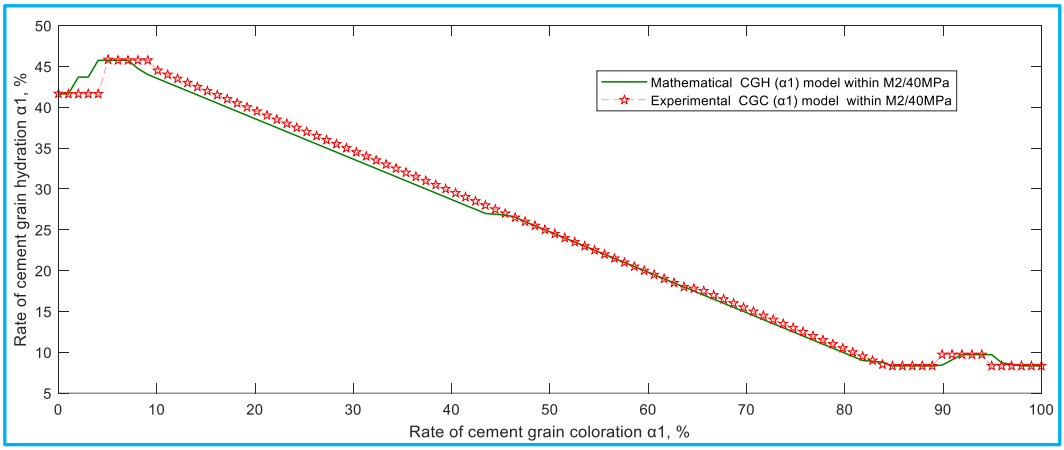

Figure 6.16: Modelling of α1-type colour frequency patterns in hydrated cement grains (M2 / 40 MPa)

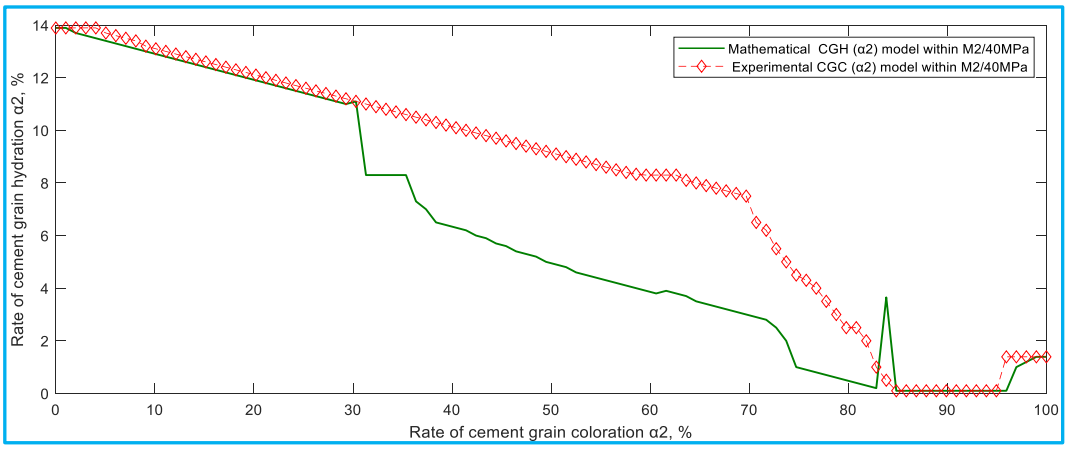

Figure 6.17: Modelling of α2-type colour frequency patterns in hydrated cement grains (M2 / 40 MPa)

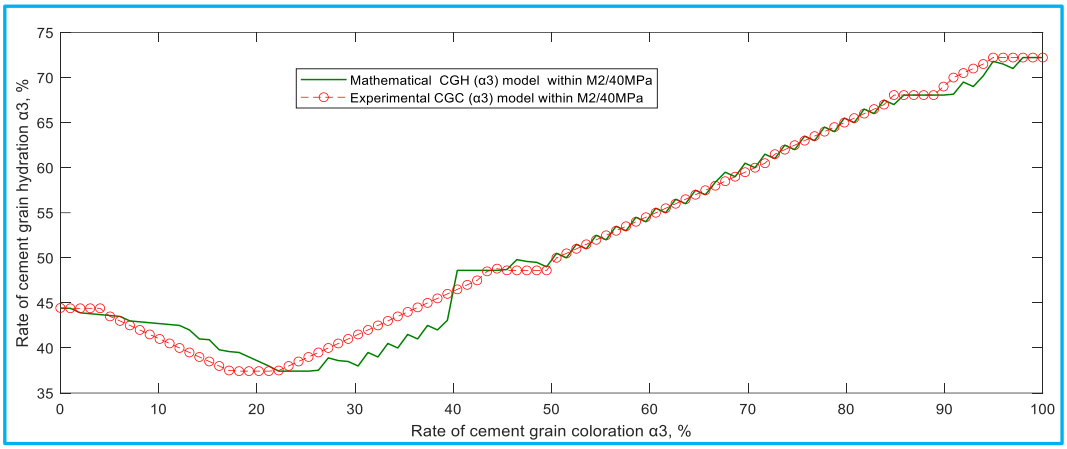

Figure 6.18: Modelling of α3-type colour frequency patterns in hydrated cement grains (M2 / 40 MPa)

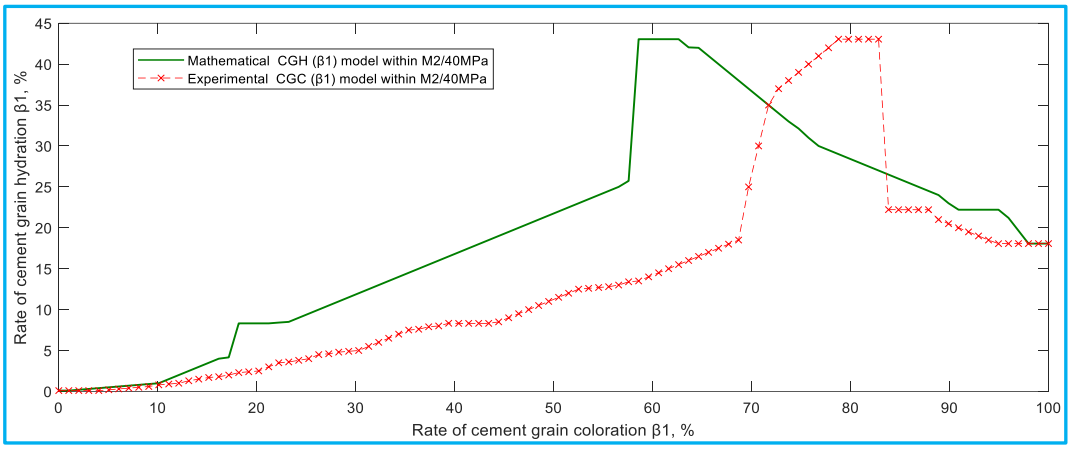

Figure 6.19: Modelling of β1-type colour frequency patterns in hydrated cement grains (M2 / 40 MPa)

Figures 6.16 – 6.19 present the experimental cement grain colouration models (α1 to β1) developed for M2 (40 MPa), aimed at tracing the evolution of CGH. Two distinct retrogressive regimes are identified: an accelerating regime characterized by coloration type α1 (Figure 6.16) and a decelerating regime represented by colouration type α2 (Figure 6.17).

In Figure 6.16, the accelerating regime exhibits a rapid step-like entry, reaching a small stagnation plateau at a high hydration level ranging between 45% and 60% CGH, corresponding to a low cement grain colouration (α1) rate of 0 – 10%. Subsequently, the hydration trajectory descends along a slope and reaches a lower stagnation plateau between 80% and 90% CGC, while hydration levels drop to 5 –

10%. The trajectory then makes a final upward movement toward a small plateau similar to that observed at the entry point, before returning to a stable trajectory with 5 – 10% CGH for a cement grain colouration rate of 100% (see Figure 6.16).

In contrast, Figure 6.17 — governed by hydration type α2 — does not display the two small stagnation plateaus observed at the entry and exit points of the CGH network. Here, the CGH (α2) entry occurs at a rate of 12%, following a retrogressive regime that immediately adopts a descending trajectory, conversely to the stepwise entry seen in CGH (α1) (Figure 6.16). This trajectory first encounters a trough, or depression, where the cement grain colouration (α2) rate ranges between 80% and 90%. It then rises briefly to form a sharp peak, culminating at 4% CGH, before dropping again into the final stagnation plateau at the exit, with 0% CGH corresponding to a CGC rate (α2) between 85% and 95%.

Figures 6.18 and 6.19 illustrate the cases related to hydration models of types α3 and β1 for M2 (40 MPa). As observed with hydration types α1 and α2, both retrogressive (α3) and accelerating (β1) regimes are also identified here, respectively in Figures 6.18 and 6.19. The CGH (α3) entry occurs at a hydration rate of 45%, after which the trajectory descends to approximately 37.5% into a stagnation basin characterized by a jagged bottom, where the CGC ranges between 20% and 40%. The trajectory then climbs to a plateau around 47.5% hydration and continues with a sawtooth pattern until it exits the CGH network — at the end of the test — at around 73% hydration rate.

The analysis reveals two contrasting hydration entry behaviours. Types α1 and α2 demonstrate a strong entry response, with α1 reaching 70% in M1 (30 MPa), whereas M2 (40 MPa) records substantially lower values of 40 – 45%. Conversely, α3 and β1 exhibit minimal entry activity, with β1 remaining at 0% across both mixtures. These results establish an inverse dependence between mix strength and initial CGH entry rate at 3 days. They also confirm that M2 follows hydration regimes comparable to M1, while presenting nuanced differences in early hydration dynamics and stagnation patterns. Collectively, the data highlight two distinct entry profiles shaped by mix composition and the functional contributions

of the C_3S and C_2S phases. Building on these hydration observations, the modelling approach for cement corrosion was evaluated using a similar analytical framework.

The outcomes of these analyses, in which a 30 MPa concrete mixture was tested to a low concentrated sulphuric acid solution at 30 g/ℓ, are illustrated in Figures 6.20 to 6.22.

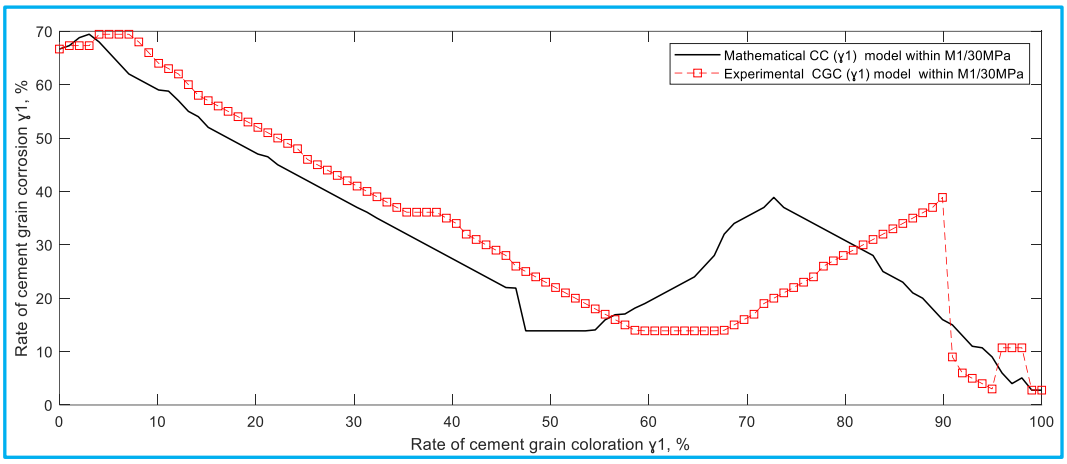

Figure 6.20: Modelling of γ1-type colour frequency patterns in corroded cement grains (M1 / 30 MPa) with a sulphuric acid concentration of 30 g/ℓ

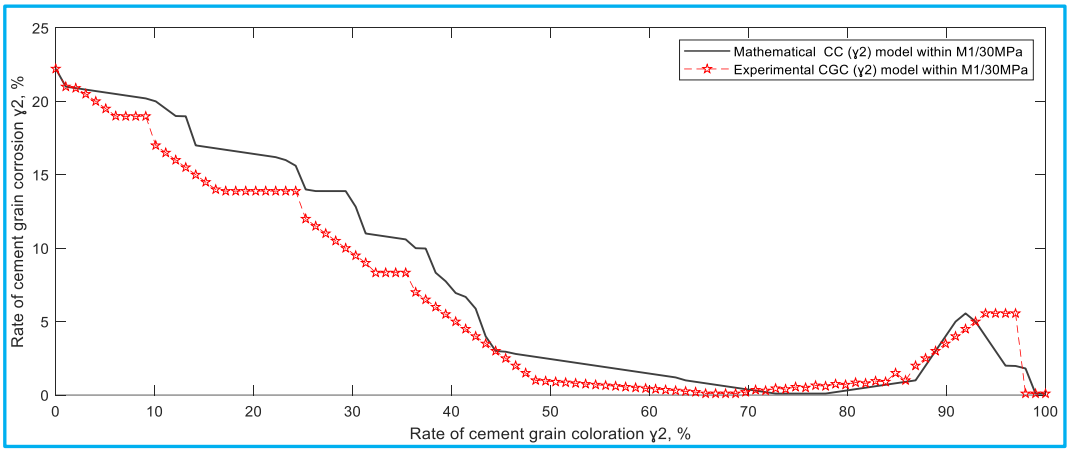

Figure 6.21: Modelling of γ2-type colour frequency patterns in corroded cement grains (M1 / 30 MPa) with a sulphuric acid concentration of 30 g/ℓ

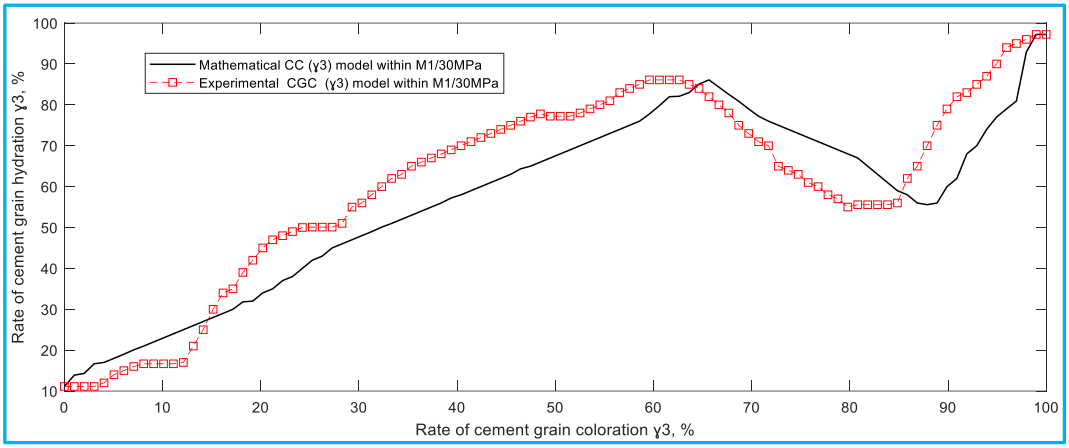

Figure 6.22: Modelling of ɣ3-type colour frequency patterns in corroded cement grains (M1 / 30 MPa) with a sulphuric acid concentration of 30 g/ℓ

Figures 6.20 to 6.22 present the experimental CGC models (ɣ1 to ɣ3) developed for M1 (30 MPa), focusing to capture the evolution of the mathematical CC model as expressed through the colour features detailed in Table 6.6. Within this framework, three distinct scenarios are identified:

In the first scenario, illustrated in Figure 6.20, the system follows an accelerating regime. The CC process begins with an entry rate of approximately 67.5%, rapidly climbing to a peak around 70%, corresponding to a CGC (ɣ1) rate ranging between 0% and 10%. Following this initial surge, the trajectory enters a descending phase, settling into a stagnation plateau where the CC rate ranges from 10% to 20%, with CGC (ɣ1) increasing to between 45% and 55%. A subsequent upward surge is observed, forming a pronounced peak — reminiscent of a mountain summit — at a CC rate of about 35%, associated with a CGC (ɣ1) rate of approximately 73%. This is followed by a final descent towards the end of the corrosion process, concluding at a CC rate of around 3% and a CGC (ɣ1) of 100%. In this case, the progression of the corrosion rate appears significantly influenced by CGC features, whereas the brown and blue colour zones — indicative of corrosion and hydration processes, respectively — are nearly evenly distributed (see Table 6.5).

The second scenario, depicted in Figure 6.21, corresponds to a retrogressive regime. Here, the corrosion process (ɣ2) begins at an entry rate of 20% to 25%, then rapidly declines into a broad stagnation basin, where the CC rate drops to 0%

while the CGC (ɣ2) reaches 75%. A minor resurgence follows, forming a modest peak at around 6%, before the trajectory ultimately returns to a 0% CC rate. This phase is predominantly characterized by light brown colouration, indicating a stronger corrosion presence relative to hydration, as further supported by the data in Table 6.6.

The third and final scenario, shown in Figure 6.22, also follows an accelerating regime but begins with a notably low entry into the corrosion process. The CC trajectory rises steadily, reaching a substantial peak at approximately 88%, in correspondence with CGC (ɣ3) values between 60% and 70%. This is followed by a descent into a stagnation plateau around 53% CC, associated with CGC values between 80% and 90%. The trajectory then ascends sharply once more, reaching a final outlet phase characterized by CC rates between 90% and 100%. In this case, there is a marked dominance of light brown colour tones over both dark and blue hues, with a notable decline in light blue regions. These colour characteristics point toward an advanced stage of cement grain corrosion (see Table 6.6).

The analysis of CC models ɣ1 through ɣ3, developed for M1 (30 MPa) and tested under low-concentration sulphuric acid solutions (30 g/ℓ), reveals three distinct corrosion behaviours that reflect the complex interplay between hydration and corrosion processes within the cement matrix. The first scenario illustrates a dynamic, multi-phase evolution of corrosion, strongly influenced by a balance between hydration and corrosion zones. By contrast, the second scenario highlights a retrogressive regime characterized by early stagnation and limited reactivity, predominantly governed by corrosion. The third scenario demonstrates an advanced and aggressive corrosion pathway, culminating in high final corrosion levels and a marked predominance of degradation indicators.

These findings align with Taheri *et al.* (2020), who investigated colour variations within corroded layers of both mortar and concrete matrices exposed to low-concentration sulphuric acid solutions (pH 1 and 0.25). Using image scanning analysis, the authors attributed the observed discoloration — red and blue tones — to the presence of distinct ions: calcium ions responsible for blue hues and

sulphur ions for red ones (see Section 2.3.2, Chapter 2). This evidence supports the second scenario described in the present study, particularly the observed colorimetric balance between brown and blue regions, which reflects the coexistence and interaction of hydration and corrosion fronts.

In summary, the comparison of the CGH and CC models confirms that colorimetric patterns provide a clearer distinction between hydration and corrosion regimes than white pixel rates. Their sensitivity to variations linked to C_2S and C_3S development makes CGC a more powerful diagnostic tool for tracking cement microstructural changes. These findings validate the working hypothesis that matrix equations based on colour features offer a more reliable assessment of gradual hydration and corrosion processes.

6.4 Concluding remarks

The mathematical formulations applied throughout this chapter effectively characterised hydration and corrosion regimes using both white pixel rates and colorimetric indicators. The enhanced performance of the colorimetric method stems from matrix equations that quantify colour features with greater sensitivity to microstructural evolution under slow hydration and corrosion. Furthermore, the successful application of these matrix equations in modelling the intricate behaviour of C_2S and C_3S microstructures validates the hypothesis regarding their capacity to address complex analytical challenges.

The results reveal two main hydration regimes, distinguished by their coloration ranges. The accelerating regime (α1) shows sharp entry, low coloration (0 – 10%), and high early CGH (45 – 60%), followed by a descent into high-coloration plateaus (80 – 90%). The decelerating regime (α2) exhibits a smoother decline, marked by troughs at 80 – 90% coloration and an exit at 0% CGH with 85 – 95% CGC. In concrete mixture M2, types α3 and β1 display similar retrogressive and accelerating patterns, with α3 in the range 37.5 – 47.5% hydration and coloration between 20% and 40%, before exiting at around 73% hydration.

Across the three CC scenarios (ɣ1 – ɣ3), corrosion behaviour separates into clear accelerating and retrogressive regimes, each defined by specific coloration ranges. Scenario ɣ1 shows an accelerating regime, with colouration rising from 0 – 10% to full brown (100%) as CC progresses from ~70% to 3%. Scenario ɣ2 presents a retrogressive regime, where CC declines from 20–25% to 0% while coloration intensifies to ~75%, dominated by light brown tones. Scenario ɣ3 follows an accelerating pattern, peaking at ~88% CC with 60 – 70% CGC, then, stabilising around 53% CC with 80 – 90% CGC before ending in a highly corroded light-brown state (90 – 100% CC). Overall, each regime is characterised by a coherent interplay between CC level, CGC intensity, and the transition from low to high brown coloration.

In conclusion, the chapter demonstrates that matrix-based colorimetric analysis provides a precise and reliable tool for distinguishing hydration and corrosion regimes. By linking colour features to microstructural evolution, it offers a robust framework for understanding and predicting the progressive behaviour of cement microstructures under slow hydration and corrosion.

CHAPTER 7: EVALUATION OF CEMENT MICROSTRUCTURES DURING THE SLOW HYDRATION PHASE

7.1 Introduction

This chapter develops a framework for understanding and predicting the progressive behaviour of cement microstructures, specifically C_3S and C_2S, during the slow hydration phase. It addresses the research questions posed in Section 1.4 of Chapter 1: what are the predominant hydration and corrosion regimes during the slow phases, and how does the concrete mix design influence the progression of microstructural changes and the dominant hydration regimes.

The chapter is organised into two main sections. The first focuses on modelling cement grain hydration governed by C_3S and C_2S microstructures, based on the colorimetric analysis presented in Chapter 6. The second examines the hydration mechanisms of these microstructures and their impact on concrete performance. Using mathematical modelling, this section evaluates how the distinct behaviours of C_3S and C_2S affect the evolution of mechanical strength and thermal response, providing predictive insight into their contributions to the performance of cementitious materials under curing conditions.

Building upon this framework, the following sections present the quantitative modelling of cement hydration and corrosion using colour similarity matrices. The analysis draws on the experimental data and matrix-based computations detailed in Chapter 6, enabling a systematic evaluation of microstructural evolution and the distinct contributions of C_3S and C_2S during the slow hydration phase.

7.2 Development of cement grain hydration mechanisms governed by C_3S and C_2S microstructures during the slow hydration phase

As reviewed in Section 2.2.2 of Chapter 2, it is well established that two primary cement microstructures, C_3S and C_2S, govern the hydration dynamics of cement grains during the slow hydration phase (Bye, 1999; Jansen *et al*., 2012; Qi *et al*., 2022; Elkhadiri *et al*., 2023; Huang *et al*., 2025). This understanding underscores the importance of modelling their behaviour under low-reactivity conditions to gain deeper insight into the progression of cement hydration. The research further demonstrates that matrix-based colorimetric analysis provides a precise and reliable method for distinguishing between hydration and corrosion regimes. By correlating colour features with microstructural evolution, this approach establishes a robust framework for predicting the progressive behaviour of cement microstructures under slow hydration.

The next two sections each address one aspect of the modelling framework: the first addresses the implementation of principles governing the progression of C_3S and C_2S during the slow hydration stage, focusing on colour types α_1, α_2, α_3, and β_1; the second presents the results of the C_3S and C_2S model.

7.3 Modelling cement grain hydration governed by C_3S and C_2S microstructures during the slow hydration stage

This section builds on the premise that colorimetric analysis offers a reliable means of distinguishing hydration and corrosion regimes. By linking colour features to microstructural evolution, it is hypothesised that a robust framework can be established to understand and predict the progressive behaviour of cement grain hydration under slow conditions.

Based on these principles, general laws and mathematical formulations are derived to model the interactions of C_3S and C_2S microstructures during this slow-

activity stage. In particular, the sum of hydration types governed by a common regime, accelerating or retrogressive, at the CGH network input equals the sum of hydrated C_3S or C_2S grains under the same regime, providing a basis for predictive equations of microstructural evolution. These principles are thus captured in Equations (7.1) and (7.2), providing a formal basis for predicting the evolution of C_3S and C_2S microstructures:

$$\sum \mathrm{CGH}(\alpha 1 + \alpha 2) = \sum \mathrm{C_3S} \tag{7.1}$$

$$\sum \check{\mathrm{R}}\Delta\left(\acute{\mathrm{M}}_1\right) = \sum \mathrm{C_3S} \tag{7.2}$$

From Equation (7.2), ŘΔ identifies the hydration rates of cement grains corresponding to types α1 and α2 in both M1 and M2, as derived from the colour frequency similarity matrices (see Tables 6.7 – 6.9). These rates follow an accelerating regime associated with C_3S hydration. The matrix $\acute{M}_1$ represents the colour frequency similarity grouping both M1 and M2 when ŘΔ identifies α1 and α2.

In contrast, Equation (7.4) employs the symbol ẬΔ to identify the hydration rates corresponding to types α3 and β1 (see Tables 6.7 – 6.9). In this case, the colour frequency similarity is presented by the symbol $\acute{M}_2$ which groups both M1 and M2 Note that, ẬΔ relates to an accelerating regime governed by C_2S hydration.

$$\sum \mathrm{CGH}(\alpha 3 + \beta 1) = \sum \mathrm{C_2\,S} \tag{7.3}$$

$$\sum \hat{\mathrm{A}}\Delta(\acute{\mathrm{M}}_2) = \sum \mathrm{C_2\,S} \tag{7.4}$$

Using frequency similarity data from Tables 6.7 – 6.9 (M1) and Tables 1.e – 5.e (M2, Appendix E), Equations (7.1) – (7.4) were applied in MATLAB R2022b to model cement grain hydration, distinguishing C_3S- and C_2S-dominated regimes. The predictions shown in Figures 7.1 and 7.2 capture the evolution of these models over the curing period running from 3 days to 28 days.

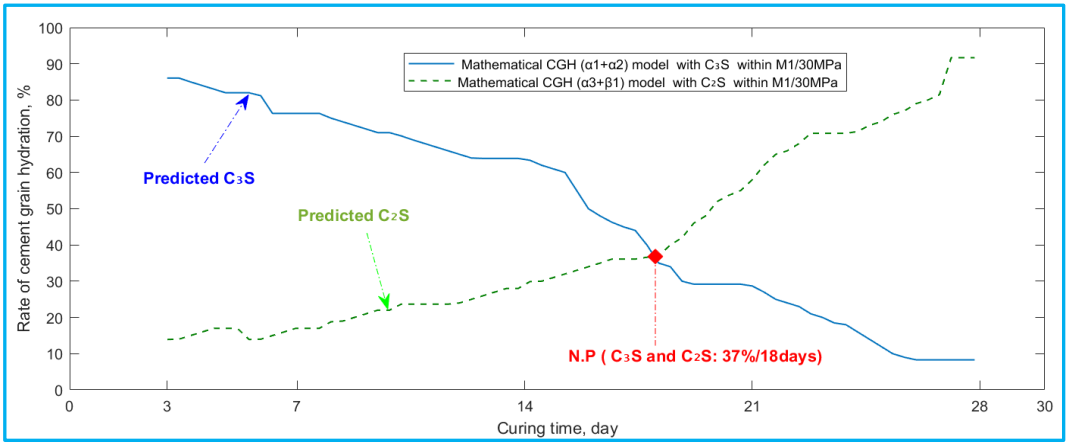

Figure 7.1: Modelling of CGH in predicting C_3S and C_2S microstructures within M1 / 30MPa as per Equations (7.1) – (7.4)

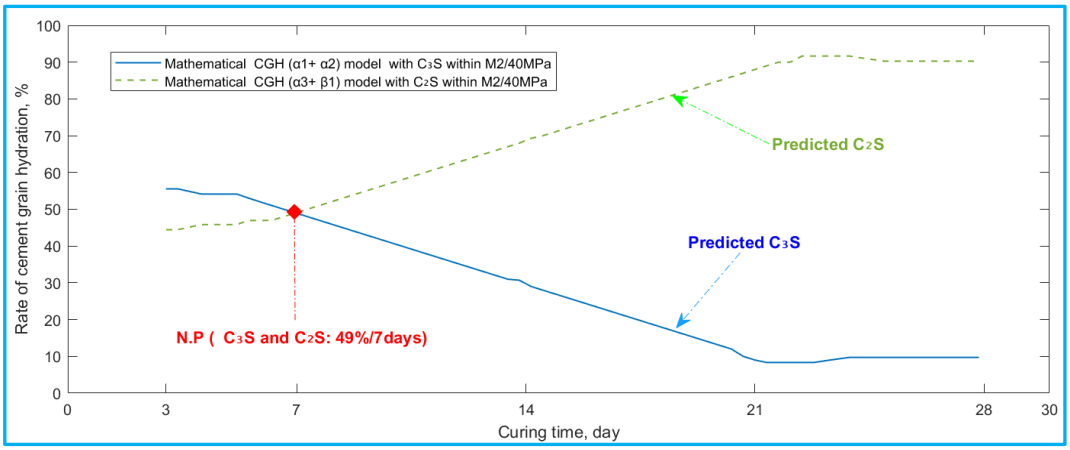

Figure 7.2: Modelling of CGH in predicting C_3S and C_2S microstructures within M2 / 40MPa as per Equations (7.1) – (7.4)

Figures 7.1 and 7.2 present the mathematical models of CGH, specifically CGH (α1+α2) and CGH (α3+β1), which assess the progression of two key cement microstructures (C_3S and C_2S respectively) during the slow hydration phase, spanning a curing period from 3 days to 28 days. These models were developed using Equation (7.1) – (7.4), based on data derived from the experimental colour-based CGC models (α1 to β1).

Figure 7.1 illustrates the case of M1 (30 MPa) (see mix composition in Table 3.1), where the solid blue line represents the predicted hydration trajectory of C_3S (CGH α1+α2), and the dashed green line corresponds to that of C_2S (CGH α3+β1). Two distinct hydration regimes emerge: a retrogressive regime dominated by C_3S,

characterized by a descending trajectory starting from a high hydration level (80 – 90%) at 3 days within sub-network SN1/CGH (3 – 7 days), and an accelerating regime dominated by C_2S, with a steadily increasing trajectory. Both hydration curves exhibit stagnation plateaus between 6 and 7 days of curing, where the hydrated grain content of C_3S remains high (80 – 90%) compared to the much lower level for C_2S (10 – 20%).

The two curves intersect at a so-called neutral point (NP) in red colour, also referred to as the balanced hydration point, at approximately 18 days of curing, where both C_3S and C_2S exhibit similar hydration levels around 37% (see Figure 7.1). Prior to this intersection (from 3 to 18 days), C_3S shows a dominant hydration behaviour, with about 50% of its grains hydrated versus only 20% for C_2S. After this point, the trend reverses: C_2S continues to hydrate more rapidly, while C_3S shows a decline. By the end of the curing period (28 days), this reversal is clearly reflected, with 50% of C_2S grains hydrated, compared to just 25% for C_3S, relative to the proportions observed at the neutral point.

In contrast, Figure 7.2 presents the corresponding CGH models for M2 (40 MPa) (see mix composition in Table 3.1). Unlike the case of M1, the retrogressive (C_3S) and accelerating (C_2S) hydration regimes in M2 begin closer together within the entry range of SN1/CGH, with initial CGH levels of approximately 55% for C_3S and 45% for C_2S. Their respective predicted trajectories, though slightly inclined and nearly parallel, intersect at 7 days of curing (representing the neutral point or NP) where both C_3S and C_2S show a balanced hydration level of 49%. At this point, only 10% of grains are hydrated for each compound, indicating a more equal distribution of hydration behaviour within the SN1/CGH window (3 – 7 days).

Beyond this point, the predicted hydration trajectories diverge: C_2S continues on an upward trend, peaking at around 22 days with approximately 48% of its grains fully hydrated. Conversely, C_3S reaches a stagnation plateau near at 21 days, with a lower hydration level of about 38%. From this point onward, both trajectories follow a nearly linear path, maintaining relatively constant hydration levels until the end of the 28-day curing period.

In conclusion, the CGH models for M1 and M2 provide clear insights into the distinct hydration behaviours of C_3S and C_2S over a curing period of 3 to 28 days. In M1, hydration is initially dominated by C_3S, gradually giving way to a C_2S-dominated regime, with a crossover occurring around 18 days. By contrast, M2 exhibits a more synchronised evolution, with a balanced transition emerging as early as 7 days. These findings underscore the significant influence of mix composition on hydration kinetics and the evolving contributions of C_3S and C_2S, thereby validating the hypothesis founded on colorimetric analysis for predicting cement grain hydration under slow conditions.

At the early stage of hydration (3 days), a consistent trend is observed in both mixtures: C_3S enters the CGH network at a higher hydration level than C_2S. This early divergence aligns with the observations of Qi *et al*. (2021), who reported contrasting evolution patterns for C_3S and C_2S during both rapid and slow hydration phases (see Section 2.2.2 as well as Figures 2.3 and 2.4 in Chapter 2). Taken together, these results highlight the importance of monitoring phase-specific hydration trends to achieve a deeper understanding of the microstructural development of cementitious materials across different mix designs.

7.4 Modelling C_3S and C_2S effects on mechanical and thermal behaviour of concrete mixtures

In this section, the implementation of the C_3S and C_2S mathematical models aims to interact with the predicted models of compressive strength (CS) and temperature evolution in concrete mixtures. In addition to this, the algorithms developed to track the hydration trajectories of cement microstructures (C_3S and C_2S) are based on formulations that take into account the curing duration of concrete samples (M1 and M2). Before incorporating the experimental data on CS and concrete temperature (CT), it was first necessary to establish the formulation of the ratios related to the materials included in the mix compositions.

Based on Table 3.1, the proportions of the various components in the concrete mixtures (M1 and M2) and their corresponding mix designs were derived from the following equations:

$$R_1 = \frac{c_a}{c_s} \quad (7.5)$$

$$R_2 = \frac{cw}{cc} \quad (7.6)$$

$$R_3 = \frac{cm}{ct} \quad (7.7)$$

$$R_{m1,2} = \frac{\sum(R_1 * R_2 * R_3)}{3} \quad (7.8)$$

Where R_1 represents the sand-aggregate ratio (Equation 7.5), R_2 is the water-cement ratio (Equation 7.6) and R_3 corresponds to the ratio of mixture and cement class values at 28 days (Equation 7.7). From Equation (7.8), $R_{m1,2}$ represents the mix design ratio. The response of calculation with regards to the material ratios and mix design parameters (M1) and (M2) is provide in Tables 7.1 and 7.2.

Table 7.1 Material ratios and mix design parameters (M1 / 30 MPa)

Composition	**Mix design proportion**	**Type I cement class (in MPa)**
Sand (kg)	900	42.5
Aggregate (kg)	900	-------
Water (ℓ)	225	-------
Cement (kg)	500	-------
Sand-aggregate ratio (R_1)	1	-------
Water-cement ratio (R_2)	0.45	-------
Mix1- cement class ratio (R_3)	0.71	-------
Mix 1 design ratio (R_{m1})	0.72	-------

Table 7.2 Material ratios and mix design parameters (M2 / 40 MPa)

Composition	**Mix design proportion**	**Type I cement class (in MPa)**
Sand (kg)	900	42.5
Aggregate (kg)	950	-------
Water (ℓ)	200	-------
Cement (kg)	500	-------
Sand-aggregate ratio (R_1)	0.95	-------
Water-cement ratio (R_2)	0.4	-------
Mix2-cement class-ratio (R_3)	0.94	-------
Mix2 design ratio (R_{m2})	0.76	-------

Table 7.1 presents a M1 / cement class-ratio (R_3) of 0.71 and a M1 design ratio (R_{m1}) of 0.72, whereas Table 7.2 indicates that M2/cement class-ratio achieves a higher ratio (R_3) of 0.94 corresponding to a mixture design ratio (R_{m2}) of 0.76.

The designation "Type I cement class" refers to a standard compressive strength of 42.5 MPa at 28 days, as mentioned by the manufacturer (refer to Table 3.2). A comparative interpretation of the data shows that the M2/cement class-ratio and the corresponding mixture design R_{m2} (Table 7.2) exceed the values recorded for the M1/cement class-ratio and R_{m1} (Table 7.1), thereby highlighting distinct formulation characteristics across the two mixtures.

The mathematical formulations used to predict the mechanical strength and temperature evolution of concrete mixtures, within the context of cement microstructure kinetics, are summarized as follows:

$$\bar{T}\Delta(\acute{C}_{m_{1,2}})_dn = (R_{m1,2})\left[0.1(u)\log e^{dn} + \frac{\sqrt{e^{u}}}{e^{u}}\right][\log(100)\,\Delta\bar{m}] \quad (7.9)$$

$$\bar{T}\Delta(\acute{C}_{m_{1,2}})_dn = (R_{m1,2})\left[0.1(v)\log e^{dn} + \frac{\sqrt{e^{v}}}{e^{v}}\right][\log(100)\,\Delta\bar{m}] \quad (7.10)$$

$$\acute{C}_{dn} = \frac{C_{dn}}{\varepsilon_s} \quad (7.11)$$

$Ć_{m1} = (Ć_{dn})(R_{m1})$ (7.12)

$Ć_{m2} = (Ć_{dn})(R_{m2})$ (7.13)

Equations (7.9) and (7.10) define $Ć_{m_{1,2}}$ and $R_{m1,2}$ as the respective parameters for concrete strength design and mix proportioning for M1 and M2. The variables u and v describe the hydration regime trajectories governed by C_3S and C_2S. The term d_n denotes the curing day at which mechanical testing is performed, where n corresponds to standard intervals (days 3, 7, 14, 21, and 28), as specified in Section 3.3.3 of Chapter 3. The algorithm $\log(100)\,\Delta\text{m}$ regulates the trajectory profiles of both compounds, with Δm serving as a trial-based calibration parameter. Convergence of the adjustment process typically required between 10 and 20 computational iterations.

In Equations (7.11) through (7.13), $Ć_{dn}$ refers to the rate of compressive strength gain (in MPa/min), while C_{dn} represents the compressive strength measured through standardized cube-press testing (see Equation 3.1 in Chapter 3). The experimental strength values used for model validation correspond to M 1 and M2 with target strength: 30 MPa and 40 MPa (Table 3.2). Thus, from Equations (7.12) and (7.13), the calculated compressive strength ratio weighed by the mix design ratio is in respect of $Ć_{m1} = 0.11$ for M1 (30 MPa) and $Ć_{m2} = 0.12$ for M2 (40MPa). Parameter $Ɛ_s$ in Equation (7.11) refers to the standardized cube-press loading rate used during experimentation, set at 350 kN/min (equivalent to 35 MPa/min). This value is derived from the operational specifications of the testing equipment itself (see Section 3.2.4 of Chapter 3).

Additional formulations concerning the influence of C_3S and C_2S microstructures in predicting concrete temperature behaviour are encapsulated as follows:

$$\bar{T}\Delta(T_{m_{1,2}})_dn = (R_{m1,2})\left[0.1(u)\log e^{dn} + \frac{\sqrt{e^{u}}}{e^{u}}\right][\log(100)\,\Delta\text{m}] \quad (7.14)$$

$$\bar{T}\Delta(T_{m_{1,2}})_dn = (R_{m1,2})\left[0.1(v)\log e^{dn} + \frac{\sqrt{e^{v}}}{e^{v}}\right][\log(100)\,\Delta\text{m}] \quad (7.15)$$

From Equations (7.14) and (7.15), $T_{m_{1,2}}$ represents experimental data of concrete temperature recorded within M1 / 30 MPa (see Table 3.3 in Chapter 3) and M2 / 40 MPa (Table 3.4), respectively.

The results of the C_3S- and C_2S-based mathematical models for predicting CS and CT in both mixtures are presented in Figures 7.3 to 7.6.

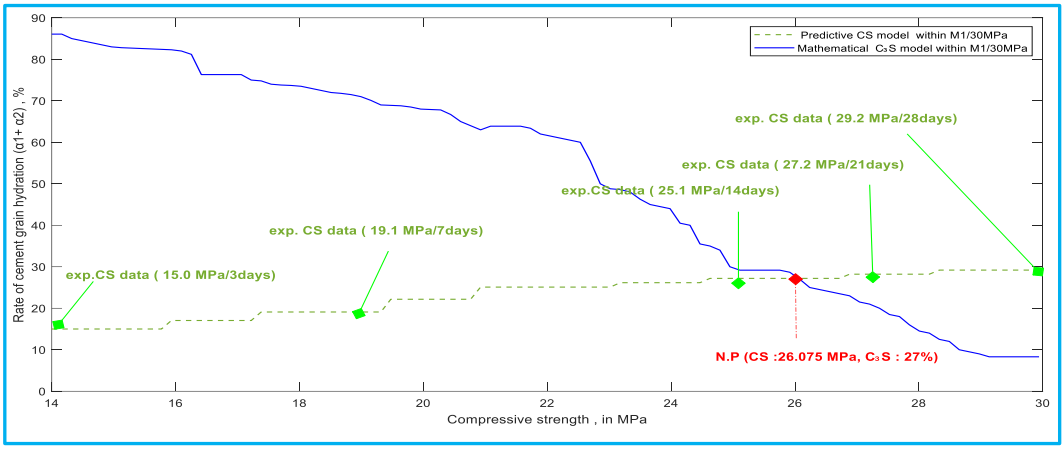

Figure 7.3: Hydration models of C_3S for predicting the CS of the M1 / 30 MPa concrete mix

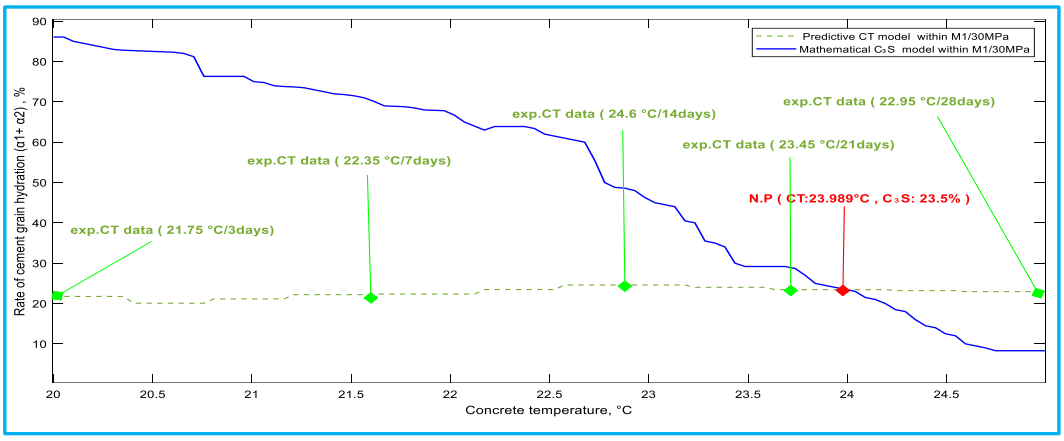

Figure 7.4: Hydration models of C_3S for predicting the CT within the M1 / 30 MPa concrete mix

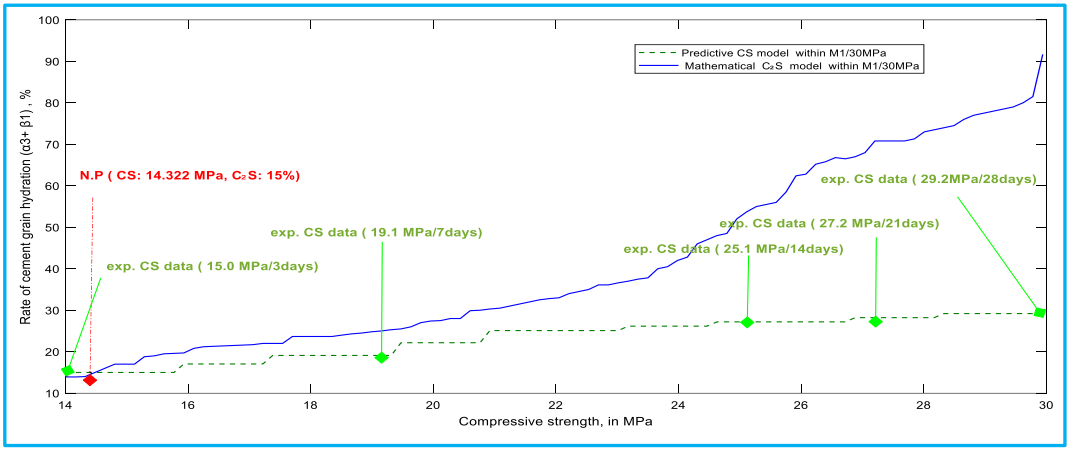

Figure 7.5: Hydration models of C_2S for predicting the CS of the M1 / 30 MPa concrete mix

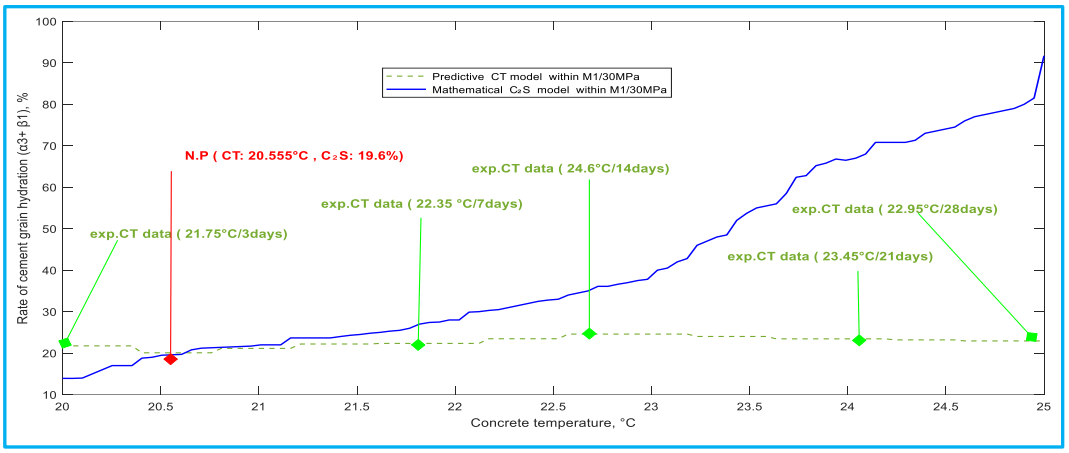

Figure 7.6: Hydration models of C_2S for predicting the CT within the M1 / 30 MPa concrete mix

Figures 7.3 – 7.6 present the interactions between the hydration models of C_3S and C_2S and the evolution of CS and CT for M1 / 30MPa, under retrograde and accelerating regimes. In addition, both CS and CT models within M1 / 30MPa are predicted-based on experimental data (see Tables 3.1 – 3.3).

For C_3S-based models shown in Figures 7.3 and 7.4, the CS/C_3S (M1) interaction reveals a stepwise strength gain under an accelerating regime: approximately 4 MPa at 3 – 7days, and 6 MPa at 7 – 14 days, coinciding with a 15% and 45% decrease in hydrated C_3S, respectively. The first peak plateau in CS is observed at 14 days (25.1 MPa), marking an approximatively 10 MPa gain from 3 days (15 MPa) for a cumulative 60% C_3S hydration. Beyond 14 days, strength increases diminish

progressively (~2 MPa per 7-day interval), with marginal C_3S consumption (±6.5%) leading to a final CS of around 29.2 MPa at 28 days.

The CT/C_3S (M1) interaction (Figure 7.4 starts with a plateau around 21.75°C at 3 days, followed by a stagnation (20.5°C – 21°C) before a gradual stepwise rise to a peak of 24.6°C at 14 days. This thermal increase remains moderate: +0.60°C (3 – 7 days for 15% C_3S hydration) and +2.25°C (7 – 14 days for 20% hydration), totalling a 2.85°C increase for 35% C_3S hydration between 3 days and 14 days. After the peak, CT decreases slightly by 1.15°C (14 – 21 days) and 0.60°C (21 – 28 days) for further hydration of 8% and 20%, respectively. The neutral point (NP), indicating the intersection of the CS or CT trajectories with C_3S hydration, occurs late (between 21 days and 28 days) at 26.075 MPa / 27% for CS/C_3S and 23.989°C / 23.5% for CT/C_3S.

Conversely, the C_2S-based models (Figures 7.3 and 7.4) show early NP intersections, occurring between 3 – 7 days: 14.322 MPa / 15% for CS/C_2S and 20.555°C / 19.5% for CT/C_2S. The CS/C_2S model (M1) follows a similar stepwise increase pattern as CS/C_3S: around 4 MPa and 10% hydration (3 – 7 days), approximatively 6 MPa and 28% (7 – 14 days), and a steady around 2 MPa gain per interval between 14 – 28 days, corresponding to 18 – 20% hydration per period.

For the CT/C_2S interaction, an initial plateau is followed by a thermal increase of 1.40°C (3 – 7 days for 8% hydration) and 2.25°C (7 – 14 days for 6%). After reaching a peak at 14 days, CT declines by 1.15°C (14 – 21 days for 38% hydration) and 0.95°C (21 – 28 days for 23%).

Based on Figures 7.7 and 7.8, the retrograde C_3S models interacting with the predicted CS and CT profiles for M2 / 40 MPa are illustrated. In this study, the CS and CT models are also predicted by incorporating the experimental data recorded in Tables 3.1 and 3.4, respectively. The NP (intersections between CS or CT and C_3S trajectories) appear late, between 21 days and 28 days. For CS/C_3S, NP is located at 33.266 MPa and 35% hydration (Figure 7.7), whereas for CT/ C_3S, it is found at 23.283°C and 22.7% (Figure 7.8).

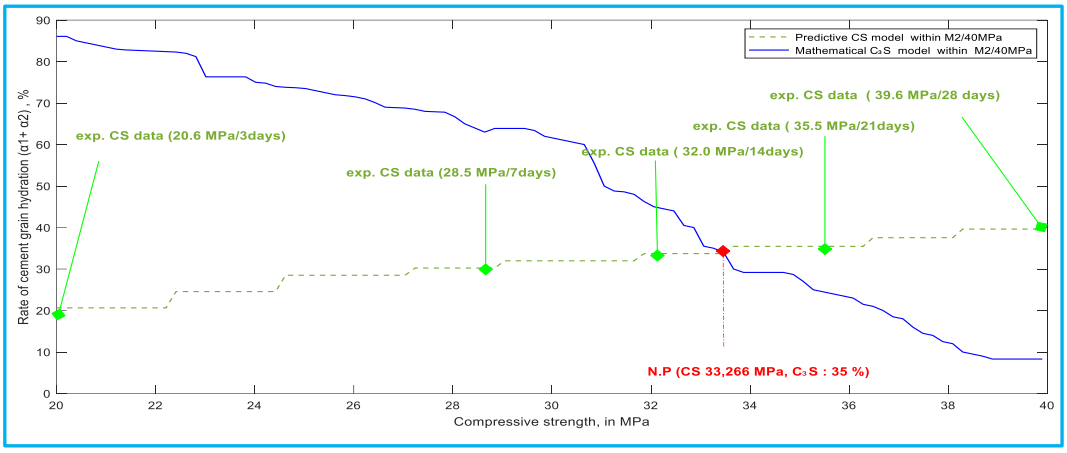

Figure 7.7: Hydration models of C_3S for predicting the CS of the M2 / 40 MPa concrete mix

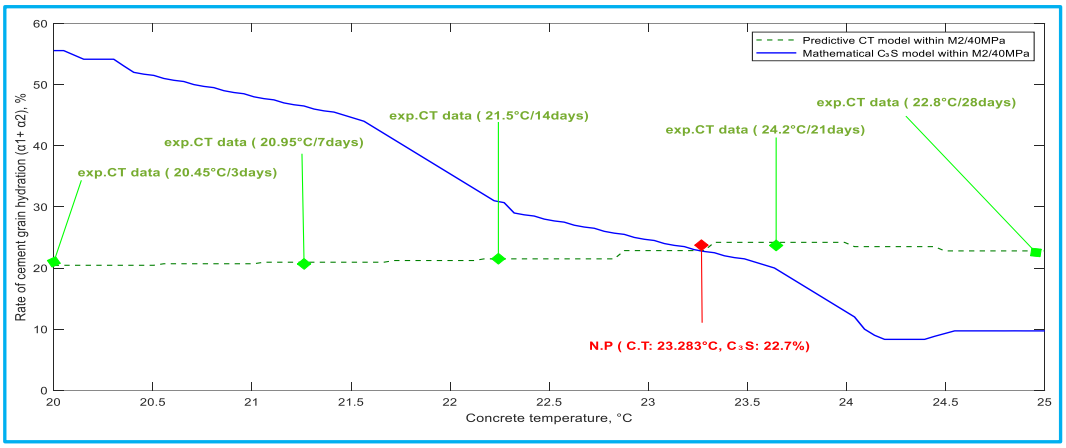

Figure 7.8: Hydration models of C_3S for predicting the CT within the M2 / 40 MPa concrete mix

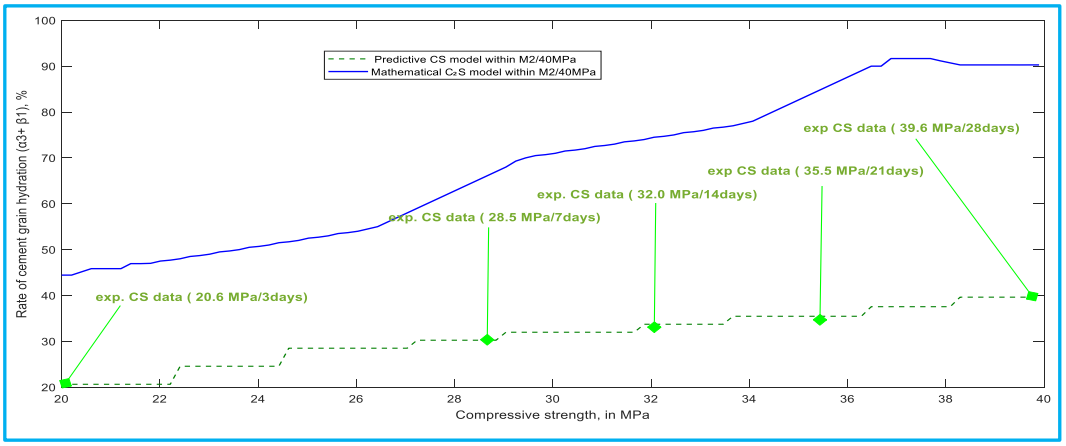

Figure 7.9: Hydration models of C_2S for predicting the CS of the M2 / 40 MPa concrete mix

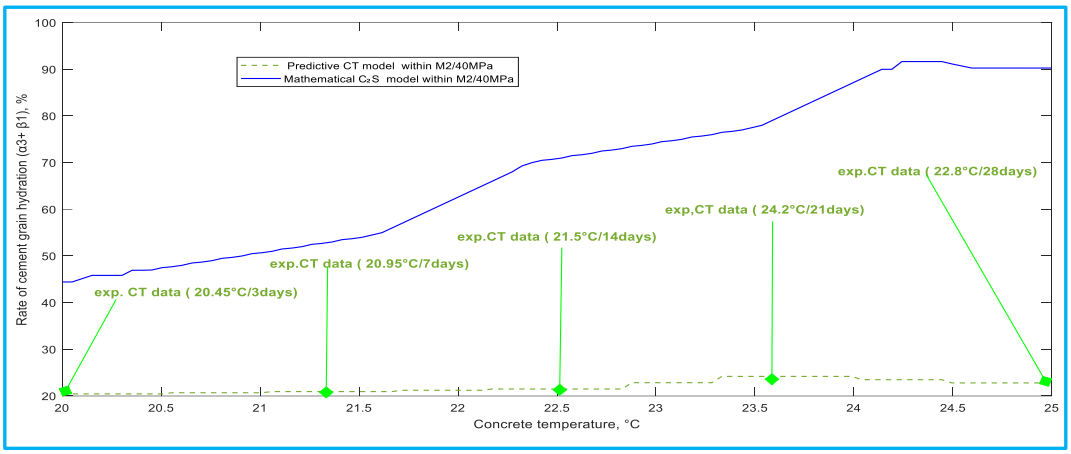

Figure 7.10: Hydration models of C_2S for predicting the CT within the M2 / 40 MPa concrete mix

The predicted CS/C_3S model within M2 follows an accelerating regime, with a pronounced strength gain of approximately 7.9 MPa between 3 days and 7 days, corresponding to 26% hydrated C_3S (Figure 7.7). At 7 days, CS reaches a high peak of 28.5 MPa, up from 20.6 MPa at 3 days, making it a dominant plateau. Thereafter, the strength increases steadily by 3.5 MPa between 7 – 14 days and 14 – 21 days, aligned with 20% additional hydration of C_3S in each interval. Between 21 days and 28 days, a secondary, smaller peak of approximately 4 MPa is observed, with CS reaching 39.6 MPa for an additional 15% C_3S hydration.

Figure 7.8 shows the CT/C_3S (M2) interaction, which begins without a stagnant plateau, unlike the M1 case. The CT trajectory starts at 20.45°C at 3 days and gradually rises to 20.95°C at 7 days (8% hydrated C_3S). Subsequent increases are 0.45°C (7 – 14 days for 28% hydration), and 0.7°C (14 – 21 days for 13% hydration), reaching a major thermal peak at 24.2°C by day 21. CT then declines to 22.8°C at 28 days, corresponding to 14% additional hydration.

Figures 7.9 and 7.10 present the C_2S-based models (M2/40MPa) interacting with CS and CT, respectively. Notably, no distinct neutral points (NP) are observed for CT/C_2S. However, the CS/C_2S model, also governed by an accelerating regime, reaches a 7-day peak of 28.5 MPa with only 20% C_2S hydration (Figure 7.9), less than the 26% required for C_3S under similar conditions. Between 7 – 14 days and 14 – 21 days, strength increases by 3.5 MPa for each interval, corresponding to 9%

C_2S hydration per period. At 28 days, a CS of 39.6 MPa is reached with only 10% additional hydration (21 – 28 days), compared to 15% for C_3S to reach the same strength under similar conditions (Figure 7.7).

In Figure 7.10, the CT/C_2S interaction shows a nearly linear temperature progression. A slight increase of 0.50°C is observed between 3 – 7 days for 8% C_2S hydration, followed by 0.55°C between 7 – 14 days for 18%. The CT peaks at 24.2°C at 21 days (5% hydrated C_2S), then, decreases in steps to 22.8°C at 28 days, with 8% additional hydration in that final period.

In summary, a comparative assessment of cement grain hydration in M1 (30 MPa) and M2 (40 MPa) underscores the functional importance of C_2S in compressive strength development during the slow hydration phase. While its hydration degree remains comparatively low relative to that of C_3S, C_2S exhibits a more pronounced contribution to early-age strength in M2 (7 days). This behaviour is caused by two influencing parameters: First, an elevated M2 design-to-cement class ratio versus to that of M1 design (see Tables 7.1 and 7.2). Second, the use of high-grade cement (42 MPa) in both mixture compositions (Tables 7.1 and 7.2). Moreover, C_2S demonstrates a minimal thermal footprint compared to C_3S, reinforcing its role as a slow-reacting phase with long-term mechanical benefits.

The moderating role of C_2S, with its limited thermal impact on mortars or concrete compared to C_3S, has also been demonstrated in similar studies by Bye (1999), Jansen *et al*. (2012), Qi *et al*. (2021), Semugaza *et al.* (2023), and Huang *et al*. (2025). This is also highlighted in Section 2.2.2 of the literature review.

7.5 Concluding remarks

This chapter was shaped by two overarching research questions concerning the influence of key cement microstructures (C_3S and C_2S) on the evolution of compressive strength and temperature during the slow hydration phase (3 – 28 days), and the extent to which concrete mix design affects microstructural progression and dominant hydration regimes. These questions structured the

analytical framework used to investigate the interplay between cement composition and microstructural activity. Together, they provided the basis for evaluating how cement chemistry and formulation shape the mechanical and thermal behaviour of concrete under slow hydration conditions.

The mathematical implementation of hydration models for both C_3S and C_2S provided predictive insights into the evolution of compressive strength and internal temperature for concrete specimens prepared using two distinct formulations (M1: 30 MPa and M2: 40 MPa). The comparative analysis of these mixtures highlighted the differential influence of C_2S and C_3S in capturing strength and thermal variations under slow hydration conditions.

The elevated mix design–cement class ratio associated with M2 (40 MPa) exerted a significant influence on the behaviour of C_2S microstructures, especially when compared to the lower ratio observed in M1 (30 MPa). Moreover, the class of cement demonstrated a measurable and consistent impact on the hydration dynamics and structural evolution of both C_3S and C_2S microstructures, suggesting a strong dependence on cement quality and formulation in long-term performance.

Furthermore, the investigation of corrosion phenomena, assessed via colorimetric variation and modelled mathematically, led to the identification of three corrosion regimes: retrograde, stagnant, and accelerating. These regimes proved essential in describing the progression of acid-induced corrosion in cement grains, particularly under exposure to a low sulphuric acid concentration of 30 g/ℓ.

A comparative assessment of the two methodological approaches for evaluating the slow-phase hydration of cement grains — namely, the white pixel detection method and the colour-type similarity frequency approach — highlights their respective domains of applicability. The white pixel method is better suited for localized analysis of hydration or corrosion phenomena across spatially distributed points on the concrete surface. In contrast, the colour-type similarity approach offers greater analytical depth in capturing the temporal evolution of the C_3S and

C_2S microstructures that drive the slow hydration mechanisms at the microstructural scale.

CHAPTER 8: CONCLUSION AND RECOMMENDATIONS

8.1 Summary of the findings

The principal objective of this thesis was to develop a mathematical framework capable of describing cement-grain hydration and corrosion as a function of grain-level activity. This goal was successfully achieved through the formulation and implementation of matrix equations designed to model the physical, geometrical, and colorimetric characteristics of scanned cement grains.

The proposed matrix structure proved effective in linking experimental conditions with the spatial configuration of scanned points and the pixel information derived from processed images. This enabled the generation of numerical values that combine both experimental parameters and their precise geometrical locations. The study also established the mathematical and algorithmic foundations necessary for transforming visual data into computable formats, introducing a set of equations for detecting, classifying, and quantifying similarity frequencies within the colorimetric dataset.

Mathematical formulations further supported the implementation of the ANN framework developed to evaluate black- and white-pixel rates. This framework successfully trained input–output patterns and produced a predictive scheme linking scanned-point locations to pixel-distribution behaviour. As a result, point-scale modelling of cement grains was effectively achieved using the proposed mathematical equations.

Another application of the matrix equations within the ANN architecture was the development of the IBWP, which proved reliable for assessing the relationship between input parameters and the distribution rates of black and white pixels in scanned images. The experimental ANN models demonstrated strong performance in evaluating pixel-rate variations in black-and-white images generated from colour images of cement grains under both curing and corrosion conditions.

Models F and I were particularly effective in recording the highest white-pixel rates and lowest black-pixel rates during the curing and corrosion phases. In Model I (M1 / 30 MPa and M2 / 40 MPa), the strongest white-pixel response and lowest black-pixel response occurred at 14 days at scanned point 9. In contrast, Model F (M1 / 30 MPa) recorded its peak performance at 12 days of corrosion at scanned point 6. The study therefore established that ANN performance in capturing the highest pixel-rate variations is influenced by three factors: concrete composition, the hydration state of cement grains, and corrosion-induced transformations.

Image-processing outcomes also highlighted a clear correlation between image area proportions and pixel-rate variations. Across both curing and corrosion periods, WAP consistently exceeded BAP, confirming the predominance of white-pixel evolution. This behaviour is likely governed by hydration during curing and by CGC induced by corrosion. These findings reinforce the suitability of the white-pixel rate as a physical indicator for monitoring the evolution of hydration and corrosion during their respective slow phases.

The use of white pixels as indicators proved particularly effective when combined with ANN-based extraction of output-rate values. This approach enabled the identification of two hydration regimes during the curing period (3 – 28 days): a retrograde regime characterised by a downward trend, and an accelerating regime showing an upward trajectory. Three regimes were identified for corrosion: retrograde, stagnant, and accelerating.

The mathematical formulations developed throughout this work successfully characterised both hydration and corrosion regimes using white-pixel rates and colorimetric indicators. The enhanced sensitivity of the colorimetric approach stems from matrix equations that quantify colour attributes with greater precision in capturing microstructural evolution during slow hydration and corrosion. Additionally, the successful application of these equations to the modelling of C_2S and C_3S microstructures provide strong validation of the initial hypothesis regarding their capacity to address complex analytical challenges.

The findings reveal two principal hydration regimes distinguished by their colouration ranges. The accelerating regime (α_1) exhibits a sharp entry, low colouration (0 – 10%), and high early CGH (45 – 60%), followed by a transition towards high-coloration plateaus (80 – 90%). The decelerating regime (α_2) presents a smoother decline, with troughs at 80 – 90% colouration and an exit at 0% CGH and 85 – 95% CGC. In mixture M2, regimes α_3 and β_1 show similar retrogressive and accelerating behaviour, with α_3 ranging from 37.5 – 47.5% hydration and colouration between 20 – 40%, and exiting at approximately 73% hydration.

A secondary objective of this thesis was to identify the types of hydration occurring during the slow phase. In addition, the objective was to assess the influence of key cement microstructures (C_3S and C_2S) on compressive strength and temperature evolution. This goal was accomplished by analysing colour images through matrix-based equations. Then, the implemented equations served to convert visual data into scalar and binary values. They also served in the identification of corrosion regimes and the assessment of how concrete mix design affects microstructural development.

The integration of colour-similarity frequency analysis allowed the identification of three dominant colour types governing slow hydration and corrosion: the α and β types, associated with hydration evolution, and the γ type, indicating corrosion progression. Strong correlations emerged between α_1 and α_2 colour types and C_3S microstructures, as well as between α_3 and β_1 types and C_2S microstructures.

By combining matrix-based formulations with algorithmic modelling, the complex kinetics of C_3S and C_2S were quantitatively characterised. The colour-frequency similarity methodology provided a new means of estimating hydration-rate variations relative to the evolving regime trajectories. The hydration models implemented for C_3S and C_2S also yielded predictive insights into the evolution of compressive strength and temperature in concrete specimens prepared with two distinct mix designs (M1: 30 MPa and M2: 40 MPa), highlighting the differential influence of C_2S and C_3S on strength and thermal development.

The higher mix-design–cement-class ratio in M2 (40 MPa) exerted a notable influence on the behaviour of C_2S microstructures, contrasting with the lower ratio in M1 (30 MPa). Furthermore, the cement class demonstrated a consistent impact on the hydration dynamics of both C_3S and C_2S, underscoring the dependence of long-term concrete performance on cement quality and formulation.

The investigation of corrosion phenomena, assessed through colorimetric variation and mathematically modelled, led to the identification of three regimes—retrograde, stagnant, and accelerating. These regimes were essential for describing acid-induced corrosion in cement grains, especially under exposure to a low sulphuric acid concentration of 30 g/ℓ.

A comparative evaluation of the two methodological approaches developed for analysing slow-phase hydration — namely, the white-pixel detection method and the colour-type similarity frequency approach — highlighted their respective areas of applicability. The white-pixel method is more suitable for localised assessment of hydration or corrosion across spatially distributed points on the concrete surface. Conversely, the colour-type similarity approach provides greater analytical depth for capturing the temporal evolution of the C_3S and C_2S microstructures that govern slow hydration at the microstructural scale.

8.2 Recommendations for future work

The findings and delimitations of the present study provide several opportunities for further research. The proposed framework could be extended to a wider range of concrete mix designs, cement classes and sulphuric acid concentrations, together with longer exposure periods and more varied environmental conditions. Such extensions would provide further evidence of the general applicability and robustness of the framework beyond the experimental conditions investigated in this study.

Future work should also consider increasing the size and diversity of the experimental dataset and applying more comprehensive statistical validation to

the proposed mathematical and ANN models. In particular, the use of standard indicators such as Root Mean Square Error (RMSE) and Average Absolute Error (AAE) would provide a more rigorous assessment of model accuracy and predictive reliability. Further investigation of ANN architectures with two hidden layers could also be undertaken to determine whether they improve the simulation and prediction of pixel-distribution dynamics at scanned points and provide more precise Identification Indices of Black and White Pixels (IBWP). The effectiveness of the present activation functions and mathematical formulations, which achieved convergence within five iterations, also warrants further investigation, particularly with regard to the contribution of the 18 secondary neurons to computational efficiency and model performance.

Another important area for future investigation concerns the behaviour of C_3S and C_2S under sulphuric acid exposure in relation to compressive strength and temperature evolution. Such studies would extend the present framework by examining the interaction between cement-phase behaviour and macroscopic performance under corrosive conditions, thereby contributing to a better understanding of long-term concrete performance.

Finally, the framework could be broadened through the inclusion of other important cement and concrete constituents, particularly C-S-H and CH, as well as aggregate-related effects and interfacial transition zones. The integration of complementary chemical and mineralogical characterisation techniques, including XRD, SEM/EDX and XCT, with colorimetric and pixel-based image analysis could facilitate correlations between mineral-phase evolution and image-derived indicators. This would provide a more comprehensive multiscale understanding of hydration–corrosion interactions and support further development of the proposed mathematical and data-driven framework.

References

Aïtcin, P.C., Flatt, R.J., 2016. Science and technology of concrete admixtures. Woodhead Publishing, Elsevier, Cambridge, United Kingdom

Allahverdi, A., Škvára, F., 2000. Acidic corrosion of hydrated cement-based materials, Part 1. Mechanism of the phenomenon. Technicka Journal, vol. 44, no. 4, pp. 114 – 120

Allahverdi, A., Hashemi, H., Mahinroosta, M., 2020. Resistance of Alkali-activated Slag Cement Against Sodium Sulfate. Iranian Journal of Materials Science & Engineering, vol. 17, no. 1, pp. 23 – 34

Altinay, E.A., Kose, U., 2021. Manipulation of artificial intelligence in image-based data: Adversarial examples techniques. Journal of Multidisciplinary Developments, vol. 6, no. 1, pp. 8 – 17

Al-Sharify, Z.T., Al-Sharify, T.A., Al-Sharify, N.T., Yahyanaser, H., 2020. A critical review on medical imaging techniques (CT and PET scans) in the medical field. IOP Conference Series: Materials Science and Engineering, vol. 870, no. 2020, p. 012043

American Society for Testing and Materials, 2001. Chemical resistance of mortars, grouts, and monolithic surfacings and polymer concretes, ASTM C 267-01. West Conshohocken, PA

American Society for Testing and Materials, 2005. Standard test method for temperature of freshly mixed hydraulic-cement concrete 1, ASTM 1064-05. West Conshohocken, PA

American Society for Testing and Materials, 2007. Standard specification for Portland cement: Type I. ASTM 150-07. West Conshohocken, PA

Ares, M., Royo, S., Vidal, J., Campderros, L., Panyell, D., Perez, F., Vera, S., Ballester, M., 2013. 3 D scanning system for in vivo imaging of human body. Springer Publisher, Berlin Heidelberg

Attiobge, K.E, Rizkalla, H.S., 1988. Response of concrete to sulphuric acid attack. ACI Materials Journal, vol. 85, no. 746, pp. 481 – 488

Azarsa, P., Gupta, R., 2017. Electrical resistivity of concrete for durability evaluation: A review. Advances in Materials Science and Engineering Journal, vol. 2017, no. 8453095, pp. 1 – 30

Basheer, I.A., Hajmeer, M., 2000. Artificial neural networks: fundamentals, computing, design, and application. Journal of Microbiological Methods, vol. 43, no. 1, pp. 3 – 31

Bentz, D.P., Snyder, K.A., Stutzman, 1997. Hydration of Portland cement: The effects of curing conditions. Proceedings of the Tenth International Congress on the Chemistry of Cement, vol. 2, June 1997, Sweden

Bentz, D.P., 2006. Influence of water-to-cement ratio on hydration kinetics: Simple models based on spatial considerations. Cement and Concrete Research, vol. 36, no. 2, pp. 238 – 244

Binici, H., Zengin, H., Zengin, G., Kaplan, H., Yucegok, F., 2009. Resistance to sodium sulfate attack of plain blended cement containing corncob ash and ground granulated blast furnace slag. Scientific research and Essay, vol.4, no 2, pp. 98 – 106

Devi, K., Saini, B., Aggarwal, P., 2022. Microstructural-structural analysis of cement composites using a stone waste: A review. IOP Conference Series: Materials Science and Engineering, vol. 1260, no. 2022, p. 012031

De Souza, D.J., de Medeiros, M.H.F., Filhoc, J.H., 2O20. Evaluation of external sulfate attack (Na2SO4 and MgSO4): Portland cement mortars containing siliceous supplementary cementitious materials. IBRACON Structures and Materials Journal, vol. 13, no. 4, pp. 1 – 16

Daanen, H., Hong, SA., 2008 Made to measure pattern development based on 3D whole body scans. International Journal of Clothing Science and Technology, vol. 20, no. 1, pp. 15 – 25

Ekolu, S.O., Ngwenya, A., 2014. Sulphate corrosion behaviour of high-volume slag concrete. Internal Conference on Construction Materials and Structures (ICCMATS), 24 – 26 November 2014, Johannesburg, pp. 788 – 796

El chabib, H., Nedhi, M., El Naggar, M.-H., 2004. Behavior of SCC confined in short GFRP. Cement and Concrete Composite Journal, vol. 27 no. 1, pp. 55 – 64

Elkhadiri, I., Palacios, M., Puertas, F., 2009. Effect of curing temperature on cement hydration. Ceramics –Silikaty, vol. 53, no. 2, pp. 65 – 75

European Committee for Standard, 2011. Cement – Part 1: Composition, specifications and conformity criteria for common cements. EN 197-1: 2011, European Committee for Standard (CEN), Brussels

Fedosov, S.V., Roumyantseva, V.E., Krasilnikov, I.V., Narmania, B.E, 2017. Formulation of mathematical problem describing physical and chemical processes at concrete corrosion. International Journal for Computational Civil and Structural Engineering, vol. 13, no. 2, pp. 45 – 49

Fernandes, I., Broekmans, A.T.M., 2013. Alkali-silica reactions: An overview. Part I. Metallography, Microstructure, and Analysis Journal, vol. 2, no. 4, pp. 257 – 267

Guimarāies, D., Oliveira, V.A., Leao, V., 2016. Kinetic and thermal of ettringite synthesized from aqueous solutions. Journal of Thermal Analysis and Calorimetry, vol. 124, pp. 1679 – 1689

Godycka, K.N., Szulwic, J., Ziółkowski, P., 2014. The method of analysis of damage reinforced concrete beams using terrestrial laser scanning. 14th International Multidisciplinary Scientific GeoConference, SGEM 2014, Poland

Gorthi, S.S., Rastogi, P., 2010. Fringe projection techniques: Whither we are?. Optics and Lasers in Engineering, vol. 48, no. 2, pp. 133 – 140

Gurney, K., 1997. An introduction to neural networks. UCL Press, London

Habib, A.F., Lichti, D.D., El-Badry, M.M., 2014. Optical remote sensing systems for structural deflection measurement and crack characterization. Ninth International Conference on Short and Medium Span Bridges Calgary, 15 – 18 July 2014, Alberta, Canada

Hakim, S.J.S., Noorzaei, J., Jaafar, M.S., Jameel, M., Mohammad Hassani, M., 2011. Application of artificial neural networks to predict compressive strength of high strength concrete. International Journal of the Physical Sciences, vol. 6, no. 5, pp. 975 – 981

Haleem, A., Javaid, M., 2019. 3D scanning applications in medical field: A literature-base review. Clinical Epidemiology and Global Health Journal, vol. 7, no. 2, pp 199 – 210

Han, J., Wang, K., Shi, J., Wang, Y., 2014. Influence of sodium aluminate on cement hydration and concrete properties. Construction and Building Materials, vol. 64, pp. 342 – 349

Hassan, A.T., Taha, S., 2012. The effect of sulfate on the electrical properties of cement pastes. World Applied Sciences Journal, vol. 19, no. 7, pp. 957 – 961

Hewayde, E., Nehdi, M., Alloche, E., Nakhla, G., 2007. Neural network prediction of concrete degradation by sulphuric acid attack. Structure and Infrastructure Engineering, vol. 3, no. 1, pp. 17 – 27

Hooton, R.D., 1993. Influence of silica fume replacement of cement on physical properties and resistance to sulphate attack, freezing and thawing, and alkali-silica reactivity. ACI Materials Journal, vol. 90, no. 2, pp. 143 – 151

Huang, C., Wang, Y., Wei, Z., Yu, Y., 2025. The Preparation of C-S-H powder seeds and their effect on the early hydration performance of cement paste. Crystals, vol. 15, no. 1, p. 73

Huang, F., Li, X., Liu, J., Xian, R., Tian, Q., Zhu, Z., Xu, J., 2025. Simulation of long-term water transport in cement paste considering the hydration process. Journal of Building Engineering, vol. 99, no. 2025, p. 111558

Hu, X., Shi, C., Shi., Tong, B., Wang, D., 2017. Early age shrinkage and heat of hydration of cement-fly ash-slag ternary blends. Construction and Building Materials, vol.153, pp. 857 – 865

Janowski, A., Nagrodzka-Godycka, K., Szulwiic, J., Ziolkowski, P., 2016. Remote sensing and photogrammetry techniques in diagnostics of concrete structures. Computers and Concrete, vol. 18, no. 3, pp. 405 – 420

Jansen, D., Goetz-Neunhoeffer, F., Lothenbach, B., Neubauer, J., 2012. The early hydration of Ordinary Portland Cement (OPC): An approach comparing measured heat flow with calculated heat flow from QXRD. Cement and Concrete Research, vol. 42, no. 1, pp. 134 – 138

Khademi, F., Jamal, S.M., Deshpande, N., Londhe, S., 2016. Predicting strength of recycled aggregate concrete using artificial neural network, adaptive neuro-fuzzy inference system and multiple linear regression. International Journal of Sustainable Built Environment, vol. 5, no. 2, pp. 355 – 369

Kithab, A., Arshad, M.T., Awan, F.M., Khan, I., 2013. Development of an acid-resistant concrete: International Journal of Sustainable Construction Engineering and Technology, vol. 4, no. 2, pp. 33 – 38

Koken, P., Mikrut, S., Pyka, K., Tokarczyk, R., Uhl, T., 2014. Photogrammetric approach in determining beam-column connection deformations. Boletim de Ciências Geodésicas, vol. 20, no. 3, pp. 720 – 733

Kriesel, D., 2005. A brief introduction to neural networks. Seminar, University of Bonn. Available at: https://www.dkriesel.com/en/science/neural_networks (Accessed: 20 April 2025)

Kwak, E., Detchev, I., Habib, A., El-Badry, M., Hughes, C., 2013. Precise photogrammetric reconstruction using model-based image for 3D beam deformation monitoring. Journal of Surveying Engineering, vol. 139, no. 3, pp. 143 – 155

Landini, L., Positano, V., Santarelli, M.F., 2008. 3D medical image processing. In: Image Processing in Radiology, Springer, pp. 67 – 85

Larsen, J., 1999. Introduction to artificial neural network. Internal Report, Technical University of Denmark, Lingby

Lataste, J.F., Sirieix, C., Breysse, D., Frappa, M., 2003. Electrical resistivity measurement applied to cracking assessment on reinforced concrete structures in civil engineering. NDT & E International, vol. 36, no. 6, pp. 383 – 394

Li, P., Gao, X., Wang, K., Tam, V.W.Y., Li, W., 2020. Hydration mechanism and early frost resistance of calcium sulfoaluminate cement concrete. Construction and Building Materials, vol. 239, p. 117862

Liu, K., Deng, M., 2015.Influence of pH on the formation of gypsum in cement materials during sulphate attack. Institution of Civil Engineering, vol. 27, no. 8, pp. 1 – 7

Madhavi, T.Ch., Annamalai, S., 2016. Electrical conductivity of concrete. ARPN Journal of Engineering and Applied Sciences, vol. 11, no. 9, pp. 5979 – 5982

Mehta, P.K., Monteiro, P.J.M., 2006. Concrete microstructure, properties, and materials. Mc-Graw-Hill, USA

McCarter, W.J., Starrs, G., Chrisp, T.M., 2000. Electrical conductivity, diffusion, and permeability of Portland cement-based mortars. Cement and Concrete Research, vol. 30, no. 9, pp. 1395 – 1400

Mindess, S., Young, J.F., Darwin, D., 2003. Concrete (Second Edition). Prentice Hall, Upper Saddle River

Molina, L., 1992. On predicting the influence of curing conditions on the degree of hydration. CBI Report 5:92, Swedish Cement and Concrete Research Institute

Mutunda, A., 2019. A predictive model of concrete corrosion due to sulphuric acid using artificial neural networks. Master's Dissertation, University of South Africa

Persson, B., 1996. Hydration and strength of high-performance concrete. Advanced Cement-Based Materials, vol. 3, pp. 107 – 123

Onyari, E.K., Ikotun, B.D., 2018. Prediction of compressive and flexural strengths of a modified zeolite additive using artificial neural network. Construction and Building Materials, vol. 187, pp. 1232 – 1241

Pandey, J.L., Banerjee, M.K., 1998. Concrete corrosion and control practices – an overview. Anti-corrosion Methods and Materials, vol. 45, no. 1, pp. 5 – 15

Pavlik, V., 1994. Corrosion of hardened cement paste by acetic and nitric acids. Cement and Concrete Journal, vol. 24, no. 3, pp.551 – 562

Qi, T., Zhou, W., Liu, X., Wang, Q., Zhang, S., 2021. Predictive hydration model of Portland cement and its main minerals based on dissolution theory and water diffusion theory. Materials, vol. 14, no. 3, p. 595

Quiroga, P.N., Fowler, D.W., 2004. The effects of aggregates characteristics on the performance of Portland cement concrete. Internal Report, International Center for Aggregates Research, University of Texas, USA

Raupach, M., 1991. History of corrosion in concrete. Internal Report, Institute for Building Materials Research, Aachen University, Germany

Remondino, F., Hakim, S.E., 2006. Image-based 3D modelling: A review. The Photogrammetric Record, vol. 21, no. 115, pp. 269 – 291

Richardson, I.G., 2008. The calcium silicate hydrates. Cement and Concrete Research, vol. 38, no. 2, pp. 137 – 138

Roy, D.M., 1993. Concrete microstructure. Strategic Highway Research Program, National Academy of Sciences, Washington, DC

Rőnnholm, P., Nuikka, M., Suominen, A., Jaakkola, A., 2009. Comparison of measurement techniques and static theory applied to concrete beam deformation. The Photogrammetric Record, vol. 24, no. 128, pp. 351 – 371

Samoshkin, A., Tikhomirov, V., 2021. Mathematical model for the reinforced concrete with nonlinearity behaviour of bond. Journal of Physics, Conference Series: Intelligent Information Technology and Mathematical Modeling, vol. 2131, no. 3, p. 032017

Santhanam, M., Cohen, M.D., Olek, J., 2002. Mechanism of sulphate attack – A fresh look. Part 1 Summary of experimental results. Cement and Concrete Research, vol. 32, no. 6, pp. 915 – 921

Semugaza, G., Mielke, T., Castillo, M.E., Gierth, A.Z., Tam, J.X., Nawrath, S., Lupascu, D.C., 2023. Reactivation of hydrated cement powder by thermal treatment for partial replacement of ordinary Portland cement. Materials and Structures, vol. 56, p. 48

Scrivener, K. L, Nonat, A., 2011. Hydration of cementitious materials, present and future. Cement and Concrete Research, vol. 41, no. 7, pp. 651 – 665

Sharma, V., Rai, S., Dev, A., 2012. A comprehensive study of artificial neural networks. International Journal of Advanced Research in Computer Science and Software Engineering, vol. 2, no. 10, pp. 278 – 284

Sharpley, I., 2015. The effect of hydration on the microstructural properties of individual phases of Ordinary Portland Cement. Master's dissertation, University College London

Shengyuan, Y., Shigang, S., Xiang, L., Yunchuan, L., 2012. Comparative study on theory and test result for dilute sulphuric acid eroded concrete. Procedia Earth and Planetary Science 5, vol. 33, no. 1, pp. 188 – 197

Shi, H., Zhao, Y., Li, W., 2002. Effects of temperature on the hydration characteristics of free lime. Cement and Concrete Research, vol. 32, no. 5, pp. 789 – 793

Shokravi, H., Shaghaghi, T.M., 2019. Experimental study on after-mixing temperature control of concrete in batching plant production. Proceeding: Conference on Material Science and Engineering, 26 – 27 August 2019, Melaka-Malaysia, pp. 1 – 10

South African Bureau of Standards, 2006. Standard specification for Concrete Tests-Compressive strength of hardened concrete (SANS 5863-2006). South African Bureau of Standards, Pretoria

South African Bureau of Standards, 2014a. Standard specification for aggregates from natural sources – Aggregates for concrete (SANS 1083: 2014). South African Bureau of Standards, Pretoria

South African Bureau of Standards, 2014b. Standard specification for concrete tests – Consistence of freshly mixed concrete-slump test (SANS 5861-1:2006). South African Bureau of Standards, Pretoria

Sultan, W.H., Hamza, D.M., 2023. Formulation of mathematical model for stress-strain relationship of normal and high strength concrete under compression. Civil and Environmental Engineering, vol. 19, no. 1, pp. 119 – 133

Taheri, S., Gerardo, G.P., Agbaje, O.B.A., Giri, P., Clark, S.M., 2020. Corrosion inhibitory effects of mullite in concrete exposed to sulfuric acid attack. Corrosion and Materials Degradation, vol. 1, no. 2, pp. 282 – 295

Taheri, S., Gerardo, G.P., Agbaje, O.B.A., Giri, P., Clark, S.M., 2020. Corrosion inhibitory effects of mullite in concrete exposed to sulfuric acid attack. Corrosion and Materials Degradation, vol. 1, no. 2, pp. 282 – 295

Taylor, H.F.W., 1997. Cement chemistry, 2nd Edition. Thomas Telford Publishing, London

Thomas, M.D.A., Fournier, B., Folliard, K.J., 2013. Alkali-aggregate reactivity (AAR) factbook. Internal Report, Office of Pavement Technology, Washington

Türkel, S., Felekoğlu, B., Dulluç, S., 2007. Influence of various acids on the physico-mechanical properties of pozzolanic cement mortars. Sadhana, vol. 32, no. 6, pp. 686 – 691

Ukrainczyk, N., Ukrainczyk, V., 2008. A neural network method for analysing concrete durability. Magazine of Concrete Research, vol. 60, no. 7, pp. 475 – 486

Vasconcellos, J.S., Bofim Fraga, Y.S., da Silva Rêgo, J.H., Sartoratto, P.P.C., Rojas, M.F., 2023. Hydration, mechanical performance and porosity of Portland cement pastes with functionalized nanosilica with APTES. Development in the Built Environment, vol 14, p. 100157

Xie, Y., Qian, C., Xu, Y., Wei, M., Du, W., 2022. Hydration heat and microstructure of SCM-blended cement under semi-adiabatic conditions: effect of initial temperatures. Construction and Building Materials, vol. 356, no. 11, p. 129329

Xu, N., Li, Y., Fang, S., Li, S., Wang, H., Xiang, R., Ouang, S., 2019. Hydration behavior and microstructural evolution of hydratable alumina with different particle size in alumina-spinel castables. Journal of the Ceramic Society of Japan, vol. 127, no. 4, pp. 199 – 206

Yu, T., Twumasi, J.O., Le, V., Tang, Q., Amico, N.D.A., 2017. Surface and subsurface remote sensing of concrete structures using synthetic aperture radar imaging. Journal of Structural Engineering, vol. 143, no. 10, p. 04017143

Zhang, Y., Sun, W., Li, Z., 2019. SEM and EDS analysis of hydrated cement paste. Construction and Building Materials, vol. 205, pp. 641 – 649

Živica, V., Bajza, A., 2001. Acidic attack of cement-based materials – A review. Part 1 Principle of acidic attack. Construction Materials Journal, vol. 15, no. 8, pp. 331 – 340

Appendices

Appendix A: Description of the cement grain colouration under curing conditions

Table 1.a: Description of the cement grain colouration under curing conditions for points corresponding to layer 1 (M2)

Colouration of scanned points in layer 1 for M2		
Face 1-Layer 1-P_1 @ 3days	Face 1-Layer 1-P_2 @ 3days	Face 1-Layer 1-P_3 @ 3days
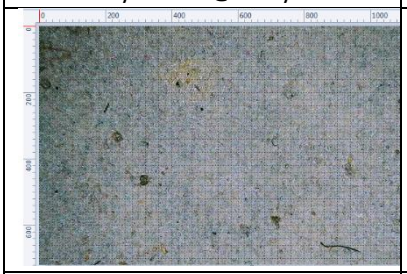		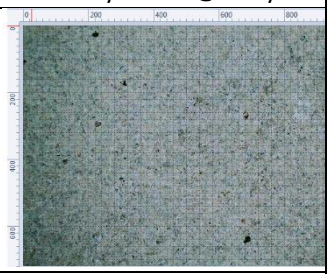
Face 1-Layer 1-P_1 @ 7days	Face 1-Layer 1-P_2 @ 7days	Face 1-Layer 1-P_3 @ 7days
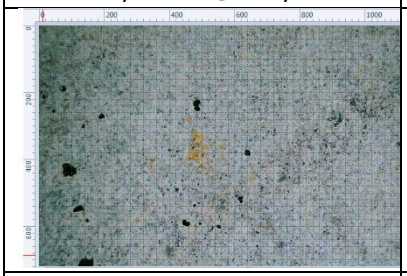	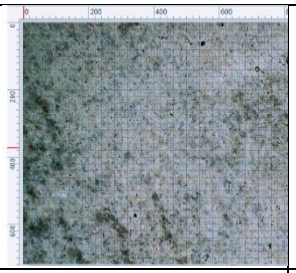	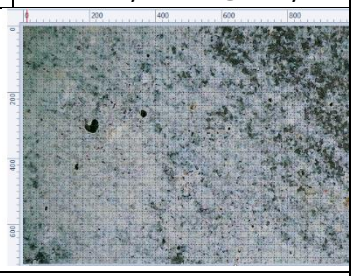
Face 1-Layer 1-P_1 @ 21days	Face 1-Layer 1-P_2 @ 21days	Face 1-Layer 1-P_3 @ 21days
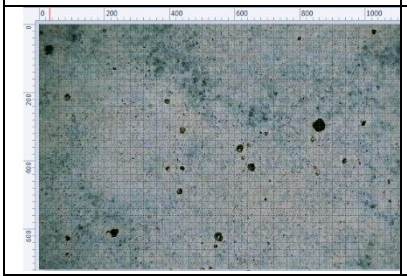	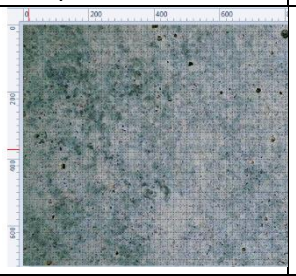	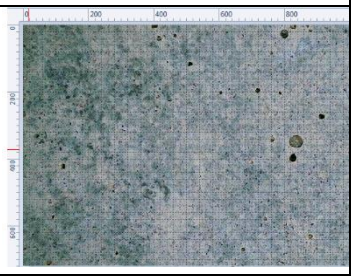
Face 1-Layer 1-P_1 @ 28days	Face 1-Layer 1-P_2 @ 28days	Face 1-Layer 1-P_3 @ 28days
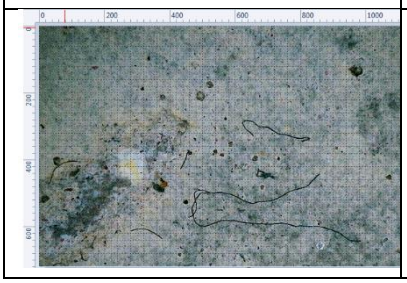	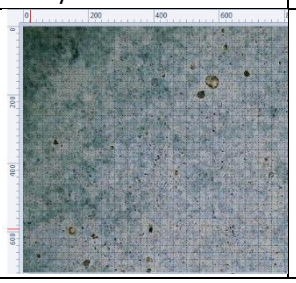	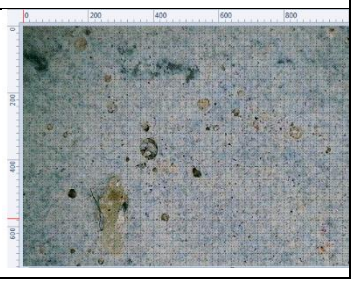

Table 2.a: Description of the cement grain colouration under curing conditions for points corresponding to layer 2 (M2)

Colouration of scanned points in layer 2 for M 2		
Face 1-Layer 2-P_4 @ 3days	Face 1-Layer 2-P_5 @ 3days	Face 1-Layer 2-P_6 @ 3days
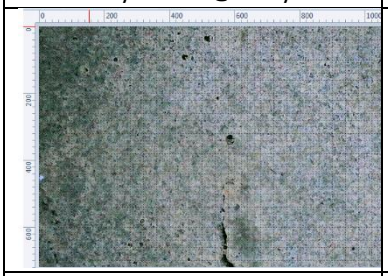	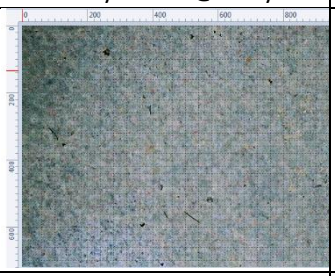	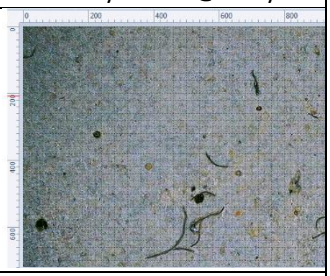
Face 1-Layer 2-P_4 @ 7days	Face 1-Layer 2-P_5 @ 7days	Face 1-Layer 2-P_6 @ 7days
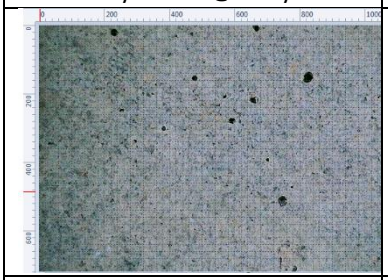	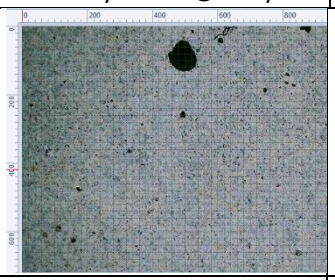	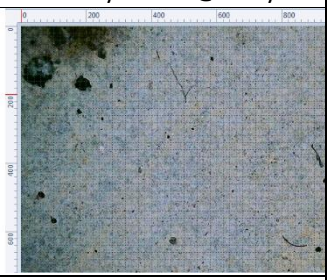
Face 1-Layer 2-P_4 @ 14days	Face 1-Layer 2-P_5 @ 14days	Face 1-Layer 2-P_6 @ 14days
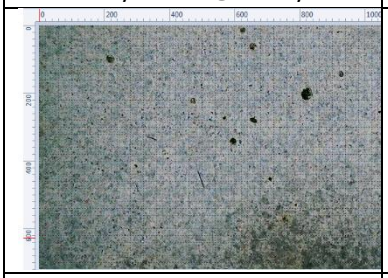	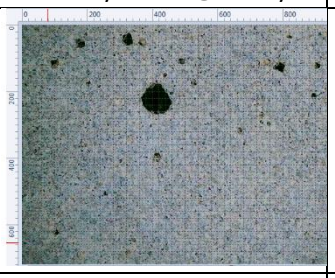	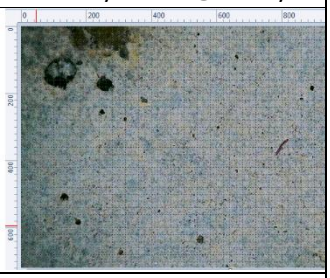
Face 1-Layer 2-P_4 @ 21days	Face 1-Layer2-P_5 @ 21days	Face 1-Layer 2-P_6 @ 21days
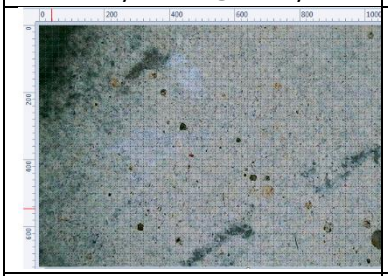	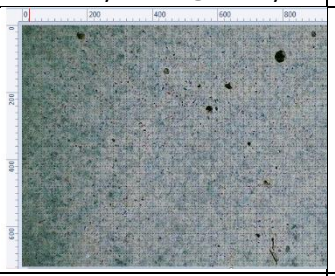	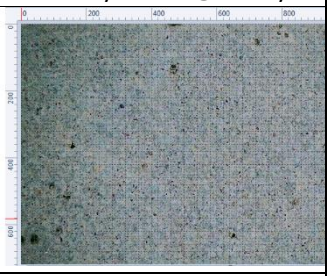
Face 1-Layer 2-P_4 @ 28days	Face 1-Layer 2-P_5 @ 28days	Face 1-Layer 2-P_6 @ 28days
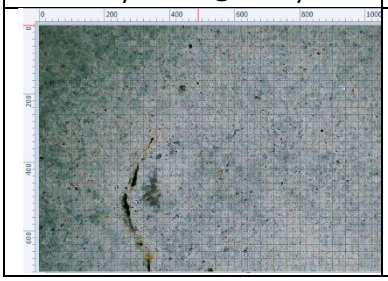	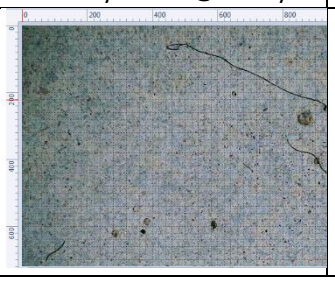	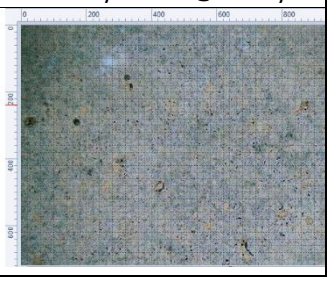

Table 3.a: Description of the cement grain colouration under curing conditions for points corresponding to layer 3, face 3 (M2)

Colouration of scanned points in layer 3 for M2		
Face 3-Layer 3-P_7 @ 3days	Face 3-Layer 3-P_8 @ 3days	Face 3-Layer 3-P_9 @ 3days
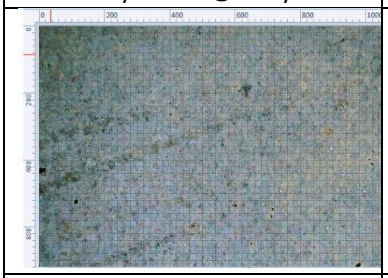	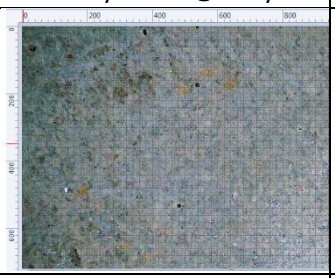	
Face 3-Layer 3-P_7 @ 7days	Face 3-Layer 3-P_8 @ 7days	Face 3-Layer 3-P_9 @ 7days
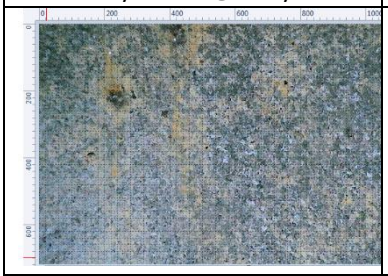	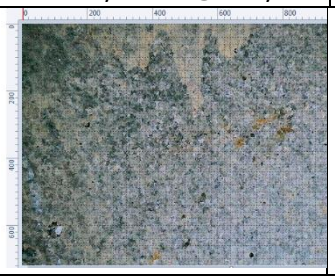	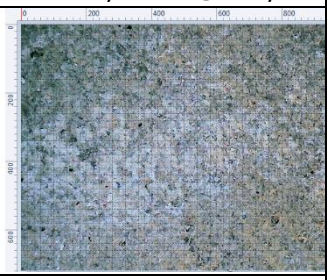
Face 3-Layer 3-P_7 @ 14days	Face 3-Layer 3-P_8 @ 14days	Face 3-Layer 3-P_9 @ 14days
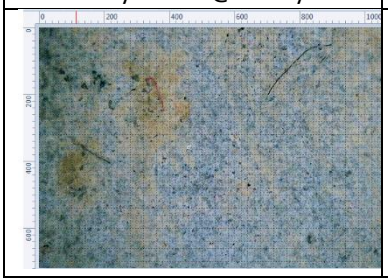	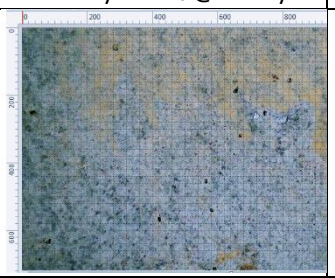	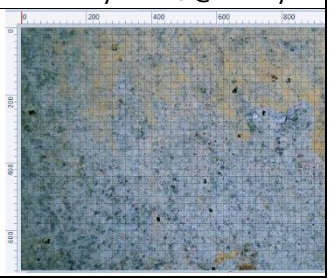
Face 3-Layer 3-P_7 @ 21days	Face 3-Layer 3-P_8 @ 21days	Face 3-Layer 3-P_9 @ 21days
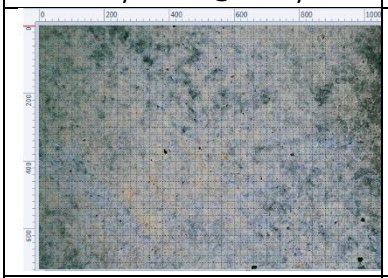	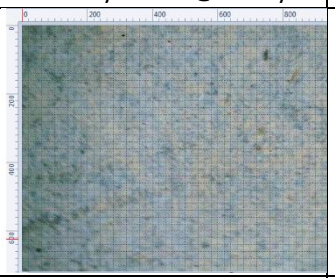	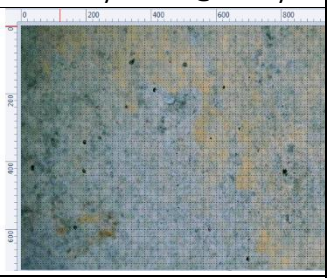
Face 3-Layer 3-P_7 @ 28days	Face 3-Layer 3-P_8 @ 28days	Face 3-Layer 3-P_9 @ 28days
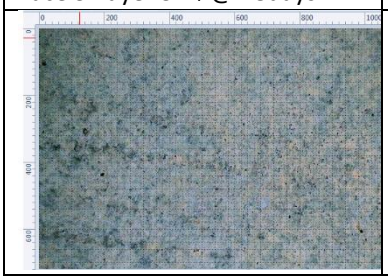	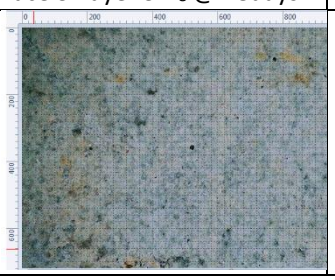	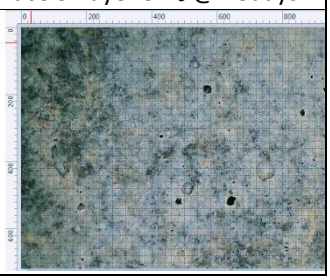

Table 4.a: Description of the cement grain colouration under curing conditions for points (P4, P5 and P6) corresponding to layer 2, face 1 (M1)

Coloration of scanned points in layer 2 for M 1		
Face 1-Layer 2-P_4 @ 3days	Face 1-Layer 2-P_5 @ 3days	Face 1-Layer 2-P_6 @ 3days
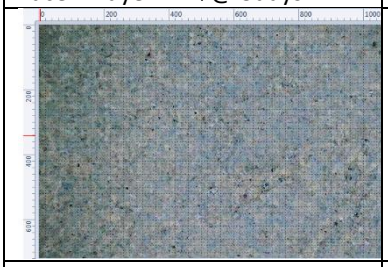	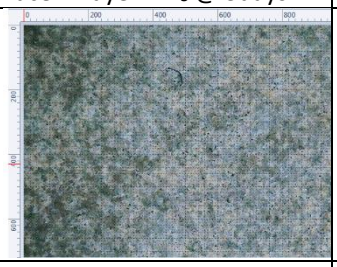	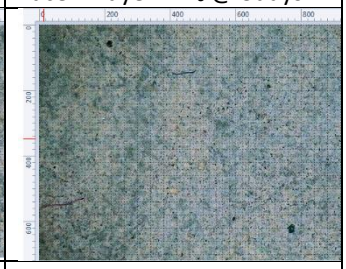
Face 1-Layer 2-P_4 @ 7days	Face 1-Layer 2-P_5 @ 7days	Face 1-Layer 2-P_6 @ 7days
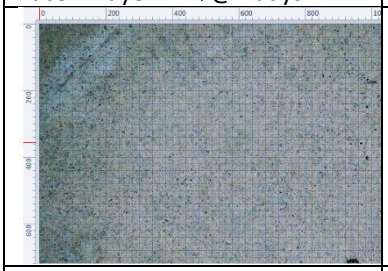	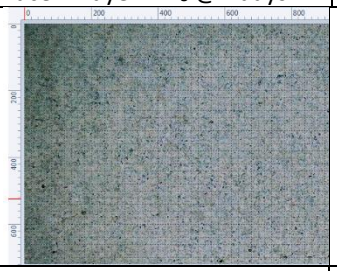	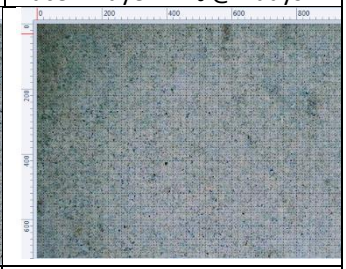
Face 1-Layer 2-P_4 @ 14days	Face 1-Layer 2-P_5 @ 14days	Face 1-Layer 2-P_6 @ 14days
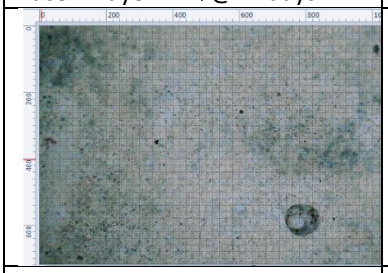	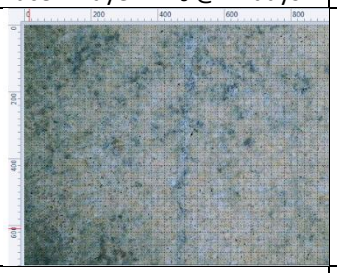	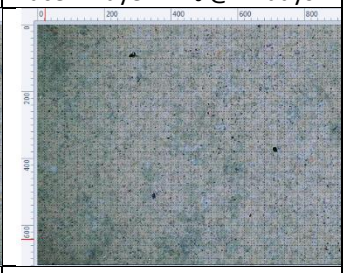
Face 1-Layer 2-P_4 @ 21days	Face 1-Layer2-P_5 @ 21days	Face 1-Layer 2-P_6 @ 21days
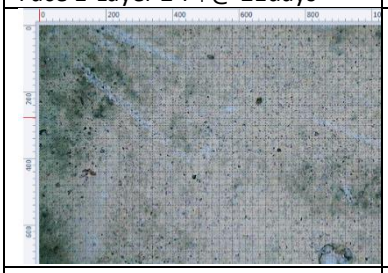	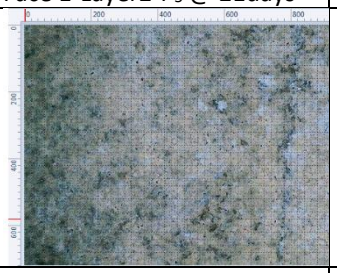	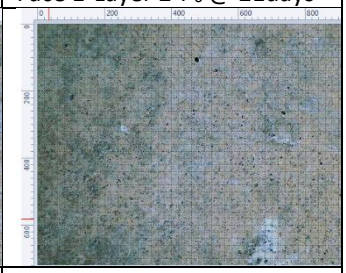
Face 1-Layer 2-P_4 @ 28days	Face 1-Layer 2-P_5 @ 28days	Face 1-Layer 2-P_6 @ 28days
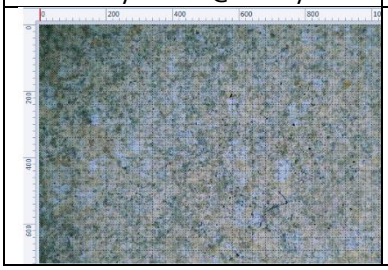	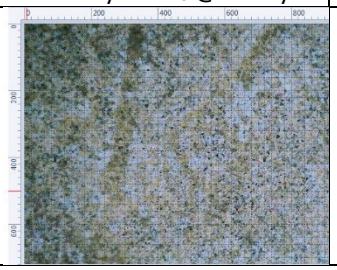	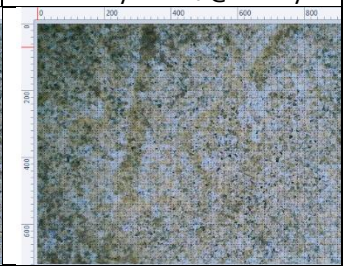

Table 5.a: Description of the cement grain colouration under curing conditions for points (P7, P8 and P9) corresponding to layer 3, face 1 (M1)

Colouration of scanned points in layer 3 for M1		
Face 1-Layer 3-P_7 @ 3days	Face 1-Layer 3-P_8 @ 3days	Face 1-Layer 3-P_9 @ 3days
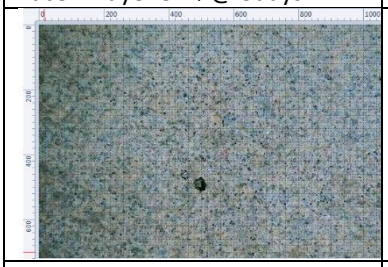	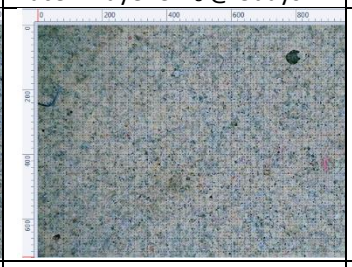	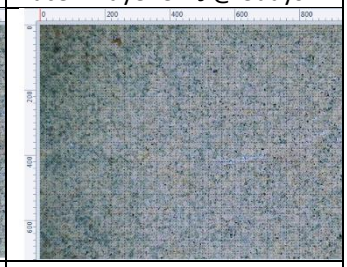
Face 1-Layer 3-P_7 @ 7days	Face 1-Layer 3-P_8 @ 7days	Face 1-Layer 3-P_9 @ 7days
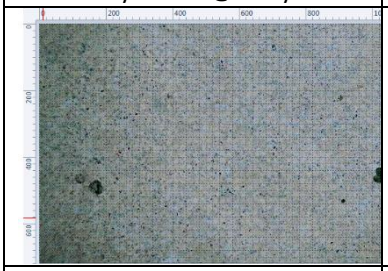	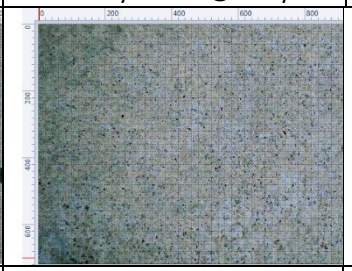	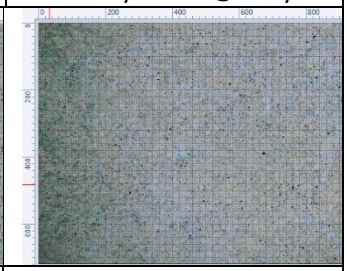
Face 1-Layer 3-P_7 @ 14days	Face 1-Layer 3-P_8 @ 14days	Face 1-Layer 3-P_9 @ 14days
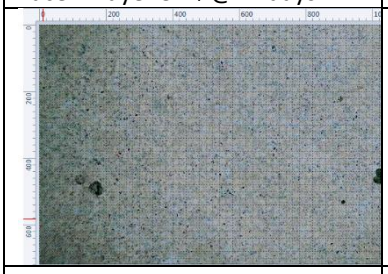		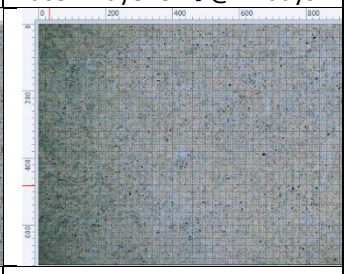
Face 1-Layer 3-P_7 @ 21days	Face 1-Layer 3-P_8 @ 21days	Face 1-Layer 3-P_9 @ 21days
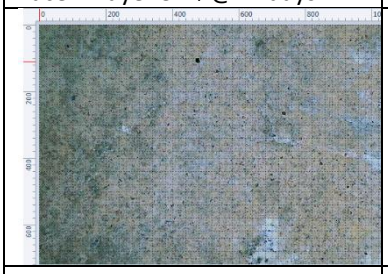	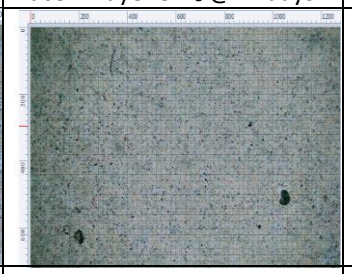	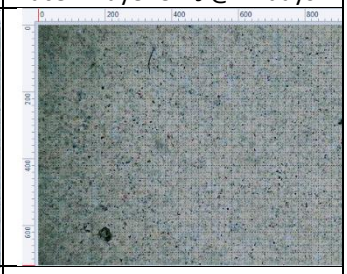
Face 1-Layer 3-P_7 @ 28days	Face 1-Layer 3-P_8 @ 28days	Face 1-Layer 3-P_9 @ 28days
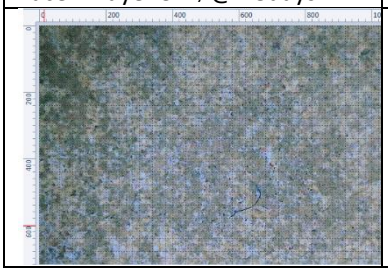	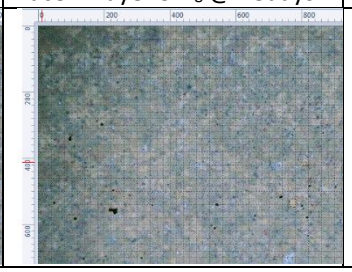	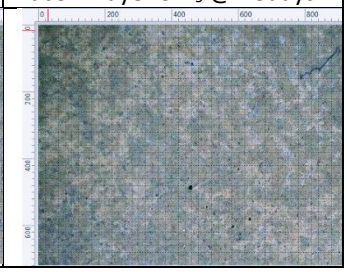

Appendix B: Description of the cement grain coloration under corrosion conditions

Table 1.b: Description of the cement grain coloration under corrosion conditions for points corresponding to face2, layer 1 (M1)

Colouration of scanned points in layer 1 for M 1		
Face 2-Layer 1-P_1 @ 3days	Face 2-Layer 1-P_2 @ 3days	Face 2-Layer 1-P_3 @ 3days
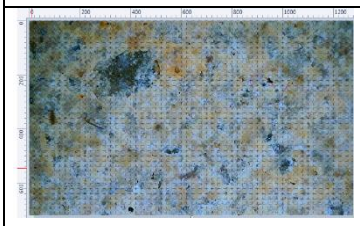	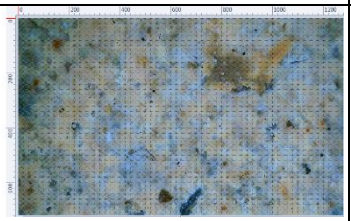	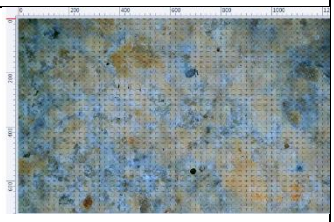
Face 2-Layer 1-P_1 @ 6days	Face 2-Layer 1-P_2 @ 6days	Face 2-Layer 1-P_3 @ 6days
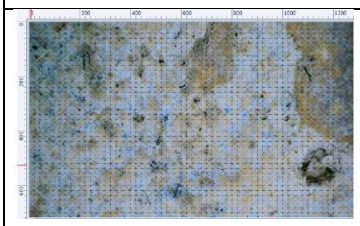	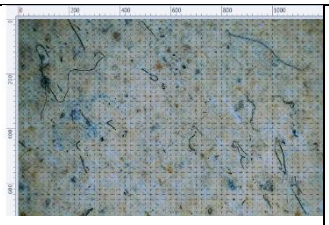	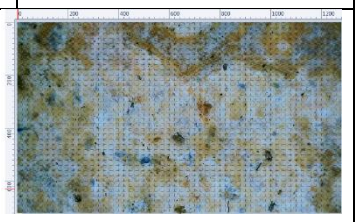
Face 2-Layer 1-P_1 @ 9days	Face 2-Layer 1-P_2 @ 9days	Face 2-Layer 1-P_3 @ 9days
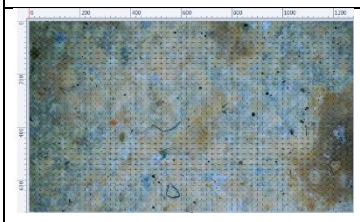	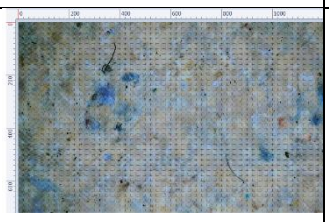	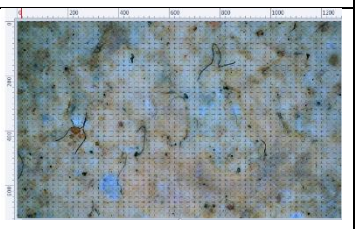
Face 2-Layer 1-P_1 @ 12days	Face 2-Layer1-P_2 @ 12days	Face 2-Layer 1-P_3 @ 12days
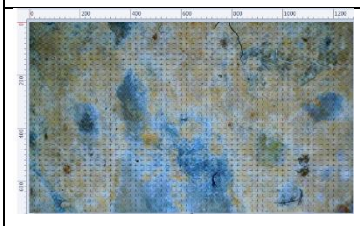	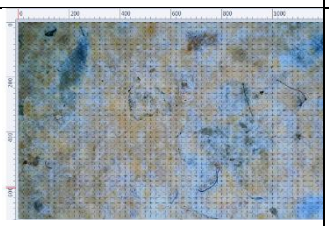	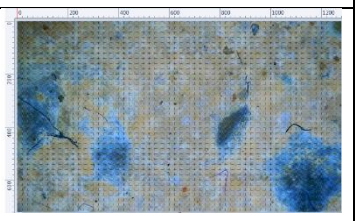
Face 2-Layer 1-P_1 @ 18days	Face 2-Layer 1-P_2 @ 18days	Face 2-Layer 1-P_3 @ 18days
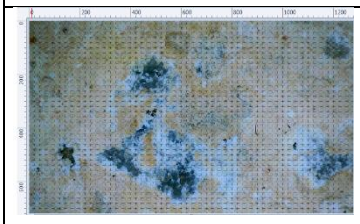	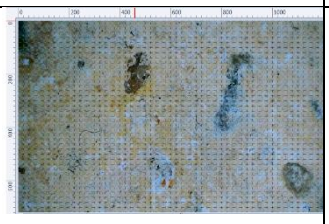	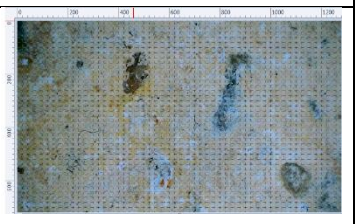

Face 2-Layer 1-P_1 @ 24days	Face 2-Layer 1-P_2 @ 24days	Face 2-Layer 1-P_3 @ 24days
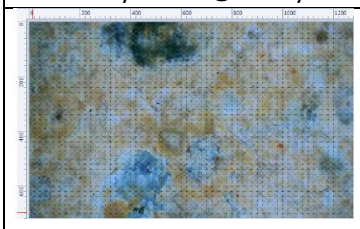	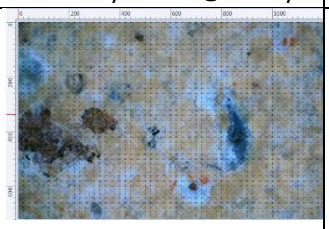	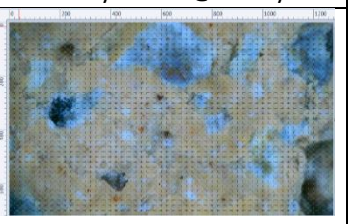
Face 2-Layer 1-P_1 @ 27days	Face 2-Layer 1-P_2 @ 27days	Face 2-Layer 1-P_3 @ 27days
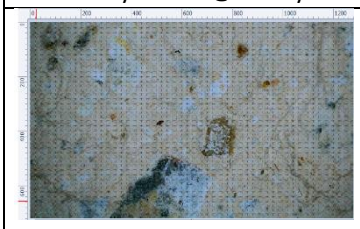	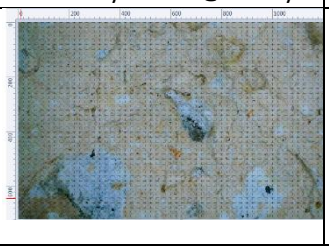	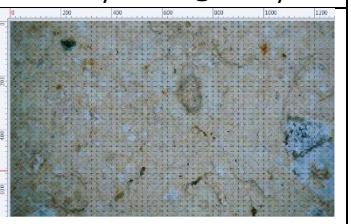

Table 2.b: Description of the cement grain colouration under corrosion conditions for points (P4, P5 and P6) corresponding to face 4, layer 2 (M1)

Colouration of scanned points in layer 2 for M 1		
Face 4-Layer 2-P_4 @ 3days	Face 4-Layer 2-P_5 @ 3days	Face 4-Layer 2-P_6 @ 3days
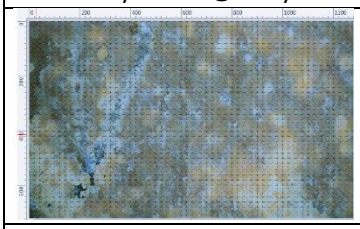	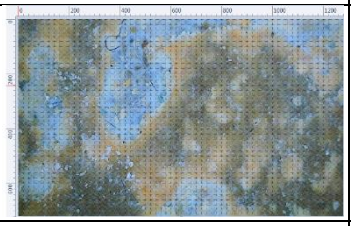	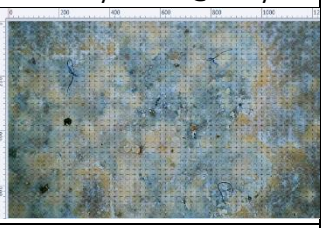
Face 4-Layer 2-P_4 @ 6days	Face 4-Layer 2-P_5 @ 6days	Face 4-Layer 2-P_6 @ 6days
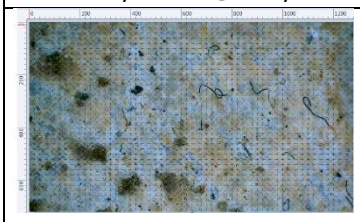	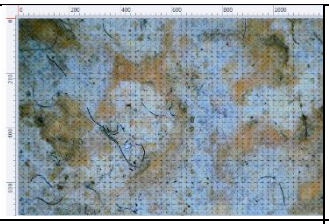	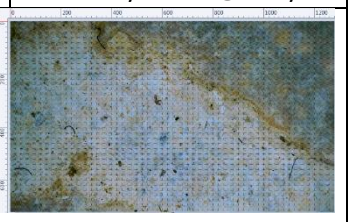
Face 4-Layer 2-P_4 @ 9days	Face 4-Layer 2-P_5 @ 9 days	Face 4-Layer 2-P_6 @ 9days
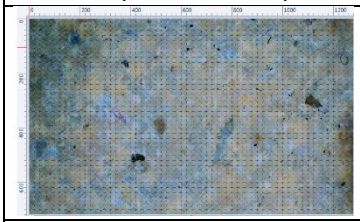	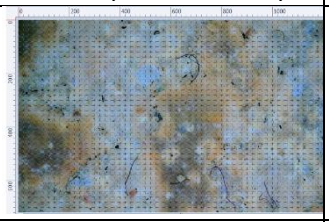	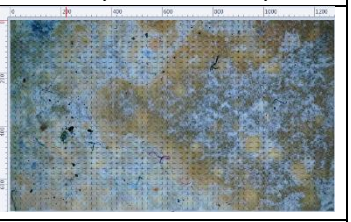
Face 4-Layer 2-P_4 @ 12days	Face 4-Layer2-P_5 @ 12days	Face 4-Layer 2-P_6 @ 12days
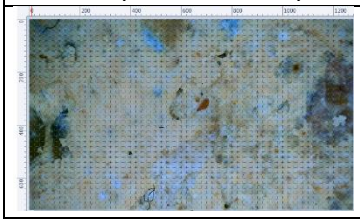	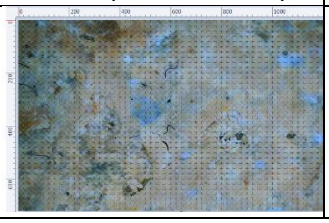	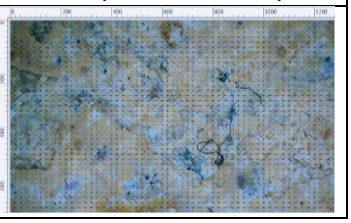

Face 4-Layer 2-P_4 @ 18days	Face 4-Layer 2-P_5 @ 18days	Face 4-Layer 2-P_6 @ 18days
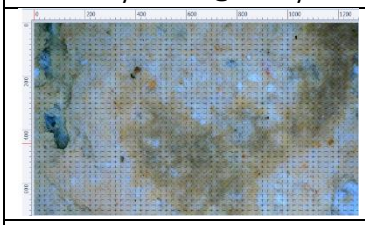	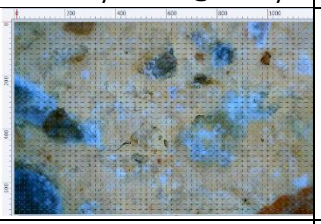	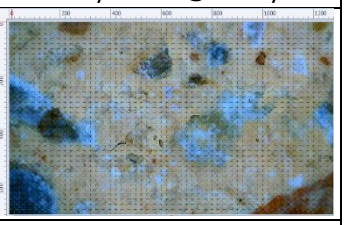
Face 4-Layer 2-P_4 @ 24days	Face 4-Layer 2-P5 @ 24days	Face 4-Layer 2-P6 @ 24days
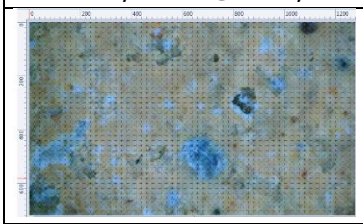	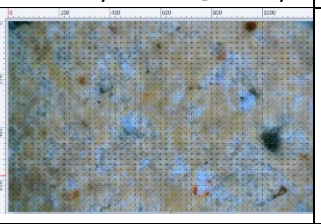	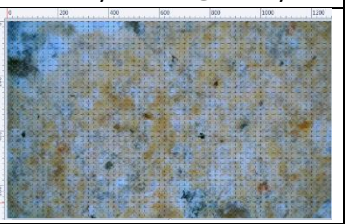
Face 4-Layer 2-P_4 @ 27days	Face 4-Layer 2-P_5 @ 27days	Face 4-Layer 2-P_6 @ 27days
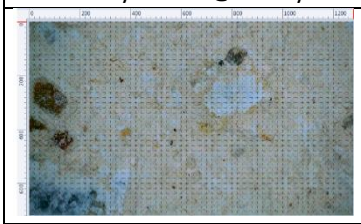	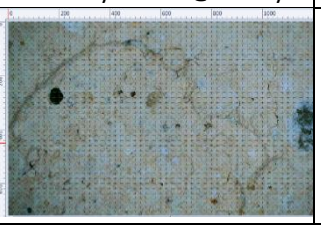	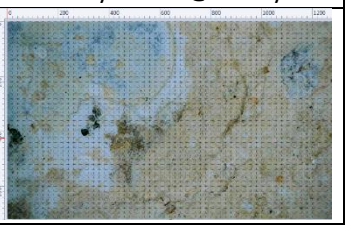

Table 3.b: Description of the cement grain colouration under corrosion conditions for points (P7, P8 and P9) corresponding to face 1, layer 3 (M1)

Colouration of scanned points in layer 3 for Mix 1		
Face 1-Layer 3-P_7 @ 3days	Face 1-Layer3-P_8 @ 3days	Face 1-Layer3-P_9 @ 3days
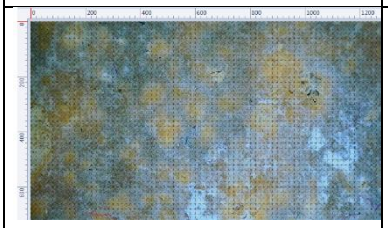	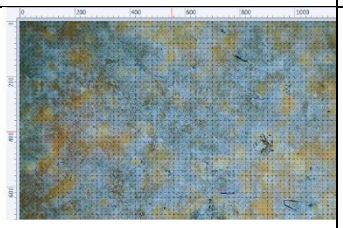	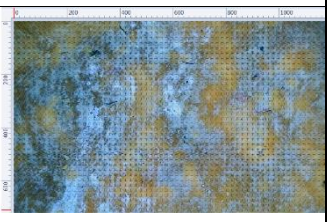
Face 1-Layer3 –P_7 @ 6days	Face 1-Layer3 –P_8 @ 6days	Face 1-Layer 3-P_9 @ 6days
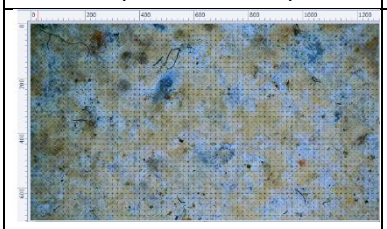	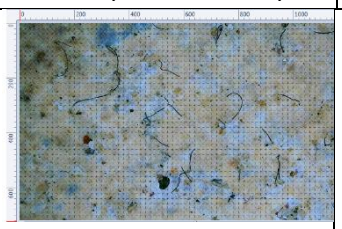	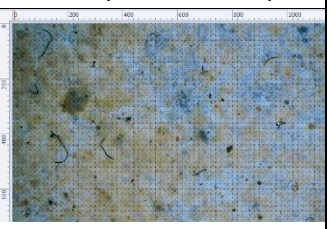
Face 1-Layer 3-P_7 @ 9days	Face 1-Layer 3-P_8 @ 9 days	Face 1-Layer 3-P_9 @ 9days
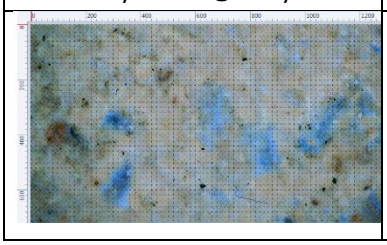	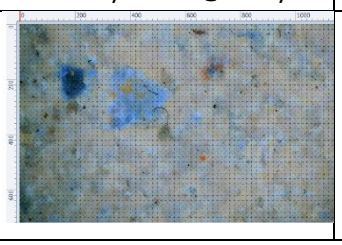	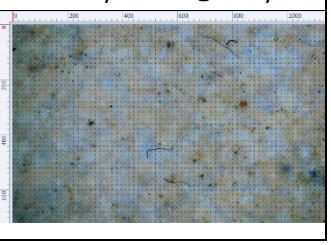

Face 1-Layer 3-P_7 @ 12days	Face 1-Layer3-P_8 @ 12days	Face 1-Layer 3-P_9 @ 12days
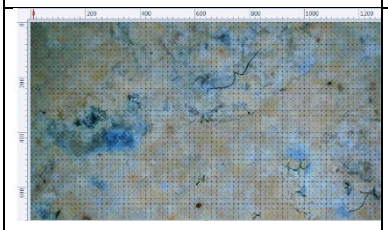	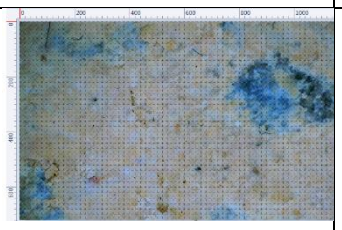	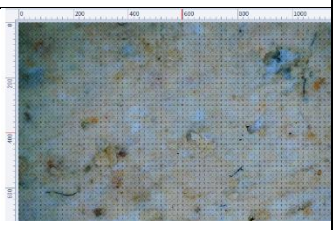
Face 1-Layer 3-P_7 @ 18days	Face 1-Layer 3-P_8 @ 18days	Face 1-Layer 3-P_9 @ 18days
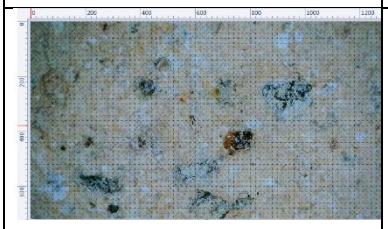	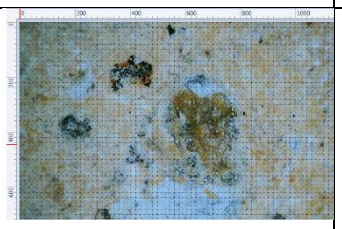	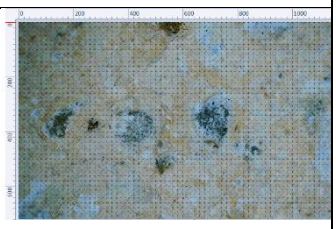
Face 1-Layer 3-P_7 @ 24days	Face 1-Layer 3-P_8 @ 24days	Face 1-Layer 3-P_9 @ 24days
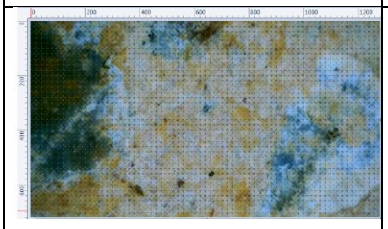	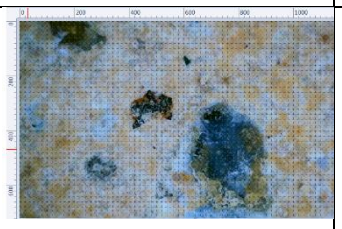	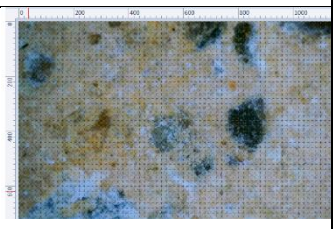
Face 1-Layer 3-P_7 @ 27days	Face 1-Layer 2-P_8 @ 27days	Face 1-Layer 3-P_9 @ 27days
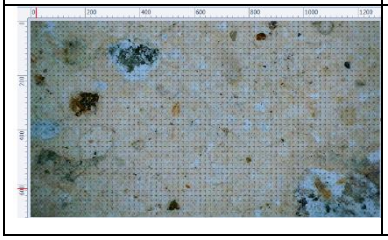	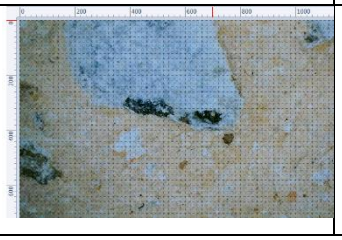	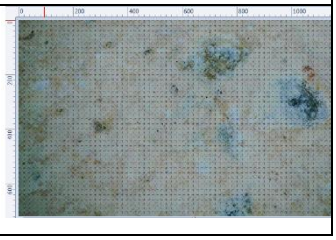

Appendix C: Statistical analysis with regards to the black and white rate for the 9 scanned points under curing and corrosion conditions

Table 1.c: Analysis of the distribution of black and white pixel rates for nine scanned points on Face 1 of the M1 concrete cube (30 MPa) under curing conditions after 7 days

Output Point 1 (Face 1)		Output Point 2 (Face 1)		Output Point 3 (Face 1)	
Black pixel	White pixel	Black pixel	White pixel	Black pixel	White pixel
29.30	70.70	31.50	68.50	26.20	73.80
Output Point 4 (Face 1)		Output Point 5 (Face 1)		Output Point 6 (Face 1)	
18.40	81.60	23.70	76.30	20.80	79.20
Output Point 7 (Face 1)		Output Point 8 (Face 1)		Output Point 9 (Face 1)	
17.00	83.00	30.00	70.00	26.20	73.80

Table 2.c: Analysis of the distribution of black and white pixel rates for nine scanned points on Face 1 of the M1 concrete cube (30 MPa) under curing conditions after 14 days

Output Point 1 (Face 1)		Output Point 2 (Face 1)		Output Point 3 (Face 1)	
Black pixel	White pixel	Black pixel	White pixel	Black pixel	White pixel
19.60	80.40	20.20	79.80	22.10	77.90
Output Point 4 (Face 1)		Output Point 5 (Face 1)		Output Point 6 (Face 1)	
21.40	78.60	18.30	81.70	20.20	79.80
Output Point 7 (Face 1)		Output Point 8 (Face 1)		Output Point 9 (Face 1)	
23.30	76.70	24.30	75.70	17.20	82.80

Table 3.c: Analysis of the distribution of black and white pixel rates for nine scanned points on Face 1 of the M1 concrete cube (30 MPa) under curing conditions after 21 days

Output Point 1 (Face 1)		Output Point 2 (Face 1)		Output Point 3 (Face 1)	
Black pixel	White pixel	Black pixel	White pixel	Black pixel	White pixel
31.10	68.90	24.60	75.40	22.90	77.10
Output Point 4 (Face 1)		Output Point 5 (Face 1)		Output Point 6 (Face 1)	
20.50	79.50	29.10	70.90	27.10	72.90
Output Point 7 (Face 1)		Output Point 8 (Face 1)		Output Point 9 (Face 1)	
27.20	72.80	23.60	76.40	23.50	76.50

Table 4.c: Analysis of the distribution of black and white pixel rates for nine scanned points on Face 1 of the M2 concrete cube (40 MPa) under curing conditions after 3 days

Output Point 1 (Face 1)		Output Point 2 (Face 1)		Output Point 3 (Face 1)	
Black pixel	White pixel	Black pixel	White pixel	Black pixel	White pixel
25.60	74.40	27.50	72.50	29.30	70.70
Output Point 4 (Face 1)		Output Point 5 (Face 1)		Output Point 6 (Face 1)	
32.50	67.50	26.90	73.10	25.40	74.60
Output Point 7 (Face 1)		Output Point 8 (Face 1)		Output Point 9 (Face 1)	
31.00	69.00	26.60	73.40	18.90	81.10

Table 5.c: Analysis of the distribution of black and white pixel rates for nine scanned points on Face 1 of the M2 concrete cube (40 MPa) under curing conditions after 7 days

Output Point 1 (Face 1)		Output Point 2 (Face 1)		Output Point 3 (Face 1)	
Black pixel	White pixel	Black pixel	White pixel	Black pixel	White pixel
28.70	71.3	38.10	61.90	37.60	62.40
Output Point 4 (Face 1)		Output Point 5 (Face 1)		Output Point 6 (Face 1)	
Output Point 7 (Face 1)		Output Point 8 (Face 1)		Output Point 9 (Face 1)	
24.5	75.5	25.7	74.3	22.6	77.4

Table 6.c: Analysis of the distribution of black and white pixel rates for nine scanned points on Face 1 of the M2 concrete cube (40 MPa) under curing conditions after 28 days

Output Point 1 (Face 1)		Output Point 2 (Face 1)		Output Point 3 (Face 1)	
Black pixel	White pixel	Black pixel	White pixel	Black pixel	White pixel
36.30	63.70	27.30	72.70	21.50	78.50
Output Point 4 (Face 1)		Output Point 5 (Face 1)		Output Point 6 (Face 1)	
24.70	75.30	24.20	75.80	23.90	76.10
Output Point 7 (Face 1)		Output Point 8 (Face 1)		Output Point 9 (Face 1)	
24.70	75.30	19.20	80.80	26.20	73.80

Table 7.c: Analysis of the distribution of black and white pixel rates for nine scanned points on Face 1 of the M1 concrete cube (30 MPa) under corrosion conditions after 6 days

Output Point 1 (Face 1)		Output Point 2 (Face 1)		Output Point 3 (Face 1)	
Black pixel	White pixel	Black pixel	White pixel	Black pixel	White pixel
20.90	79.10	19.00	81.00	22.20	77.80
Output Point 4 (Face 1)		Output Point 5 (Face 1)		Output Point 6 (Face 1)	
33.60	66.40	26.60	73.40	24.30	75.70
Output Point 7 (Face 1)		Output Point 8 (Face 1)		Output Point 9 (Face 1)	
28.20	71.80	19.30	80.70	23.00	77.00

Table 8.c: Analysis of the distribution of black and white pixel rates for nine scanned points on Face 1 of the M1 concrete cube (30 MPa) under corrosion conditions after 18 days

Output Point 1 (Face 1)		Output Point 2 (Face 1)		Output Point 3 (Face 1)	
Black pixel	White pixel	Black pixel	White pixel	Black pixel	White pixel
28.40	71.60	29.70	70.30	25.50	74.50
Output Point 4 (Face 1)		Output Point 5 (Face 1)		Output Point 6 (Face 1)	
20.00	80.00	24.40	75.60	27.40	72.60
Output Point 4 (Face 1)		Output Point 5 (Face 1)		Output Point 6 (Face 1)	
23.10	76.90	20.30	79.70	21.00	79.00

Table 9.c: Analysis of the distribution of black and white pixel rates for nine scanned points on Face 1 of the M1 concrete cube (30 MPa) under corrosion conditions after 24 days

Output Point 1 (Face 1)		Output Point 2 (Face 1)		Output Point 3 (Face 1)	
Black pixel	White pixel	Black pixel	White pixel	Black pixel	White pixel
32.10	67.90	31.40	68.60	30.70	69.30
Output Point 4 (Face 1)		Output Point 5 (Face 1)		Output Point 6 (Face 1)	
26.10	73.90	34.00	66.00	29.70	70.30
Output Point 7 (Face 1)		Output Point 8 (Face 1)		Output Point 9 (Face 1)	
35.00	65.00	22.50	77.50	29.90	70.10

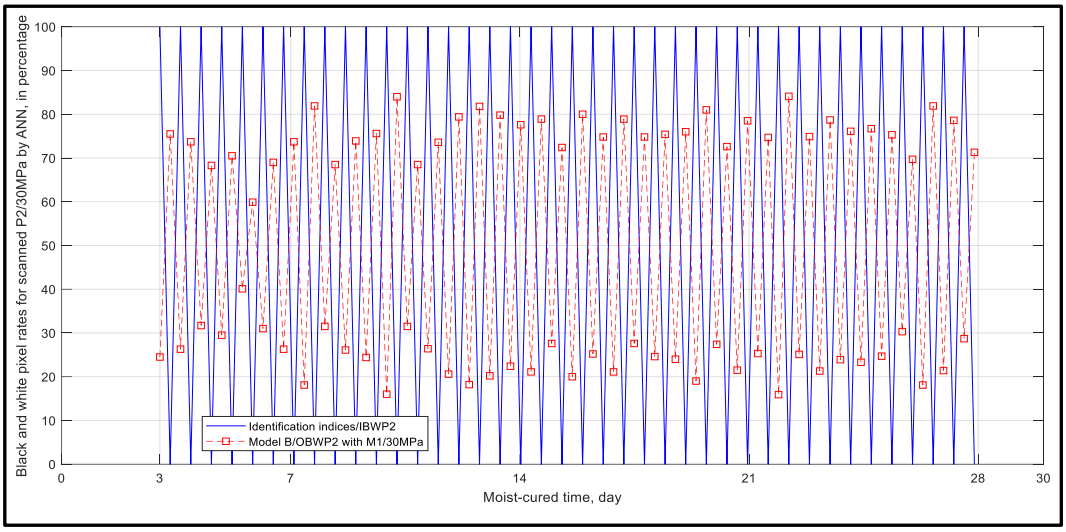

Figure 1.c: Model B/OBWP2 with M1/30MPa and IBWP2 for evaluating the black and white pixel rates into scanned point 2 under curing conditions

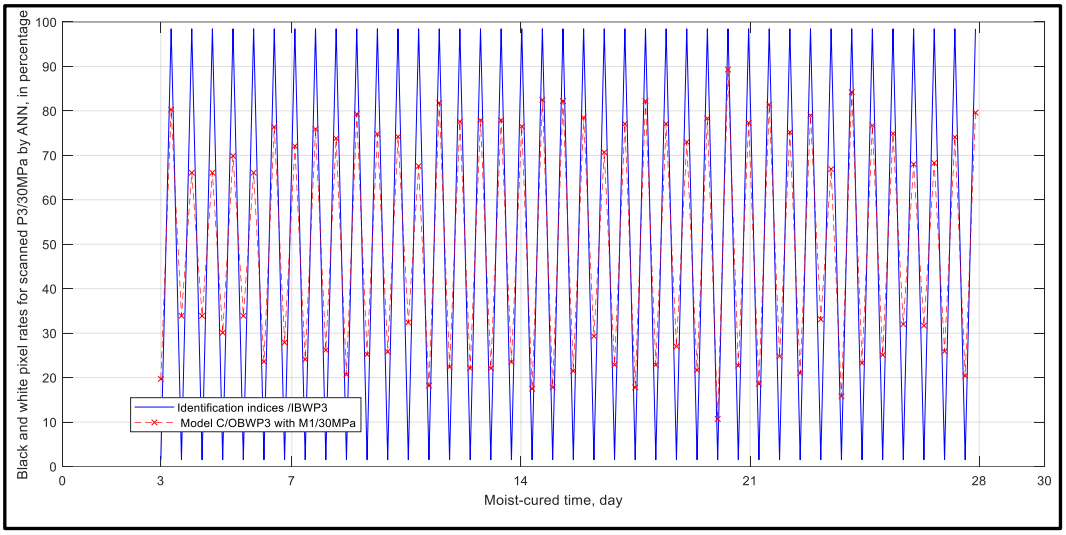

Figure 2 .c: Model C/OBWP3 with M1/30MPa and IBWP3 for evaluating the black and white pixel rates into scanned point 3 under curing conditions

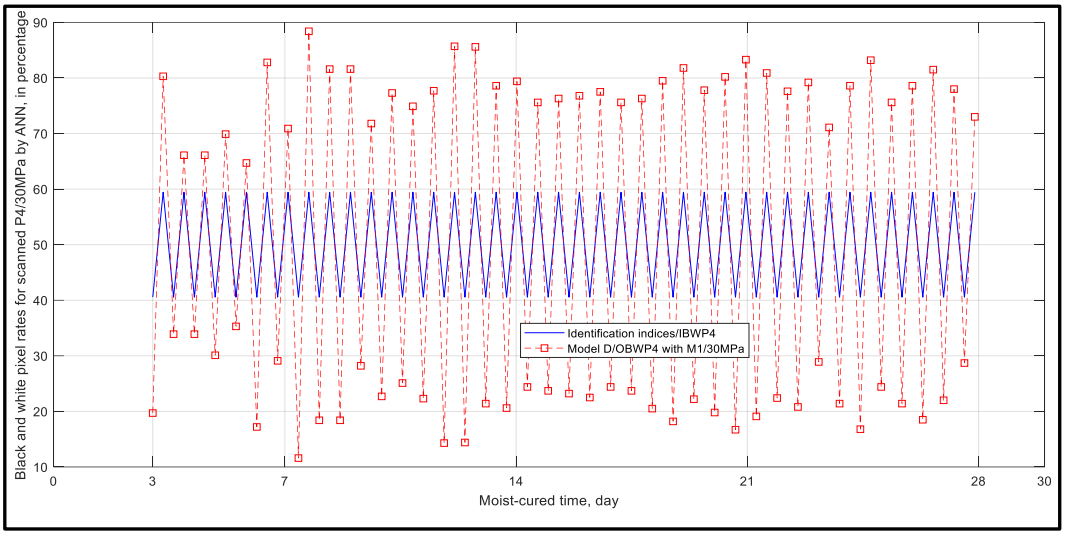

Figure 3.c: Model D/OBWP4 with M1/30MPa and IBWP4 for evaluating the black and white pixel rates into scanned point 4 under curing conditions

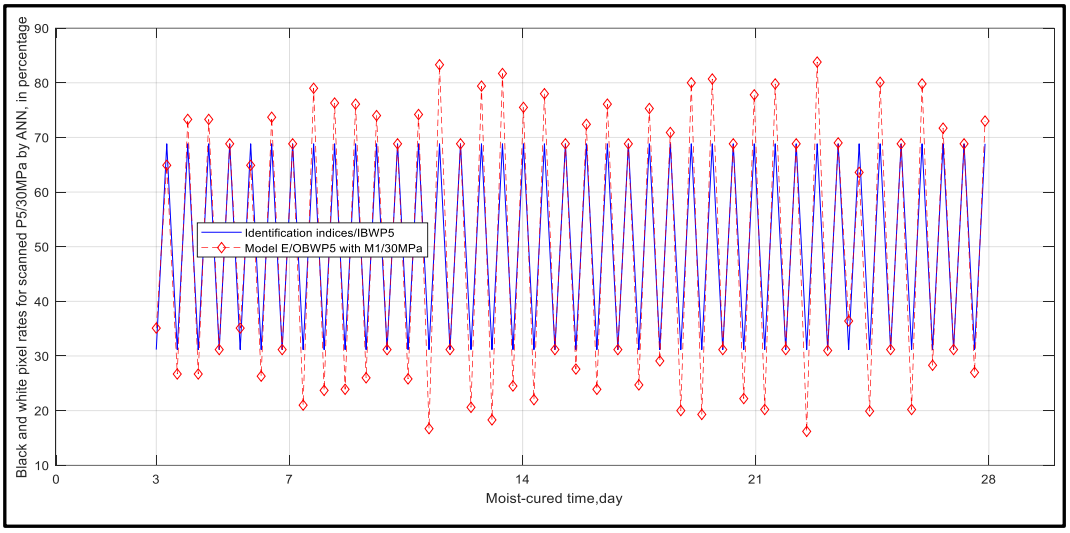

Figure 4.c: Model E/OBWP5 with M1/30MPa and IBWP5 for evaluating the black and white pixel rates into scanned point 5 under curing conditions

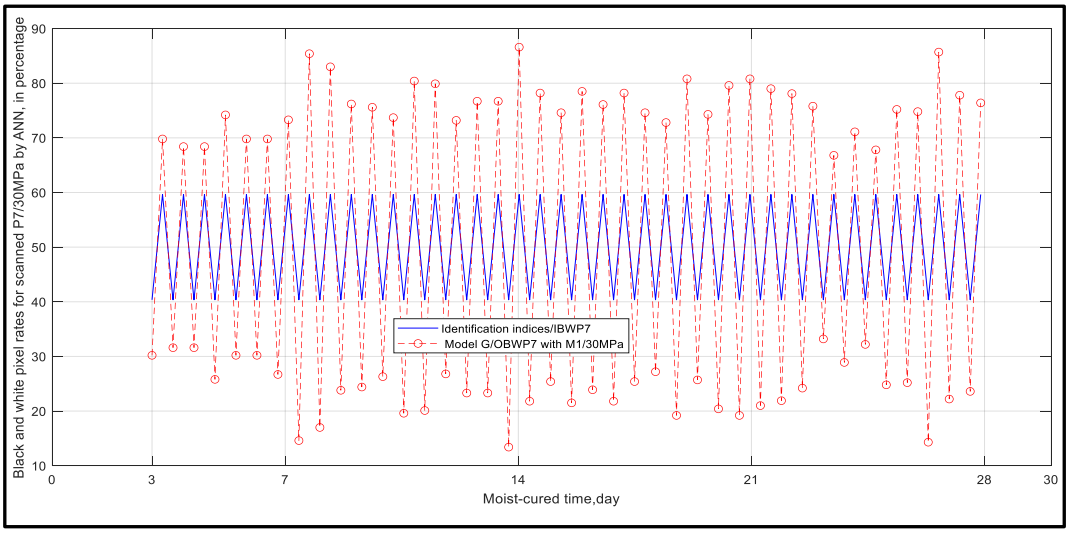

Figure 5.c: Model G/OBWP7 with M1/30MPa and IBWP7 for evaluating the black and white pixel rates into scanned point 7 under curing conditions

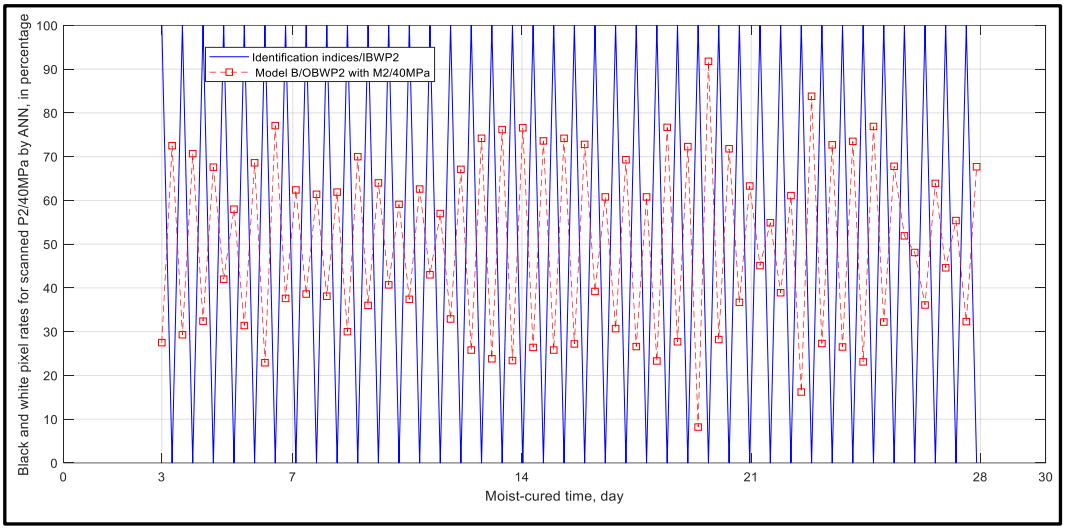

Figure 6.c: Model B/OBWP2 with M2/40MPa and IBWP2 for evaluating the black and white pixel rates into scanned point 2 under curing conditions

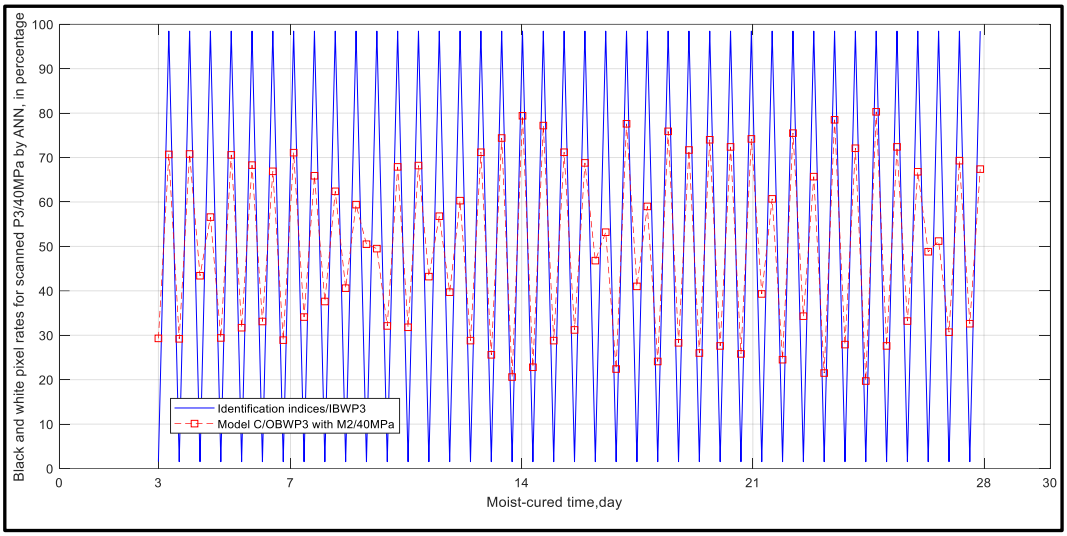

Figure 7.c: Model C/OBWP3 with M2/40MPa and IBWP3 for evaluating the black and white pixel rates into scanned point 3 under curing conditions

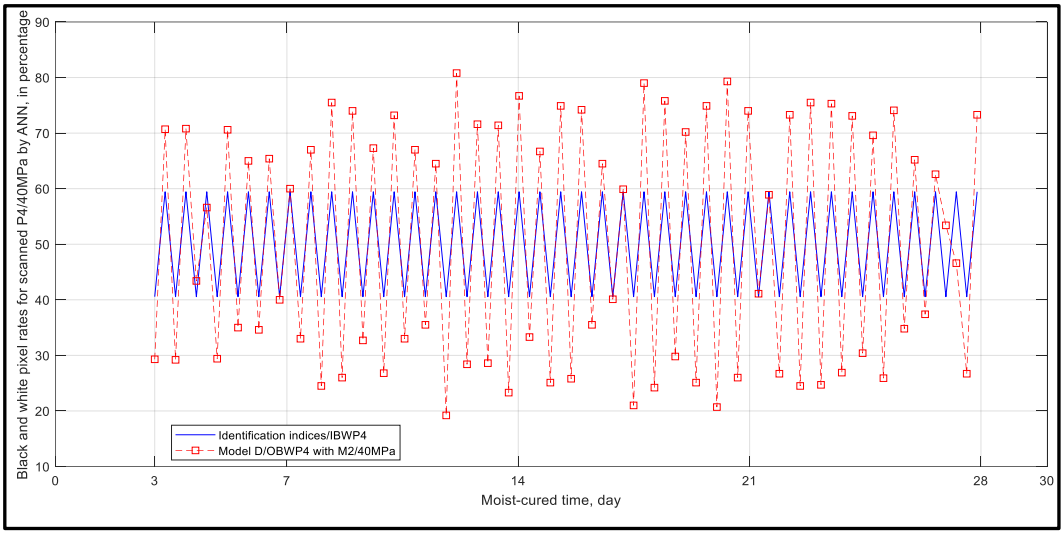

Figure 8.c: Model D/OBWP4 with M2/40MPa and IBWP4 for evaluating the black and white pixel rates into scanned point 4 under curing conditions

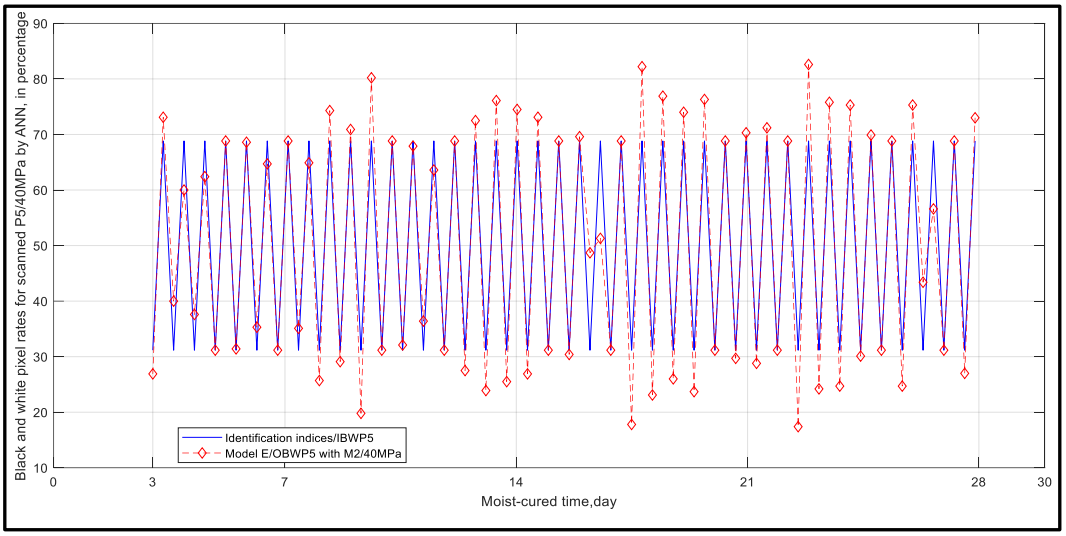

Figure 9.c: Model E/OBWP5 with M2/40MPa and IBWP5 for evaluating the black and white pixel rates into scanned point 5 under curing conditions

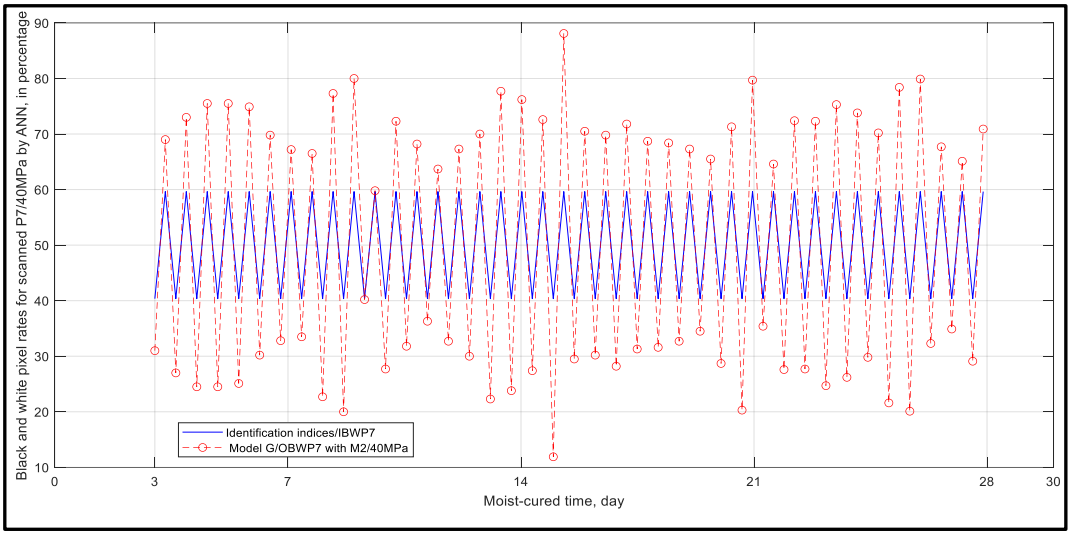

Figure 10.c: Model G/OBWP7 with M2/40MPa and IBWP7 for evaluating the black and white pixel rates into scanned point 7 under curing conditions

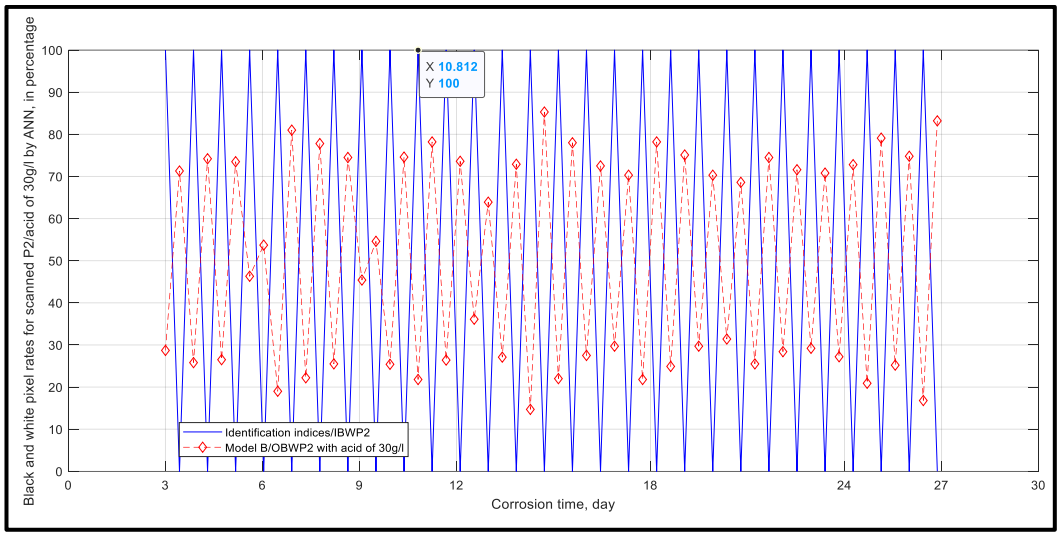

Figure 11.c: Model B/OBWP2 with M1/30MPa and IBWP2, tested to sulphuric acid of 30 g/ℓ, for evaluating the black and white pixel rates into scanned point 2 under corrosion conditions

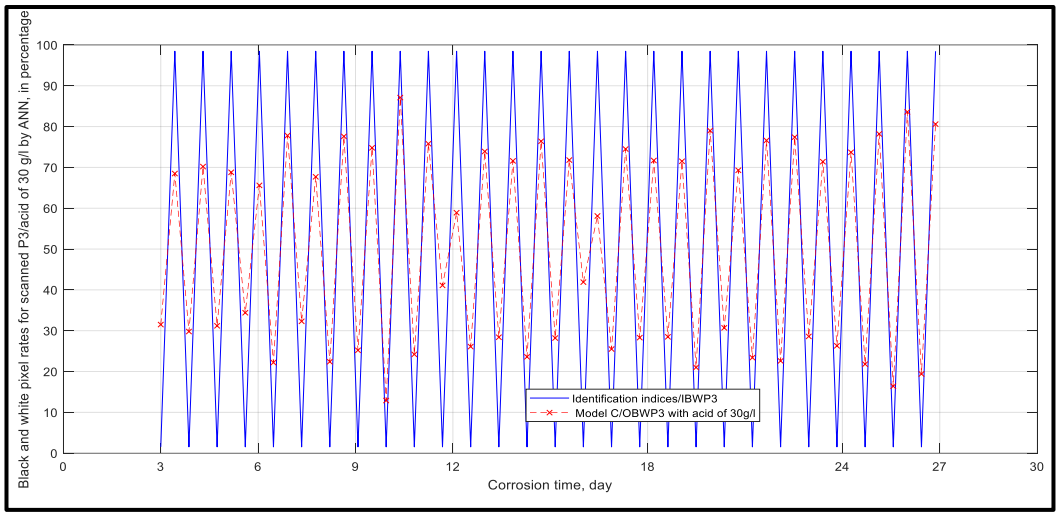

Figure 12.c: Model C/OBWP3 with M1/30MPa and IBWP3, tested to sulphuric acid of 30 g/ℓ, for evaluating the black and white pixel rates into scanned point 3 under corrosion conditions

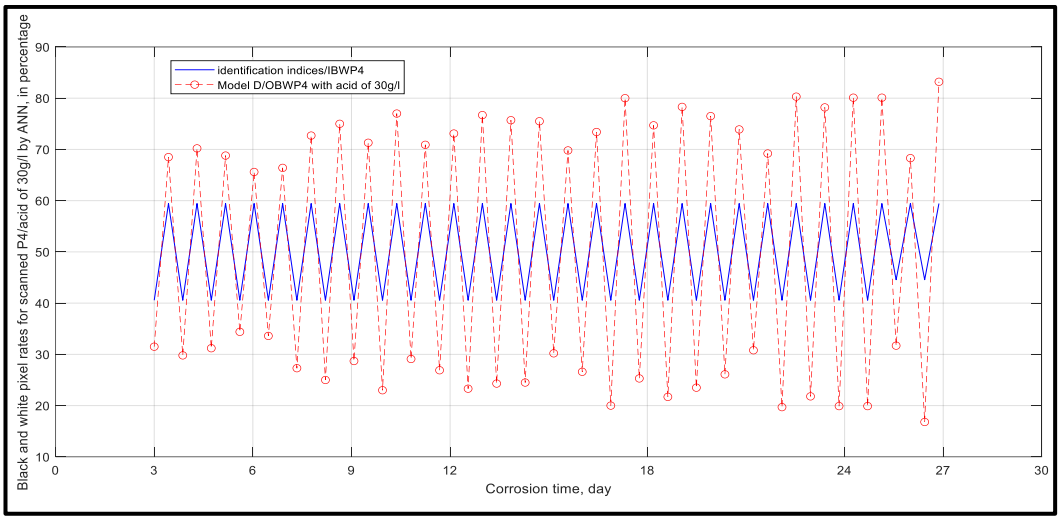

Figure 13.c: Model D/OBWP4 with M1/30MPa and IBWP4, tested to sulphuric acid of 30 g/ℓ, for evaluating the black and white pixel rates into scanned point 4 under corrosion conditions

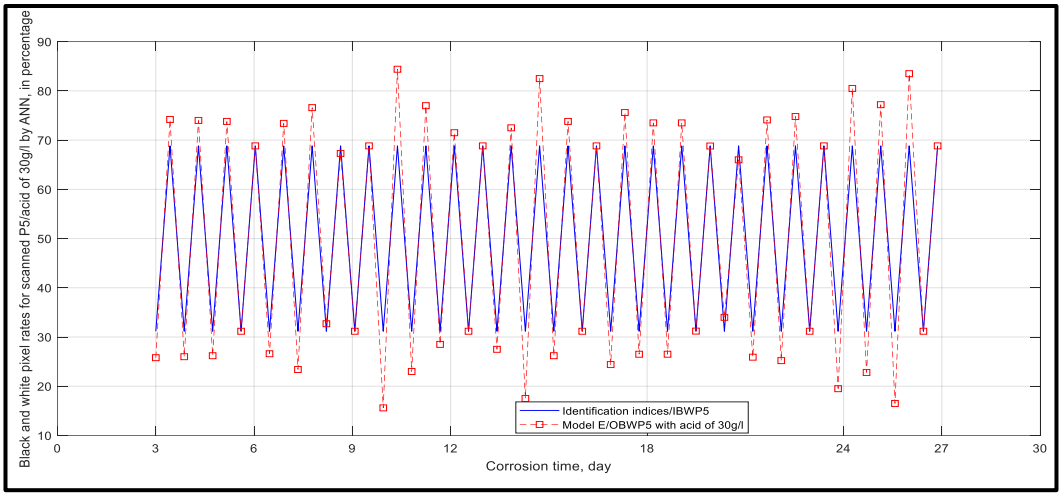

Figure 14.c: Model E/OBWP5 with M1/30MPa and IBWP5, tested to sulphuric acid of 30 g/ℓ, for evaluating the black and white pixel rates into scanned point 5 under corrosion conditions

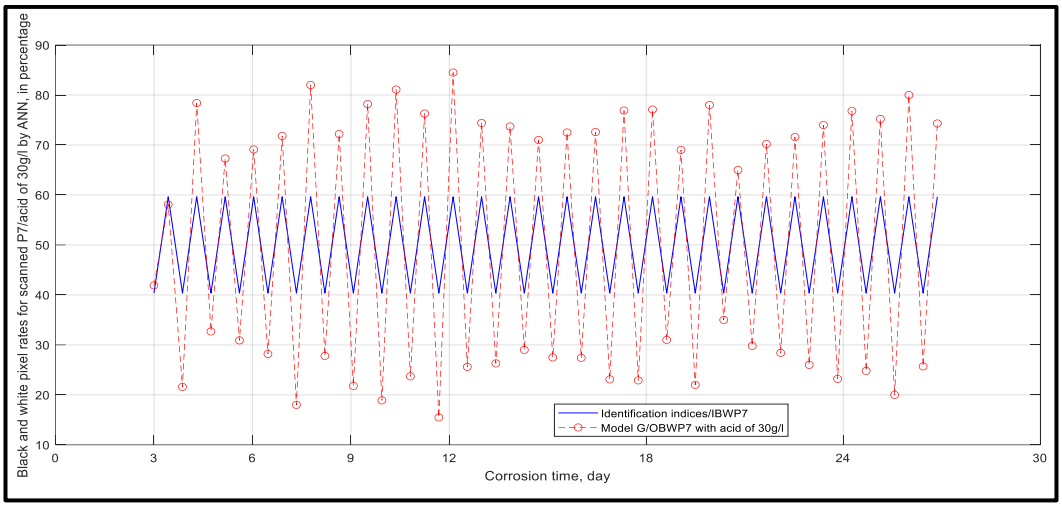

Figure 15.c: Model G/OBWP7 with M1/30MPa and IBWP7, tested to sulphuric acid of 30 g/ℓ, for evaluating the black and white pixel rates into scanned point 7 under corrosion conditions

Appendix D: Additional equations with regards to the SCFr_CGC$_{(\gamma 1\text{-}3)}$ versus six points (P_4 to P_9)

$$M_{x5} = M_{f1}^{l2} = \begin{vmatrix} \mu(\gamma 1,4)_{f_1,l_2} & \mu(\gamma 1,5)_{f_1,l_2} & \mu(\gamma 1,6)_{f_1,l_2} \\ \mu(\gamma 2,4)_{f_1,l_2} & \mu(\gamma 2,5)_{f_1,l_2} & \mu(\gamma 2,6)_{f_1,l_2} \\ \mu(\gamma 3,4)_{f_1,l_2} & \mu(\gamma 3,5)_{f_1,l_2} & \mu(\gamma 3,6)_{f_1,l_2} \end{vmatrix} \quad (5.19.d)$$

$$M_{x6} = M_{f2}^{l2} = \begin{vmatrix} \mu(\gamma 1,4)_{f_2,l_2} & \mu(\gamma 1,5)_{f_2,l_2} & \mu(\gamma 1,6)_{f_2,l_2} \\ \mu(\gamma 2,4)_{f_2,l_2} & \mu(\gamma 2,5)_{f_2,l_2} & \mu(\gamma 2,6)_{f_2,l_2} \\ \mu(\gamma 3,4)_{f_2,l_2} & \mu(\gamma 3,5)_{f_2,l_2} & \mu(\gamma 3,6)_{f_2,l_2} \end{vmatrix} \quad (5.20.d)$$

$$M_{x7} = M_{f3}^{l2} = \begin{vmatrix} \mu(\gamma 1,4)_{f_3,l_2} & \mu(\gamma 1,5)_{f_3,l_2} & \mu(\gamma 1,6)_{f_3,l_2} \\ \mu(\gamma 2,4)_{f_3,l_2} & \mu(\gamma 2,5)_{f_3,l_2} & \mu(\gamma 2,6)_{f_3,l_2} \\ \mu(\gamma 3,4)_{f_3,l_2} & \mu(\gamma 3,5)_{f_3,l_2} & \mu(\gamma 3,6)_{f_3,l_2} \end{vmatrix} \quad (5.21.d)$$

$$M_{x8} = M_{f4}^{l2} = \begin{vmatrix} \mu(\gamma 1,4)_{f_4,l_2} & \mu(\gamma 1,5)_{f_4,l_2} & \mu(\gamma 1,6)_{f_4,l_2} \\ \mu(\gamma 2,4)_{f_4,l_2} & \mu(\gamma 2,5)_{f_4,l_2} & \mu(\gamma 2,6)_{f_4,l_2} \\ \mu(\gamma 3,4)_{f_4,l_2} & \mu(\gamma 3,5)_{f_4,l_2} & \mu(\gamma 3,6)_{f_4,l_2} \end{vmatrix} \quad (5.22.d)$$

$$M_{x9} = M_{f1}^{l3} = \begin{vmatrix} \mu(\gamma 1,7)_{f_1,l_3} & \mu(\gamma 1,8)_{f_1,l_3} & \mu(\gamma 1,9)_{f_1,l_3} \\ \mu(\gamma 2,7)_{f_1,l_3} & \mu(\gamma 2,8)_{f_1,l_3} & \mu(\gamma 2,9)_{f_1,l_3} \\ \mu(\gamma 3,7)_{f_1,l_3} & \mu(\gamma 3,8)_{f_1,l_3} & \mu(\gamma 3,9)_{f_1,l_3} \end{vmatrix} \quad (5.23.d)$$

$$M_{x10} = M_{f2}^{l3} = \begin{vmatrix} \mu(\gamma 1,7)_{f_2,l_3} & \mu(\gamma 1,8)_{f_2,l_3} & \mu(\gamma 1,9)_{f_2,l_3} \\ \mu(\gamma 2,7)_{f_2,l_3} & \mu(\gamma 2,8)_{f_2,l_3} & \mu(\gamma 2,9)_{f_2,l_3} \\ \mu(\gamma 3,7)_{f_2,l_3} & \mu(\gamma 3,8)_{f_2,l_3} & \mu(\gamma 3,9)_{f_2,l_3} \end{vmatrix} \quad (5.24.d)$$

$$M_{x11} = M_{f3}^{l3} = \begin{vmatrix} \mu(\gamma 1,7)_{f_3,l_3} & \mu(\gamma 1,8)_{f_3,l_3} & \mu(\gamma 1,9)_{f_3,l_3} \\ \mu(\gamma 2,7)_{f_3,l_3} & \mu(\gamma 2,8)_{f_3,l_3} & \mu(\gamma 2,9)_{f_3,l_3} \\ \mu(\gamma 3,7)_{f_3,l_3} & \mu(\gamma 3,8)_{f_3,l_3} & \mu(\gamma 3,9)_{f_3,l_3} \end{vmatrix} \quad (5.25.d)$$

$$M_{x12} = M_{f4}^{l3} = \begin{vmatrix} \mu(\gamma 1,7)_{f_4,l_3} & \mu(\gamma 1,8)_{f_4,l_3} & \mu(\gamma 1,9)_{f_4,l_3} \\ \mu(\gamma 2,7)_{f_4,l_3} & \mu(\gamma 2,8)_{f_4,l_3} & \mu(\gamma 2,9)_{f_4,l_3} \\ \mu(\gamma 3,7)_{f_4,l_3} & \mu(\gamma 3,8)_{f_4,l_3} & \mu(\gamma 3,9)_{f_4,l_3} \end{vmatrix} \quad (5.26.d)$$

Appendix E: Matrices of colour frequency similarity values related to M2/40MPa

Table 1.e: Colour frequency similarity values associated with cement grain hydration (CGH) on Faces 1 – 8 after 3 days of curing (M2 / 40 MPa)

Reference to layers of concrete cubes	Rate of cement grain hydration within CGC images at 3 days, in percentage			
	α1	α2	α3	β1
L_1	9.72	9.72	13.89	0.00
L_2	13.89	1.39	18.06	0.00
L_3	18.06	2.78	12.50	0.00

Table 2.e: Colour frequency similarity values associated with cement grain hydration (CGH) on Faces 1 – 8 after 7 days of curing (M2 / 40 MPa)

Reference to layers of concrete cubes	Rate of cement grain hydration within CGC images at 7 days, in percentage			
	α1	α2	α3	β1
L_1	18.06	2.78	12.50	0.00
L_2	12.50	5.56	15.28	0.00
L_3	15.28	0.00	9.72	8.33

Table 3.e: Colour frequency similarity values associated with cement grain hydration (CGH) on Face 1 – 8 after 14 days of curing (M2 / 40 MPa)

Reference to layers of concrete cubes	Rate of cement grain hydration within CGC images at 14 days, in percentage			
	α1	α2	α3	β1
L_1	0.00	0.00	11.11	22.22
L_2	4.17	0.00	19.44	9.72
L_3	4.17	0.00	18.06	11.11

Table 4.e: Colour frequency similarity values associated with cement grain hydration (CGH) on Face 1-8 after 21 days of curing (M2 / 40 MPa)

Reference to layers of concrete cubes	Rate of cement grain hydration within CGC images at 21 days, in percentage			
	α1	**α2**	**α3**	**β1**
L_1	4.17	0.00	25.00	4.17
L_2	1.39	0.00	25.00	6.94
L_3	4.17	0.00	18.06	11.11

Table 5.e: Colour frequency similarity values associated with cement grain hydration (CGH) on Faces 1 – 8 after 28 days of curing (M2 / 40 MPa)

Reference to layers of concrete cubes	Rate of cement grain hydration within CGC images at 28 days, in percentage			
	α1	**α2**	**α3**	**β1**
L_1	0.00	0.00	25.00	8.33
L_2	4.17	1.39	26.39	1.39
L_3	4.17	0.00	20.83	8.33

Table 6.e: Colour frequency similarity values associated with cement grain hydration (CGH) on Faces 1 – 8 after 7 days of curing (M1 / 30 MPa)

Reference to layers of concrete cubes	Rate of cement grain hydration within CGC images at 7 days, in percentage			
	α1	**α2**	**α3**	**β1**
L_1	26.39	2.78	0.00	4.17
L_2	22.22	6.94	0.00	4.17
L_3	13.89	4.17	2.78	12.50

Table 7.e: Colour frequency similarity values associated with cement grain hydration (CGH) on Face 1-8 after 21 days of curing (M1 / 30 MPa)

Reference to layers of concrete cubes	Rate of cement grain hydration within CGC images at 21 days, in percentage			
	α1	α2	α3	β1
L_1	6.94	5.56	0.00	20.83
L_2	8.33	0.00	0.00	25.00
L_3	8.33	0.00	0.00	25.00

Table 8.e: Colour frequency similarity values associated with cement grain corrosion (CC) on Faces 1 – 4 after 6 days of exposure

Reference to layers of concrete cubes	Rate of cement grain corrosion within CGC images at 6 days, in percentage		
	ɣ1	ɣ2	ɣ3
L_1	22.22	8.33	2.78
L_2	27.78	2.78	2.78
L_3	19.44	2.78	11.11

Table 9.e: Colour frequency similarity values associated with cement grain corrosion (CC) on Faces 1 – 4 after 9 days of exposure

Reference to layers of concrete cubes	Rate of cement grain corrosion within CGC images at 9 days, in percentage		
	ɣ1	ɣ2	ɣ3
L_1	19.44	8.33	5.56
L_2	11.11	5.56	16.67
L_3	5.56	0.00	27.78

Table 10.e: Colour frequency similarity values associated with cement grain corrosion (CC) on Faces 1 – 4 after 12 days of exposure

Reference to layers of concrete cubes	Rate of cement grain corrosion within CGC images at 12 days, in percentage		
	ɣ1	ɣ2	ɣ3
L_1	8.33	8.33	16.67
L_2	2.78	0.00	30.56
L_3	2.78	0.00	30.56

Table 11.e: Colour frequency similarity values associated with cement grain corrosion (CC) on Faces 1 – 4 after 24 days of exposure

Reference to layers of concrete cubes	Rate of cement grain corrosion within CGC images at 24 days, in percentage		
	ɣ1	ɣ2	ɣ3
L_1	8.30	0.00	25.00
L_2	2.78	2.78	27.80
L_3	27.80	2.78	2.78

Appendix F: Sensitivity of the experimental white pixel model at scanned point within M1 (30 MPa) and M2 (40 MPa)

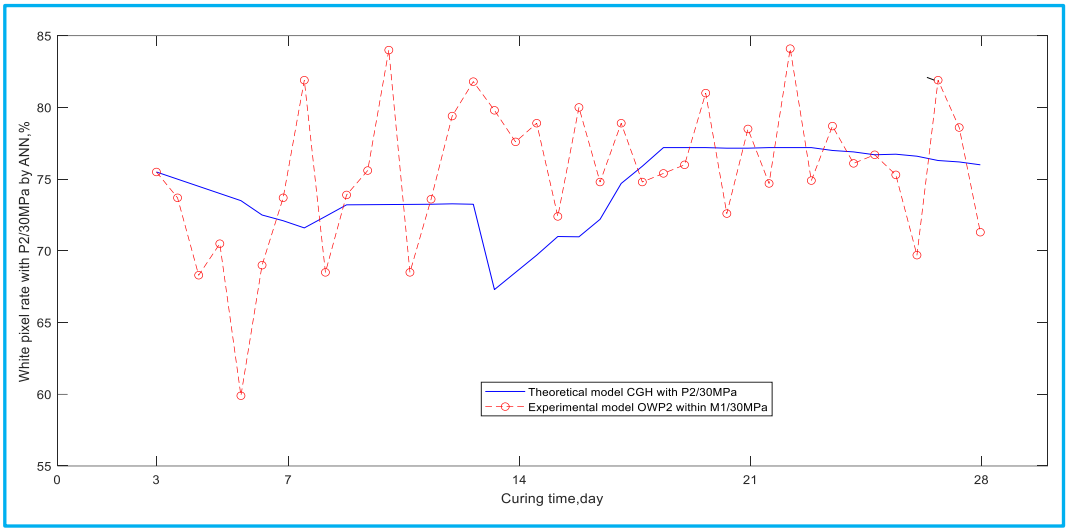

Figure 1.f: Sensitivity of the experimental white pixel (OWP2) model at scanned point P2 within M1 (30 MPa) in capturing the variation of the theoretical cement grain hydration (CGH) model

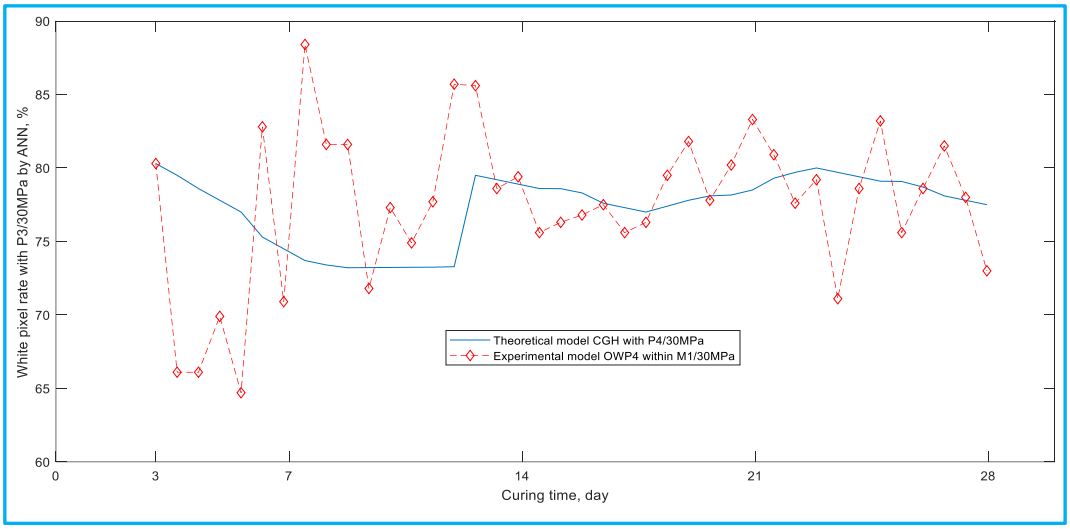

Figure 2.f: Sensitivity of the experimental white pixel (OWP4) model at scanned point P4 within M1 (30 MPa) in capturing the variation of the theoretical cement grain hydration (CGH) model

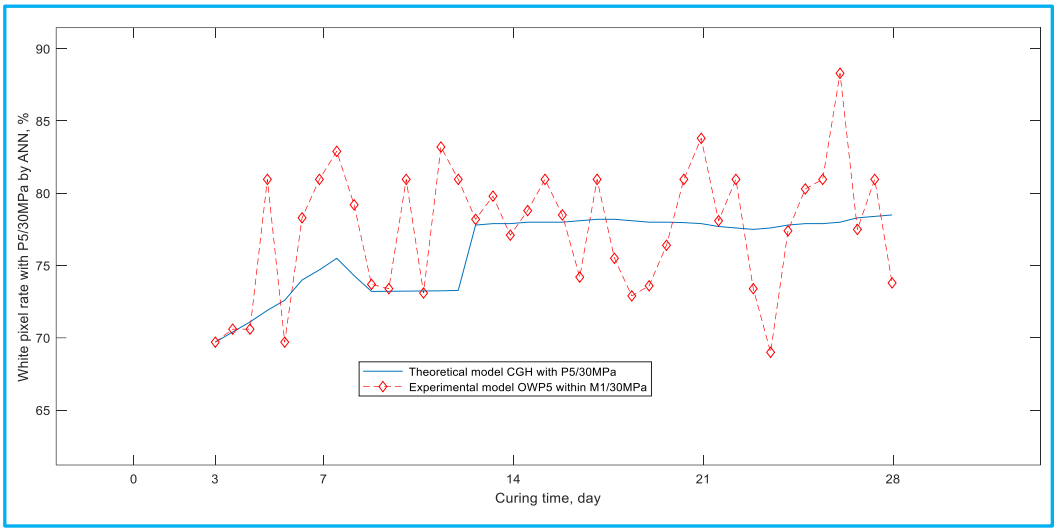

Figure 3.f: Sensitivity of the experimental white pixel (OWP5) model at scanned point P5 within M1 (30 MPa) in capturing the variation of the theoretical cement grain hydration (CGH) model

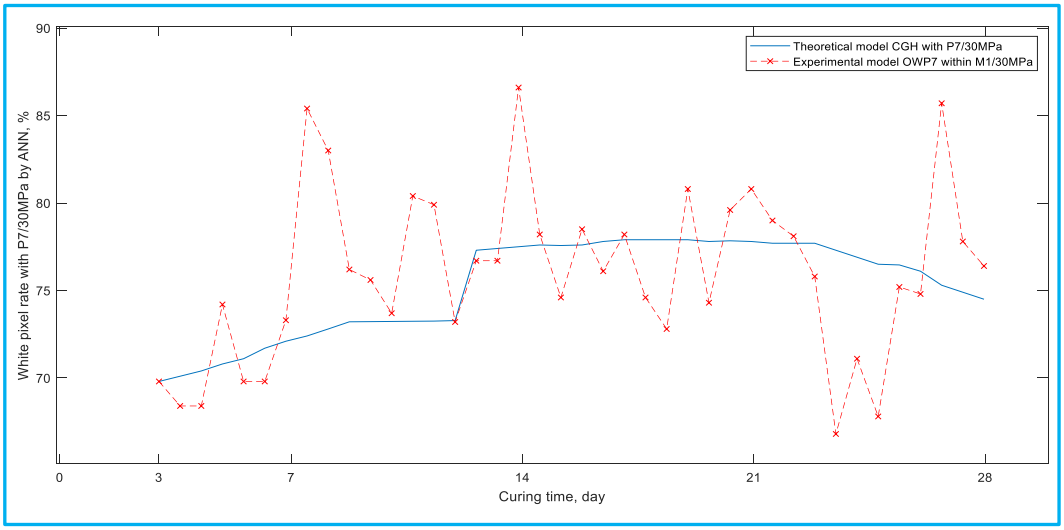

Figure 4.f: Sensitivity of the experimental white pixel (OWP7) model at scanned point P7 within M1 (30 MPa) in capturing the variation of the theoretical cement grain hydration (CGH) model

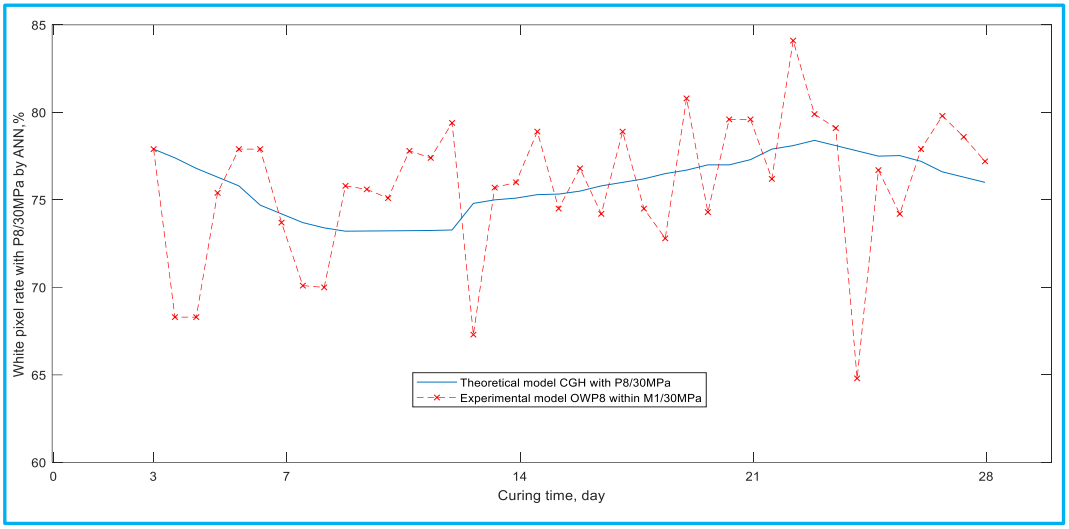

Figure 5.f: Sensitivity of the experimental white pixel (OWP8) model at scanned point P8 within M1 (30 MPa) in capturing the variation of the theoretical cement grain hydration (CGH) model

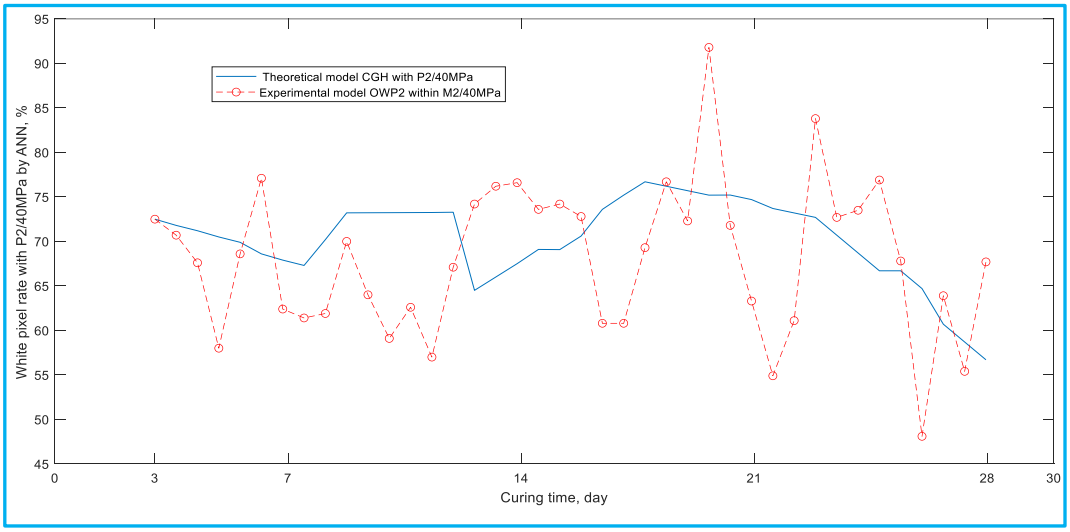

Figure 6.f: Sensitivity of the experimental white pixel (OWP2) model at scanned point P2 within M2 (40 MPa) in capturing the variation of the theoretical cement grain hydration (CGH) model

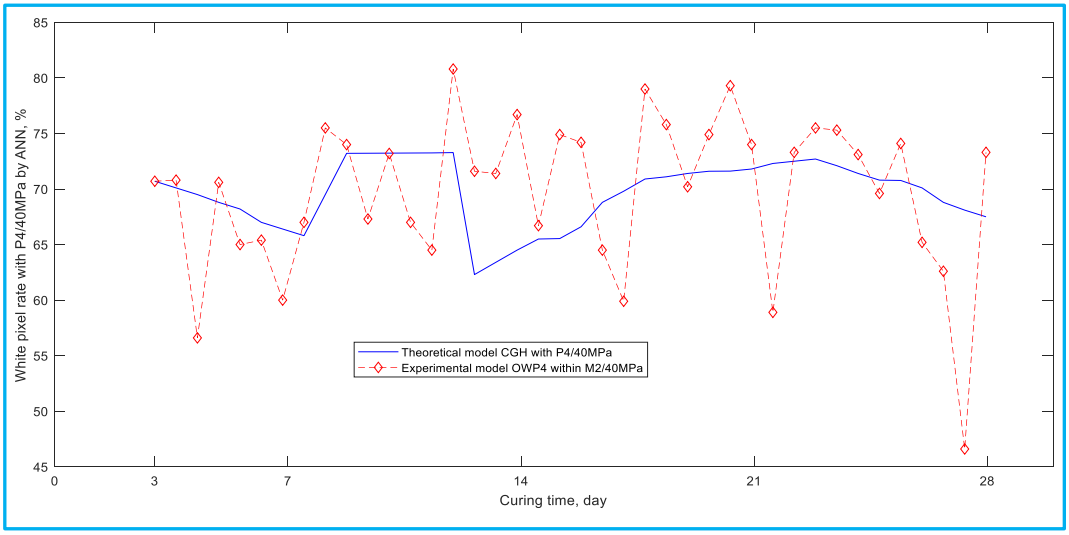

Figure 7.f: Sensitivity of the experimental white pixel (OWP4) model at scanned point P4 within M2 (40 MPa) in capturing the variation of the theoretical cement grain hydration (CGH) model

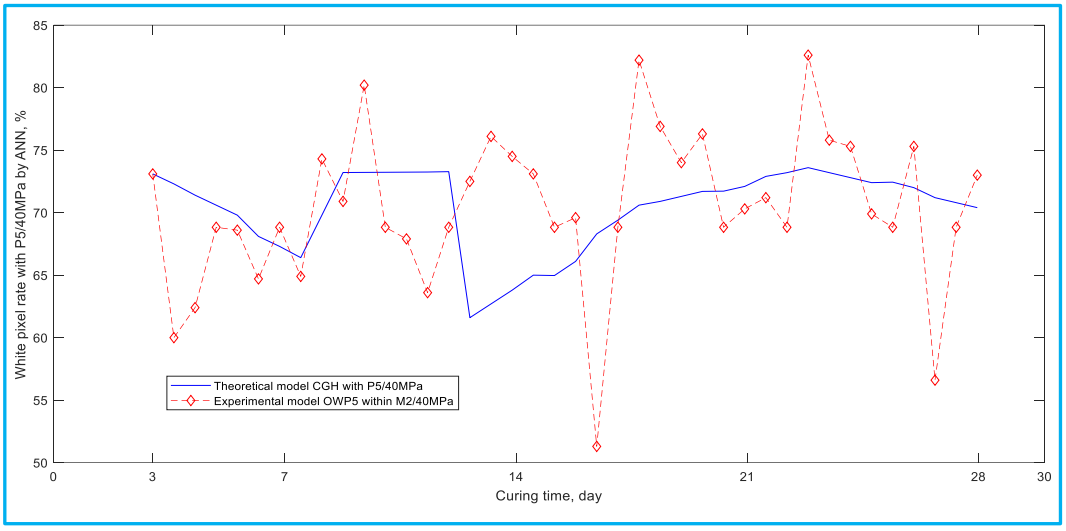

Figure 8.f: Sensitivity of the experimental white pixel (OWP5) model at scanned point P5 within M2 (40 MPa) in capturing the variation of the theoretical cement grain hydration (CGH) model

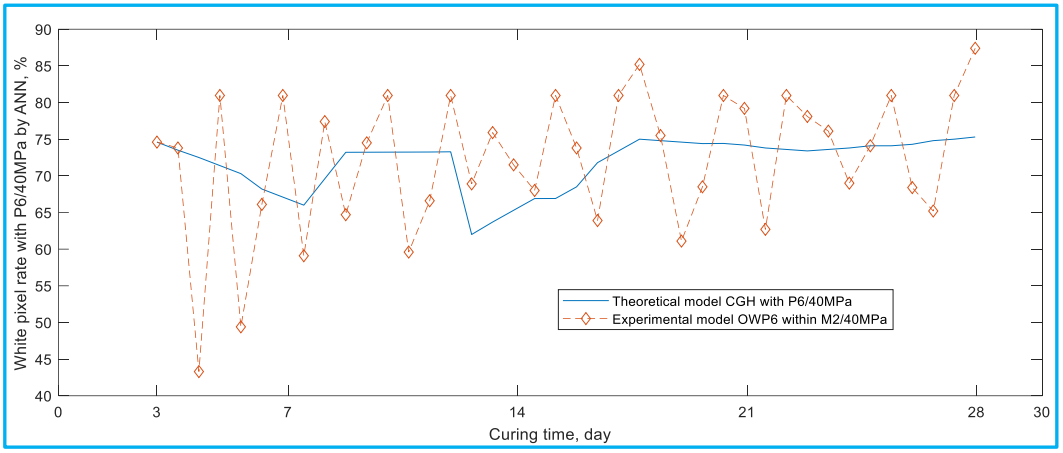

Figure 9.f: Sensitivity of the experimental white pixel (OWP6) model at scanned point P6 within M2 (40 MPa) in capturing the variation of the theoretical cement grain hydration (CGH) model

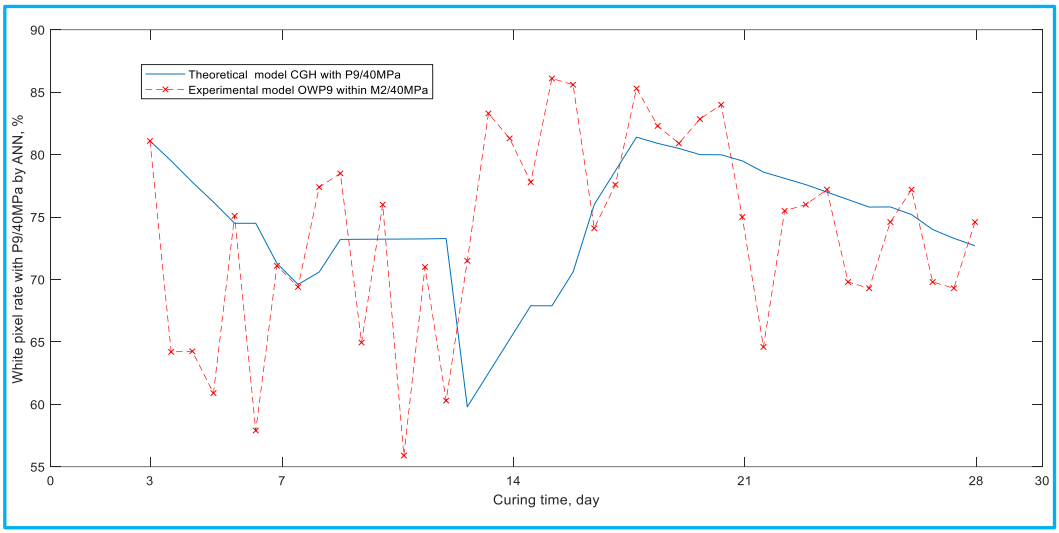

Figure 10.f: Sensitivity of the experimental white pixel (OWP9) model at scanned point P9 within M2 (40 MPa) in capturing the variation of the theoretical cement grain hydration (CGH) model

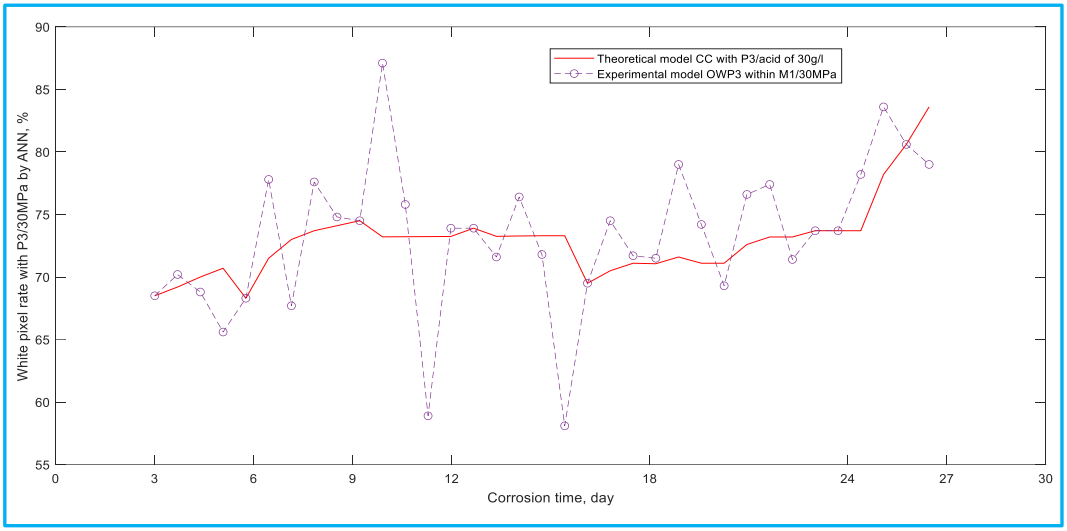

Figure 11.f: Sensitivity of the experimental white pixel (OWP3) model at scanned point P3 within M1 (30 MPa) in capturing the variation of the theoretical cement grain corrosion (CC) model tested to sulphuric acid concentration of 30 g/ℓ

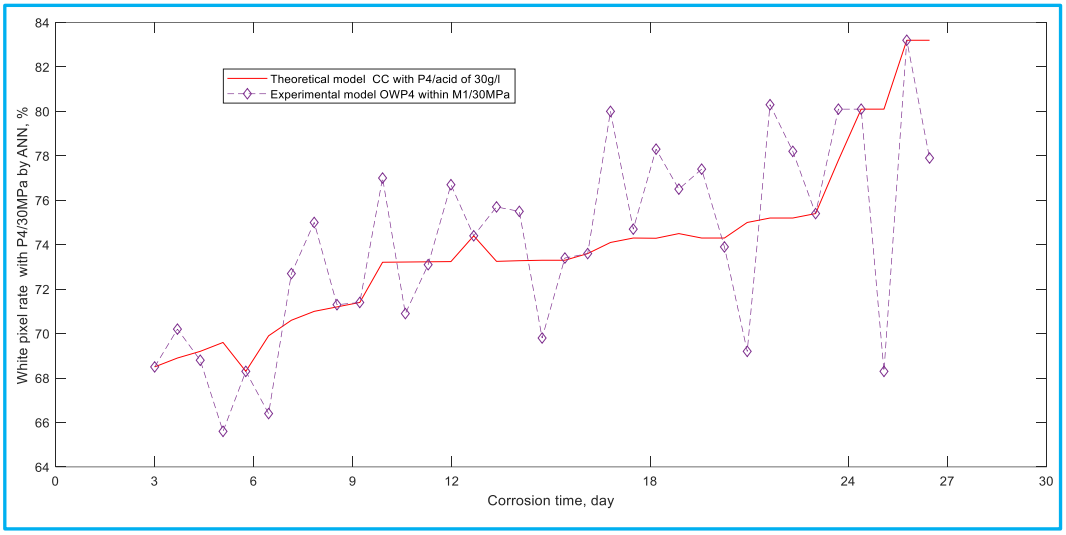

Figure 12.f: Sensitivity of the experimental white pixel (OWP4) model at scanned point P4 within M1 (30 MPa) in capturing the variation of the theoretical cement grain corrosion (CC) model tested to sulphuric acid concentration of 30 g/ℓ

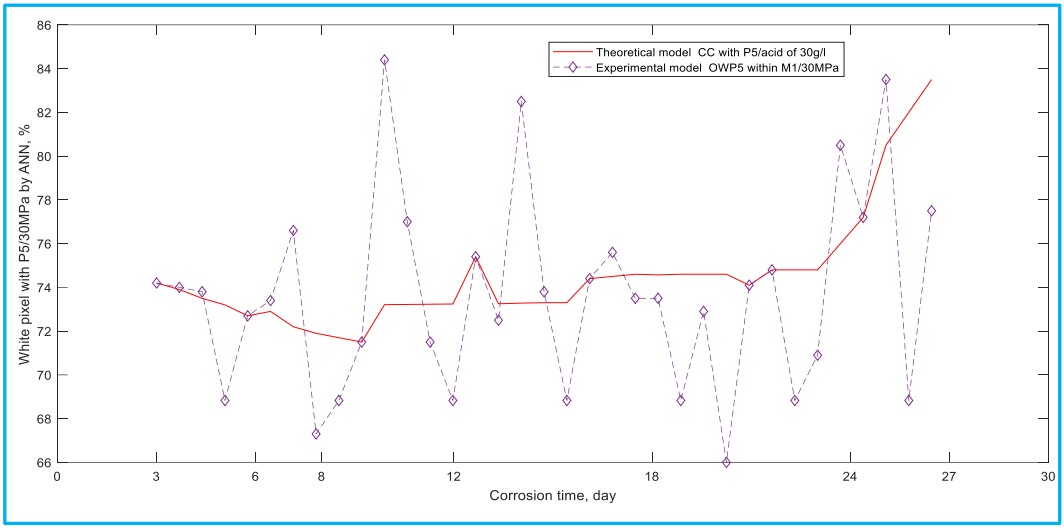

Figure 13.f: Sensitivity of the experimental white pixel (OWP5) model at scanned point P5 within M1 (30 MPa) in capturing the variation of the theoretical cement grain corrosion (CC) model tested to sulphuric acid concentration of 30 g/ℓ

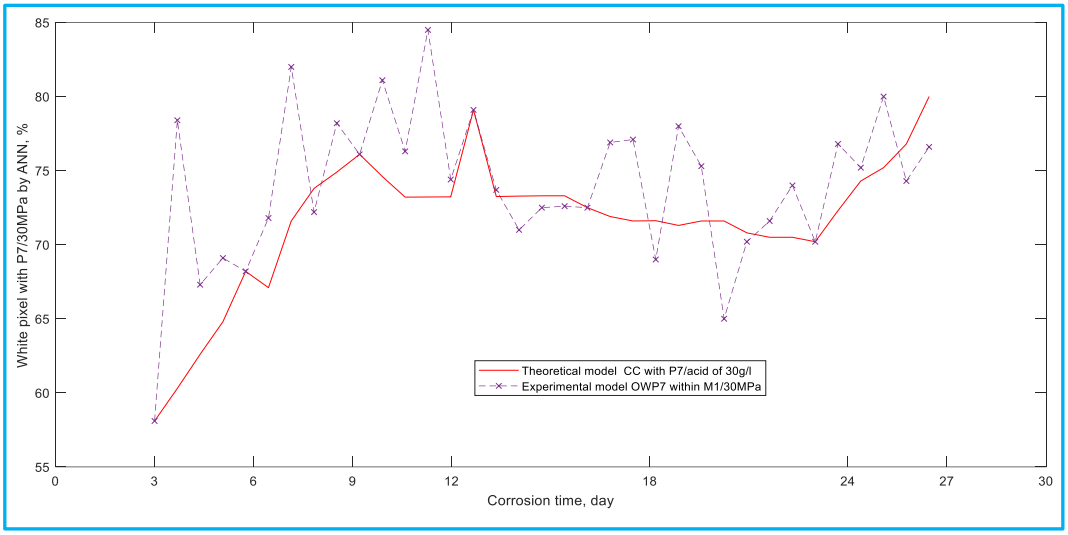

Figure 14.f: Sensitivity of the experimental white pixel (OWP7) model at scanned point P7 within M1 (30 MPa) in capturing the variation of the theoretical cement grain corrosion (CC) model tested to sulphuric acid concentration of 30 g/ℓ

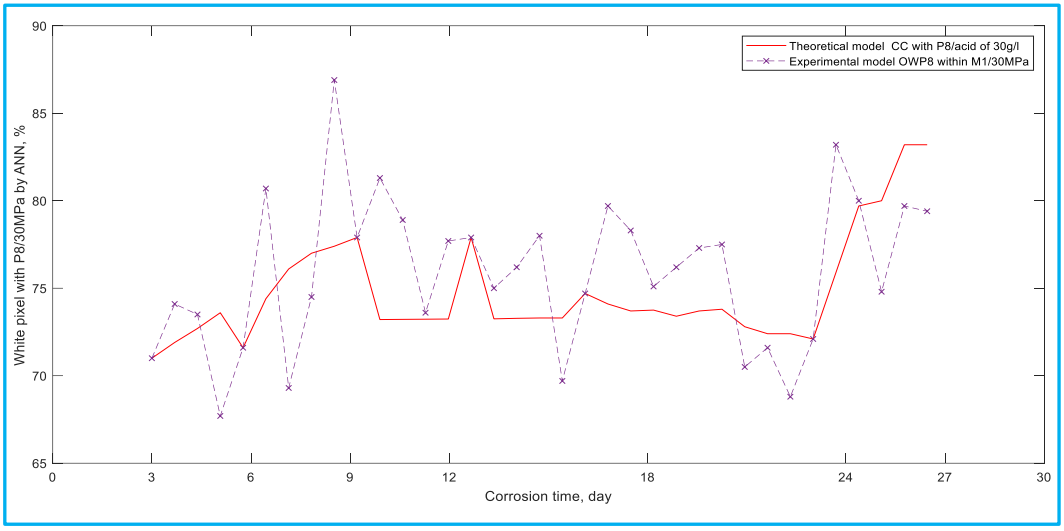

Figure 15.f: Sensitivity of the experimental white pixel (OWP8) model at scanned point P8 within M1 (30 MPa) in capturing the variation of the theoretical cement grain corrosion (CC) model tested to sulphuric acid concentration of 30 g/ℓ

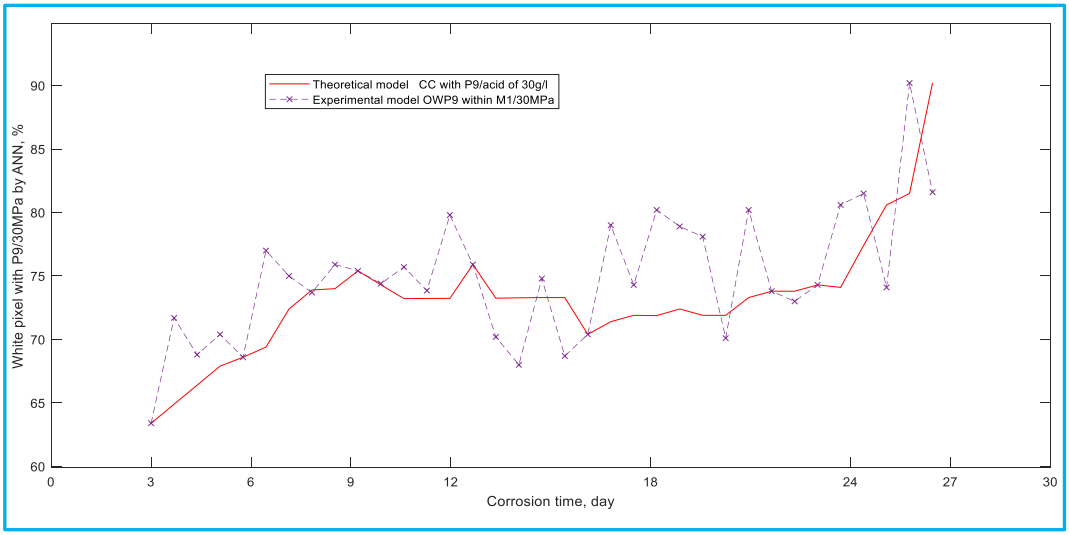

Figure 16.f: Sensitivity of the experimental white pixel (OWP9) model at scanned point P9 within M1 (30 MPa) in capturing the variation of the theoretical cement grain corrosion (CC) model tested to sulphuric acid concentration of 30 g/ℓ